MISSIONE 4
ISTRUZIONE
RICERCA

SCUOLA DI DOTTORATO
UNIVERSITA DEGLI STUDI DI MILANO-BICOCCA

UNIVERSITA' DEGLI STUDI DI MILANO BICOCCA

Department of Fisica

Dottorato di Ricerca in / PhD program Fisica e Astronomia Ciclo / Cycle XXXVIII

Curriculum in Fisica dei Plasmi e Biofisica

Surface Modification of Polymeric Substrates and Its Application in Textile Graphene-Based Smart Gas Sensors

Rabia Maryam

Registration Number: 906834

Tutor: Prof. Claudia Riccardi

Coordinator: Laura D'Alfonso

Finanziato dall'Unione europea NextGenerationEU | Ministero dell'Università e della Ricerca | Italiadomani PIANO NAZIONALE DI RIPRESA E RESILIENZA | UNIVERSITA DEGLI STUDI DI MILANO BICOCCA

Università degli Studi di Milano Bicocca
Dipartimento di Fisica
"Giuseppe Occhialini"

Corso di Dottorato in Fisica e Astronomia

XXXVIII ciclo

Curriculum Fisica dei Plasmi e Biofisica

Anno Accademico 2025-2026

Surface Modification of Polymeric Substrates and Its Application in Textile Graphene-Based Smart Gas Sensors

Dottoranda

Rabia Maryam **Tutor Prof. Claudia Riccardi**

906834

Acknowledgement

First and foremost, I would like to express my sincere gratitude to my supervisor, **Professor Claudia Riccardi,** for her continuous guidance, support, and encouragement throughout my PhD journey. At every stage of this work, she helped me overcome challenges with patience and clarity, and her mentorship played a crucial role in shaping both my research and personal growth. I am especially grateful for her understanding and support as an international student, which made my academic journey in Italy both comfortable and motivating. I would also like to sincerely thank the members of my department, **Prof. Ruggero Barni**, **Alessandro Meitner**, and **Alessandro Bao**, for their kindness, support, and willingness to help whenever needed throughout my PhD journey

I am also grateful to **Professor Tawfique Hassan** for providing valuable direction and insight during my research period abroad, which significantly contributed to the development of this work. During my time in Cambridge, I would like to sincerely thank **Dr Osarenkhoe Ogbeide (Dr. Ozzy)** for his support, guidance, and encouragement.

I would like to thank my parents, **Muhammad Riaz** and **Tabinda Jabeen**, for their unconditional love, constant encouragement, and unwavering support. Their belief in me and their encouragement to pursue my studies in Italy gave me the confidence and strength to complete this journey.

My heartfelt thanks go to my family members, especially my brother **Ashar Riaz**, my sister-in-law **Masooma Zahra**, and my beloved nephew **Muhammad Ibrahim** and niece **Abeeha Fatima**, whose love and presence always brought comfort and motivation.

Finally, I would like to thank my dear friend **Fareeha Maqbool**, who shared this PhD journey with me. Through every challenge and milestone, we supported each other, shared experiences, and grew together, making this demanding journey much more meaningful.

Abstract

Rapid urbanisation and industrialisation demand flexible and wearable air-quality monitoring technologies. This thesis reports the development of textile-based chemiresistive gas sensors using hand-embroidered silver interdigitated electrodes on nylon substrates and rGO/metal-oxide sensing inks for room-temperature detection of NO_2, NH_3, and CH_2O. Unlike conventional MOx gas sensors that rely on rigid substrates and elevated operating temperatures, the proposed approach enables low-temperature operation, mechanical flexibility, and textile compatibility. Oxygen plasma treatment was systematically investigated as a surface modification strategy for polymer substrates. On PTFE, plasma pressure–dependent changes in wettability, morphology, and surface chemistry were analysed using contact angle measurements, SEM, and FTIR, revealing ageing behaviour governed by competing morphological roughening and chemical functionalisation. Three ageing regimes were identified: morphology-dominated hydrophilicity, chemistry-controlled hydrophobic recovery, and eventual surface stabilisation. On nylon textiles, plasma treatment induced a transition from hydrophobic to superhydrophilic behaviour, with partial hydrophobic recovery dependent on exposure time. Enhanced rGO/CuO adhesion on plasma-treated nylon was confirmed by SEM/EDS mapping. Graphene-based nanomaterials were synthesised for sensing applications, including graphene oxide, graphene quantum dots, and reduced graphene oxide hybridised with metal oxides. While GQDs exhibited size-dependent quantum behaviour, limited yield restricted their applicability. rGO/CuO and rGO/CuO/SnO_2 nanocomposites was successfully synthesized for gas sensing. Textile gas sensors fabricated using rGO/CuO exhibited reliable responses to NO_2, NH_3, and CH_2O at low-ppm concentrations, with a minimum detectable NO_2 level of 6 ppm. Further enhancement of NO_2 sensitivity was achieved using dual metal oxide functionalisation (rGO/$CuCoO_x$), highlighting the critical role of sensing material composition in device performance.

Overall, this thesis demonstrates a feasibility of the new approach fo flexible, and textile based gas sensor development that avoids the need for advanced fabrication facilities. By integrating surface-engineered textiles with graphene-based hybrid sensing materials, the work presents a viable pathway toward distributed and indicative gas monitoring in industrial and resource-limited environments, with potential for future adaptation to indoor air-quality monitoring following further sensitivity optimisation.

Publications

R Maryam, H. Eduardo Roman, Ruggero Barni, Anastasia A. Anceschi, Alessia Patrucco, Katia Alexander, Igor Levchenko, Claudia Riccardi, Smart graphene oxide-based advanced textiles: A review of wearable smart clothing, personal thermal management, and sensor applications, *Carbon*, 121519

Roman, H. E., Cesura, F., **R Maryam**, Levchenko, I., Alexander, K., & Riccardi, C. (2024). The fractal geometry of polymeric materials' surfaces: surface area and fractal length scales. *Soft Matter*, *20*(14), 3082-3096.

Memon, H., Liao, S., **R Maryam**, Patrucco, A., & Riccardi, C. (2024). Development of medical masks: performance, properties, and prospects. *Materials Advances*, *5*(21), 8333-8350.

R Maryam, Ruggero Barni, H.Eduardo Roman, Claudia Riccardi Ageing Analysis of Oxygen Plasma-treated PTFE surfaces: Role of Plasma Pressure on Wettability and Surface Chemistry. Under the process (To be submitted)

Conferences

C Piferi, M Daghetta, E Tucci, **R Maryam**, E. H. Roman, and C. Riccardi. Plasma etching polymeric surfaces: from nanostructure to fractals 49th EPS Conference on Plasma Physics, EPS 2023 **Abstract and Poster Presentation**

R Maryam, E Tucci, C. Riccardi, Tuning the surface wettability of graphene-coated polymeric substrate by plasma treatment, 49th EPS Conference on Plasma Physics, EPS 2023 **Abstract and Poster Presentation**

R Maryam, J Fornara, R Barni, C Riccardi Regulating the wettability properties of Polytetrafluoroethylene (PTFE) via oxygen plasma treatment: influence of the operating pressure and examining the ageing behaviour 50th EPS Conference on Plasma Physics, EPS 2024 **Abstract and Poster Presentation**

R Maryam, H Roman, C Riccardi, Enhancing polyethylene terephthalate (PET) surface wettability properties through Oxygen Plasma Treatment and Graphene Coating 50th EPS Conference on Plasma Physics, EPS 2024 **Abstract and Poster Presentation**

R. Maryam, J. Fornara, R. Barni, C. Riccardi, A Study on Aging of Polytetrafluoroethylene (PTFE) after Plasma Treatment, PCCP 25th anniversary symposium, Amsterdam, Netherlands **Poster presentation**

R. Maryam, H.E Roman, C. Riccardi. Development and characterisation of Graphene (GO) coated polyethylene terephthalate (PET) plasma treated by oxygen PCCP 25th anniversary symposium, Amsterdam, Netherlands **Poster presentation**

Courses

- New lignin-based sustainable materials: science and technological aspects
- Introduction to Deep Learning for Physicists
- Master class big data
- Photonic Crystals
- Scanning and Transmission Electron Microscopy, Principles and Applications

Seminars And Workshops

Seminars

Atomic-scale Quantum Light by Prof. Jeremy Baumberg, Atomic-scale Quantum Light (University of Cambridge, UK)

Quantum Fluids of Light by Dr Daniele Sanvitto, Quantum Fluids of Light (CNR Nanotec, Italy) (University of Cambridge, UK)

Metal-Organic Vapour Phase Epitaxy and Its Application In Quantum Technologies Dr Emanuele Pelucchi (Tyndall National Institute, Ireland) (University of Cambridge, UK)

Workshops

AFM Workshop & User Training at Royce, University of Cambridge, UK

XPS Data Processing Workshop Trainer: Shaoliang Guan at Royce, University of Cambridge, UK

Table of Contents

List of Figures

LIST OF TABLES

CHAPTER 1 Introduction

1. Introduction

1.1 Air pollution and Human Health relationship

Air pollution is among the significant challenges to health and the environment and affects well-being worldwide. It can be classified into two broad categories, namely, ambient (outdoor) and household (indoor) pollution, which are among the second major causes of death worldwide. During the past ten years, more than 80 million people have died from diseases linked to inhaling polluted air. The World Health Organisation (WHO) now estimates that air pollution takes seven million people's lives every year all over the world from exposure to anthropogenic outdoor pollutants such as carbon monoxide (CO), carbon dioxide (CO2), nitrogen dioxide (NO_2), sulphur dioxide (SO_2), ozone (O_3) and particulate matter (PM2.5 and PM10), emitted mostly from vehicles and industries in urban areas In rural areas, the burning of solid fuels such as wood, crop wastes, charcoal and cow dung in open fires emit vast quantities of CO and NO_2, causing an array of diseases from pneumonia and heart disease to lung cancer. For instance, breathing in NO_2 can damage the lungs and respiratory system. It is deadly if inhaled and causes serious burns to the skin and eyes. Another dangerous gas in the air is NH_3. It burns the skin and eyes severely, is poisonous to breathe, harms aquatic life significantly, and can ignite easily.

1.2 Background and Motivation

The significance of gas detection was evident during the Industrial Age, when the population of workers started to experience severe health and safety issues because of exposure to dangerous gases. As one of the measures, the industries in which people were also in danger had to have an opportunity to detect harmful gases and notify the workers in time. One of the first areas where such protection was required is coal mining. In the bid to enhance mine safety, there was the coming of early gas detection mechanisms. The Davy lamp was one of the earliest gas detectors, invented in 1816[1]. It utilised an oil flame that was enclosed in a metal mesh. The mesh would allow the gas to pass through the lamp and not the flame outside the lamp, thus minimising the hazard of explosions. Flammable gases like methane would increase the height of the flame in the lamp and alter the colour. With further exposure, the flame would increase even more, heat the lamp, and make it red[2], evidently indicating to the miners that the environment was not favourable and that they were to exit the mine. Even with its historical significance, the Davy lamp possesses a questionable heritage. In some instances, its

application has been linked to a rise in deadly mine accidents and explosions. This was largely attributed to poor handling of the device and a false sense of security, which prompted miners to venture into places in the mines that were once thought to be too dangerous.

At the beginning of the twentieth century, the Davy lamp was gradually changed by a safer, cheaper and more effective one, the canary bird[3]. The canaries were used to give a warning signal of dangerous gases like carbon dioxide (CO_2), carbon monoxide (CO) and methane (CH_4). Since 1911, British coal miners used to carry canaries in cages into mine tunnels on a regular basis. Even when canaries were subjected to dangerous gases, even in low concentrations, they would immediately respond by ceasing to sing or they would display signs of visible distress or they would perish thus giving a rapid alert that they have to evacuate. In British coal mines this was still practised until the year 1986, when the practice was superseded by electronic gas detection systems, all of which were cheaper, more reliable, and able to give measurable and objective results. Through the study of the use of canaries in the past and the types of gas safety mechanisms that have been developed in the mining sector, it becomes easy to determine the background concerns that have led to the resurgence of research in this field. The industrial need is high in gas sensors with faster response times, high safety, ease of use, portability, less expensive and high sensitivity to a target gas in comparison with the available solutions. Thus the study in this area is aimed at enhancing sensing parameters to suit such industrial needs[4-7].

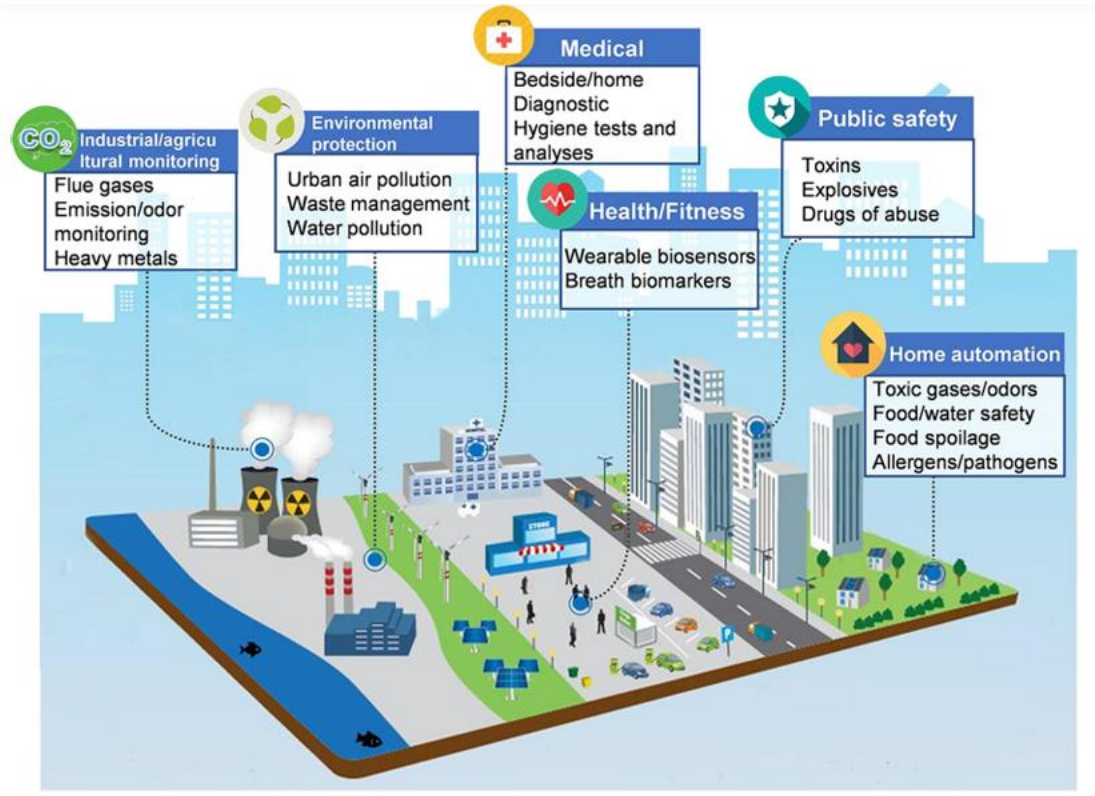

Figure 1. 1Illustration of sensor use in different aspects of human life [8]

After the gas detection technologies were first deployed in the coal mining industry, they were gradually transferred to a broad variety of industries, such as pharmaceutical production, industrial safety, security, health and air-quality monitoring of the environment[8]. The continuous and reliable nature of gas monitoring made the requirements of such applications paramount thus the development of different sensing technologies which served these purposes. Currently, metal oxide (MOx)-based sensors are dominating the commercial gas sensor market. This is largely because of their relatively cheap cost, good performance in sensing, and suitability with simple fabrication and integration process and also because of their possible miniaturisation and integration in multi-gas detection systems[9, 10]. Irrespective of these strengths, MOx sensors have a number of known weaknesses, including high operating temperatures, high power consumption, low selectivity, poor long-term stability, and slow response and recovery times[9, 11-13]. These limitations limit their applicability in portable, wearable and low-power sensing scenarios. Simultaneously, graphene and other two-dimensional (2D) have become the subject of considerable attention as gas sensors. Their large surface-volume ratio, adjustable electrical characteristics and abundant surface chemistry render them extremely responsive to gas adsorption reactions[8]. Though 2D-material-based sensors also have their own set of problems, especially making them selective, they are highly

electrically conducting, which allows them to rapidly transduce signals, operate with low power and in some instances even room-temperature sensing. Moreover, the surfaces of 2D materials can serve as viable surfaces upon which other functional components can be immobilised e.g. metal or metal oxide nanoparticles, and this can be used to enhance the sensing activity [14, 15]. These complementary properties have inspired an integrated approach of sensing that incorporates MOx materials with 2D materials in nanocomposites. The incorporation of 2D material in the construction of MOx-based gas sensors is an active research direction because it aims to address the inherent drawbacks of each material separately despite the improved sensitivity, selectivity and electrical properties[16]. Moreover, the high-throughput deposition of MOx/2D nanocomposite inks can be achieved using scalable and well-developed fabrication methods, such as printing, which lowers the manufacturing cost and enhances industrial feasibility [17]. The recent tendencies in research are directed at flexible and wearable gas sensors to be used in real-time monitoring of the environment. Particularly, sensing platforms made out of textiles have become a promising alternative because of their mechanical adaptability, power efficiency, comfort, and interoperability with smart-fabric technologies.

1.3 Technical And Graphene based Smart Textile

In general, textile materials are typically categorised into *apparel textiles*, which are primarily aesthetic, and technical textiles, which serve functional purposes[18]. The inherent properties of textile materials offer clear and compelling advantages over traditionally bulky or flat electronic structures. Bulky systems are generally inflexible, while planar electronic devices can be made into thin, flexible films. However, these films often deform when bent in one direction and are prone to failure under extreme twisting or other mechanical stress. In contrast, smart fabrics are typically composed of fibres that can endure significant deformation while maintaining mechanical stability. Additionally, smart textiles possess low density and inherent breathability, which are essential for both microelectronics integration and wearable comfort, respectively[19].

1.3.1 Electronic textiles with sensing applications

Electronic textiles (ETs), or e-textiles, integrate fabrics with components like batteries, light emitters, controllers, or sensors. Smart clothing and wearables widely use them today, especially fibre-based ETs with sensing for autonomous robotics, sports motion tracking, daily activities, medical monitoring (respiration, skin hydration, tactile sensing, wound care), and

humidity sensors for respiration/moisture detection. In austere environments such as space, extraterrestrial surfaces (the Moon, Mars), or underwater, reliable monitoring of movement is critical. The authors report wearable, flexible graphene oxide stress sensors for real-time monitoring of human body parameters, states, and positions, as well as automatic equipment monitoring [20]. These sensors have excellent sensitivity and signal strength across a wide strain range, alleviating the need for additional instrumentation for signal processing and amplification. Their low cost makes them virtually disposable, which may bene fit such applications as smart clothing. In [21], the authors investigate ET humidity sensors made from both natural and synthetic fibers such as cotton, wool, and the widely used Coolmax, which is a fabric specifically engineered to wick moisture away from the skin to its outer surface, helping to keep the wearer dry during intense physical activity. The study demonstrates that a graphene oxide (GO)-functionalized Coolmax sensor (GO-Coolmax) achieves an ultrafast response and recovery time, typically under 0.6 seconds, marking a significant advancement over existing ET humidity sensor technologies. Qureshi et al.[22] designed embroidered moisture sensors in the form of a fabric-based sensor with an interdigitated mesh of polyamide thread (Silver-tech 150/HC12) as electrodes on cotton fabric to detect biomedical fluids, including sweat and blood serum, in wound dressing. Kang et al. [23] demonstrated very sensitive and wearable NO_2 gas sensors by coating cotton yarn with chemically functionalized graphene oxide to develop a flexible and textile-based sensing element, which has high adsorption due to thermal/chemical treatments.

1.3.2 Current Status and Research Gap

Recent progress in wearable and textile-based gas sensors has been mainly aided by the fast progression of printed electronics and functional nanomaterials, which allowed making flexible, lightweight, and sensitive environmental monitoring gadgets. According to reviews published recently[24], a wide range of different materials, including graphene derivatives and metal-based sensing layers, are able to be incorporated with flexible substrates, including textiles through scalable fabrication methods. These advancements show the good potential of textile platforms to be used in gas sensing applications and, at the same time, be wearable and flexible in its mechanical aspect.

Although printed electronics is a well-established and popular fabrication pathway, it demands specialised equipment, controlled processing environments, and infrastructure that are not easily available everywhere. Conversely, hand embroidery provides a low-cost, equipment-

free, and simple method that aligns naturally with textile production and can be adopted in resource-limited or rural environments. However, the use of hand-embroidered interdigitated electrodes (IDEs) for chemiresistive textile-based gas sensing has not been sufficiently explored. In particular, the integration of rGO/metal-based sensing ink on embroidered nylon substrates for NO_2 and NH_3 detection remains limited, indicating a research gap in developing accessible, wearable, and robust textile gas sensors using embroidery as a practical alternative or complementary fabrication approach.

1.4 Plasma

Plasma is often known as the fourth state of matter, which is separate from solids, liquids, and gases, and is created when enough energy is input into a gaseous system to partially or wholly ionise it. In this state, the electrons are no longer attached to the nuclei of atoms, thus forming an assortment of neutral atoms, ions and free electrons among other reactive species[25]. Plasma is capable of responding to external electric and magnetic fields and is highly electrically conductive because of the presence of charged particles, unlike normal gases. Plasma may be produced by providing energy in either thermal excitation or, more often, controlled pressure conditions by supplying an electric field. Although the total composition of plasma is electrically neutral, its density of free charge carriers is large, and it is the combination of these characteristics that leads to the appearance of unique physical and chemical properties of the plasma. These attributes render the use of plasma a versatile material in surface modification, as it allows physical etching and chemical activation of the material without changing the bulk properties of the material[26].

1.4.1 Oxygen Plasma

Oxygen plasma consists of a complex mixture of energetic species, including free electrons, neutral oxygen atoms and radicals, metastable and excited molecular oxygen species, ions, and ultraviolet radiation[27]. These reactive parts are produced by electron-molecule collisions in the plasma discharge and cause high chemical activity of oxygen plasma. Of these species, neutral atomic oxygen is the predominant modifier of polymer surfaces since it is very reactive, whereas the ozone produced in the plasma is also a minor contributor. There are also positively and negatively charged oxygen ions and electrons, all of which are involved in reactions in the gas phase and at the surface. These charged species recombine in the gas phase or at material surfaces, depending on operating pressure, with surface recombination prevailing at low pressure. The combination of these reactive oxygen species with polymer surfaces causes bond

scission, surface etching, and functional group quantities, including oxygen, to form effective surface activation, and it does not influence bulk material properties[28].

1.4.2 Plasma Etching of Polymers with Oxygen Plasma

Plasma etching is a surface modification process in which polymer materials are exposed to energetic plasma species that remove surface material at the micro- to nanoscale. This process is typically carried out using non-polymerising gas plasmas, where charged particles and reactive species generated within the plasma interact with the surface[29, 30]. During plasma etching, energetic electrons transfer energy through collisions with gas molecules, producing ions, radicals, and excited species via ionisation, excitation, and dissociation processes[31]. These reactive species interact with the polymer surface, leading to bond scission and the formation of volatile reaction products. The etched fragments are subsequently desorbed from the surface and continuously removed from the plasma chamber by the vacuum system, while fresh process gas is supplied, allowing sustained material removal[32].

The etching mechanisms that involve plasma etching can be generally categorized as physical and chemical etching based on the plasma gas, and the plasma condition. Physical etching is commonly done in an inert gas plasma, like argon, where energetic ions are incident on the surface and push material off the surface, causing sputtering with a very low degree of chemical selectivity. By comparison, chemical etching uses reactive gases, including oxygen, in which neutral radicals diffuse to the surface and react chemically with the polymer to produce volatile products resulting in isotropic and more selective material ablation[33]. The contribution of ions and neutral species varies remarkably with pressure, where at higher pressures the contribution of the neutral species is larger, and at lower pressures the contribution of the ion-assisted etching is more important. The consistency of the etching of a surface in plasma is determined by the plasma density, distribution of gas flow, and the geometry of the reactor, and constant working conditions are sought to ensure that the reactive species are not depleted in the localised areas of surface etching[34].

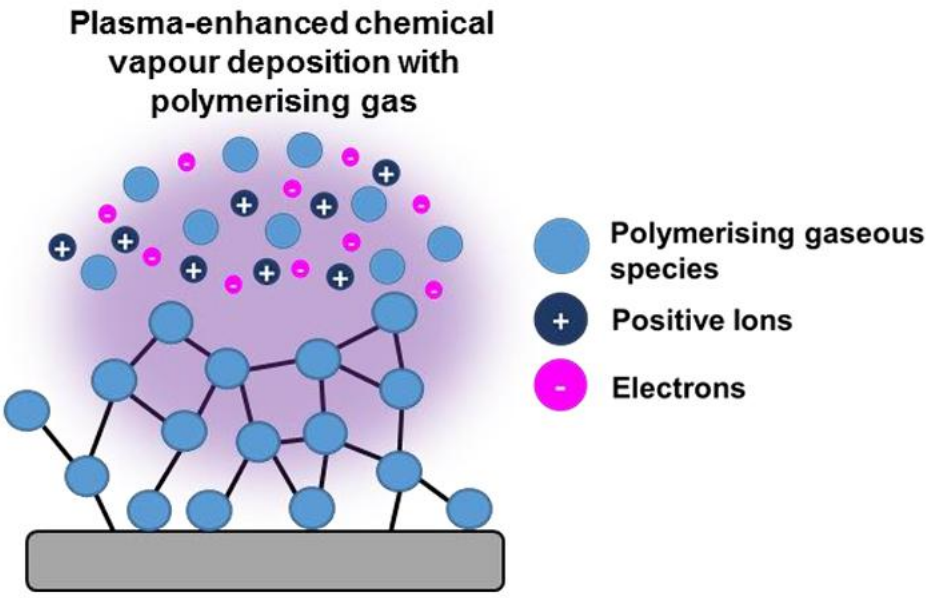

Figure 1. 2 Schematic illustration of the effects of plasma etching on a polymer surface using a non-polymerising gas plasma.

When polymer materials are exposed to oxygen plasma, a range of physical and chemical surface modifications can occur, depending on processing parameters such as gas flow rate, discharge power, plasma type, and treatment duration. These effects include the incorporation of oxygen-containing polar functional groups (e.g., hydroxyl and carbonyl groups), surface etching, and partial degradation of near-surface polymer chains caused by energetic species and ultraviolet radiation. Atomic oxygen radicals play a primary role in the etching process by breaking chemical bonds and abstracting hydrogen atoms from polymer backbones, leading to the formation of reactive surface sites[35]. These sites may further react with molecular oxygen, resulting in chain scission and removal of surface material rather than simple functionalisation. In addition to oxygen radicals, ions, metastable species, and UV/VUV photons contribute to polymer etching through energetic collisions that can exceed typical polymer bond energies. Since these plasma–surface interactions are generally exothermic, excessive treatment can lead to unwanted heating and over-etching of the polymer surface[35].

1.5 Aim of Research

This research aims to investigate plasma-induced surface modification and ageing behaviour of polymer materials, and to apply this understanding toward the development of a flexible, low-cost textile-based sensing platform using hand-embroidered electrodes and graphene-based functional materials.

1.6 Structure of thesis

Chapter 1 introduces the broader context of air pollution and its impact on human health, followed by an overview of the development and evolution of gas sensing technologies. The emergence of smart and sensing textiles is discussed, highlighting their potential for flexible and wearable sensing applications. The current status of textile-based sensing systems and the associated research gaps are then identified, motivating the need for alternative fabrication and material approaches. Plasma surface modification of polymers is subsequently introduced as a supporting technology for tailoring material surfaces and understanding ageing effects. Finally, the aim and scope of the research are presented, outlining the framework for the experimental studies and device development described in the following chapters.

Chapter 2 describes the characterisation techniques used to analyse the structural, morphological, and chemical properties of the materials studied in this research. The principles and relevance of each technique are also briefly explained to help in interpreting the experimental results.

Chapter 3 focuses on the ageing behaviour of oxygen plasma-treated PTFE surfaces. This chapter introduces PTFE and the applied plasma processing parameters, followed by an evaluation of plasma-induced wettability changes using contact angle measurements. Morphological modifications are examined, and surface chemical changes associated with ageing are analysed using FTIR, providing both qualitative and quantitative insights into the influence of plasma pressure on surface wettability and chemistry over time.

Chapter 4 examines the surface modification and ageing behaviour of nylon treated with oxygen plasma, including an assessment of plasma processing parameters, wettability changes, morphological evolution, and surface chemical modifications. In addition, the chapter investigates the deposition and interaction of rGO/metal oxide inks on plasma-treated nylon, highlighting the role of plasma-induced surface changes in supporting material adhesion and functional integration.

Chapter 5 describes the synthesis of graphene oxide, graphene quantum dots, and rGO/metal oxide composites, followed by their structural, morphological, and chemical characterisation. Techniques including XRD, FTIR, Raman spectroscopy, SEM, and TEM are used to evaluate the properties of the synthesized materials and their suitability for subsequent integration into textile-based devices.

Chapter 6 focuses on the fabrication of smart textile gas sensors using hand-embroidered and inkjet-printed electrodes with rGO–metal oxide inks. It reviews the state of the art in gas-sensing materials and device architectures, followed by the formulation and characterisation of rGO/CuO and rGO/$CuCoO_x$ inks. The chapter then describes the fabrication of textile-based gas-sensing devices and the experimental setup used for sensing measurements. Finally, the sensing mechanism and performance of the fabricated devices are discussed.

CHAPTER 2 Characterisation Techniques

This chapter outlines the key experimental methods used to probe the morphology, crystal structure, and surface chemistry of the synthesised samples through various analytical techniques. Specifically, X-ray Diffraction (XRD), Scanning Electron Microscopy (SEM), Transmission Electron Microscopy (TEM), Raman Spectroscopy, Fourier Transform Infrared Spectroscopy (FTIR), and UV-Vis Spectroscopy, as applied to the materials investigated in this thesis.

2. Characterisation Techniques

2.1 X-ray Diffraction Technique

X-ray diffraction (XRD) is a widely used technique for investigating the structural properties of materials. It measures the atomic spacing between planes of atoms within a crystalline structure[36]. XRD is commonly used to obtain information about the molecular arrangement and crystalline phases present in a material. Through this technique, key parameters such as , crystallite size, phase composition, crystal orientation, and degree of crystallinity can be determined[37]. Furthermore, it is a nondestructive technique i.e it does not damage the sample's surface during characterisation[38]. From the 1940s, the instrumentation of X-ray diffraction measurement is not much more changed. The difference observed is the use of computers for control, data processing, and data acquisition in modern instrumentation[37].

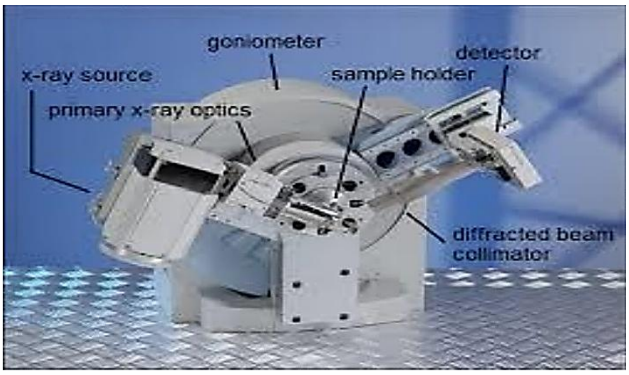

Figure 2. 1 Instrumentation of X-ray Diffraction

2.1.1 Working Principle

X-ray diffraction works on the principle of Bragg's law. When the interaction between the sample and the incident rays generates constructive interference, the condition is satisfied that Bragg's law condition.

$$n\lambda = 2dsin\theta \quad (1)$$

Where n = order of reflection (an integer)

λ = wavelength of X-rays

d = atomic spacing

θ = diffraction angle

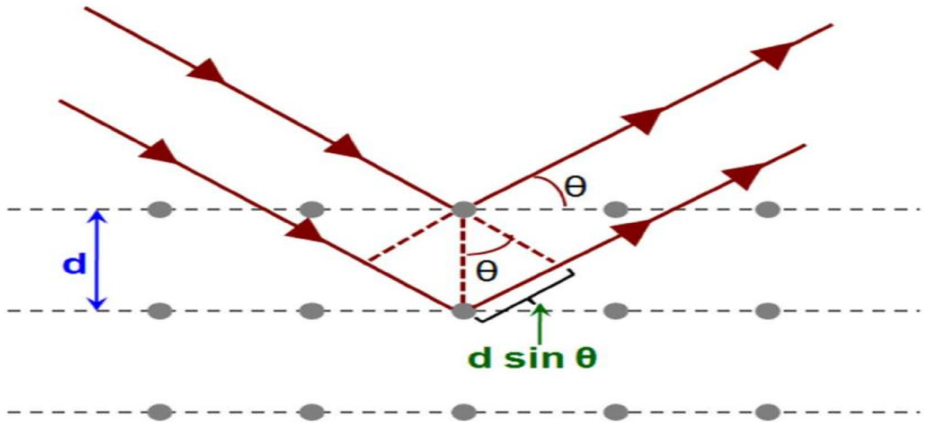

Figure 2. 2 Schematic Diagram of X-ray Diffraction

This equation relates the wavelength to the lattice spacing and the diffraction angle. The X-rays that are diffracted from the sample are detected by the detectors, processed and, calculated. By examining the sample via a range of 2 theta angle, the diffraction directions should be achieved because of random directions of the powdered sample. Every compound has a unique d-spacing between the layers of the atom, so the conversion to d-spacings from diffraction peaks allows us to the identification of the sample's compound. Normally, it is attained by comparison of d-spacing to the reference patterns.

2.1.2 Instrumentation

X-ray characterization has three basic components

- X-ray Tube
- A holder in which the sample is placed
- A Detector that detects the X-rays[39]

Electrons are produced by heating the filament. These electrons move towards the target by applying the voltage and strike the electrons on the target material. X-rays are generated when enough energy of electrons removes the inner shell electrons of the sample. Mostly copper is used for single diffraction as a target material with CuK_{α} = 1.54 **Å**. The X-rays are directed at the sample. The detector and the samples are rotated continuously, the intensity of the X-rays is verified. The detector collects the data and then processes the signals. A converter converts the signal which is monitored by a computer.

2.2 Scanning Electron Microscope

A Scanning Electron Microscope (SEM) is a powerful characterization technique used to obtain detailed information about the surface topography, structure, shape, size, morphology, and chemical composition of a sample. It gives a clear and 3-D image version of the samples. The pieces of information which we obtained from SEM are due to focusing high energy beam of electrons on the sample[40].

2.2.1 Zeiss FEG Gemini 500 Electronic Microscope

The Zeiss Gemini 500 Scanning Electron Microscope (SEM) features a field emission electron (FEG) source. The microscope can operate with accelerating voltages of 0.5–30 kV, beam currents of 3 pA–20 nA, and has a nominal resolution of 0.6 nm at 15 kV. In addition to the common in-camera detectors for secondary (SE) and backscattered electrons (BSE), the instrument is equipped with an in-lens detector (BSE/SE) for high-resolution imaging and a STEM detector for transmission observations of thin and biological samples. The FEG-SEM also features an integrated Bruker QUANTAX EDS/WDS (Energy Dispersive/Wave Dispersive) microanalysis system , specifically designed for the analysis of light elements, which are notoriously limited by X-ray fluorescence-based microanalysis systems. Finally, the FEG-SEM is equipped with a QUANTAX EBSD (Electron Backscattered Diffraction) system for crystallographic analysis of samples. The EBSD system is equipped with an Argus detector for forward-scattered electrons (FSE) and backscattered electrons, for the acquisition

of images in which the contrast is determined by the different orientations of the grains. The wide range of detectors with which the FEG-SEM is equipped makes it an extremely powerful instrument for the characterization of synthetic materials, geological samples, and biological samples at the submicroscopic scale.

Figure 2. 3 Zeiss FEG Gemini 500 Electronic Microscope

(https://piattaformadimicroscopia.unimib.it/strumenti/microscopio-elettronico-zeiss-feg-gemini-500/)

2.2.1 Working Principle

A scanning electron microscope uses the beam of electrons to produce an image. The beam of electrons is produced from the filament and then strikes on the sample's surface by the use of lenses in the electron column. By striking the beam of electrons, different types of emissions are produced, such as Backscattered electrons, Auger electrons, visible light, heat, X-ray photons, which carry different types of sample information. When a ray of electrons bounces back from the nucleus of atoms that are present on the surface of the sample, these are called backscattered electrons. They have greater energy than other electrons and carry topographical information. Incident electrons that are scattered in the sample and create inelastic collisions with electrons that are inside the shells of atoms result in the formation of X-rays. When electrons are excited back from low state, the X-rays of fixed wavelengths are created**[41]**. When an electron from a higher energy shell transitions to fill a vacancy in an inner shell, the excess energy can be released in the form of an Auger electron. While X-ray emission provides

information about the elemental composition of the sample, Auger electrons offer additional insight into the chemical and ionization states of the elements present on the sample surface.**[42]**.

2.2.2 Instrumentation

SEM has following components

- Electron Gun
- Focus lens
- Magnetic lens
- Scanning Coils
- Specimen Holder
- Signal Detector

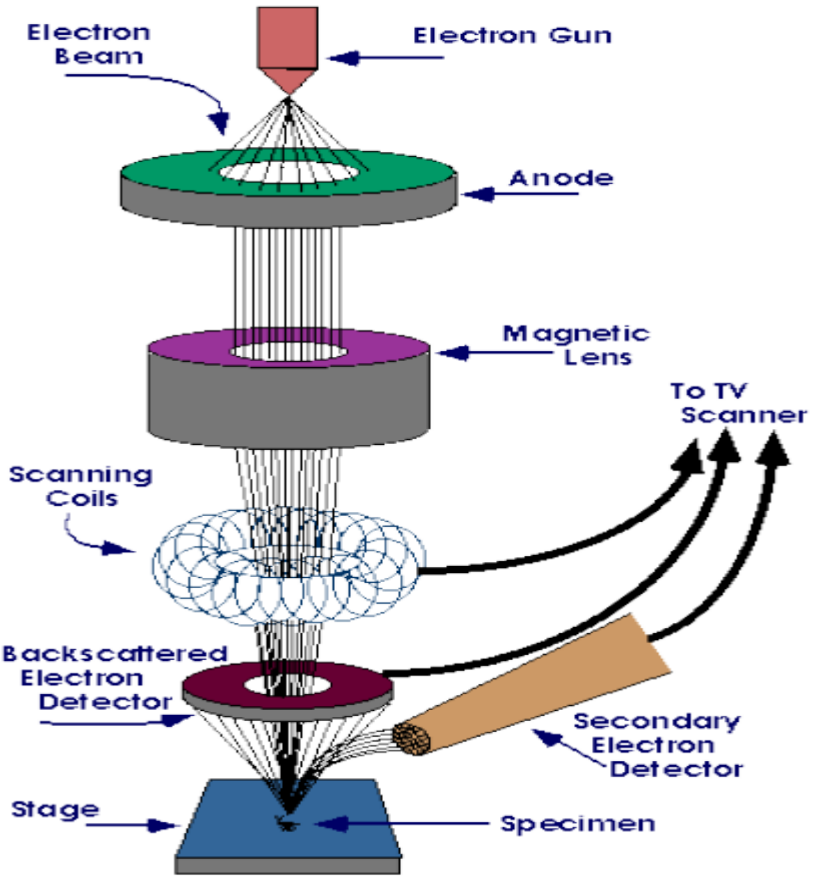

Figure 2. 4 Instrumentation of Scanning Electron Microscope[43]

Moreover, SEM is considered a nondestructive characterisation technique, as the X-rays generated by the interaction of the electron beam with the sample surface do not cause

permanent damage to the material[44]. Moreover, SEM is considered a nondestructive characterisation technique, as the X-rays generated by the interaction of the electron beam with the sample surface do not cause permanent damage to the material

2.3 Transmission Electron Microscope (TEM)

The Transmission Electron Microscope (TEM) is a crucial technique in nanomaterials, enabling in-depth analysis of both surface and internal structures by utilising transmitted and scattered electrons from a sample. This technique generates highly detailed images with fine resolutions as the unit cell level. TEM achieves atomic-scale magnification without pixel loss, enabling visualization of lattice fringes, atomic arrangements, and critical structural elements such as dopants, interfaces, and defects. These insights prove invaluable for photocatalysis, gas sensing, bioimaging, and related fields, where such features directly dictate performance.

2.3.1 JEOL JEM 2100 Plus Transmission Electron Microscope (TEM)

The JEOL JEM 2100 Plus Transmission Electron Microscope (TEM) has a LaB 6 source and can operate at acceleration voltages ranging from 80 to 200 kV. The high-resolution pole pieces with which the instrument is equipped allow a spatial resolution of 0.24 nm, which, together with the wide tilt range (+/- 45° with a standard double-tilt specimen holder), makes it extremely versatile and suitable for a variety of types of investigations. The instrument can also operate in STEM (scanning) mode and is equipped with a detector for bright field (BF) observations and an annular detector for high-angle diffraction dark field (HAADF) observations. TEM images are acquired using a highly sensitive Gatan CMOS camera with a 9-megapixel sensor. This, combined with the ability to insert a special in-gap aperture under the sample to reduce radiation damage, makes the instrument particularly suitable for working with sensitive samples. The JEM 2100P is equipped with an Oxford EDS (Energy Dispersive System) nanoanalysis system with an 80 mm2 sensor , which is particularly sensitive and efficient, even in compositional mapping, for which a drift correction system is provided. Finally, a special aperture to be inserted upstream of the sample allows for the reduction of spurious peaks in the spectrum, improving the peak-to-background ratio. The variety of possible observation modes combined with the great instrumental performance make the JEM 2100P a very versatile instrument suitable for the characterization of very different samples, such as synthetic materials, biological and geological samples and nanoparticles.

Figure 2. 5 JEOL JEM 2100 Plus Transmission Electron Microscope (TEM)

(https://piattaformadimicroscopia.unimib.it/strumenti/microscopio-elettronico-a-trasmissione-tem-jeol-jem-2100-plus/)

2.3.2 Working Principle

TEM works by producing a focused electron beam from an electron gun, using thermionic emission from a tungsten filament that is accelerated to high energies (80-400 kV) through an electromagnetic column under high vacuum. The gun generates electrons from a hot tungsten wire or field tip. Condenser lenses focus on the beam: C1 sets probe size, C2 adjusts brightness, and C3 controls the angle, with holes limiting signals. Samples must be thin, which is under 80 microns on 3 mm grids and made by slicing, grinding, dimpling metal pieces or ion-milling nonmetals. The objective lens focuses on the eccentric spot for sharp images or diffraction patterns. Intermediate lenses switch modes and fix electron spiral, while projector lenses blow up the picture onto a glowing screen, CCD camera, or out to tools like EELS for extra data.

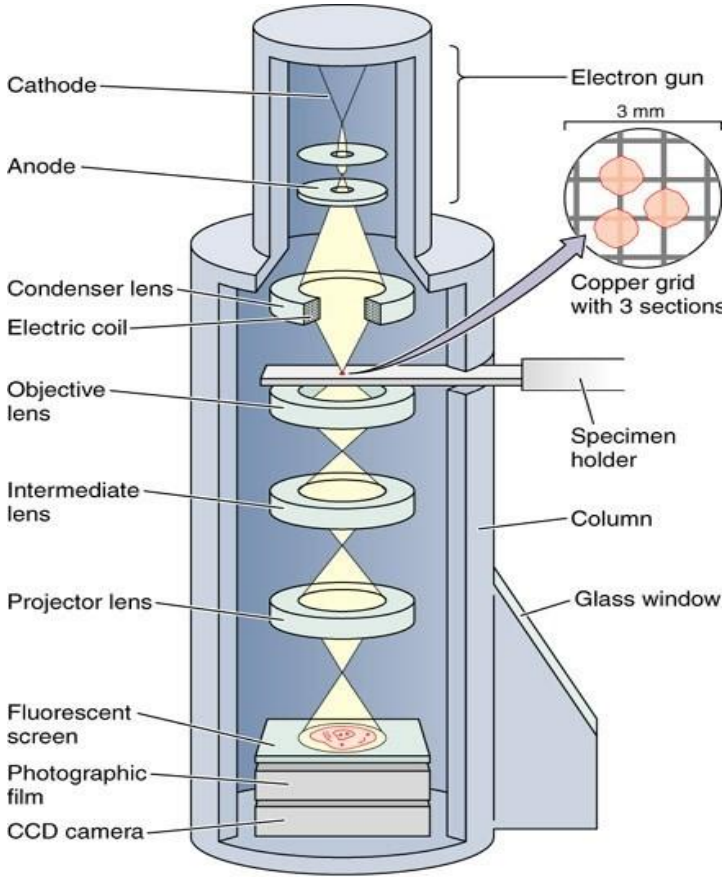

Figure 2. 6 Schematic diagram of Transmission Electron Microscope showing electron gun, condenser lens, objective lens, projector lens, specimen holder and fluorescent screen

2.4 Raman Spectroscopy

Sir Chandrasekhara Venkata Raman introduced Raman spectroscopy in 1928. In his original experiment, sunlight was used as the excitation source, a telescope served as the light collector, and the scattered light was observed directly with the human eye. For this pioneering discovery, he was awarded the Nobel Prize in Physics in 1930[45]. Raman spectroscopy is a widely used technique in materials science, as it provides rotational, vibrational, and structural fingerprints that enable the identification of different materials[46]. It is a fast characterisation tool for the samples. It is dependent on inelastic or Raman scattering of monochromatic light, generally from the laser in the near-ultraviolet and visible range. The light relates to phonons, subatomic vibrations, and also results in the peaks' shift. The information patterns about vibrational modes are due to the rise and fall shifts of energy[47]. The schematic representation of a Raman spectroscopy instrument is shown in Figure ( ).

Figure 2. 7 Instrument of Raman spectroscopy

2.4.1 Working Principle

In Raman spectroscopy, monochromatic light is used as the excitation source. When this light interacts with the sample, electrons are promoted to higher energy levels. Following this excitation, a portion of the scattered photons undergo elastic scattering, known as Rayleigh scattering, in which the energy of the scattered photons remains nearly identical to that of the incident light. During inelastic scattering, energy exchange occurs between the incident photons and the molecular vibrations of the sample. If the scattered photons possess lower energy than the incident photons due to vibrational relaxation, the process is referred to as Stokes Raman scattering. Conversely, when the scattered photons exhibit higher energy than the incident photons, the process is termed Anti-Stokes Raman scattering. In most Raman spectroscopic measurements, Stokes lines are preferentially recorded because they exhibit significantly higher intensity compared to Anti-Stokes lines[48].

The Raman shift corresponds to the energy difference between the incident photons and the scattered photons. This energy difference provides valuable information about the rotational and vibrational modes of the sample. As a result, the Raman shift serves as a characteristic fingerprint for material identification and structural analysis. The Raman scattering mechanism is illustrated schematically in Figure ( ).

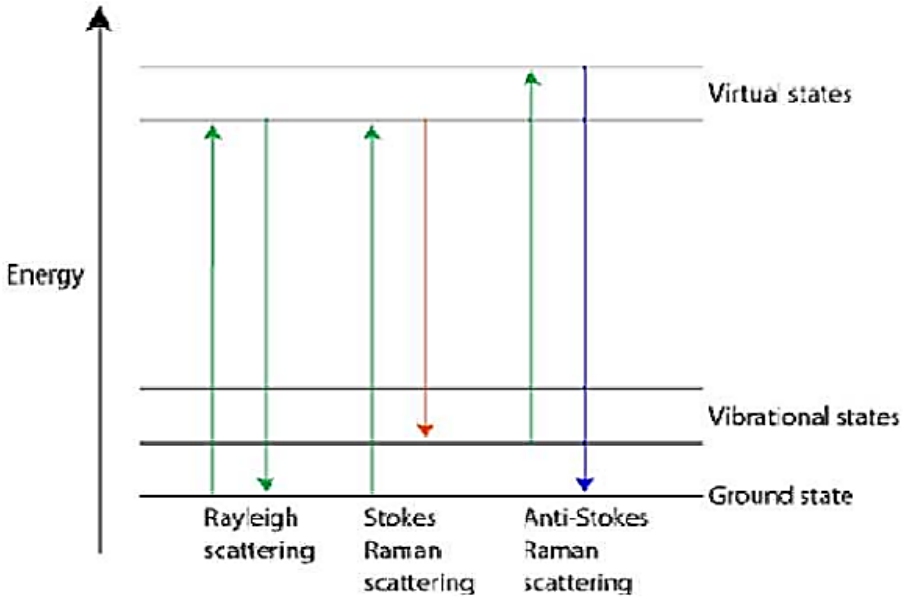

Figure 2. 8 Schematic illustrations of the Raman Scattering mechanism

2.4.2 Instrumentation

- Laser Beam
- Notch Filter
- Entrance Slit
- Monochromator

Figure 2.6 illustrates the experimental setup of a Raman spectroscopy system. A laser beam is used as the excitation source and is directed through a notch filter before passing through the entrance slit and striking the surface of the sample. The scattered radiation from the sample is then collected by a lens positioned in the optical path. Subsequently, a monochromator is used to separate the scattered light into its constituent wavelengths. The resulting signal is detected by a sensitive photomultiplier, which converts it into an electrical signal. This signal is then transferred to a computer system for data processing, storage, and display[49].

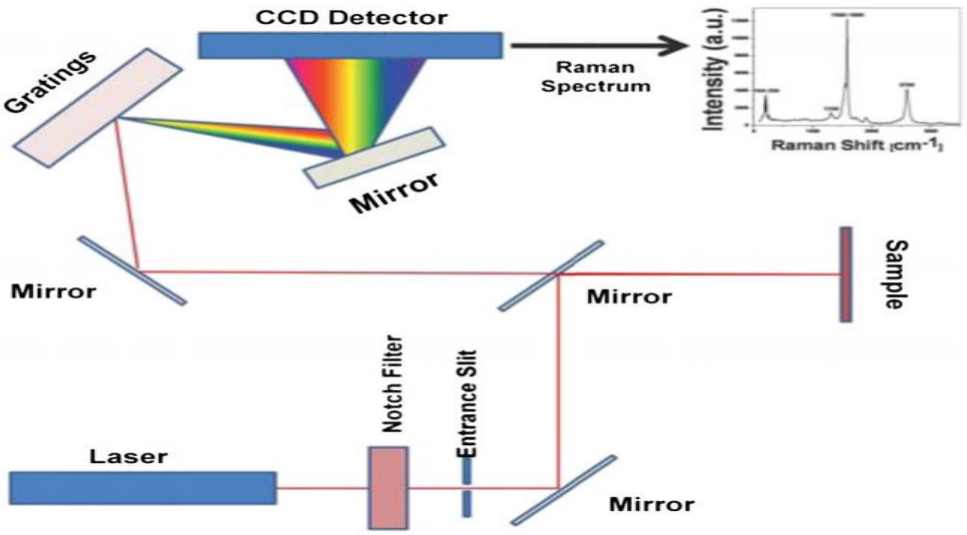

Figure 2. 9 Schematic Diagram of Raman Spectroscopy

2.5 Fourier Transform Infrared Spectroscopy (FTIR)

Fourier Transform Infrared (FTIR) spectroscopy is a technique used to identify the vibrational characteristics of functional groups present in a sample[50]. It is considered a versatile analytical method because it provides spectral information over a wide range of infrared regions, including near-IR (4000–14,000 cm^{-1}), mid-IR (400–4000 cm^{-1}), and far-IR (4–400 cm^{-1}). When infrared radiation interacts with a sample, the chemical bonds undergo various vibrational motions such as stretching, bending, and twisting. The absorption of IR radiation by specific functional groups occurs at characteristic wavenumber ranges, producing a unique spectral fingerprint of the material.[51].

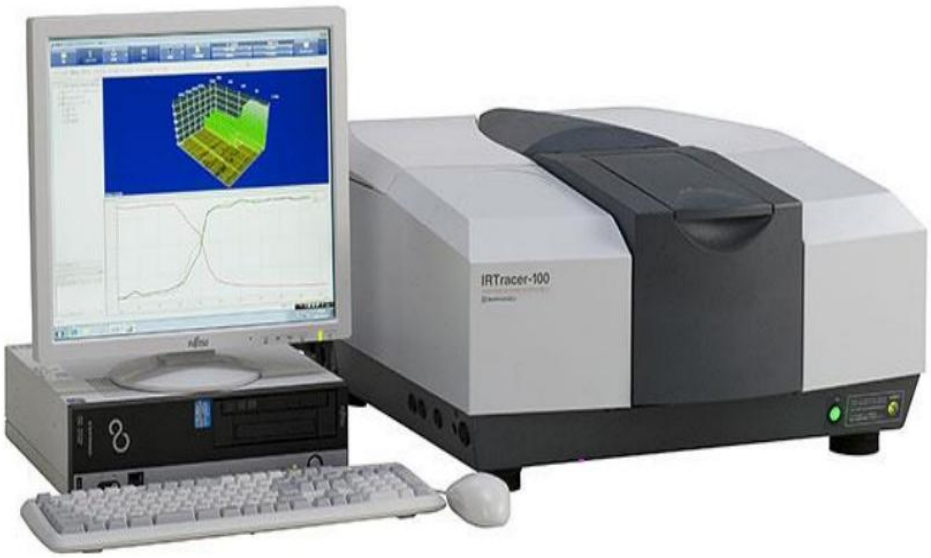

Figure 2. 10 FTIR Spectroscopy

https://uwm.edu/chemistry/instrumentation/shimadzu-laboratory-of-advance-andapplied-analytical-chemistry/instrumentation/ftir-ir-tracer/)

2.5.1 Working Principle

When infrared radiation is applied to a sample, specific wavelengths are absorbed by the molecules, causing their vibrational energy to transition from the ground state to an excited state. This absorption is accompanied by a change in the dipole moment of the molecules. The intensity of the resulting absorption bands depends on both the energy level transitions and the magnitude of the dipole moment[52].

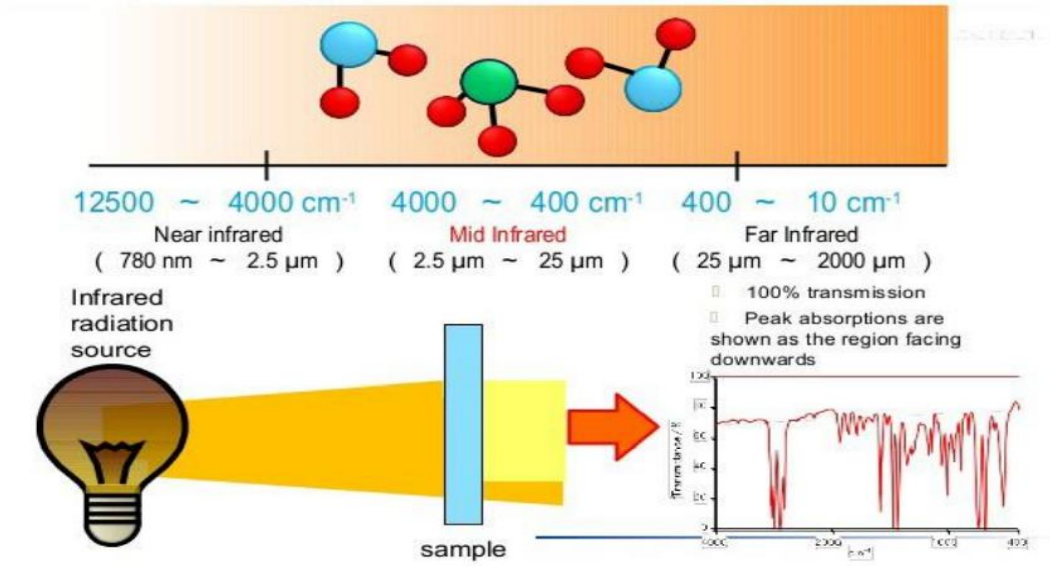

Figure 2. 11 Working Principle of FTIR

2.5.2 Instrumentation

FTIR is based on the following components

- Source of Radiations
- Amplifier
- Detector
- Converter
- Interferometer
- Computer for display

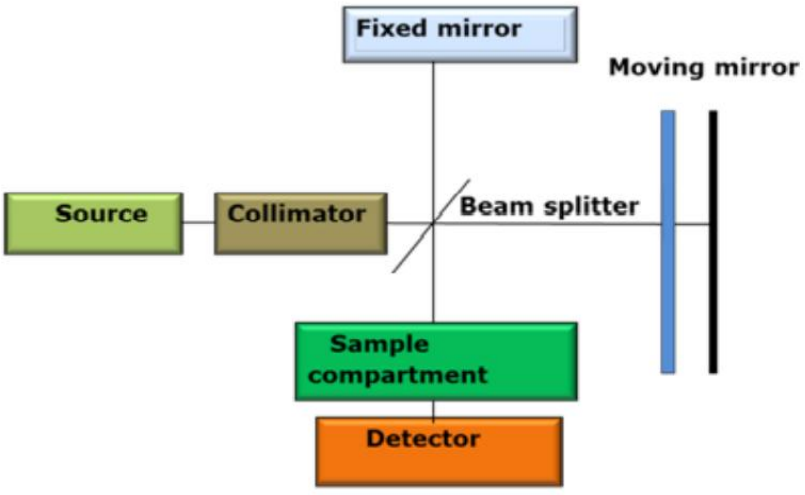

Figure 2. 12 Schematic illustrations of FTIR [53]

From the source, the radiations are produced which then strikes the sample by using an interferometer. Radiation reaches the detector after moving across the sample. Amplifier picks the signal, and then the digital converter converts the analogue signal into a digital signal. Lastly, the digital signal is transferred into the computer, in which the FT (Fourier transform) takes place[54].

2.6 UV-Visible Spectroscopy

UV-Vis Spectroscopy (or Spectrophotometry) is a quantitative technique used to measure how a material absorbs light. By comparison of intensities of the reference sample and under observation sample UV-visible spectroscopy is carried out. This technique can be utilized for multiple sample types including glass, thin films, solids, and liquids[55].

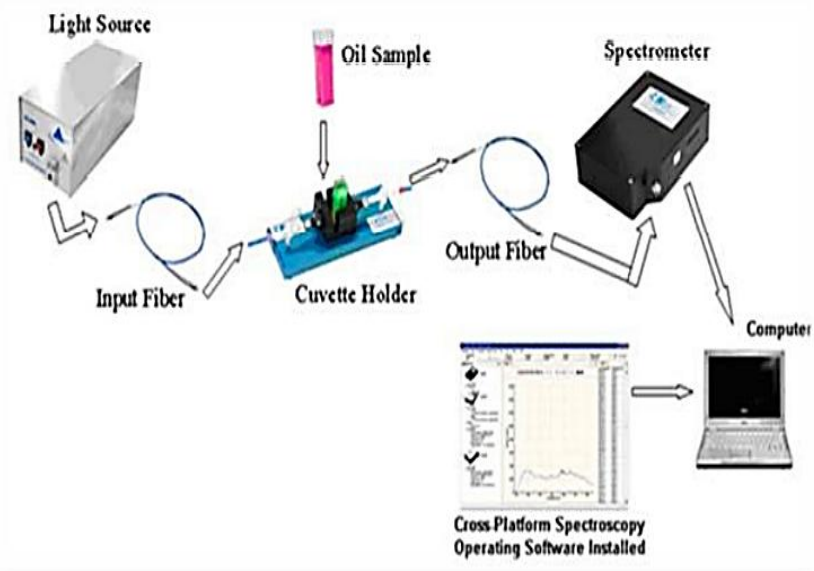

Figure 2. 13 Experimental Setup for UV-visible spectroscopy[56]

2.6.1 Working Principle

The Principle of UV-visible spectroscopy depends on the assimilation of visible light or ultraviolet light by chemical compounds, from which different spectra are produced. The interaction between light and matter is known as spectroscopy. When light is absorbed into the matter, the process of excitation and de-excitation starts then as a result of this process the spectrum is produced. When ultraviolet radiation is absorbed in the matter, the excitation of electrons starts. From this excitation, process electrons start to jump from lower energy states to higher energy states. Note that the variation in lower energy state and higher energy state is

consistently equal to the amount of visible radiation or ultraviolet radiations which are absorbed by it[57].

2.6.2 Instrumentation

Following instruments are used in UV-visible spectroscopy:

- Light Source
- Monochromator
- Sample and reference cells
- Detector
- Amplifier
- Recording devices

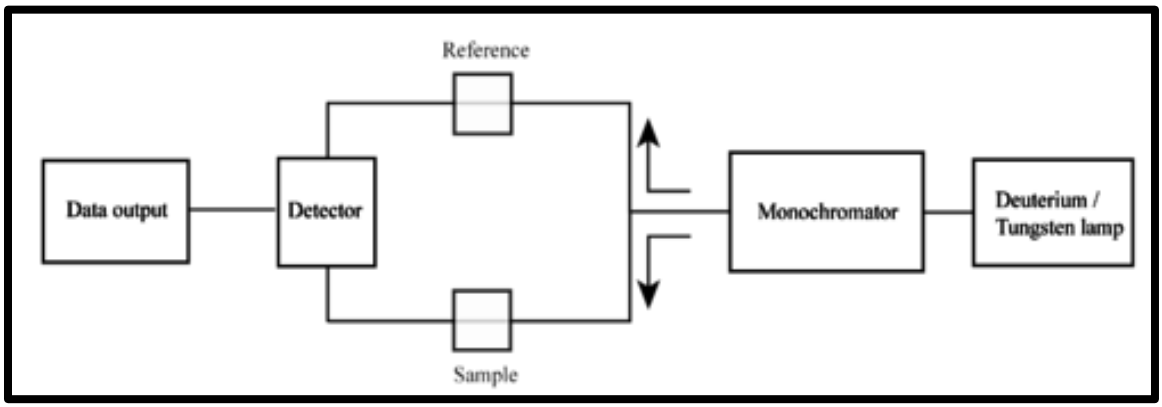

Figure 2. 14 Schematic diagrams of UV-Visible spectroscopy

Hydrogen-Deuterium and tungsten filament lamps are generally used. The Tungsten filament lamps emit 375nm of radiations whereas the intensity of Hydrogen-Deuterium lamps falls under 375nm. Monochromators are made up of slits ad prisms. With the help of rotating prisms, the radiations coming from the primary source are scattered. From the prism, several wavelengths of light are separated. The particular wavelength is selected to create monochromatic light. In a UV-Visible spectrophotometer, two types are used. One is a single monochromator and the other is a double monochromator. Beams are passed from the sample and reference cells. Sample and reference cells are made of either quartz or silica. The purpose of the detector in UV spectroscopy is served by two photocells. One photocell gets the beam from the sample cell and the other gets from the reference cell. The stronger intensity of radiation gets from the reference cell as compared to the sample cell. This process current alternates in the photocells. Generated alternating current in photocells is moved to the amplifier. The purpose of an amplifier is to amplify the signal several times that's why we get

recordable and clear signals. A recorder is connected via computer, this records the data and spectrum of the desired compound are produced[58].

2.7 Setup/Instrumentation used in the synthesis

The setup for the synthesis of GO, GQDs, rGO/CuO/SnO_2, and rGO/CuO contains the following items:

- Stainless steel autoclave
- Centrifuge
- Magnetic stirrer
- Sonicator
- Laboratory Oven
- Stainless Steel Autoclave

The hydrothermal autoclave is used to achieve hydrothermal synthesis at high pressure and high temperature. It has two parts: one is an internal part made of Teflon liner, and the other is an external stainless-steel outerpart, as shown in Figure 2.15. It can be used for the synthesis of variety of nanostructured particles with high crystallinity. For the Teflon line autoclave, the non-violent temperature range is up to 250°C but it is secure to use it till 200℃.

Figure 2. 15 Stainless-steel autoclave used for hydrothermal synthesis

- **Centrifuge**

The centrifuge is a significant research laboratory instrument used for the parting of atoms on the basis of their density. This separation is carried out in a huge speed spinning container as shown in Figure 2.16 The sediments of suspension take unlike density particles at different rates, dependent upon centrifugal force. Highly condensed elements in suspension sediments inside the tube, while lighter elements float on the surface. The tubes used in the laboratory for centrifugation are made of plastic or glass.

Figure 2. 16 Centrifuge employed to collect precipitates after synthesis

- **Magnetic Stirrer with Hot Plate**

The magnetic stirrer consists of a trivial bar magnet. It uses a spinning magnetic field to stir the bar magnet engrossed in a liquid solution to interchange it very rapidly, therefore, to stir it. The spinning magnetic field is formed by revolving the magnet. A magnetic stirrer has a hot plate used for central heating the solution, as shown in Figure 2.17

Figure 2. 17 Hot plate used for heating and stirring of solutions

- **Sonicator**

Sonicator is the most important instrument in the laboratory for sonication. It is also known as an ultrasonic probe. Sonication is the process of applying sound energy to disperse the particles in the liquid mixture. A frequency of greater than 20 kHz is used in this procedure which is why it is known as ultrasonication. Although the most important part of sonication is the time of sonication. The stability of the solution relies on the sonication time, concentration and solvent. The purposes of sonication are to deagglomerate the nanoparticles and to reduce the size and dispersion.

Figure 2. 18 Bath sonicator used in the experimental procedure

- **Laboratory Oven**

A laboratory oven consists of a chamber with thermal insulation used for the synthesis of nanostructures. It can be used for drying, annealing, conditioning, evaporating, baking, sterilizing and dehydrating a sample. The operating temperature range for the laboratory oven is up to 235˚C. These ovens provide uniform temperature throughout. First, we push the power button on to operate the oven system then we press the temperature increasing or decreasing button to achieve the required temperature. During hydrothermal synthesis, the temperature should be kept less than 200˚C for precautionary measures.

Figure 2. 19 Laboratory oven used for hydrothermal synthesis

CHAPTER 3

Ageing Analysis of Oxygen Plasma-treated PTFE surfaces: Role of Plasma Pressure on Wettability and Surface Chemistry

This chapter investigates the surface modifications produced by oxygen plasma treatment of initially hydrophobic polytetrafluoroethylene (PTFE) and their evolution over time under atmospheric conditions. Different oxygen plasma pressures (0.06, 0.1, and 0.2 mbar) were employed to modify polytetrafluoroethylene (PTFE) surfaces, while all other plasma parameters, including RF power, treatment duration, and the distance between the plasma source and the sample, were kept constant. The untreated and plasma-treated PTFE surfaces were characterised using water contact angle measurements, scanning electron microscopy (SEM), Fourier-transform infrared (FTIR) spectroscopy, and mass spectrometry. Oxygen plasma treatment initially transformed the hydrophobic PTFE surface into a superhydrophobic state, with water contact angles of approximately 135°, followed by a gradual transition toward hydrophilicity, reaching values around 70°. After treatment, the samples were exposed to ambient air at atmospheric pressure and monitored periodically over a period of approximately 67 days. SEM observations revealed time-dependent changes in the morphology of plasma-induced nanostructures, while qualitative FTIR analysis indicated corresponding changes in surface chemical composition. Quantitative FTIR analysis was performed using the specified area under band (SAUB) methodology to determine the carbonyl and hydrocarbon indices. The results demonstrate ageing behavior that alters over time, driven by both surface morphology and chemistry, where oxygen plasma pressure strongly affects the stability and long-term evolution of plasma-treated PTFE surfaces.

3.1 Introduction to PTFE

Polytetrafluoroethylene (PTFE) is a fluorinated material that has excellent properties, including chemical inertness, mechanical stability, resistance to degradation, low friction coefficient, thermal stability, and low surface energy[59]. It has numerous applications from these properties, such as in sealing products, low-friction films, and biomedical industries. Furthermore, different types of surface treatments can enhance its properties in various applications such as electronics, packaging, aeronautical and agricultural industries[60]. Many researches have been conducted in recent years on the wetting properties of polymer surfaces through plasma etching, mainly due to their wide range of applications in different fields

PTFE, also called Teflon, typically exhibits a hydrophobic nature. The wetting nature of PTFE is mostly due to fluoropolymers, with PTFE exhibiting the largest water contact angle (WCA) ~ 112˚. Therefore, the largest challenge is to change the wettability properties of PTFE surfaces to extend its applications. Different techniques, such as plasma jet, capacitively coupled plasma, ion beam, microwave plasma, and inductively coupled plasma (ICP), have been used to alter the PTFE surfaces through plasma methods. These methods imply introducing various types of gases to make superhydrophobic and hydrophilic PTFE[61-63].

Surface modification by plasma treatment is a cost-effective, scalable, and environmentally friendly approach, as it can alter the surface without altering the bulk properties of the material. Plasma treatment amends the surface by physically bombarding it with energetic ions, cross-linking and chemical reactions on the surface. Even a very short time period of plasma treatment is enough to bring changes in the wettability of the surface[64, 65]. By optimising parameters of plasma (power, time, pressure, and gas flow rate) and by altering the plasma gas (such as N_2, CO_2, Ar, NH_3, Ar+H_2), various types of surface functionalization can be performed for the materials[66, 67].

3.1.1 State of the art on PTFE plasma treatments

Atmospheric plasma treatment of PTFE has been studied with a focus on surface characterisation[68]. In particular, the authors examine how an atmospheric dielectric barrier discharge (DBD) (10–20 kHz AC, 20 kV peak-to-peak, 320 W power) alters PTFE surface wettability, chemistry, and topography immediately after treatment and during ageing. A 1-minute treatment strongly increases surface energy and wettability within the first 24 hours; using the Owens–Wendt method, the polar surface-energy component rises by 3650% versus pristine PTFE. Over time, however, “hydrophobic recovery” occurs: after 80 days the polar component drops by 72% from its post-treatment peak as the surface trends back toward its original state. XPS confirms oxidation of the surface, with higher oxygen content and reduced fluorine and carbon levels (increased O/C and decreased F/C), consistent with the formation of oxygen-containing polar groups responsible for improved wettability. The treatment also slightly smoothens the surface at first (within 24 hours, average roughness decreases ~10% and maximum height ~20%), likely due to removal of the top layer and melting of asperities, although polishing grooves remain. After ~800 hours, roughness increases again, which the authors link to surface recovery. Overall, DBD plasma effectively but temporarily boosts PTFE surface energy and reactivity through oxidation, while both wettability and the initial smoothing effect gradually fade with ageing.

It is known that atmospheric-pressure plasma can improve water repellency. The key challenge is achieving superhydrophobicity (WCA > 150°) with low hysteresis, which requires both low surface energy and adequate surface roughness[69], where three possible routes are assessed: (1) direct PTFE modification, (2) plasma deposition on fluorinated coatings (DBD-PECVD), and (3) hybrid nanoparticle coatings. In (1), pure helium plasma slightly lowers WCA because layer-by-layer etching smooths the surface via polymer-chain scission. In contrast, He–O_2 raises WCA up to ~155°, that is, atomic oxygen preferentially etches the amorphous phase, creating alveolar features and increasing RMS roughness from 17 to 58 nm with little change in chemistry. In (2), carrier gas strongly affects film structure, where Ar produces a filamentary discharge with higher fragmentation, yielding rougher, more hydrophobic coatings (WCA ~135°–140°), while He gives a glow discharge that better preserves precursor chemistry but forms smoother films with lower WCA (~115°). C_6F_{12} is discovered to deposit more rapidly than C_6F_{14} because of its active double bond. Lastly, in (3), slippery superhydrophobic surfaces can be obtained by deposition of approximately 80 nm SiO_2 nanoparticles before a layer of fluorinated plasma-polymer; at densities of greater than 0.5 g/L, nanoparticles WCAs exceed 160°C and hysteresis is reduced to below 5%. In general, the paper states that atmospheric plasma is a high-performance, inexpensive substitute for vacuum processing and that gas composition and discharge mode tuning allow balancing etching and polymerisation to generate hydrophobic to non-adherent superhydrophobic surfaces. The issue of finding simple, eco-friendly ways to make PTFE superhydrophobic using oxygen and argon plasmas has attracted considerable attention [70]. Rather than applying chemical coatings, this approach uses plasma etching to reshape the surface topography while leaving the material's chemistry essentially unchanged. Two etching setups can be considered: (1) plasma etching (PE), where power is applied to the upper electrode, resulting in lower ion impact and more isotropic etching; and (2) reactive ion etching (RIE), where power is applied at the sample holder, creating a self-bias and higher ion energy with combined physical and chemical etching. Consequently, the treated samples are characterized by: (1) higher water repellency than pristine PTFE, which has a water contact angle (WCA) of 113.8°, while PE reaches 152.3° (sliding angle 43.4°) and RIE achieves 172.5° with a sliding angle below 1°; (2) a topography-driven effect, as evidenced by both FTIR and XPS analysis, in which PTFE chemistry stays largely unchanged and the wettability effect of increasing the ambient power is due to surface topography; (3) distinct surface structures, with PE forming a leaf-vein-like microstructure and RIE producing a denser columnar texture with spherical tips, enabling a

Cassie–Baxter state that traps air and resists wetting; and (4) key process dependencies, with RF power having the strongest effect on WCA, followed by exposure time. Suggested applications include: (1) strong self-cleaning behavior in RIE-treated PTFE, which sheds graphite contaminants rapidly, removing most particles within 20 s as droplets roll off; and (2) enhanced droplet dynamics, where water droplets bounce faster on RIE (contact time 18 ms) than on PE (24 ms). Overall, the study concludes that Ar/O_2 RIE is an effective, economical, and more sustainable route to transform PTFE into a superhydrophobic, self-cleaning surface.

For practical applications, the development of durable, long-lasting superhydrophobic surfaces produced by simple plasma treatments has attracted considerable interest. The method discussed in [71] presents a safe, low-cost, one-step route to highly water-repellent PTFE, proposed as a cleaner alternative to multi-step chemical or nanoparticle coatings. Using dry plasma etching with Ar/O_2 (avoiding hazardous gases such as SF_6 or CHF_3), the authors optimized the conditions via the Taguchi method and identified RF power (150 W) and exposure time (3 h) as the key factors. Under these settings, PTFE transitioned from hydrophobic (~111° WCA) to nearly perfect superhydrophobic, reaching 178.9° with a sliding angle below 1°. SEM showed a marked increase in roughness (ranging 111 nm → 342 nm) and the formation of nanoscale spherical, crown-like tips critical for extreme repellency, while XPS indicated that PTFE chemistry remained essentially unchanged—confirming that the effect is primarily morphological. The surfaces were also highly durable: after 80 days of air aging, they retained a contact angle of ~170° and a sliding angle <1°, and they remained superhydrophobic (164°) after a 6 h droplet impact test (~21,600 drops), despite minor nanostructure damage. Finally, the treated PTFE showed strong lotus-like self-cleaning: droplets detached at lower wind speeds than from pristine PTFE, and rolling drops removed carbon nanopowder contaminants that persisted on untreated surfaces. Overall, the authors conclude that one-step Ar/O_2 plasma etching is a robust, scalable way to produce durable, self-cleaning PTFE nanotextures without hazardous chemistry.

In [72], the authors describe converting PTFE from hydrophobic to superhydrophobic using RF O_2 plasma, which is related to the approach adopted in this thesis. By tuning the plasma conditions, they form surface nanostructures that increase water repellency without changing PTFE's underlying chemistry. The experimental setup uses a high-vacuum etching system (50–300 W, 5–30 min) and includes a sacrificial PTFE disk placed between the sample and the stainless-steel electrode to help limit metal contamination and reduce overheating during etching. In terms of wettability, pristine PTFE (WCA ~112–115°) reached 152° after 30 min of treatment. The WCA increased with RF power up to ~200 W and then leveled off. With

longer exposure, surface energy and contact-angle hysteresis decreased, indicating a less adhesive surface. AFM and SEM images showed increased roughness and the formation of nanopillars and dense microstructures (Ra from 91 nm to 296 nm at 300 W), promoting a Cassie–Baxter state via trapped air. Chemical stability was confirmed by FTIR and XPS, which showed that PTFE chemistry remained essentially unchanged (CF_2 bonds and F/C ratio preserved); therefore, the wettability changes were attributed to morphology. The authors also compared O_2 and Ar plasmas, reporting that O_2plasma performs better for longer treatments, whereas Ar plasma can induce defluorination and even render the surface hydrophilic after ~30 min due to stronger bond breaking and UV effects. In contrast, oxygen enables more controlled etching that preserves superhydrophobicity. Overall, they conclude that optimized RF oxygen plasma is a robust route to durable, self-cleaning PTFE surfaces, providing high water repellency while maintaining the polymer's chemical resistance and purity.

In [73], The authors examine how O_2 plasma stabilises and tunes PTFE wettability from hydrophilic to superhydrophobic. The authors show that O_2 plasma can precisely tune and even stabilise PTFE surface wettability: by varying the plasma discharge energy, the same gas can produce either hydrophilic or superhydrophobic surfaces that remain stable over time. They report a clear link between discharge energy (180–2160 kJ) and the water contact angle. At low energy (180 kJ), pristine PTFE (WCA 119°) became hydrophilic, with the WCA dropping to ~87°. At high energy (2160 kJ), the surface became superhydrophobic, reaching a WCA of 151° with a low sliding angle (~4°) and low contact-angle hysteresis (<5°). A key contribution of the study is the long-term stability assessment: samples stored in air or water for up to 552 h showed no statistically significant changes in advancing, receding, or hysteresis angles, although stability was slightly better in air than in water. The work attributes these wettability changes primarily to morphology rather than chemistry. Higher energies increased RMS roughness (from 1.79 μm for untreated PTFE to 2.98 μm at 2160 kJ), consistent with enhanced air trapping and a Cassie–Baxter-type wetting state, whereas low-energy treatment slightly smoothed the surface due to etching. FTIR confirmed chemical stability, with no meaningful changes in PTFE functional groups (CF_2 features preserved). Experimentally, Tecaflon PTFE was treated in an oxygen plasma system operating at 13.56 MHz; wettability was measured by sessile-drop goniometry, surface topography by optical profilometry, and chemical bonding by FTIR. Overall, the authors conclude that oxygen plasma offers a robust way to tailor PTFE wetting behavior—from hydrophilic to superhydrophobic—while maintaining stable performance during extended storage, making it attractive for industrial and biomedical uses.

Transitions from hydrophobic to superhydrophobic behavior in Ar plasma-treated PTFE surfaces, and, under harsher conditions, to strongly hydrophilic states, are discussed in [74]. Although Ar plasma is often associated with defluorination and hydrophilization, the authors show that superhydrophobic PTFE is achievable by carefully controlling plasma power and exposure time. Untreated PTFE is hydrophobic, with a WCA of ~105°. A short treatment (5 min at 100 W) produces a superhydrophobic surface (WCA ~156°), attributed to isotropic nanostructuring and the formation of regular nanopillars. In contrast, prolonged high-power exposure (e.g., 30 min at 300 W) drastically reduces wettability (WCA down to ~14°), consistent with severe chemical modification and the formation of an altered surface layer. A key observation is the formation of a yellowish layer during long, high-power treatments. XPS and FTIR analyses indicate crosslinking, defluorination (F/C ratio decreasing from 1.49 to 0.13), redeposition of fluorocarbon species, and iron contamination from the plasma system. At 150 W power, this layer is water-soluble; and after rinsing, the underlying surface remains white and superhydrophobic (WCA ~155°). At higher powers (≥ 200 W), the layer becomes insoluble and more intensely colored. The authors also report post-plasma auto-oxidation during ambient aging, which increases oxygen content through reactions with residual radicals. To reduce contamination and overheating, the experimental setup employed a single-electrode configuration (with the chamber acting as ground), a sacrificial PTFE disk behind the sample as a heat and impurity shield, and water cooling of the electrode although energetic ion bombardment and UV radiation still promoted chemical changes at longer exposures. In conclusion, the paper recommends achieving durable superhydrophobic PTFE using low power and short treatment times (e.g., 100 W for 5 min), combined with a single-electrode design and sacrificial PTFE shielding, and reports long-term durability, with the WCA remaining ~151° after 180 days of ambient exposure.

Ageing mechanisms and kinetics in plasma-modified PTFE stored in either air or phosphate-buffered saline (PBS) for up to one month are examined in [75]. Surface chemistry and wettability were tracked using X-ray photoelectron spectroscopy (XPS), static secondary ion mass spectrometry (SIMS), and dynamic contact angle (DCA) measurements after treatments with O_2, Ar, N_2 and NH_3 plasmas. Two main ageing mechanisms are identified: (1) chemical reactions between the plasma-treated surface and the storage medium, leading to further modification (in PBS, this includes the introduction of polar groups and replacement of nitrogen by oxygen in N_2 and NH_3 treated samples); and (2) surface relaxation, i.e., rearrangement of chain segments and side groups that partially restores the untreated surface character, particularly during air storage. While untreated PTFE remains largely inert, plasma-

treated samples show pronounced time-dependent changes. PBS storage increases oxygen content and promotes further defluorination; for N_2 and NH_3 treated PTFE, nitrogen is rapidly replaced by oxygen within the first ~20 min of storage. Angle-resolved XPS suggests these reactions extend to depths of ~6 nm, consistent with fluid penetration. Air storage generally leads to slower chemical evolution and favors relaxation, often seen as an increase in the fluorine-to-carbon (F/C) ratio as the surface trends back toward its virgin state. Wettability changes closely follow surface chemistry. In PBS, treated samples become more hydrophilic, with a marked decrease in the advancing contact angle ($\boldsymbol{\theta_A}$), attributed to increased surface polarity and possible swelling due to fluid uptake. In air, advancing angles tend to recover toward untreated values, whereas receding angles remain comparatively stable. Importantly, air-ageing effects are partly reversible: a brief 10 min reconditioning in PBS can restore wettability to levels comparable to those of samples stored exclusively in PBS. These findings are relevant for biomedical use of PTFE, particularly the time between plasma treatment and implantation. The authors suggest pre-ageing in an aqueous medium (e.g., PBS) to help stabilize surface properties prior to in vivo use, potentially by converting less stable functionalities (e.g., amines) into more stable species (e.g., amides).

The question of how remote, atmospheric-pressure microwave plasmas modify PTFE surfaces is discussed in [76]. PTFE is used as a model substrate because of its simple C–F chemistry and high thermal stability, enabling insight into cold atmospheric-pressure plasma (CAPP) interactions. PTFE samples were treated with an atmospheric-pressure microwave surfatron torch operated in argon. Surface modifications were assessed mainly by WCA measurements (reflecting both chemistry and roughness) and X-ray photoelectron spectroscopy (XPS), probing the stoichiometry of roughly the top 8–9 monolayers. A key result is the contrasting behavior with and without oxygen addition. Pure Ar slightly decreased WCA (reduced hydrophobicity), attributed primarily to surface smoothing rather than compositional change. In contrast, adding a small amount of oxygen (~0.1% O_2) increased WCA, i.e., enhanced hydrophobicity, which the authors ascribe to increased roughness induced by chemical etching. Importantly, XPS showed minimal chemical modification in both cases: oxygen grafting remained below ~1%, and the C:F ratio was essentially unchanged. To rationalize morphology changes without a measurable shift in surface stoichiometry, the authors propose a three-step kinetic scheme: (1) activation, where the plasma preferentially breaks C–C bonds in the backbone (via electrons, photons, or Ar metastables), generating radicals; (2) re-association/etching, where in Ar/O_2 these radicals react mainly with O_2 to form transient oxygenated species (e.g., peroxides/alkoxides); and (3) desorption, where these

unstable products rapidly leave as volatile species (e.g., CO, CO_2, CF_2O). Overall, they argue that remote Ar/O_2 treatment modifies PTFE primarily through mild chemical etching that tunes roughness while preserving surface chemistry and stoichiometry, driven by afterglow radical processes rather than thermal effects or ion sputtering.

Ageing behavior of PTFE surfaces modified by an air glow-discharge plasma to improve wettability is examined in [77]. Although PTFE is inherently hydrophobic and chemically resistant, a brief ~3 min plasma exposure introduces polar surface groups (e.g., hydroxyl, carbonyl, carboxyl), substantially increasing hydrophilicity. The work then evaluates how storage environment and temperature affect the long-term stability of this modification. Ageing i.e., loss of the plasma-induced hydrophilicity is strongly environment-dependent. When stored in air at room temperature, treated PTFE gradually recovers hydrophobicity, whereas in a dry environment at elevated temperature (100 °C) the recovery is rapid, with wettability returning to near-original levels within about one day. In contrast, storage in a hydrophilic medium (distilled water) suppresses ageing: even at elevated temperatures, the aqueous environment stabilizes polar functionalities at the interface and maintains hydrophilicity for at least 180 days. The authors attribute hydrophobic recovery to surface restructuring driven by molecular mobility: polar groups migrate into the near-surface/bulk region or polymer chains reorient to minimize exposure of polar moieties to a nonpolar environment. A notable result is that this process is reversible—samples aged in air can recover hydrophilicity upon immersion in water, consistent with polar groups remaining in the subsurface and re-migrating to the interface under aqueous conditions. Finally, the modification is reported to be surface-specific, confined to only the outer few nanometers, enabling improved adhesion or dyeability without altering bulk PTFE properties (e.g., mechanical or electrical performance). Overall, the study emphasizes the importance of controlling ageing for reproducible plasma treatments and suggests that reversible wettability could be exploited in sensor-type applications.

A study of low pressure plasma modification of PTFE to enhance its efficiency in medical applications is found in [78]. Despite the outstanding bulk properties of PTFE (chemical inertness and mechanical stability), the native surface of the material causes undesirable biological reactions (e.g., chronic inflammation or thrombosis), which inspires attempts to make it more hydrophilic and biocompatible. The primary goal was to find a plasma process that improves the wettability by adding functional groups and minimises degradation (ablation). Three plasmas, CO_2, H_2/H_2O (2%), and pure H_2O vapour were compared on commercial PTFE foils and thin model films (PDFP). Plasma species were characterised by mass spectrometry (MS) and optical emission spectroscopy (OES), while surface chemistry,

morphology, and wettability were assessed using XPS, AFM, spectroscopic ellipsometry, and dynamic contact-angle measurements. Overall, pure H_2O plasma was the most effective in converting PTFE from hydrophobic to hydrophilic, with performance following H_2O > H_2/H_2O (2%) > CO_2. Some ablation was unavoidable (≈ 3–40 nm), but treatments introduced oxygen-containing functionalities and reduced the fluorine-to-carbon ratio. Notably, surface radicals were produced by H_2O plasma, which was verified by labelling with nitric oxide (NO) followed by detection of nitrogen in the XPS, which showed reactive sites that could be used in post-plasma grafting or functionalization. Storage conditions were critical towards stability. The hydrophilicity remained after two weeks in air in the H_2O and H_2/H_2O treatments, and the effect induced by H_2O was said to be stable up to six months. Conversely, the CO_2 plasma-treated surfaces displayed hydrophobic recovery in air, whereas wettability was enhanced at the storage in water, which was in agreement with reversible polymer-chain rearrangements. Overall, the authors conclude that microwave-excited (MW-ECR) H_2O plasma is the most promising route to obtain stable, hydrophilic PTFE surfaces with reactive sites for subsequent functionalization while preserving bulk integrity.

The primary aim of our study is to enhance the wettability of PTFE using oxygen plasma and study the ageing effect of the plasma-treated PTFE to discover the chemistry and morphological changes on the surface. We used oxygen plasma treatment and polytetrafluoroethylene (PTFE) as a model material due to its unique properties and wide use in both industrial and fundamental studies. This study is organised as follows: In Section 3.2, we describe the experimental setup and methods. The results are presented in Section 3.3 Specifically, Section 3.3.1 is devoted to surface wettability analysis and contact angle measurements. Section 3.3.2 presents the SEM results after the plasma treatments and describes morphological properties as a function of pressure and time of ageing. In Section 3.3.3, we present the detailed analysis of the chemical changes on the surface after plasma treatment with the help of Fourier transform infrared spectroscopy (FTIR). In Section 3.3.4, we discuss the mass spectroscopy (MS) of the plasma gas-phase, which allows us to investigate how the process of PTFE etching proceeds and the species that are formed in the discharge. Our concluding remarks are summarized in Section 3.4.

3.2 Experimental Details

3.2.1 Plasma Treatment Experimental Setup

The oxygen plasma treatment was performed on the PTFE samples. The high-purity O_2 gas was introduced inside the cylindrical vacuum chamber, which has a 30 cm diameter and 30 cm

height. The PTFE samples (6 × 6 cm^2, thickness = 1 mm) were placed in the chamber at a distance of 65 mm. The discharge is ignited by a radiofrequency antenna, which is externally connected through an automated matching network to an RF power supply (Cesar Technologies, 300 W, 13.56 MHz). The RF power supply provides an RF voltage which is applied to a perforated stainless steel plate (diameter 25 cm) insulated from the grounded chamber. (Diameter 20 mm) This configuration allows to produce a diffuse plasma in the volume below the electrode, interacting with the samples placed onto the holder. The gas flows through the hole network in the electrode along a downward vertical path. Before processing, the chamber is evacuated using a rotary pump. The plasma treatments were operated at different pressures (1×10^{-1} mbar, 2×10^{-1} mbar, and 6×10^{-2} mbar) and fixed RF power at 150W. All the plasma treatment was carried out at a fixed time of 30 minutes.

Under such conditions the device will behave as a well mixed reactor, so we could expect to have radial and axial uniformity of the plasma and the gas-phase, as soon as the flow exits the the thin sheath region facing the electrode. A sketch of the setup is provided in Figure 1.

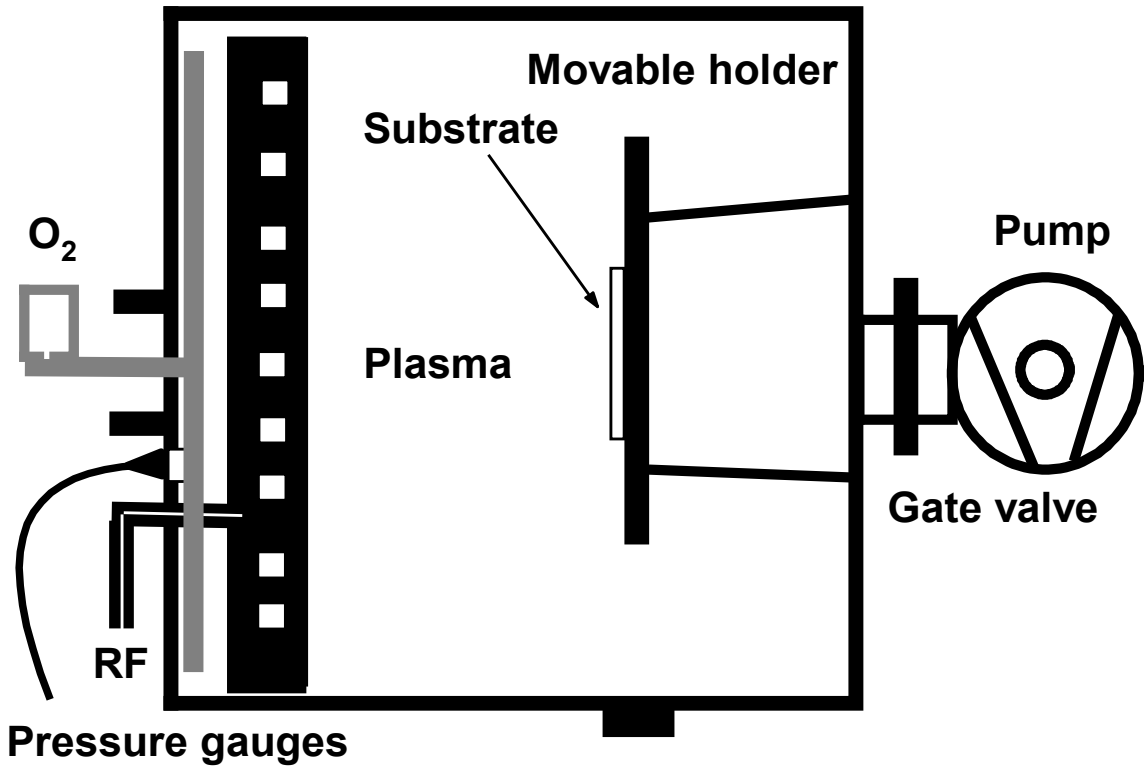

Figure 3. 1 Schematic Diagram of Plasma Treatment

3.2.2 Sample preparation

The PTFE samples were cut into 6 × 6 cm^2 from 1mm thick PTFE sheets.. Before being in process, the samples were washed with isopropyl alcohol to eliminate the dust particles from the surface of the PTFE, and they were well dried.

3.2.3 Surface Characterisations

The hydrophilicity was measured before and after the plasma treatments by determining the water contact angles (WCAs)of PTFE by using a demineralized water droplet of 3µl volume. An apparatus equipped with PC software SCa20 was used for taking measurements. All the WCAs were obtained at 6 to 7 different points and determined the mean values for each sample surface.

The chemical behavior of the PTFE samples was determined by ATR-FTIR (FTIR-ATR Nicolet iN10 Thermo Fisher, ATR mode, reflection and transmission.), and the spectra were obtained in the range 4000 cm^{-1} - 400 cm^{-1}, 256 scans for 51 seconds using a cooled detector. The untreated and plasma-treated samples were positioned on the sample disc and the data was recorded. To analyze the aging effect of surface chemistry the FTIR was measured over time and the spectrum was recorded at 7 to 8 different spots on the PTFE to detect the uniformity in the sample.

A scanning electron microscope SEM, (Zeiss FEG Gemini 500) was used to examine the surface morphology of PTFE (untreated and plasma-treated) and analyze the aging effect on the surface over time.

3.2.4 Mass Spectroscopy

A dedicated plasma reactor was used to perform a mass spectroscopic investigation of the discharge gas-phase, using a source developed by CCR Technologies Gmbh. A more detailed description of the setup can be found in our previous works [79]. Here we discuss only the relevant aspects to our discussion. A inductively coupled RF discharge producing an uniform, diffuse plasma can be operated in a wide range of power level and of pressure. PTFE samples were exposed to the discharge, being held floating in the plasma region. On the reactor side opposite to the source, a movable flange connects the chamber to an Hiden Ltd., EQP-1000 Model ion energy analyzer and quadrupole mass spectrometer. This instrument allows to perform mass spectroscopy of neutral and charged (both positive and negative) species up to 1000 amu. For neutrals, electron impact energies could be varied between 4 and 150 eV, even

if the standard energy of 70 eV was used for the data shown here. In particular, abundances and also energy distribution (in a ±100 eV range) of ions can be measured. Ions and molecules enter the spectrometer through an orifice (100 μm) at the center of the cap of a hollow tube (diameter 50 mm). A dedicated system of electrodes allows to collect with high efficiency neutral fragments that are ionized along their path, or, in alternative, ions which could be selected based on their mass and energy [79]. As stated above, the orifice can be moved along the cylinder axis scanning up to 300 mm to probe plasma well inside the chamber and the electrode plate. Apart from the identification of neutral and charged fragments, it is also possible to measure the energies of ions impinging on a substrate, which could be directly held on the spectrometer surface or in alternative to it. When the spectrometer is used inside the discharge, a sheath develops between the plasma and the grounded surface surrounding the orifice. Ions have to cross the sheath and their energy spectra are thus shifted by a value corresponding to the plasma potential. Besides the shift, the energy distribution spectra are generally broad. Their shape will determine the average ion energies and presence of high energy populations, both quantities that affects greatly the surface modification processes. Here we discuss the neutral radicals that are produced in the plasma during the PTFE etching and observed in the flow downstream.

Table 3. 1 Plasma Treatments for selected samples, applied powers, treatment time, and the chamber pressure

Sample Names	Power	Treatment Time	Pressure
Sample 1	150W	30 min	0.1 mbar
Sample 3	150W	30 min	0.2 mbar
Sample 5	150W	30 min	0.06 mbar

3.3 Results

3.3.1 Surface Wettability Analysis by Contact Angle

Figure 3.2 shows the water contact angles (WCA) of PTFE samples plasma treated with oxygen (30 min, 150W) at different pressures (0.1 mbar, 0.2 mbar, 0.06 mbar) and measure each sample with ageing times. Dashed horizontal line used at 105.3° shows the contact angle of the untreated PTFE sample while the other dashed line at 90° shows the hydrophilic-hydrophobic

threshold. Four ageing regimes were used to discuss the changing behaviour of PTFE after plasma treatment. Regime I (4-15 days), Regime II (15-22 days), Regime III (22-45 days), and Regime IV (45-67 days). These regimes are showed as a vertical dotted line in Figure 3.2

In Regime I (1-15 days), all PTFE samples show a significant change in surface wettability after the plasma treatment. After one day, the WCA of all samples remains above 120°, indicating a superhydrophobic surface behaviour. This trend is consistent with previous reports, where, after oxygen plasma exposure, PTFE becomes superhydrophobic [80]. However, in this regime window, an instant decrease in WCA is detected for all samples as ageing proceeds from 1 to 15 days. Linear fitted WCA in this window shows negative slopes (Table 2), suggesting fast surface wettability moves towards hydrophilic behaviour. Among the treated samples, Sample 1 indicates the steepest decrease in contact angles, as compared to Sample 3 and Sample 5, indicating that processing pressure in plasma treatment impacts the rate of early surface ageing.

In Regime II (15 – 22 days), Sample 1 continues decreasing in WCA and we can see that it clearly crosses the hydrophilic (90˚) threshold limit also showing a negative slope, whereas Sample 3 also shows a negative slope, illustrating a reduction in contact angle but remains close to the hydrophilic threshold. Sample 5 shows a positive slope, indicating partial hydrophobicity recovery during this regime window.

In the next Regime III (22-45 days), Sample 1 and Sample 3 show near-zero slopes, demonstrating a quasi-stable hydrophilic behaviour with minor changes in WCA. Sample 5, the water contact angle decreases to 82˚at 42 days, showing hydrophilic trend. To maintain consistency in kinetic analysis, a single water contact angle at 45 days in sample 5 was attained by linear interpolation using nearby experimental values, and this point data is used only for slope purposes in regime III.

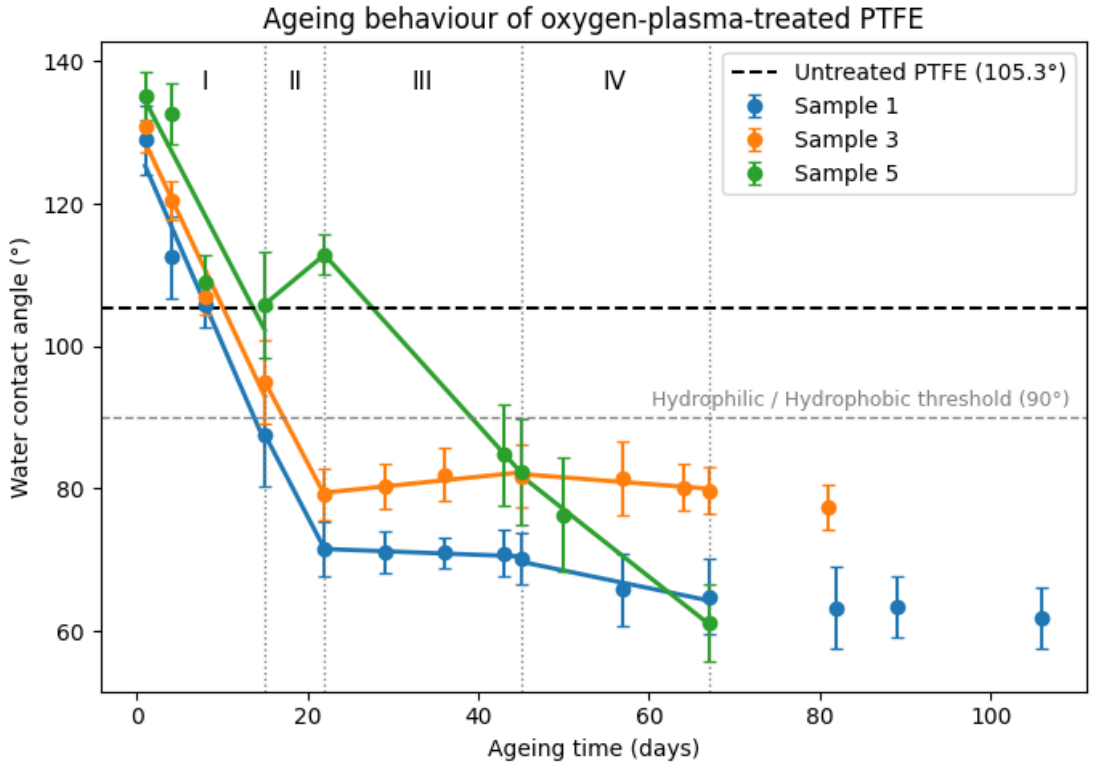

Figure 3. 2 Evolution of the water contact angle on oxygen plasma–treated PTFE surfaces as a function of ageing time (T, days) for three plasma pressures: (a) 0.1 mbar (Sample 1), (b) 0.2 mbar (Sample 3), and (c) 0.06 mbar (Sample 5).

Regime IV (45-67 days) represents the long term ageing trend of the oxygen plasma-treated samples. Sample 1 and Sample 3 exhibit small negative slopes, showing the hydrophilic behaviour is now stabilised with very small changes in WCA. Although Sample 5 shows a prominent decrease in water contact angle and reaches a hydrophilic state. This trend shows that the lowest plasma pressure remains unsaturated after a long time and continues to reorganise in this regime.

Table 3. 2 Piecewise ageing rates of WCA of plasma-treated PTFE samples, slope values (deg day^{-1}) in four ageing regimes.

Regimes	**1-15 days**	**15-22 days**	**22-45 days**	**45-67 days**
Sample 1 (0.1 mbar)	-2.766	-2.299	-0.046	-0.247
Sample 3 (0.2 mbar)	-2.545	-2.274	0.124	-0.093
Sample 5 (0.06 mbar)	-2.299	0.995	-1.329	-0.947

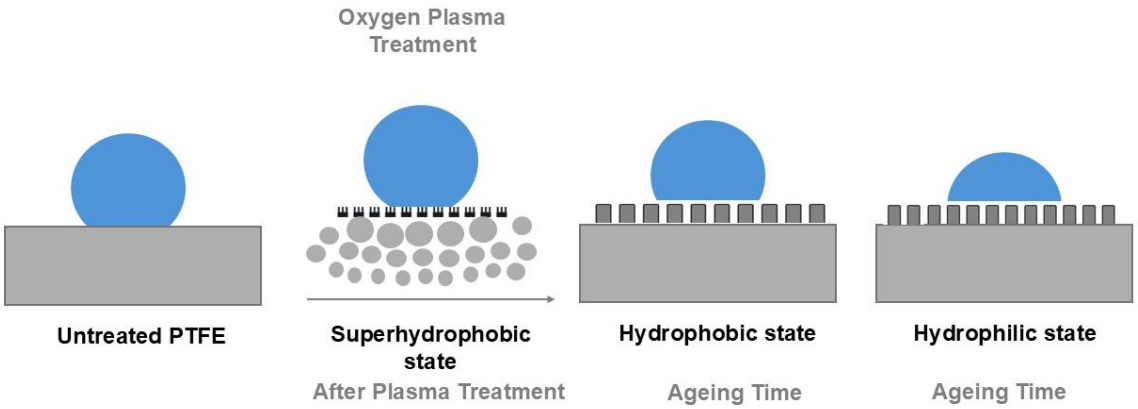

Figure 3. 3 A schematic of wettability phenomena observed on plasma treated PTFE surfaces with time

3.3.2 Surface Morphology Analysis by SEM

SEM was used to study the surface morphology of untreated and plasma-treated PTFE surfaces. Figure 3.4 shows the SEM images of untreated PTFE obtained at different ageing times. For reliability of results, the untreated PTFE sample was examined with the SEM and the same ageing conditions as the oxygen plasma-treated samples. These SEM images will be used as a reference to validate the morphological stability of plasma-treated samples. The untreated PTFE samples display smooth morphology without any roughness on the surface. Such morphology relates to the characteristic hydrophobic nature of pristine PTFE.

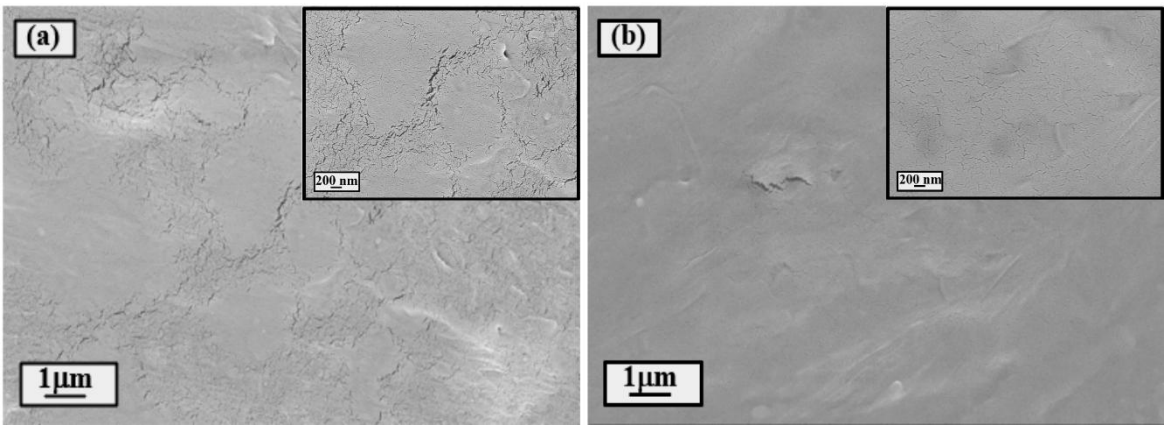

Figure 3. 4 SEM images of untreated PTFE at various ageing times a) Initial days b) 83 days at 1 mm and 200 nm scales

Figure 3.5 shows the SEM images of Sample 3 (0.2 mbar) at different ageing times comparable to the four regimes. In terms of wettability trends, Sample 1 and Sample 3 demonstrated similar

behaviour, and we selected Sample 3 to explain the evolution of surface morphology. In Regime I, Sample 3 surface shows some micro and nanoscale features as observed in Figure 5 a). Such surface roughness can trap air bubbles under the water droplet, reducing the contact between the solid and water. The Cassie-Baxter model fits this state, which describes how surface roughness boosts hydrophobicity, where a droplet stays on air-filled gaps[81]. During Regime II, a partly smooth surface can be observed in Figure 3.5 b), and a noticeable reduction of sharp nano-features. These surface morphology changes are related to a decrease in WCA in regime II $\sim 80^{\circ}$, signalling a shift toward hydrophilicity. In the next Regime III, morphology shows further changes compared to Regime II, the surface becoming smoother and more homogeneous at both nanometer and micrometre scales. Nanoscale features seen at the beginning of the ageing stages are largely reduced in Figure 3.5c. While the water contact angle remains $\sim 80^{\circ}$, these surface morphology changes suggest structural reorganisation and surface relaxation. In Regime IV (figure 3.5d), the surface morphology indicates minimal changes in surface evolution and maintains a smoother and more stable appearance, suggesting that the plasma-treated surface has accomplished a quasi-steady state in both wettability and morphology after longer ageing times. The continuity of similar wettability, although morphological evolution shows that surface chemistry progressively dominates the wetting behaviour in this phase.

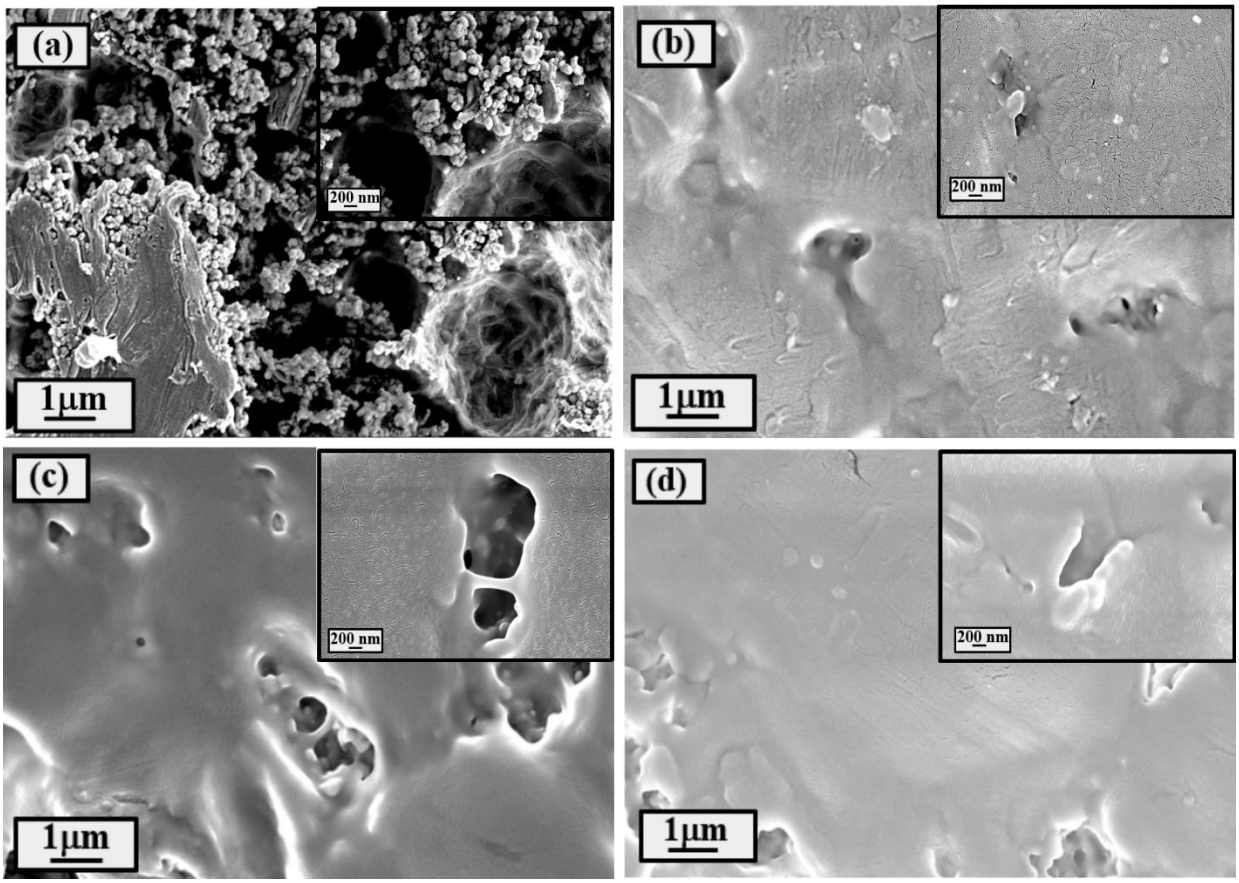

Figure 3. 5 SEM images illustrating the surface morphology evolution of plasma-treated Sample 3 (0.2 mbar) at different ageing stages: (a) 3 days (Regime I), (b) 21 days (Regime II), (c) 39 days (Regime III), and (d) 63 days (Regime IV). Images were acquired at micrometer (1 µm) and nanometer (200 nm) length scales.

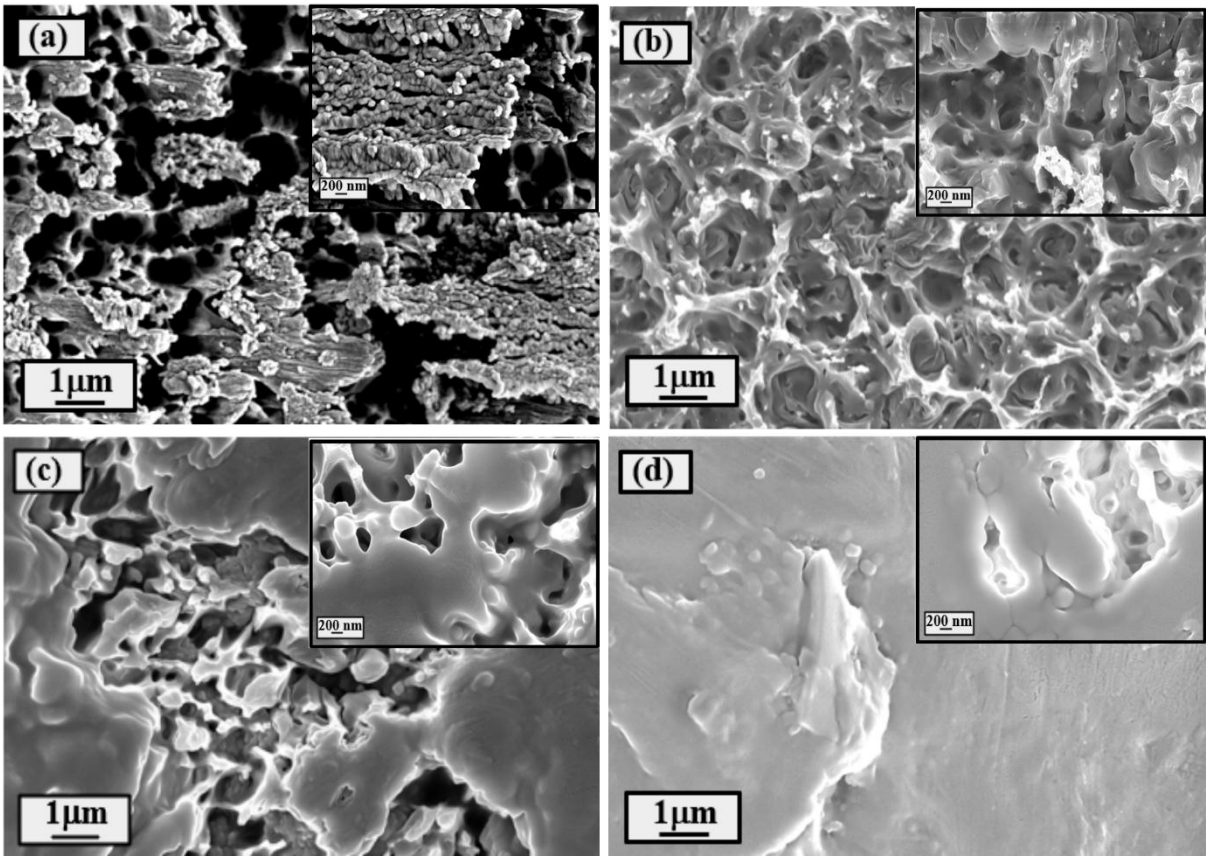

Figure 3. 6 SEM images illustrating the surface morphology evolution of plasma-treated Sample 5 (0.06 mbar) at different ageing stages: (a) 3 days (Regime I), (b) 22 days (Regime II), (c) 30 days (Regime III), and (d) 55 days (Regime IV). Images were acquired at micrometer (1 µm) and nanometer (200 nm) length scales.

Sample 5, treated at 0.06 mbar plasma pressure, shows a different ageing behaviour compared with Sample 3, depicted by a delayed evolution from hydrophobic to hydrophilic nature. Figure 3.6 shows the SEM images at defined regimes' evolution of surface morphology. In Regime I (Figure 3.6a), the lowest pressure plasma-treated PTFE indicates a strongly altered morphology at both nanometer and micrometre scales. In the first few days, the surface shows nanostructure and microstructures produced bumps or buds, which reduced the number of water contact sites with the surface and formed a hierarchical fractal structure [82] [83]. As discussed previously for Sample 3, this type of hierarchical surface change relates to a Cassie-Baxter wetting state [84]. This phenomenon increased the contact angle further, as shown in Fig. 3.6a (WCA 135°), improving the surface hydrophobicity and favouring superhydrophobic surfaces. In Regime II, Figure 3.6 b) shows continuous and interconnected surface morphology along with rounded features, showing partial surface relaxation, though maintaining micrometre structures. This is enough to maintain the hydrophobic nature with WCA values at 22 days around ∼115˚. Low-pressure treated PTFE sample keeps these features more persistently as compared to high-

pressure treated samples, as surface evolution occurs slowly, delaying hydrophilicity. In the next Regime III (Figure 3.6c), the PTFE sample shows a visible transition. The surface looks more homogenous and smooth at micrometer scale, and nanoscale features are diminished. Similarly, the WCA shifted to ∼80°, showing a transition to a hydrophilic nature. Further wettability changes at this stage are no longer closely related to surface topography, suggesting to a role of surface chemistry reorganisation.

In Regime IV, the surface shows further smoothing and stabilisation in morphology, as shown in Figure 3.6(d). The WCA after 55 days ∼80°, showing that the surface becomes a stable and hydrophilic state. A comparable behaviour occurs at high-pressure plasma-treated PTFE: after the plasma treatment, the WCA boost is due to the intense morphological change at micrometre and nanometer scales, followed by a slight decrease in the disappearance of nanostructures with ageing. Low-pressure plasma-treated PTFE, however, shows a delayed morphological evolution, prolonging its hydrophobic nature, after which surface chemistry drives long term wettability.

3.3.3 Chemical Analysis by FTIR

Qualitative Analysis using FTIR

The chemical analysis of the samples was recorded by FTIR between 400 to 4000 cm^{-1} and the corresponding results are shown in Fig. 3.7. The untreated PTFE (Sample 0), shown in Fig.3.7 a, has a spectrum showing two main bands, at 1149 cm^{-1} and 1203 cm^{-1}, which can be ascribed to asymmetric and symmetric stretching of the CF_2 groups. With time, the small bands at 2924 cm^{-1} and 2850 cm^{-1} are observed, which is due to the C-H stretching by atmospheric attraction.

Figure 3.7 (b-d) shows the plasma-treated PTFE samples; the carboxyl group (-COOH) band is observed in the range 1700-1750 cm^{-1} [85]. The oxygen groups are incorporated by the residual free radicals, which readily react with the oxygen plasma. Moreover, the absorbance peaks at 1457 cm^{-1} and around 2924 cm^{-1} are typically due to the stretching vibrations of C-H. However, these bands are not observed in the untreated samples. Hence, for all the samples, the peaks for $-CF_3$ (trifluoro methylene group) and $-CF_2$ (difluoro methylene group) are observed at 1149 cm^{-1} and 1203 cm^{-1} [86]. The bands at lower wavelengths in both spectra in the range of 700 cm^{-1} represent the wagging modes and chain stretching of the CF groups.

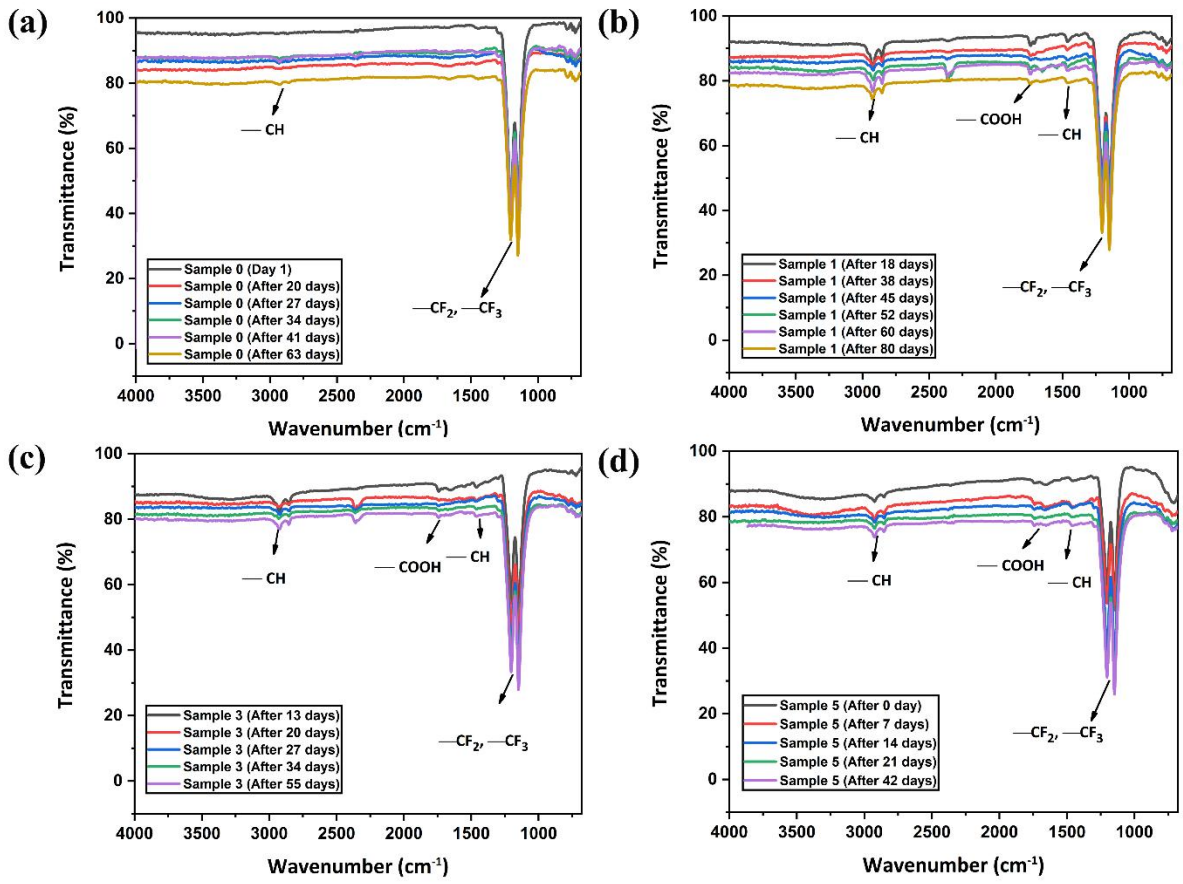

Figure 3. 7 FTIR spectra of PTFE samples showing functional groups at specific regions: (a) Untreated (Sample 0). (b) PTFE treated at 0.1 mbar (Sample 1). (c) PTFE treated at 0.2 mbar (Sample 3). (d) PTFE treated at 0.06 mbar (Sample 5).

Figure 3.8 shows the untreated sample's area analysis after different time intervals. In Fig. 3.8a for an untreated sample 0, we can see that there are no differences in the peaks in the specific region of COOH and CH. In Figure 3.8b, Sample 1 shows the clear broadening of the COOH peaks, which also satisfies the contact angle results that this is hydrophilic. In Fig. 3 .8c, Sample 3 also shows hydrophilicity from broad COOH peaks with narrow CH bands. As we know, sample 5 is the lowest-pressure-treated sample and shows a low ageing effect compared to the other samples. In this graph, we can see that the CH bands in Fig. 3.8d are also as wide as compared to the other samples and show the hydrophilicity after a long time due to surface chemistry. The Quantitative analysis was also performed in the next section.

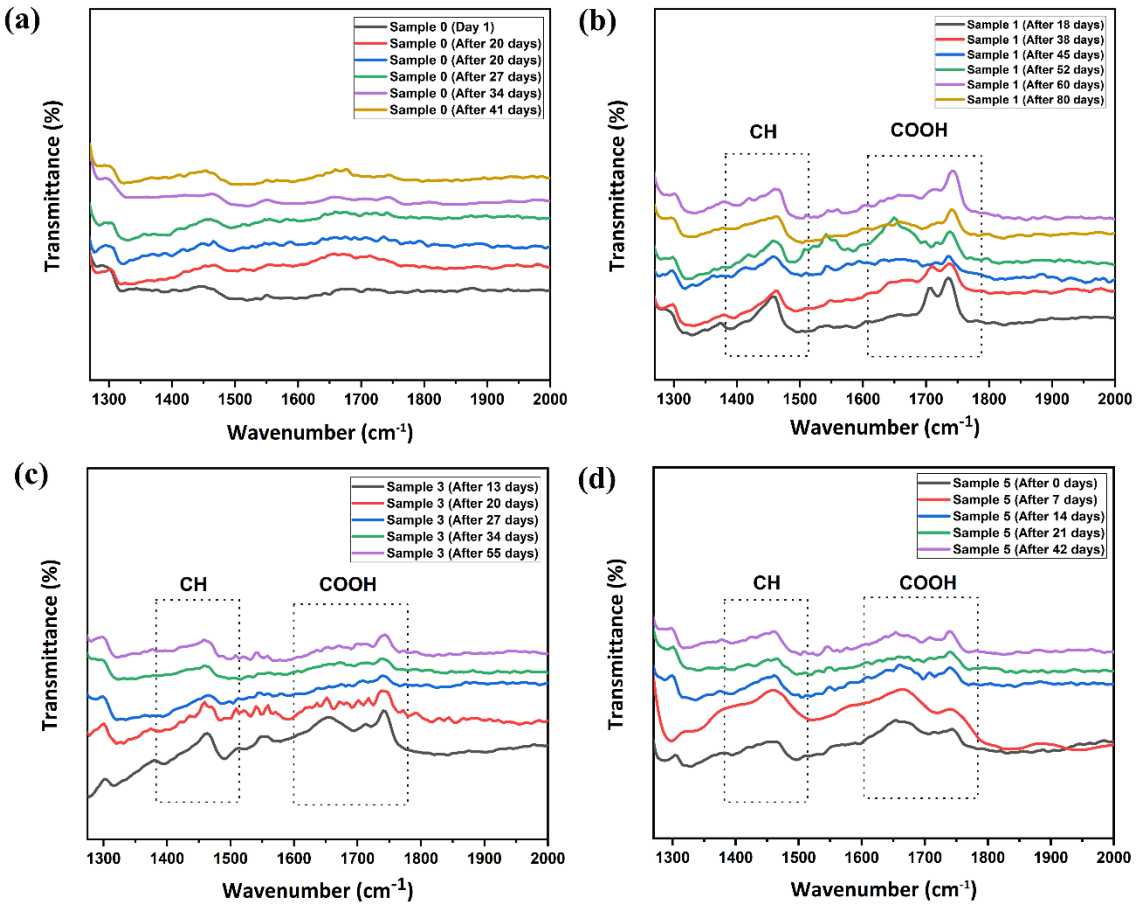

Figure 3. 8 Enlarged view of FTIR spectra of region (1300-2000 cm^{-1}) indicating the presence of CH and COOH bands in the plasma treated samples as compared to untreated samples: (a) Untreated, (b) Sample 1, (c) Sample 3, and (d) Sample 5.

Quantitative FTIR Analysis

Following the qualitative FTIR analysis, a quantitative analysis was also performed to gain a deeper understanding of the chemical evolution of the plasma-treated PTFE surfaces with different pressures. As qualitative analysis does not allow for deeper comparison between samples, a method called Specified Area Under Band (SAUB) was used to quantify the functional groups. The SAUB method was first proposed for the calculation of the carbonyl index of polyolefins, and integrates the area under the functional group rather than relying on peak height[87].

In this study, the SAUB method was adopted to plasma-treated PTFE surfaces, considering the fluorinated fingerprint region as a reference. Carbonyl Index ($COOH/CF_2$) and hydrocarbon Index (CH/CF) were used to analyse the evolution of surface chemistry of plasma-treated surfaces. Table 3. Summarises the mean and standard deviation values of Carbonyl Index (CI) and Hydrocarbon Index (HI) calculated from the FTIR data. The high standard deviation (SD) observed for some values reflects the heterogeneity of plasma-modified surfaces. Oxygen plasma incorporates non-uniform functionalization and surface reorganisations. The large standard deviations are consistent with previous studies on plasma-treated surfaces, where large error bars appear due to non-uniform surface modification with plasma [88].

Table 3. 3 Mean values and standard deviations of carbonyl index ($COOH/CF_2$) and Hydrocarbon index (CH/CF_2) obtained from FTIR peaks measurement for Sample 3 and Sample 5

Sample	**Time (days)**	**Regime**	**COOH/CF2 (mean ± SD)**	**CH/CF2 (mean ± SD)**
Sample 3	13	I	0.033 ± 0.004	0.0094 ± 0.00089
Sample 3	20	II	0.019 ± 0.011	0.0062 ± 0.00083
Sample 3	34	III	0.0172 ± 0.004	0.0070 ± 0.0020
Sample 3	55	IV	0.013 ± 0.004	0.0064 ± 0.0017

Sample 5	14	I	0.020 ± 0.008	0.0095 ± 0.0045
Sample 5	21	II	0.026 ± 0.006	0.0082 ± 0.0014
Sample 5	42	III	0.032 ± 0.015	0.011 ± 0.0045

In Regime I, after the plasma treatment, both samples, Sample 3 and Sample 5, show non-zero carbonyl indices (Figure 3.9a), suggesting that oxygen plasma introduces some polar oxygen functional groups at the plasma-treated surfaces. Meanwhile, high hydrocarbon CH indices are also observed in Figure 3.9 b). Since untreated PTFE does not show a CH group, Mass Spectroscopy (next section) confirms that CH_3 and other carbon-containing groups are present in the gas phase during plasma treatment, showing that the CH signal is induced from plasma treatment rather than the post-treatment contamination. Although the presence of carbonyl groups, the WCA remains high after the plasma treatment. SEM images indicate noticeable roughness, which raises a Cassie-Baxter wetting concept and masks the hydrophilicity of surface chemistry.

In the next Regime, the quantitative analysis of FTIR shows a clear change in chemical evolution between Sample 3 and Sample 5. For Sample 3, the carbonyl index (COOH/CF) and hydrocarbon index (CH/CF) drop relative to Regime I, suggesting the onset of relaxation of surface chemistry. This indicates the partial reorientation or some loss of plasma-induced

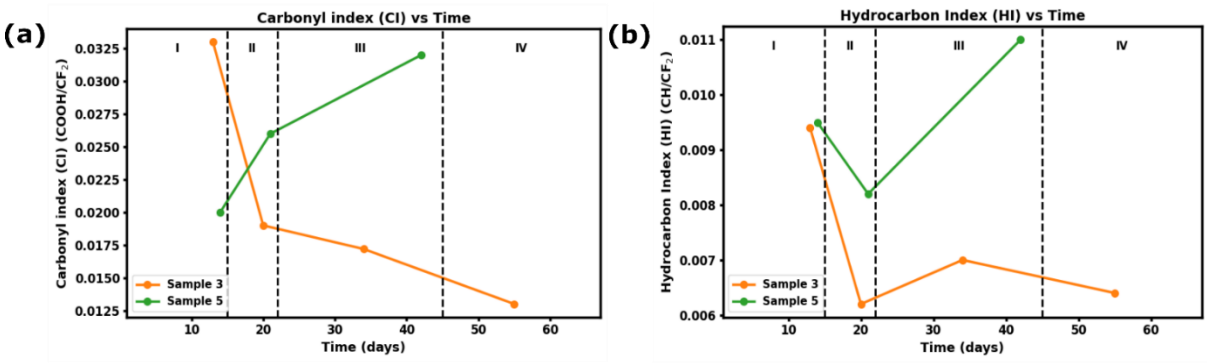

Figure 3. 9 Quantitative analysis using the SAUB method: a) Carbonyl Index vs Time b) Hydrocarbon Index vs Time

COOH group and chemical effects initiate to dominate over morphology effects in Regime II. However, Sample 5 shows a rise in carbonyl index in this regime, and the hydrocarbon index shows relatively high. This combination suggests the chemical heterogeneity rather than relaxation. Despite the presence of carboxyl groups, the presence of CH-containing species indicates that the hydrocarbon group contributions remain significant. Significantly, for Sample 5, the quantitative analysis suggests that the chemical functionality only is not enough to govern the wettability in this regime. The persistent influence of plasma-treated roughness and chemical heterogeneity delays the evolution to chemistry-dominated behaviour. Thus, Sample 5 persists effectively, with morphology dominant in Regime II, leading to an increase in WCA despite an increase in carbonyl index. Sample 3 shows chemistry-dominant wetting, driven by the relaxation of nonpolar group contributions and stability in surface chemistry.

In Regime III, the quantitative analysis of FTIR shows a further transition toward a chemistry-dominant region, especially for sample 5. The CI index for Sample5 reaches the highest point in this regime, and the same goes for the HI index. This pattern suggests the chemical evolution rather than the surface relaxation, indicating continued stabilisation or the formation of carbonyl functional groups. At this stage, this analysis shows that the impact of carbonyl groups become dominat. So the presence of this group outweighs the contribution of nonpolar hydrocarbon groups, permitting surface chemistry to play a determining role in surface wettability. Thus, Sample 5 shows a decrease in WCA, signalling a clear shift to chemistry dominated weting properties. For Sample 3, the CI continues to decrease slightly, though the HI increase slightly. These trends show that surface chemistry of this sample has mostly stabilised, with minimal further surface relaxation. So, both samples enter to chemistry dominated regions, but differently. High-pressure plasma-treated sample reaches this state

earlier and has a slow relaxation as compared to low pressure plasma treated sample, which experienced a delayed but intensified chemical activation, resulting a steeper move towards hydrophilic behaviour.

In the last Regime IV, quantitative analysis suggests that surface chemistry reaches to quasi-equlibrated state. The CI decreases slightly, indicating some reorientation of polar groups, or some loss of weakly bound oxidised groups. And the HI index also shows minimal decrease, indicating that plasma-induced species have largely ceased. In this region, the surface chemistry continues to dominant factor and influences the surface wettability, and further changes are insignificant, showing a steady state of surface wetting behaviour. For sample 5, the FTIR measurement data are not present. The CI and HI evaluated at the end of regime III indicate that the chemical stabilisation develops later as compared to sample 3.

3.3.4 Mass Spectroscopy of PTFE etching in oxygen plasmas

PTFE samples were exposed to the oxygen plasma at two different pressures of 0.06 and 0.1 mbar under the same conditions discussed in Section 2.1. Spectra of neutral radicals were recorded, and the area of the peaks at different masses was calculated. Figure 3.10 shows the time evolution of the most relevant radicals during both treatments. We have also measured the impurity level, both in vacuum, before treatment, and after the sample placement and the start of the oxygen flow. Apart from some water vapour outgassing, the impurity level is below a few per cent and in particular, no signal is observed from fluorine-containing radicals, which could originate from the sample. After the breakdown, when plasma starts to interact with the sample, we observe a very fast change in the gas-phase composition. Molecular oxygen level declines and remains stable during the subsequent 30 minutes, as well the signal of the main oxidation products, carbon dioxide (M=44, with its fragment peaks at M=12 and 28). A slower evolution can be seen in the fluorine-containing radicals. Their abundance increases with time, reaching somewhat of a saturation after about 15 minutes. At later times, near the end of the treatments, some peaks show a slight decrease. The most abundant radical corresponds to the mass M=85 amu (that corresponds to the COF_3 radical, which forms from the oxidation of PTFE chain ends). In sharp contrast, the formation of COF_2 radicals, which presuppones the PTFE chain resection, appears to be much less probable, all the more so at later times. Production of COF and, to a much lesser extent, of COF_4 radicals was observed too. This oxidation of a part of the polymer chain appears to be the main pattern that PTFE etching in plasma follows. Incorporation of oxygen into the polymer chain can be expected too, as a

mirror of this etching pattern, but cannot be assessed only by the gas-phase composition analysis. At a much lower concentration level, it was also observed that the process of polymer chain fragmentation, witnessed by the formation of CF_3, CF_2 and also C_2F_5 radicals. This pattern is possibly mediated by electrons or by interactions with ions or neutrals, where oxygen is not directly chemically react. Direct abstraction of fluorine from the PTFE can also be evaluated as a minor pattern, since we could exclude any relevant concentration of OF, OF_2 or O_2F. We also have some indications that impurities were present in the discharge region and that plasma stimulates outgassing, both contributing to the gas-phase, with the formation of HF, for instance, and the observation of H_2 and CH_3 notwithstanding the strongly oxidative character of the gas-phase. Also, some hint of reactions happening between the produced radicals in the gas-phase can be grasped, such as in the formation of M=86 amu, tentatively $HCOF_3$, which cannot originate at the PTFE surface.

Broadly, the same picture was observed at the larger pressure, but a few stark differences were observed. The most obvious is the much slower and lesser build-up of COF_3 radicals, which only in the end, become the major etching product. Also, the relative weight of non-oxidised PTFE fragments is bigger, despite the larger concentration of oxygen. This is possibly due to the different balance between the polymer fragmentation patterns. This opens up some interesting question, which requires some correlation with the plasma properties (ionisation level and electron temperature, above all).

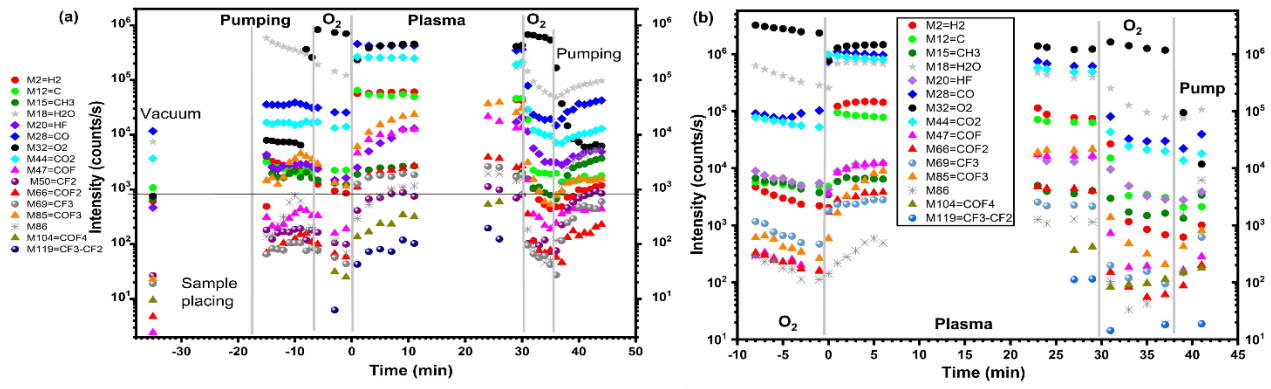

Figure 3. 10 Concentration of main neutral molecules and radicals during the etching of PTFE samples by oxygen plasmas. (a) Treated at 0.06 mbar, and (b) at 0.1 mbar.

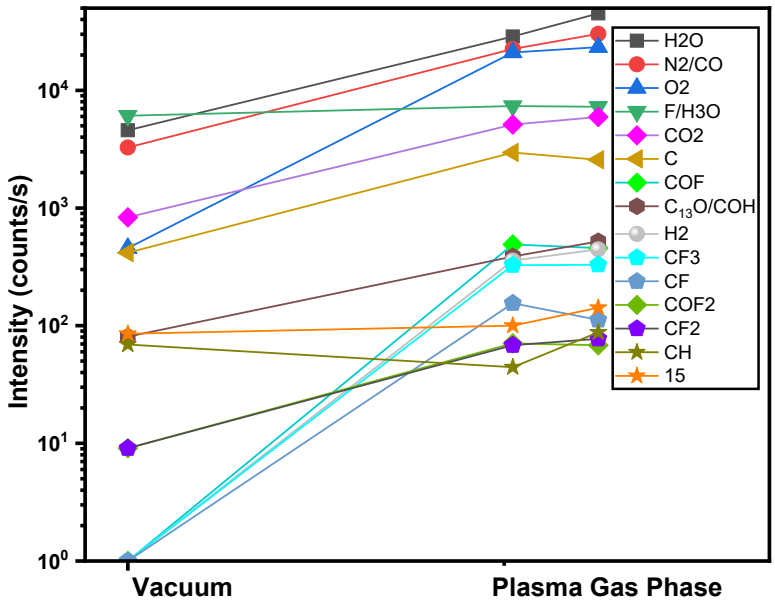

Figure 3. 11 The gas-phase composition measured after 5 minutes exposure of Sample 5, see above (Fig.3.10a), is reported for comparison.

We also made a comparison with the gas-phase composition that develops during the etching of the PTFE samples discussed previously. A small volume of the discharge gas-phase was prelevated at some time during the process and then analysed after spilling into the vacuum of the mass-spectrometer chamber. The mass spectra composition is displayed in Figure 8. Although some radicals could have reacted before being analysed, the picture that we observed is consistent, with a strong oxidation with CO_2 formation as well as the etching through oxidised as well as non-oxidised PTFE fragments. This strongly supports our view that the relevant etching pattern is indeed the one we grasped in our previous discussion.

3.4. Summary

In this study, the effect of oxygen plasma processing and ageing on the polytetrafluorethylene (PTFE) surfaces has been examined, with particular focus on the role of plasma pressure in directing the surface evolution. Following plasma treatment, PTFE surfaces exhibited superhydrophobic characteristics; however, with increasing ageing time in air, a gradual transformation toward hydrophilic behaviour was observed. This evolution occurred for all investigated samples and across the different plasma pressure conditions. Water contact angle measurements and scanning electron microscopy were employed to monitor the temporal evolution of surface wettability and morphology. SEM observations revealed significant plasma-induced surface modification, including non-uniformity and localised surface damage accompanied by the formation of nanometric and micrometric structures. These morphological features evolved with ageing time, indicating a progressive relaxation of the plasma-modified surface.

Fourier-transform infrared spectroscopy was used to investigate changes in surface chemistry and to identify newly formed functional groups. Compared to untreated PTFE, the plasma-treated samples exhibited clear alterations in their FTIR spectra, with the appearance of hydrocarbon (CH) and carbonyl (C=O) related bands after plasma exposure. Variations in the absorbance peak areas over time indicated ongoing chemical changes at the surface during ageing. The presence of these functional groups confirms the successful incorporation of hydrophilic moieties onto the PTFE surface through oxygen plasma treatment. Quantitative FTIR analysis using the SAUB method revealed the formation and evolution of carbonyl and hydrocarbon groups. The ageing behaviour was examined through divided regimes, showing a dynamic competition between surface morphology and chemical changes on the surface. In the early ageing stages, surface morphology played a dominant role and masked the chemical effects on the surface. After some days, the chemical functionality increasingly governed wettability, and here morphological features relaxed; however, long-term ageing behaviour led to stabilised state for both surface chemistry and surface wetting behaviour. The results explain that plasma pressure strongly affects the stability and ageing dynamics of plasma-treated PTFE surfaces. These findings offer valuable insight into the reason behind hydrophobic recovery and long-term functionality of fluoropolymer surfaces, and also focus on the importance of plasma parameters to modify surface properties for real-world applications.

CHAPTER 4 Surface Modification and Ageing Behaviour of Nylon Treated by Oxygen Plasma

4.1 Introduction to NYLON

Nylon belongs to the polyamides (PAs) family of semi-crystalline synthetic polymers, characterised by amide linkages (-CO-NH-) between monomers produced through either natural or synthetic routes[89]. Natural polyamides occur in materials like silk and wool, whereas synthetic variants such as Kevlar, Perlon, and Nomex, which emerge from polymerisation processes, fall into categories including aliphatic, aromatic, and polyphthalamides[90]. Nylon primarily consists of aliphatic or semi-aromatic types. Discovered accidentally in 1930, systematic research began in 1935, leading DuPont to commercialize it as "Nylon" in 1938; the initial nylon 66 variant debuted as toothbrush bristles. During World War II, nylon fibres supported parachutes, cords, fabrics, and military clothing[91].

Nylon 6 or poly(hexano-6-lactam), or polyamide 6 or Nylon 6, is an aliphatic polyamide polymer consisting of repeating -NHCO-linkages[92] and is produced by the ring-opening polymerisation of caprolactam and high temperature condensing the polymer to create high-molecular-weight chains. Its T_g (glass transition temperature) is approximately 48°C, and T_m (melting temperature) is approximately 214°C, which provides good thermal stability in processing and end-use applications. Due to its tensile strength, elasticity, wrinkle and abrasion resistance, nylon 6 is industrially considered in the emerging markets in the packaging, textile, and engineering plastics. But in its purest state, it cannot be used in advanced applications, especially in technical textiles as it is poor in surface wettability, making coating, printing, painting, and bonding processes more complicated[93]. Because of this, surface modification processes like plasma treatments are becoming more significant, so that the surfaces of nylon 6 are modified to suit the process, and thus to gain a better insight into the behaviour of nylon 6 concerning plasma gases, it is necessary to have a better comprehension of the interactions between it and plasma gases.

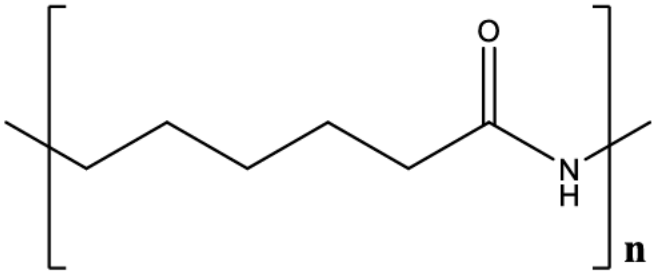

Figure 4. 1 The chemical structure of nylon 6 repeating units

Yip et al.[94] reported that low-temperature plasma (LTP) treatment of nylon 6 fabrics with the various gases, including oxygen (O_2), argon (Ar), and tetrafluoromethane (CF_4), has shown considerable changes and modifications in the physical and surface characteristics of the material. For instance, Oxygen and Argon plasma treatments produce different ripplet-like pattern on the fibre surface, at perpendicular orientation to the fibre axis, which are enhanced with treatment time. CF_4 plasma, on the contrary, is more likely to form granular materials on the surface when exposed to a shorter period. These morphological variations, commonly known as plasma etching or ablation, directly affect the low-stress mechanical behaviour of fabrics, such as enhancing surface friction and bending rigidity, while reducing air permeability in the fabric, and, to a lesser extent, increasing surface roughness.

Thompson et al.[95] applied low-frequency (40 kHz) oxygen plasma at 10 W for 10–40 s to homogeneously activate nylon 6 sheets, incorporating polar COH, CO, and OCOH groups to enhance wettability. SEM and AFM confirmed no changes in surface morphology or roughness. Hydrophobic recovery was fastest in the first 1–5 days, with O/C ratio dropping from 0.31 to 0.19 by day 7 before stabilizing; this was attributed to polar group reorientation and polymer chain rotation. Residual hydrophilicity persisted after 20 days, likely due to atmospheric moisture interactions, making the first week the most volatile period for surface chemistry. While Thompson et al.[95] reported that low power (10 W) and short duration (up to 40 s) oxygen plasma treatment of nylon 6 produces no detectable changes in morphology. My study involves the use of more power (100 W) and more time (2-4 min), resulting in unique surface ablation and ripplet-like morphological pattern formation that can be observed under SEM, as suggested by Yip et al.[94]

A frequent motivation for plasma activation is to enhance coating adhesion and coating uniformity on polymer substrates by increasing surface energy and creating functional groups that promote interfacial interactions (hydrogen bonding, polar interactions, or chemical

anchoring). Recebtly Primc et al.[29] focused on polymer-coating systems, summarising that plasma treatment is widely used to improve the results of adhesion from many types of coating, but correlations may depend on the substrate as well as coating chemistry.

An important and practical use of plasma functionalization is the improvement of the adhesion of coatings or nanoparticles to polymer surfaces. Plasma-treated polymers have, in general, increased attachment of metallic oxides, carbon-based materials, and metal-organic frameworks; these materials are relevant for protective and functional textile applications. Karande et al.[96] reported that open-air oxygen plasma treatment of nylon-based fabrics significantly enhances the concentration and stability of the surface of nanoparticles such as ZnO and UiO-66-NH_2 with respect to the untreated substrates. Their results revealed that nanoparticle adhesion is, in turn, dependent on the particle characteristics, smaller UiO-66-NH_2 nanoparticles showing greater adhesion and durability due to their high surface area and abundance of polar functional groups. Although plasma-assisted methods do not yield thick coatings, they are suitable for applications that have thin or near-monolayer particle coverage requirements.

In summary, previous studies have shown that oxygen plasma treatment is an effective method for modifying polymer and textile surfaces by increasing surface energy, improving wettability, and enhancing nanoparticle or coating adhesion. However, plasma-induced surface modifications are known to be time-dependent and subject to hydrophobic recovery, with the extent and kinetics of recovery strongly influenced by plasma parameters and material type. Despite reports on plasma-treated nylon and textile substrates, systematic investigations correlating plasma treatment time, wettability ageing, surface morphology, and chemical changes with subsequent functional coating deposition remain limited. Therefore, the present study aims to investigate the effect of oxygen plasma treatment time 2 minutes and 4 minutes using same other parameters and studied the effect of plasma treatment time on the ageing behavior of nylon surfaces and also check the morphology and chemistry changes with SEM and FTIR analysis, as well as with the deposition behaviour of rGO/CuO coatings on treated and untreated nylon surface.

4.2 Experimental Setup for Nylon samples

The oxygen plasma treatment was performed on the nylon samples. The high-purity O_2 gas was introduced inside the cylindrical vacuum chamber, which has a 30 cm diameter and 30 cm height. The Nylon samples (3×3 cm^2) were placed in the chamber at a distance of 65 mm. The

discharge is ignited by a radiofrequency antenna, which is externally connected through an automated matching network to an RF power supply (Cesar Technologies, 300 W, 13.56 MHz). The RF power supply provides an RF voltage which is applied to a perforated stainless steel plate (diameter 25 cm) insulated from the grounded chamber. (Diameter 20 mm) This configuration allows to produce a diffuse plasma in the volume below the electrode, interacting with the samples placed onto the holder. The gas flows through the hole network in the electrode along a downward vertical path. Before processing, the chamber is evacuated using a rotary pump. The plasma treatments were operated at different times (2 minutes and 4 minutes) and fixed RF power at 100 W. All the plasma treatment was carried out at a fixed pressure of 0.1 mbar.

4.3 Results and Analysis

4.3.1 Surface Wettability: Contact Angle

Figure4.2 shows the surface wettability of nylon textile after the plasma treatment, calculated through static water contact angle, with the ageing behaviour of nylon textile samples over time. P1 shows the untreated nylon, P2 and P4 are plasma-treated samples for 2 minutes and 4 minutes, respectively. As depicted in Figure 4.2 (a), P1 shows a high-water contact angle of around 107.8˚, showing a hydrophobic surface. With the oxygen plasma treatment, there is a substantial decrease in water contact angle for both samples. The water contact angles shifted to less than 5˚ for P2 and P4, indicating the transformation of the nylon surface from hydrophobic to superhydrophilic. This reduction in water contact angles is ascribed to the plasma-induced surface, which makes polar functional groups on the surface. Figure 4.2 (b) shows the recovery behaviour towards the hydrophobicity of the plasma-treated samples with time. After 1 day, both samples P2 and P4 exhibit almost half recovery towards hydrophobicity, showing contact angles of around 46° and 52°, respectively. With continued ageing for 7 days, the water contact angles increase notably, and reach 90 for P2 and 105.5˚for P4, very close to the contact angle of the P1 untreated sample. This behaviour indicates that plasma exposure time and ageing duration play crucial roles in such polymer treatments, owing to the reorientation of polar surface groups.

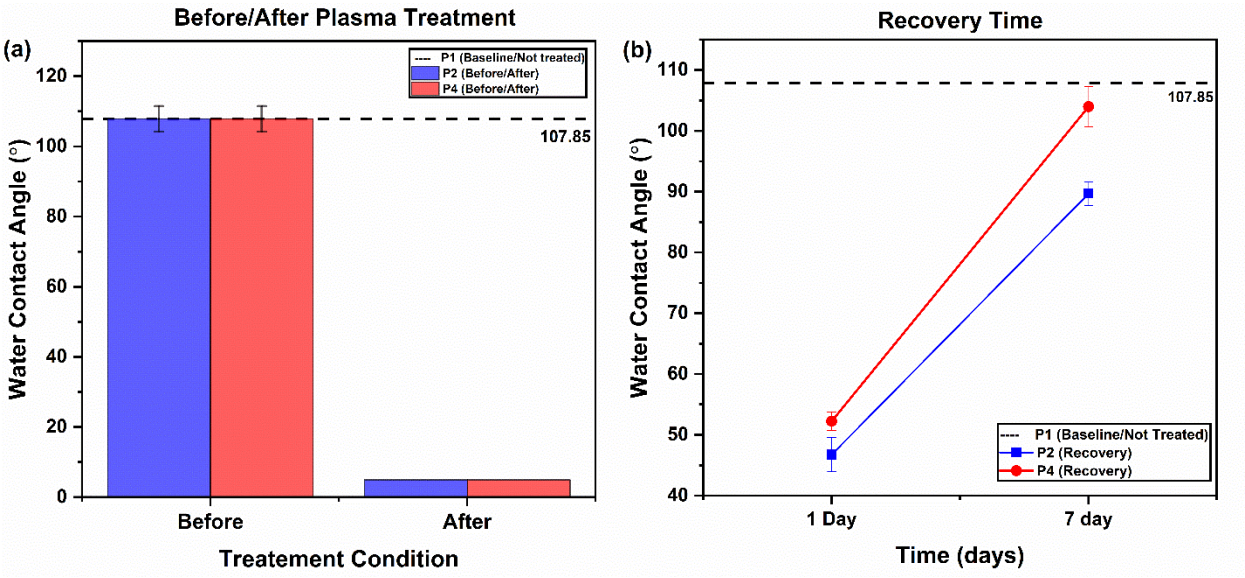

Figure 4. 2 Ageing of Plasma Treatment on Nylon surface: a) WCA before and after oxygen plasma treatment, b) ageing behaviour after 1 and 7 days

4.3.2 SEM Analysis

Scanning Electron Microscopy (SEM) was used to study the surface morphology of nylon textile caused by oxygen plasma treatment, and also study the ageing phenomena of plasma-treated samples over time. SEM was performed on the untreated (P1) sample and the oxygen plasma-treated samples for 2 minutes (P2) and 4 minutes (P4), after the treatment, after 1 day of treatment, and after 7 days of treatment. Images were captured at the same spot of nylon in ageing days at different magnifications, 100 µm, 10 µm, 1 µm, and 200 nm scale bars, to study the overall surface topography in detail. This study provides insight towards plasma-treated surface etching, morphological changes and roughness during ageing time.

Figures 4.3 – 4.11 show SEM images of P1, P2 and P4 at different magnifications and ageing times. For each sample, SEM micrographs are shown to compare the surface morphology at different magnifications.

- **SEM Images After Plasma Treatment**
- **P1 Untreated Nylon**

SEM images of the untreated nylon (P1) exhibit a uniform and smooth surface with no surface damage. At 100 mm, the woven fabric composition is well maintained. The surface is relatively featureless and smooth, as shown in Figure 4.3

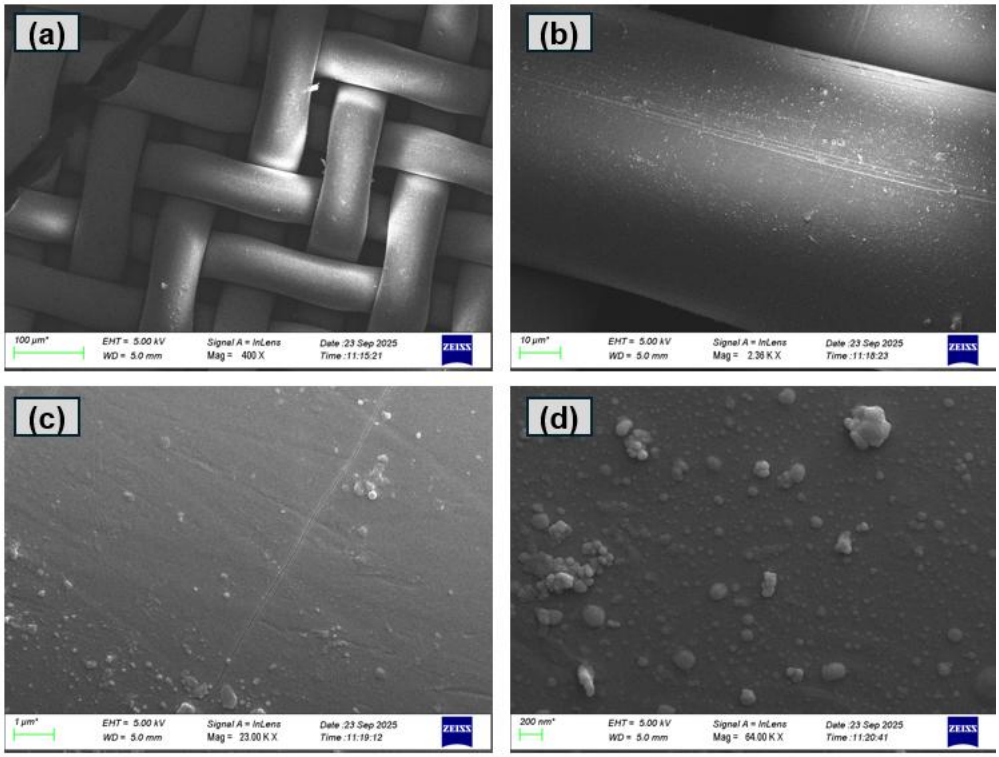

Figure 4. 3 SEM images of P1 showing surface morphology at different magnifications (scale bars: 100 μm, 10 μm, 1 μm and 200 nm)

- **P2 (2 Minutes Treated Nylon)**

Figure 4.4 displays the SEM images of nylon treated with oxygen plasma for 2 minutes (P2), examined immediately after the treatment. At 100 μm Figure a), we can see that the woven structure of the fabric is still the same, showing that the treatment does not affect the fibres at the macroscopic level, so the overall morphology remains smooth as in the untreated sample. At 1 μm, P2 shows noticeable surface changes in topography compared to the P1 sample. Minor surface roughness and some etched regions are observed on the surface, which is due to the energetic oxygen species interaction with the polymer surface. However, the nanoscale image at 200 nm indicates the presence of some nanoscale irregularities, with small buds on the surface.

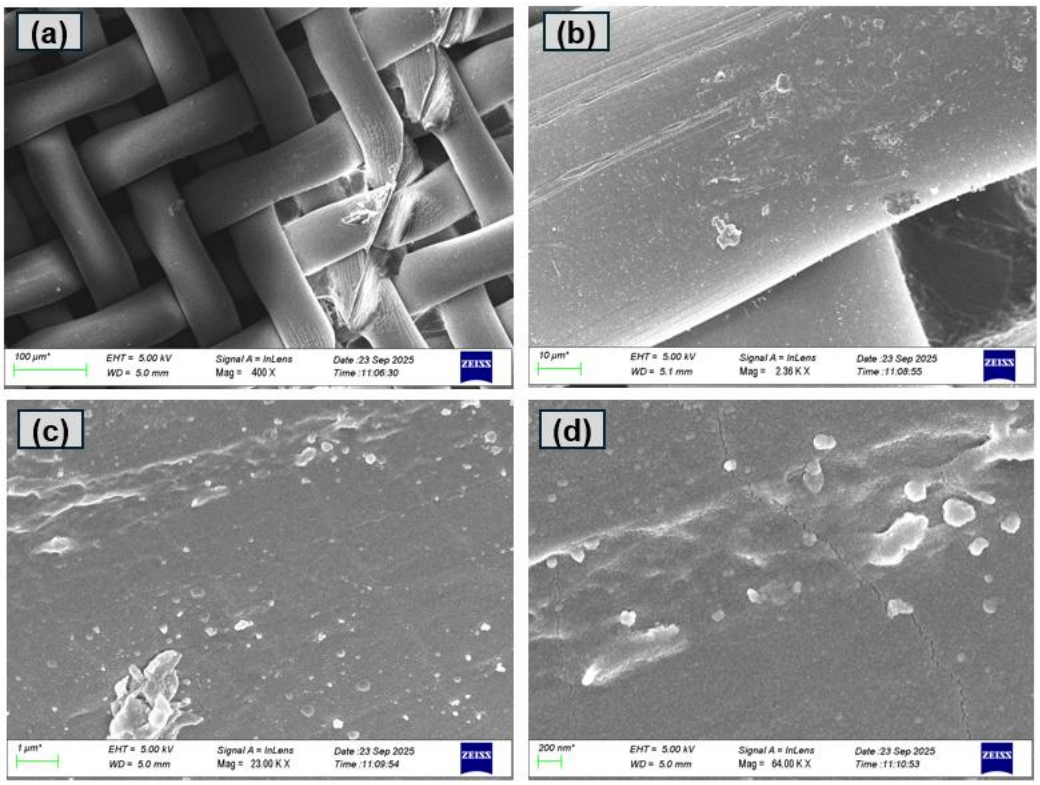

Figure 4. 4 SEM images of P2 showing surface morphology at different magnifications (scale bars: 100 µm, 10 µm, 1 µm and 200 nm) after plasma treatment

- **P4 (4 Minutes treated Nylon)**

In Figure 4.5, SEM images of nylon textile treated for 4 minutes (P4) are examined immediately after plasma treatment. At 100 µm, the woven structure remains the same even at longer plasma time, showing that prolonged plasma also does not result in damage at the macroscopic level. At 1 µm, this sample significantly enhanced the roughness of the surface as compared to 2 minute plasma-treated sample. Wrinkled, Etched patterns and irregular surface morphology can be seen, indicating more extensive interactions with the polymer during the plasma treatment. However, at the 200 nm scale, the wrinkled structure and some deep grooves are also observed. The depth of these nanogrooves and irregularities is higher than P2, showing long-term plasma treatment affects the surface more intensely.

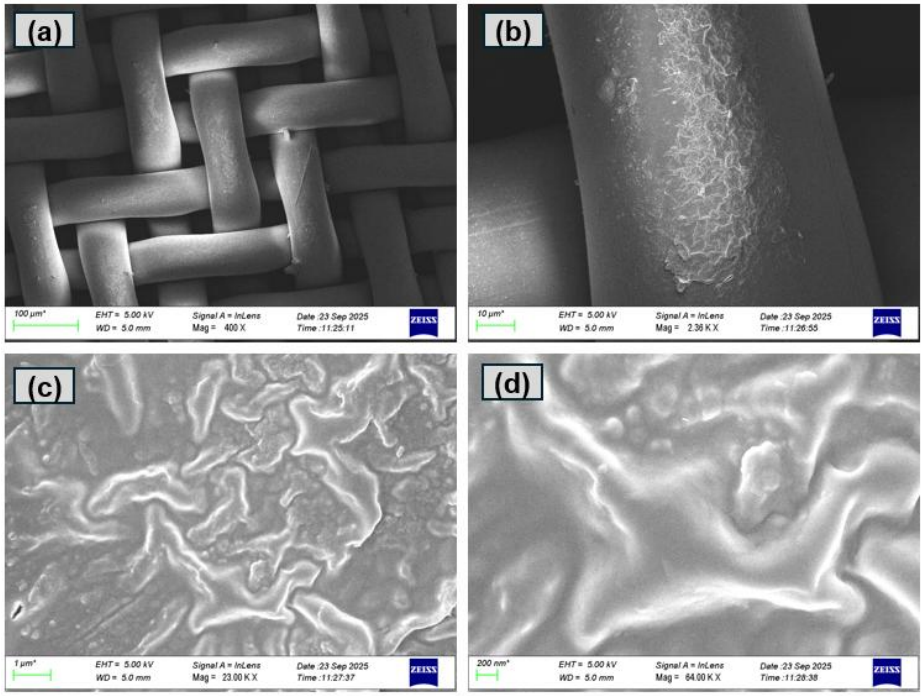

Figure 4. 5 SEM images of P4 showing surface morphology at different magnifications (scale bars: 100 µm, 10 µm, 1 µm and 200 nm) after plasma treatment

- **SEM Images After One Day**
- **P1 Untreated Nylon**

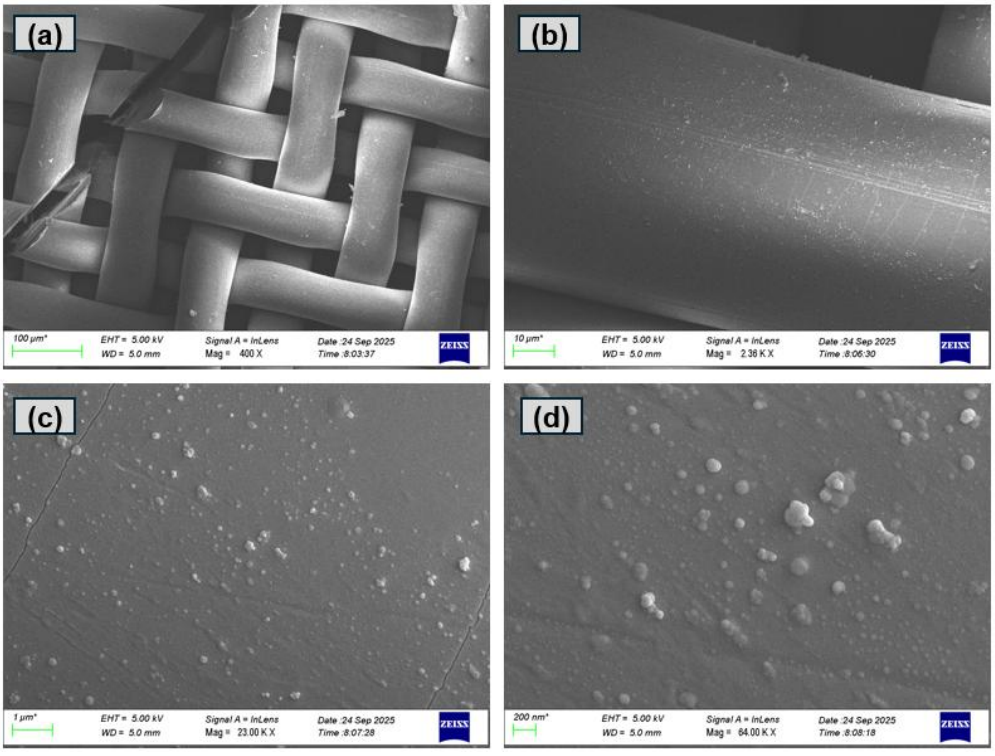

Figure 4. 6 SEM images of P1 showing surface morphology at different magnifications (scale bars: 100 µm, 10 µm, 1 µm and 200 nm) after one day of plasma treatment

- **P2 (2 Minutes Treated Nylon)**

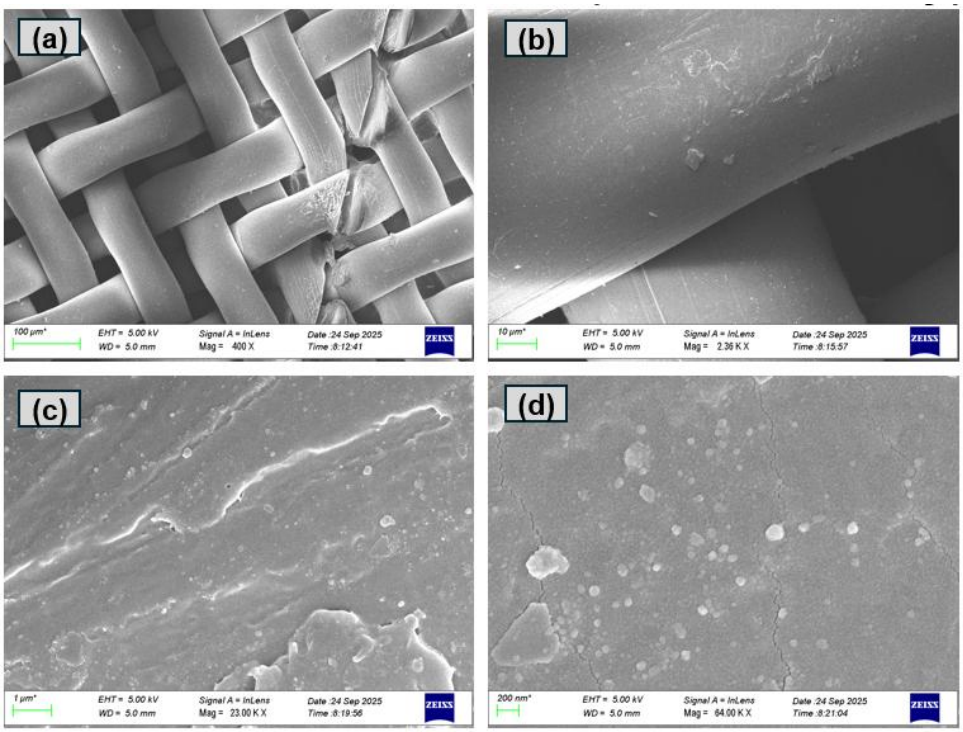

Figure 4. 7 SEM images of P2 showing surface morphology at different magnifications (scale bars: 100 µm, 10 µm, 1 µm and 200 nm) after one day of plasma treatment

- **P4 (4 Minutes Treated Nylon)**

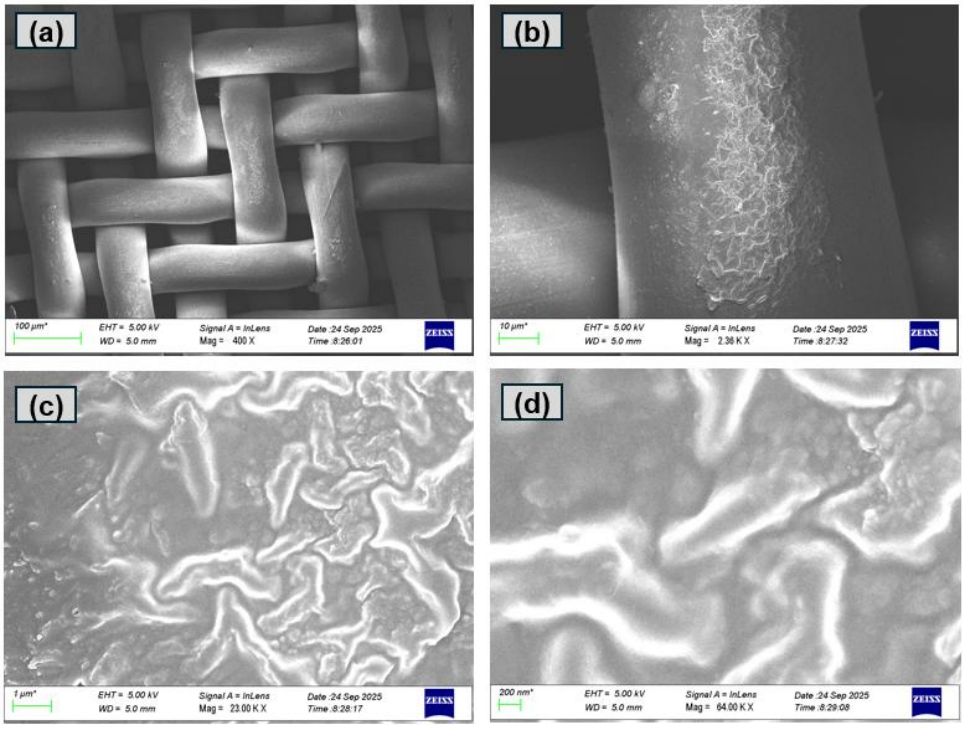

Figure 4. 8 SEM images of P4 showing surface morphology at different magnifications (scale bars: 100 µm, 10 µm, 1 µm and 200 nm) after one day of plasma treatment

- **SEM Images After Seven Days**
- **P1 Untreated Nylon**

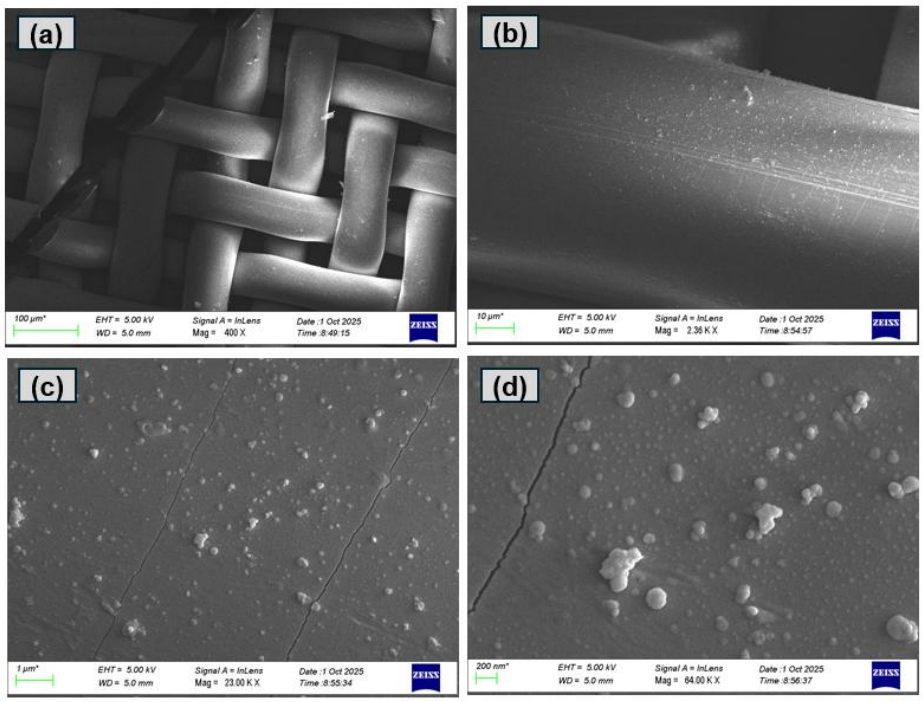

Figure 4. 9 SEM images of P1 showing surface morphology at different magnifications (scale bars: 100 µm, 10 µm, 1 µm and 200 nm) after seven days of plasma treatment

- **P2 (2 Minutes Oxygen Plasma Treatment)**

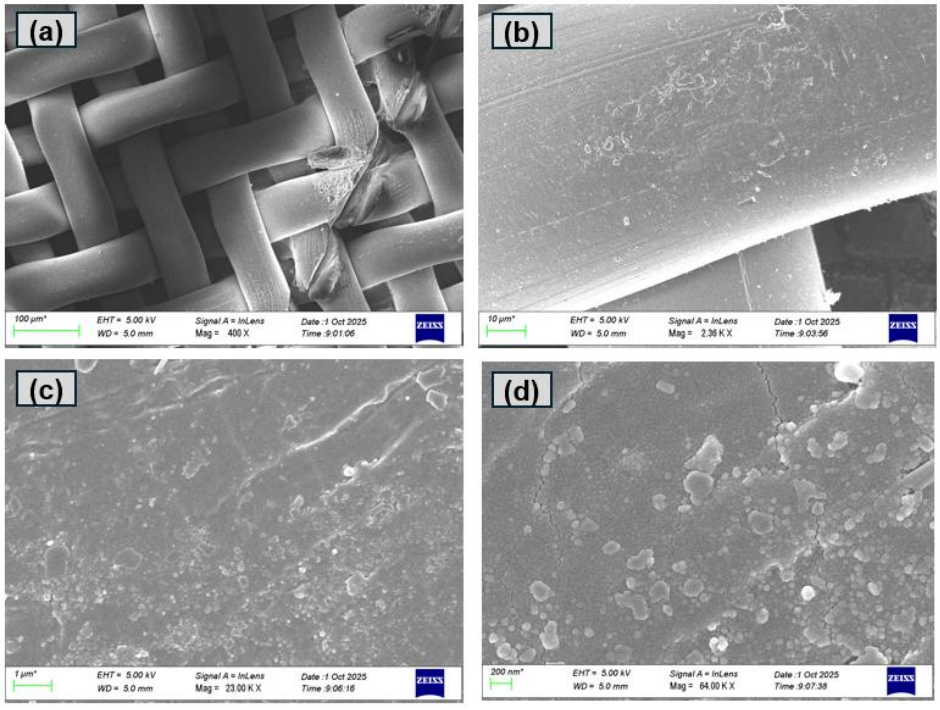

Figure 4. 10 SEM images of P2 showing surface morphology at different magnifications (scale bars: 100 µm, 10 µm, 1 µm and 200 nm) after seven days of plasma treatment

- **P4 (4 Minutes Oxygen Plasma Treatment)**

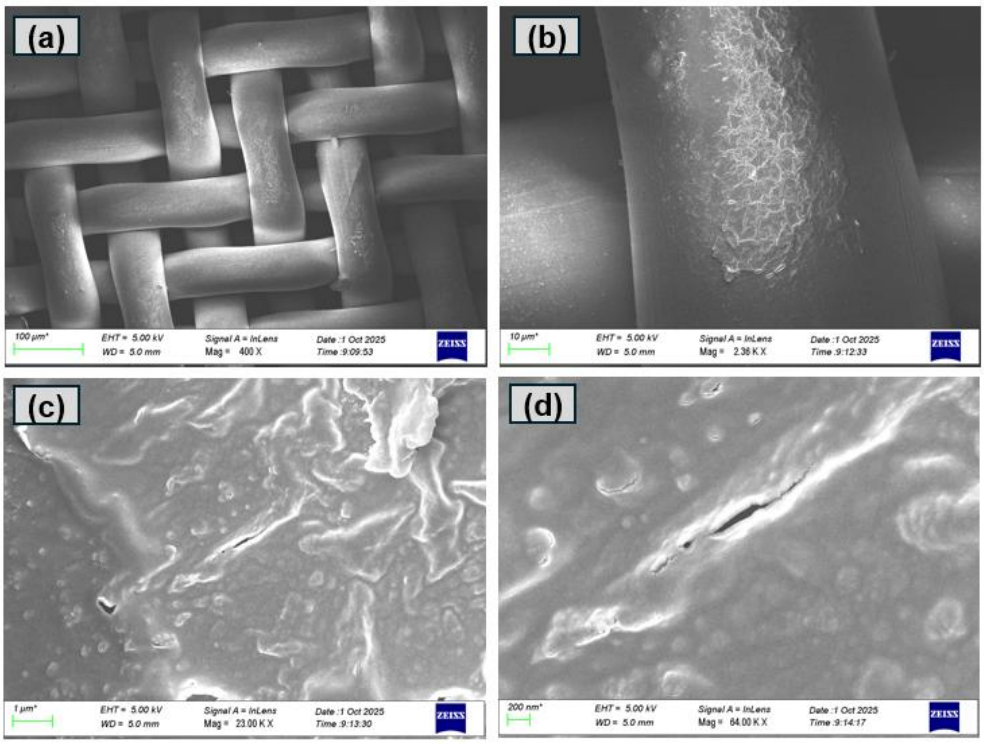

Figure 4. 11 SEM images of P4 showing surface morphology at different magnifications (scale bars: 100 µm, 10 µm, 1 µm and 200 nm) after seven days of plasma treatment

- **Ageing effect of Oxygen Plasma on P2 sample**

Figure 4.12 shows the SEM morphology of the nylon textile with 2-minute oxygen plasma treatment (P2) at different ageing times: a) after the plasma treatment, b) after one day, and c) after 7 days. At the 1 mm scale, Figure 4.12 (a), the image confirmed that there are some changes on the surface after plasma treatment and observed pits and cracks features across the surface by introducing polar group exposure to the surface. After one day, Figure 4.12 (b), the surface shows partial smoothing and softens etching, indicating partial relaxation and reorientation into the bulk polymer of the plasma-treated surface, which is also reflected in recovery towards hydrophobicity. After 7 days, Figure 4.12 (c), the morphology appears more homogeneous and smoother as compared to previous days.

The inset 200 nm scale SEM images are shown in the figure 4.12 (d), which provides additional information on surface morphology after ageing at the nanoscale. After the plasma treatment, the surface displays nanoscale irregularities. With time, the density of these nanoscale irregularities gradually decreases, and after 7 days, the surface shows reduced heterogeneity. The nanoscale morphology also reveals the gradual relaxation of plasma-induced modification.

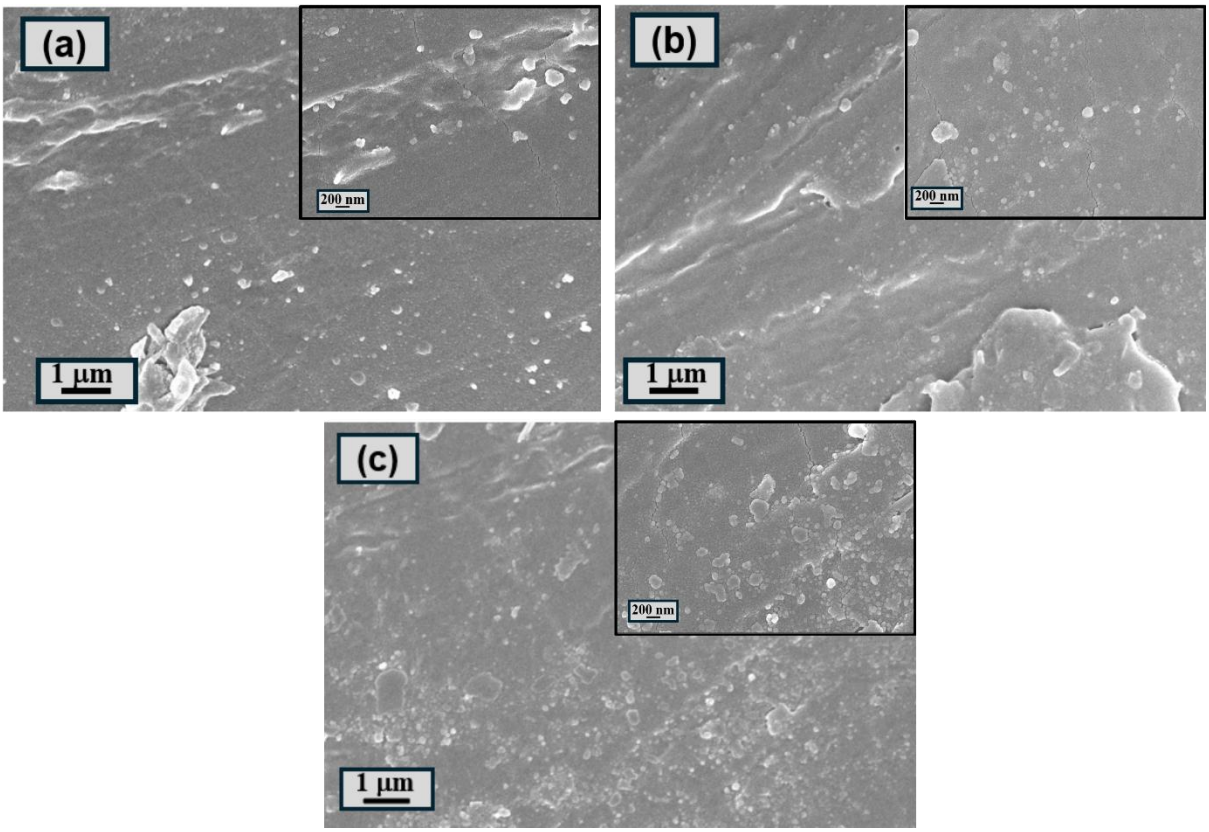

Figure 4. 12 Surface morphology evolution of nylon after 2-minute plasma treatment (a) immediately after plasma treatment, (b) after one day, and (c) after seven days.

- **Ageing effect of Oxygen Plasma on P4 sample**

Figure 4.13 shows the SEM images of P4 plasma-treated nylon for 4 minutes at different ageing times: a) after the plasma treatment, b) after one day, and c) after 7 days. At the 1 mm scale, the SEM images were recorded immediately after treatment, which shows pronounced roughening showing wrinkled, folded type morphology, showing extensive plasma-induced surface. After 1 day of ageing, this wrinkled morphology remains clearly visible, although partial relaxation of some sharp features and slight smoothing can be seen. After 7 days of ageing, the surface, however, retains relatively rough morphology; the features appear broader and less sharply compared to the morphology of previous days, suggesting gradual stabilisation rather than complete recovery of the surfaces.

At 200 nm, the inset figures 4.13 (c) show clear nanoscale modifications induced after plasma treatment and showing ageing. After seven days of ageing, the nanoscale morphology becomes more uniform, with broader and less distinct features, suggesting surface relaxation also at the nanoscale and maintaining overall roughened structures at the nanoscale.

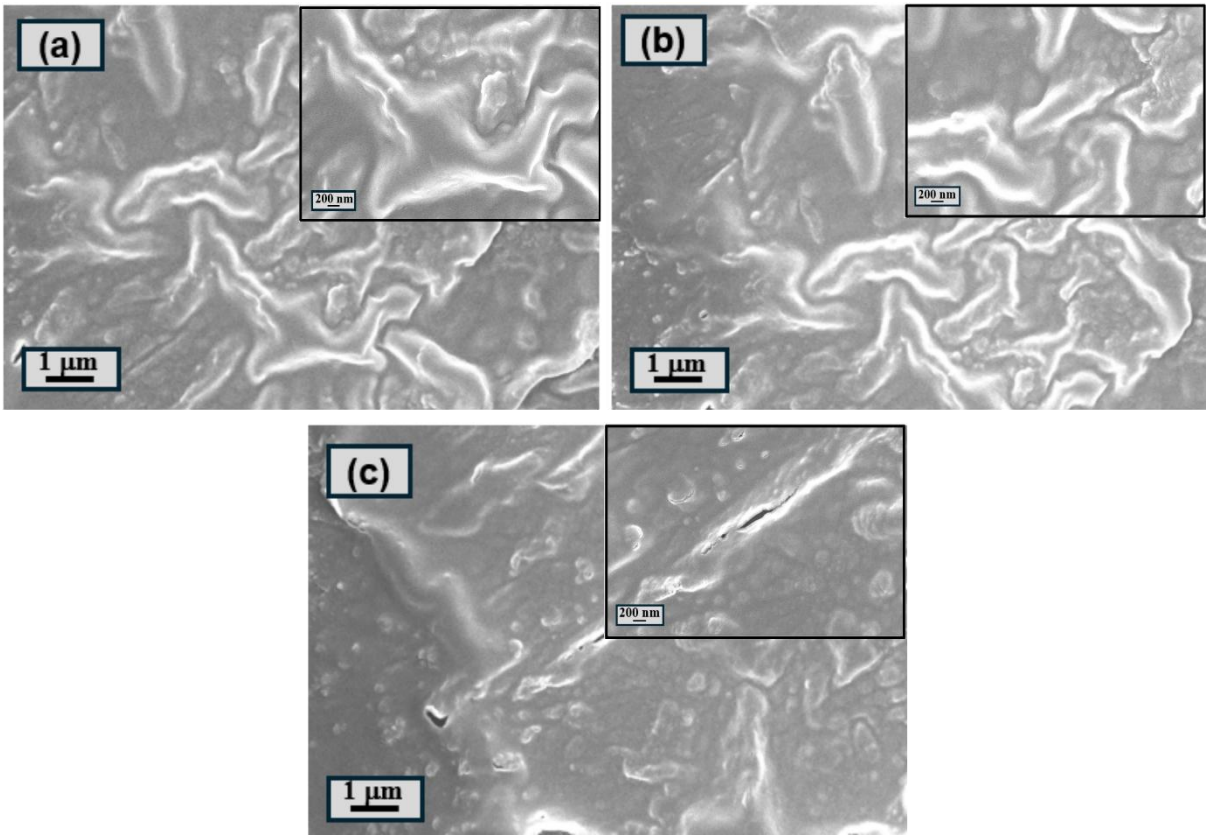

Figure 4. 13 Surface morphology evolution of nylon after 4-minute plasma treatment (a) immediately after plasma treatment, (b) after one day, and (c) after seven days.

4.3.2 FTIR Analysis

ATR-FTIR measurements were performed using a Nicolet iN10 micro-FTIR spectrometer equipped with an ATR accessory and an MCT-cooled detector, operating in the spectral range of 4000–675 cm^{-1}. All spectra were recorded in ATR mode. Two independent measurement series were conducted: the first used a resolution of 8 cm^{-1} with 256 scans and a collection time of approximately 51 s, and is presented for qualitative spectral comparison, while the second used a higher resolution of 4 cm^{-1} and a longer acquisition time of approximately 1 min 30 s to improve signal-to-noise ratio. The semi-quantitative peak-area ratio analysis is based on the second measurement series to ensure more reliable peak integration.

The surface chemistry of untreated nylon (P1) and plasma-treated samples (P2 and P4) was studied by using ATR-FTIR spectroscopy, and the samples were also analysed in terms of their change with ageing. Figure 4.14 presents some plots of FTIR transmission spectra of samples P1, P2, and P4 on the day of plasma treatment (Figure 1a), one day after the treatment (Figure 4.14b), and one week after the treatment (Figure 4.14 c). All of the spectra display the typical

absorption bands of nylon, with the broad N-H stretch at 3200-3400 cm^{-1}, C-H stretching frequencies at 2930 and 2850 cm^{-1}, amide I (1650 cm^{-1}) and amide II (1540 cm^{-1}) bands[97, 98]. All the samples treated or untreated by plasma treatments always show these properties at any ageing time, which means that oxygen plasma treatment does not affect the bulk chemical structure of the nylon substrate. Minor variations in the intensity of transmittance between untreated and plasma-treated specimens can be observed on the day of plasma treatment (Figure 4.14a), particularly within the high-wavenumber (N-H stretching) spectrum. Samples P2 and P4 that are treated with plasma exhibit a reduced transmittance at this region compared to untreated nylon, indicating that the samples have an increased absorption because of the increased surface polarity and the number of hydrogen bonds formed by the exposure to plasma.

One day later (Figure 4.14b), the general spectral profiles are the same, but the transmittance intensity of the samples differs slightly. This shows that the main nylon functional groups have not been broken yet, as the surface changes due to the influence of the plasma have been relaxed in the first place.

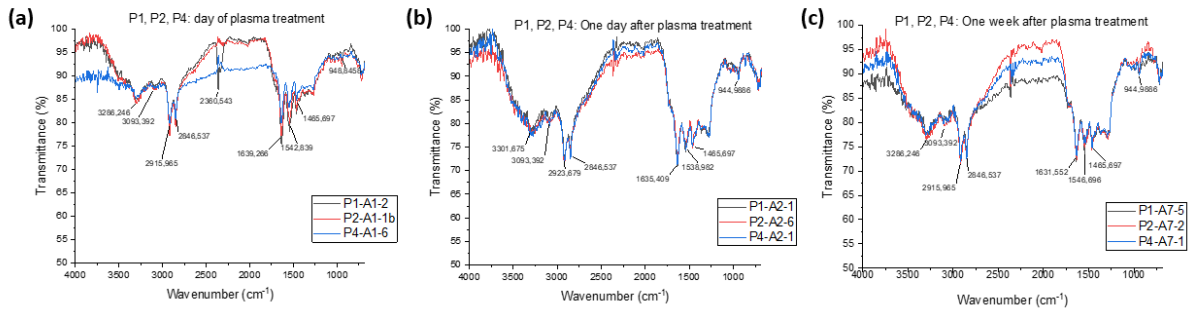

Figure 4. 14 ATR-FTIR transmission spectra of untreated nylon (P1) and plasma-treated samples (P2: 2 min, P4: 4 min) measured (a) on the day of plasma treatment, (b) one day after treatment, and (c) one week after treatment.

After one week (Figure 4.14c) the transmission spectra of the plasma-treated samples remain similar to those of untreated nylon, although slight changes in the N-H and C-H regions are present. The occurrence of no new absorption bands and the integrity of typical nylon peaks demonstrate that the chemical modifications that occur when plasma is used are limited to the near-surface area and do not extend into the chemistry of the bulk polymer. It is noted that the transmission spectra are here being compared only qualitatively, to ensure that there is a chemical integrity and reproducibility between samples and ageing times. The more specific

analysis of surface chemical changes is performed in terms of absorbance spectrum analysis and semi-quantitative analysis of peak area ratios, as it is discussed below.

In comparison with the transmission spectra, the representation of the absorbance by ATR-FTIR Figure 4.15a) makes more apparent the presence of delicate changes in the intensities and allows the qualitative comparison of the surface changes induced by the plasma. The typical absorption properties of nylon are observed in all the spectra: the broad NH/OH band between 3200 and 3400 cm^{-1}, CH stretching bands at approximately 2930 and 2850 cm^{-1} and amide I and amide II bands at approximately 1650 and 1540 cm^{-1}, respectively. All the spectra indicate that the plasma-treated samples (P2 and P4) have an increased absorbance and a wider profile in the NH/OH stretching region than the untreated samples. This is in line with the development of polar surface functionality as well as increased hydrogen bonding that occurs due to exposure to oxygen plasma. The same action of the sample P4 is more significant, which displays the higher level of surface activation with the increased duration of plasma treatment. Even one day of ageing (Figure 4.15b), the differences between the untreated and the plasma-treated samples are still present, though the relative absorbance of the N–H/O/H region is partially diminished. This implies the beginning of the surface chemical relaxation, probably in the form of polar groups reorientation off the nearest surface and contact with the species in the environment. After one week (Figure 4.15c), the absorbance spectra of the plasma-treated samples change closer to that of the untreated nylon, especially in the high-wavenumber range. Nevertheless, there are minor variations, which means that surface modification due to plasma is not entirely removed. The progressive overlap of spectral profiles with ageing is also in agreement with hydrophobic recovery, and the banning of additional absorption bands testifies that no bulk chemical degradation occurs because of plasma treatment. It has to be mentioned that here the absorbance spectra are relied upon in order to provide qualitative analysis of chemical changes on the surface. In order to further evaluate changes in time-dependent variations of surface polarity, a semi-quantitative analysis with regards to the ratio of peak areas is found in the next section.

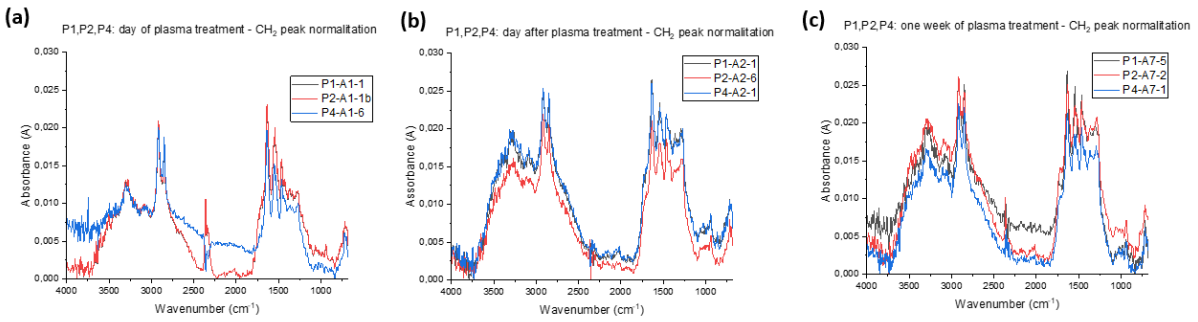

Figure 4. 15 ATR-FTIR absorbance spectra of untreated (P1) and plasma-treated nylon samples (P2 and P4) measured on the day of plasma treatment, normalised with respect to the CH_2 reference band.

Same Sample over time Absorbance

Figure 4.16 compares the CH_2-normalized absorbance spectra of untreated (P1) and plasma-treated nylon samples (P2 and P4) as a function of ageing time (day 0, 1, and 7). For the P2 sample, the relative intensity of the N–H/O–H stretching region decreases with ageing, indicating a reduction in surface polarity consistent with hydrophobic recovery. In contrast, the P4 sample shows smaller and non-monotonic variations with time, suggesting that surface chemical changes are subtle and influenced by local heterogeneity. The untreated sample exhibits larger fluctuations, reflecting measurement variability and moisture sensitivity rather than true chemical modification

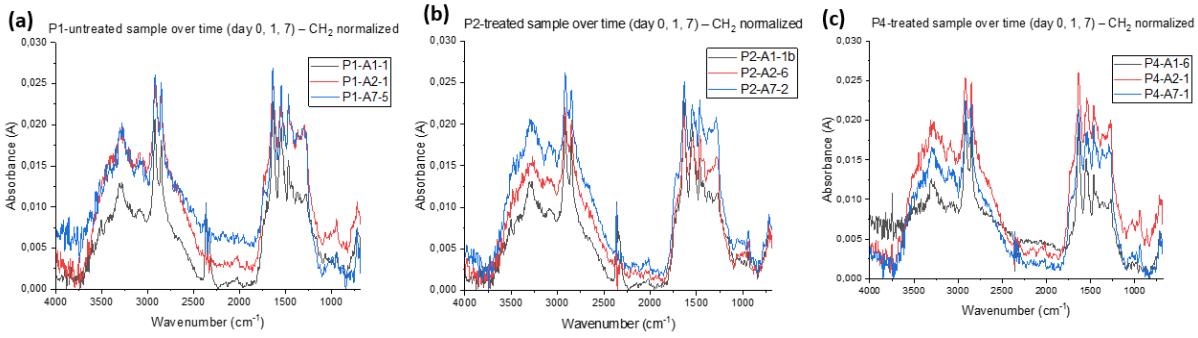

Figure 4. 16 ATR-FTIR absorbance spectra of (a) untreated nylon (P1), (b) 2 min plasma-treated nylon (P2), and (c) 4 min plasma-treated nylon (P4) measured as a function of ageing time (day 0, day 1, and day 7). The spectra illustrate time-dependent variations in the N–H/O–H stretching region, indicating surface chemical evolution after plasma treatment.

Figure 4.17 summarises the semi-quantitative ATR-FTIR analysis by showing the evolution of the N–H/CH_2 peak-area ratio for untreated (P1) and plasma-treated nylon samples (P2 and P4) as a function of ageing time. Immediately after plasma treatment, both P2 and P4 exhibit higher N–H/CH_2 ratios compared to the untreated sample,

indicating an increase in relative surface polarity due to plasma-induced functionalization. With ageing, the N–H/CH_2 ratio for the P2 sample decreases, consistent with the reduction in surface polarity inferred from the absorbance spectra and with the observed hydrophobic recovery in contact-angle measurements. In contrast, the P4 sample shows only minor changes in the ratio over time, suggesting that surface chemical rearrangement is less clearly captured by ATR-FTIR for the more strongly plasma-treated surface, likely due to the surface-limited nature of the modification and the influence of measurement variability.

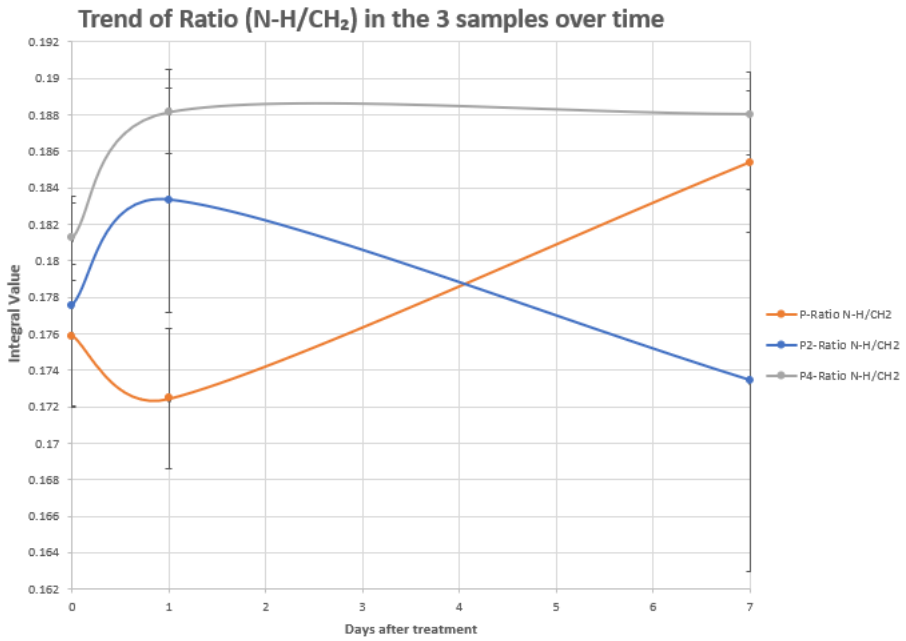

Figure 4. 17 Evolution of the N–H/CH_2 peak-area ratio for untreated (P1) and plasma-treated nylon samples (P2 and P4) as a function of ageing time. The ratios were calculated from ATR-FTIR spectra acquired using higher spectral resolution and longer acquisition time and are presented as a semi-quantitative indicator of relative surface polarity changes following plasma treatment and during ageing.

4.4 Effect of rGO/Metal Oxide Deposition on Plasma-Treated Nylon

4.4.1 rGO/Metal Oxide Deposition on Untreated Nylon

Figure 4.18 depicts images of SEM of rGO/CuO deposited on non-treated nylon fibres at various magnifications. The surface of untreated nylon is relatively smooth, and the deposited rGO/CuO is dispersed with a clear agglomeration and unequal coverage. The coating is mostly in the form of isolated flakes or clusters and not in the form of a continuous layer, which means that there is not much interaction between the rGO/CuO material and the untreated nylon surface.

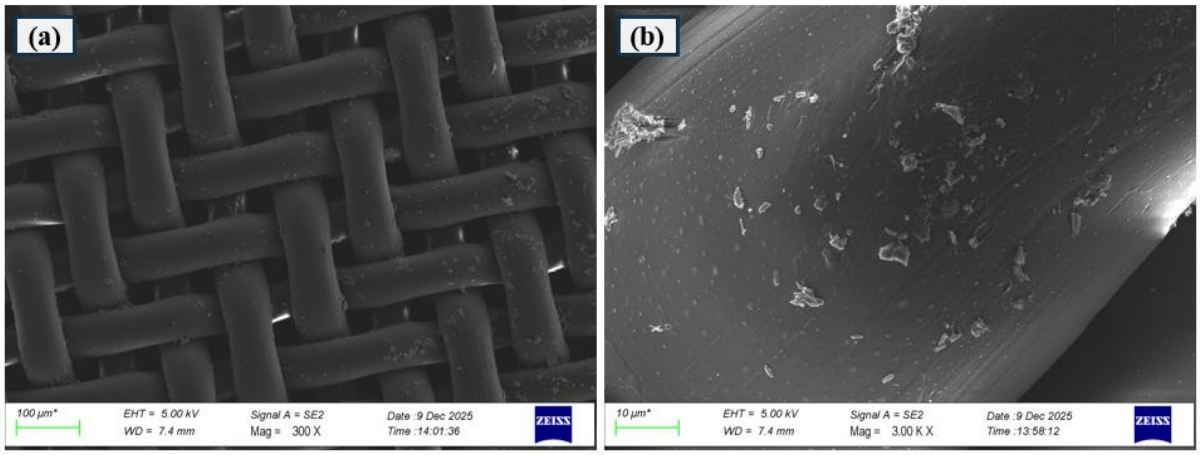

Figure 4. 18 SEM images of rGO/CuO deposited on untreated nylon fibres at (a) at 100 µm low magnification showing the textile structure and (b) at 10 µm higher magnification illustrating sparse and agglomerated rGO/CuO deposition on individual fibres.

- **EDX Mapping of rGO/CuO on Untreated Nylon**

The analysis of EDS (Figure 4.19) proves the existence of carbon, copper, and oxygen, confirming the deposition of rGO/CuO on the nylon fibres. Elemental mapping, however, shows that there is an inhomogeneous distribution of Cu and O on the fibre surface, which agrees with the observations with the SEM of poor dispersion and weak adhesion. Such findings indicate that when no plasma treatment is applied, the low surface polarity and smooth morphology of nylon hinder effective anchoring of rGO/CuO and result in non-uniform formation of coatings.

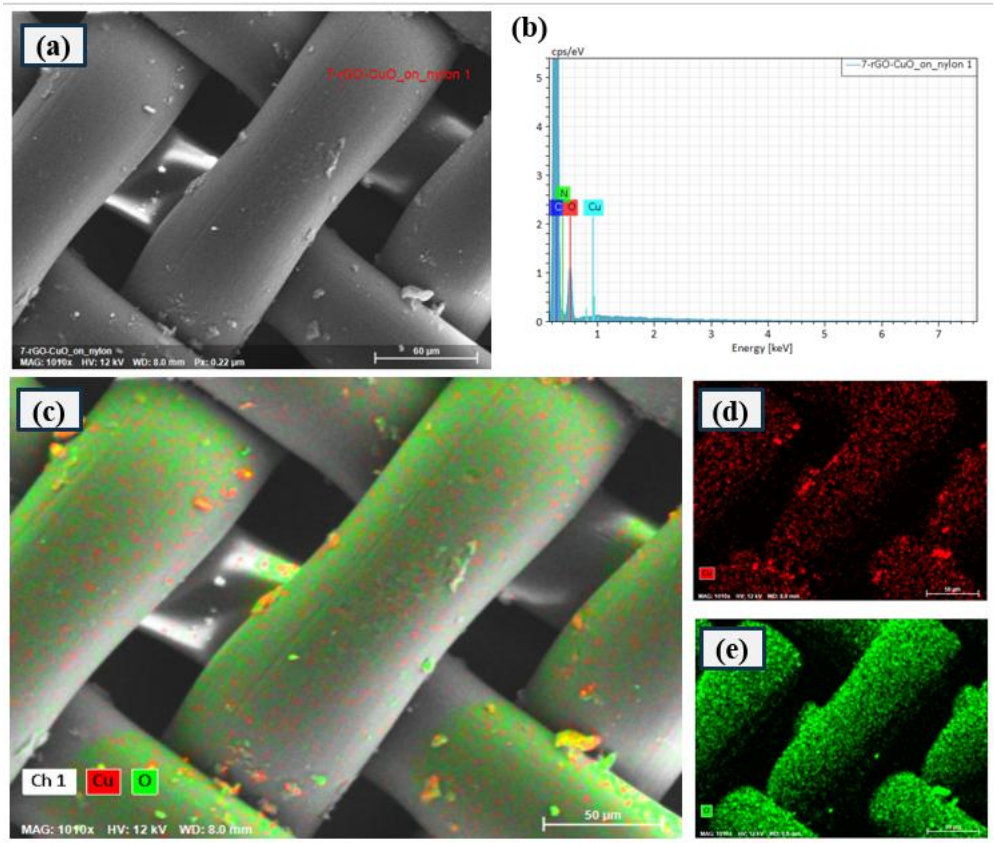

Figure 4. 19 (a) SEM image of rGO/CuO-coated untreated nylon used for EDS analysis, (b) corresponding EDS spectrum confirming the presence of C, Cu, and O, and (c–e) elemental mapping showing the distribution of Cu and O on the nylon fibers, indicating non-uniform coverage.

4.4.2 rGO/CuO on Plasma Treated (P2) Nylon

SEM images of rGO/CuO dipcoating on the plasma-treated P2 nylon fibres are presented in Figure 4.20. A low-magnification image shows that the coating is distributed throughout the textile structure, whereas increasing the magnification allows seeing rGO/CuO aggregates strongly fixed to the surface of the fibres. Plasma-treated nylon has increased surface roughness and surface activation, resulting in a high adhesion of the deposited material and preventing large-scale delamination.

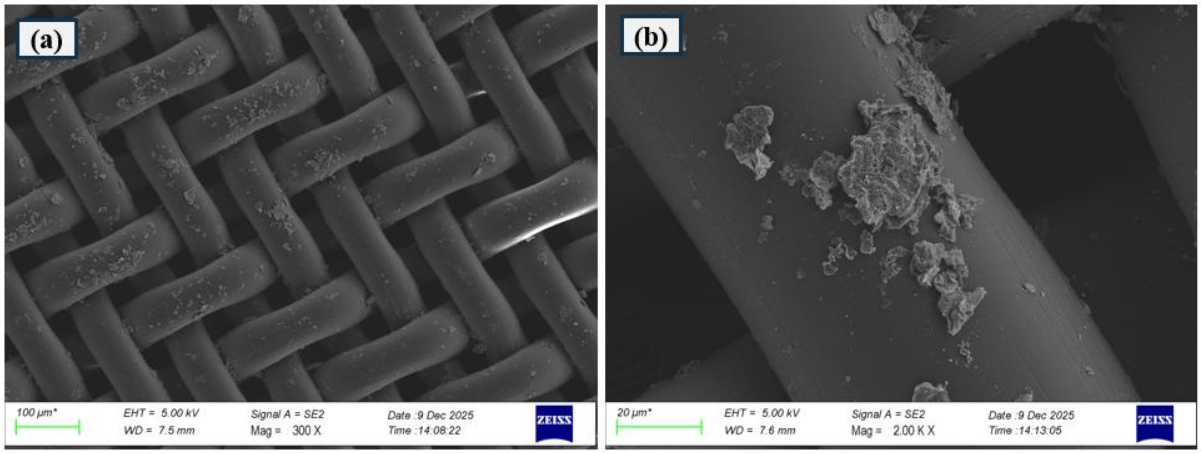

Figure 4. 20 SEM images of rGO/CuO deposited on plasma-treated P2 nylon: (a) 100 µm low-magnification image showing coating presence over the textile structure and (b) 10 µm higher-magnification image highlighting rGO/CuO aggregates adhered to the fiber surface.

- **EDX Mapping of rGO/CuO on Plasma Treated (P2) Nylon**

The above EDS analysis (Figure 4.21) reveals the presence of carbon, copper and oxygen, which proves that rGO/CuO is successfully deposited on the plasma-treated fibres. The elemental mapping shows that both Cu and O are spread over the fibre surface, which proves the good anchoring of the CuO component in the rGO matrix. Other smaller signals of elements (Mg, Si, Ca and Mn) are also believed to be background contributions of the textile substrate, processing residues, or environmental contamination and are not regarded as a part of the coating. In general, the findings of the SEM and EDS tests prove that rGO/CuO has stable attachment and surface coverage on plasma-treated P2 nylon.

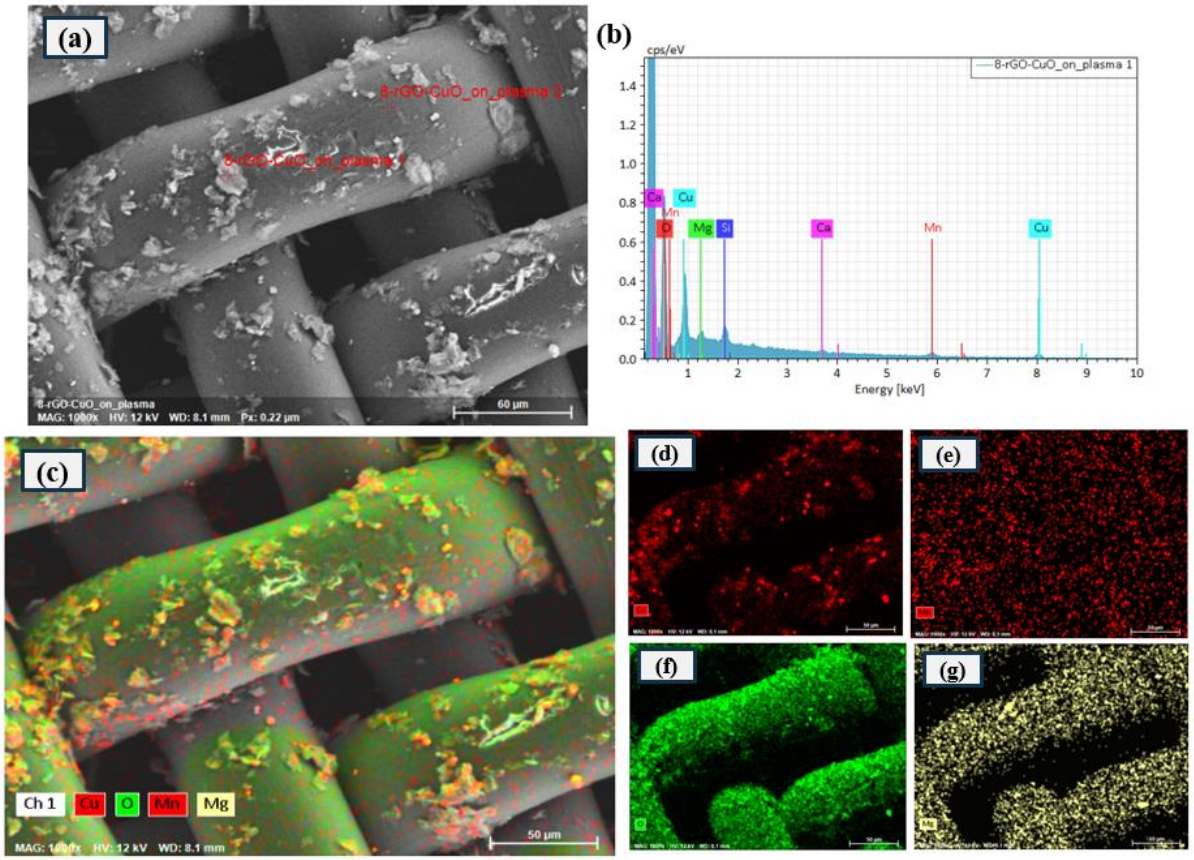

Figure 4. 21 SEM–EDS analysis of rGO/CuO deposited on plasma-treated P2 nylon: (a) SEM image of coated fibers, (b) EDS spectrum confirming the presence of C, Cu, and O, while minor elements are attributed to background contributions (c) combined elemental map, and (d–g) individual elemental maps showing the distribution of Cu and O on the fiber surface.

4.4 Summary

In this chapter, the effect of oxygen plasma treatment on the surface properties of nylon textiles and their subsequent ageing behavior was systematically investigated. Plasma treatment provided a radical change in the surface wettability by turning the originally hydrophobic nylon surface (water contact angle 107 degrees) into super hydrophilic one after treatment. The ageing studies have shown that hydrophobic recovery is partially recovered with time, and the degree of recovery is dependent on the duration of plasma treatment. The sample that was treated with plasma over 4 min recovered faster and more complete recovery compared to the 2 min treated sample, approaching the wettability of the untreated nylon after seven days.

The SEM analysis revealed that the morphology of the surface of the nylon fibers was largely altered by the plasma treatment and strong surface roughening and wrinkled patterns were immediately obtained after the treatment. Despite the partial smoothing that was evidenced in the ageing process, the topographical characteristics caused by plasma were still observable

after a week, which implies morphological modification to persist. These structural changes contribute to the observed wettability evolution by altering surface roughness and available interaction sites.

The analysis of ATR-FTIR showed the presence of surface chemistry alterations associated with the use of the plasma, in particular, the transformation of N-H and C-H functional groups. Semi-quantitative analysis of peak-area ratios (N –H/CH_2) showed that the surface underwent time-dependent reorganization related to chemical reactions at the surface associated with hydrophobic recovery through the reorientation and diffusion of polar groups off the surface.he combined FTIR and wettability results confirm that both surface chemistry and morphology play complementary roles in the ageing behavior of plasma-treated nylon.

Lastly, the practical implication of the plasma treatment was also shown by the deposition of rGO/CuO coatings onto the plasma-treated nylon. SEM and EDS analyses confirmed stable attachment and improved surface coverage of rGO/CuO on plasma-treated fibers, with clear detection and uniform distribution of Cu and O across the surface. This enhanced adhesion is attributed to plasma-induced surface activation and roughening, which facilitate stronger interfacial interactions between the coating and the nylon substrate. These results highlight the effectiveness of plasma treatment as a surface modification strategy to improve functional coating deposition on nylon textiles.

Overall, this chapter establishes a clear relationship between plasma-induced surface activation, wettability evolution, chemical ageing, and coating adhesion, providing a strong foundation for subsequent functionalization and application of plasma-treated nylon textiles.

CHAPTER 5 Synthesis of Graphene Oxide (GO), and Reduced Graphene Oxide Quantum Dots (RGOQDs), Reduced Graphene Metal Oxide

Following the Oxygen Plasma treatment to modify the surface of nylon, which induces the functional groups and improves surface energy for material adhesion, this chapter focuses on the Synthesis part of graphene-based nanomaterials, which will be further used for the development of smart textiles. Graphene Oxide (GO), Reduced Graphene Oxide Quantum dots (rGOQDs), reduced Graphene metal Oxide nanocomposites appeared as a promising functional material due to their exceptional properties such as high surface volume ratio, electrical conductivity, tunable surface chemistry, and strong interactions with gas molecules. Previous research has shown that GO, GQDs, and rGO-metal oxide show superior gas sensing performance, and can be able to detect hazardous gases at very low concentrations at room temprature [99-101]. In this context, the formation of graphene-based nanomaterials and the deposition on treated nylon substrates are explored to impart gas-sensing performance to textiles.

5.1 Graphene Oxide (GO)

2D materials, particularly graphene or graphene-related materials, have been widely investigated over the last ten years due to their extraordinary properties, such as chemical inertness, mechanical strength, thermal conductivity and high electrical and optical transmittance[102]. These features suggest that the graphene-related materials are a potential candidate that can be used in various field applications like batteries, radio frequency devices, high-power electrical devices, and as water purification and chemo sensors[103].

Graphene was discovered by Geim and Novoselov in 2004 for the first time from graphite and using a scotch tape method[104]. Due to the fascinating characteristics, a 2D hybridised carbon sp^2 is a highly exacting material that attained significant goals. As graphene has several sheets, and they are set by some physical and chemical properties like π-π stacking and Van der Waals interactions[105]. The schematic structure of graphene oxide, showing the distribution of oxygen-containing functional groups on the basal plane and edges, is shown in Figure 5.1 Graphene oxide (GO) is a two-dimensional basal plane of graphene, which is functionalized with oxygen functional groups. The epoxide and hydroxyl groups are mostly found on the basal plane and carbonyl and carboxyl groups are mostly found on the sheet edges. These oxygen functionalities interfere with the sp 2 carbon framework and create defects and partial sp 3

hybridization. Consequently, GO is strongly polarized and hydrophilic on its surface and this allows it to interact strongly with polar substrates and metal oxides.

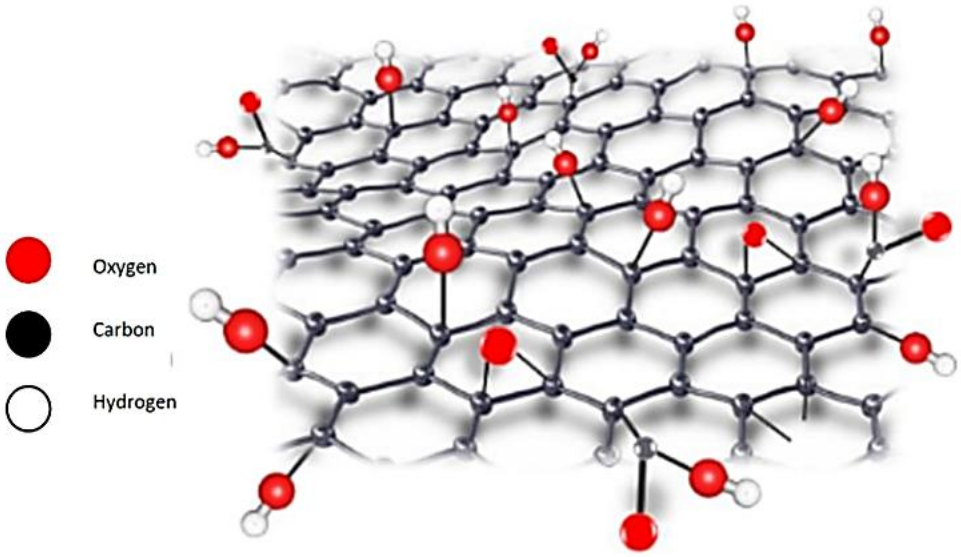

Figure 5. 1 Schematic representation of the graphene oxide (GO) structure illustrating the distribution of oxygen-containing functional groups on the basal plane and edges (adapted from [106]).

5.1.1 Modified Hummer's Method

For the synthesis of Graphene Oxide (GO), I used modified Hummers' method by using graphite powder (GP). Firstly, I used 27 ml of sulfuric acid (H_2SO_4) and 3 ml of phosphoric acid (H_3PO_4) in a 9:1 volume ratio. Both acids were mixed and then stirred for 10 minutes. 0.225 g of graphite powder was included in the acid solution. This mixture was stirred for 10 minutes, and then 1.32 g of potassium permanganate ($KMnO_4$) was added slowly to this solution. Then, leave it to stir for the next 6 hours, until the mixture becomes dark green. To eliminate extra $KMnO_4$, 0.675 ml of hydrogen peroxide H_2O_2 dropped slowly into the mixture and stir that mixture for 10 minutes. From H_2O_2, an exothermic reaction happened and let it cool down to room temperature for the next few hours. And then add 10 ml of hydrochloric acid (HCL) and 50 ml of DI water, and wash the solution by using a centrifugation machine (Bench top centrifuge R-5S plus) at 5300 rpm for 10 minutes. Then, the supernatant was decanted, and the pellet was again rewashed with HCl and DI 3 to 4 times. The washed GO was dried in an oven at 90˚C for 24 hours and then stored the dried GO in a laboratory desiccator.

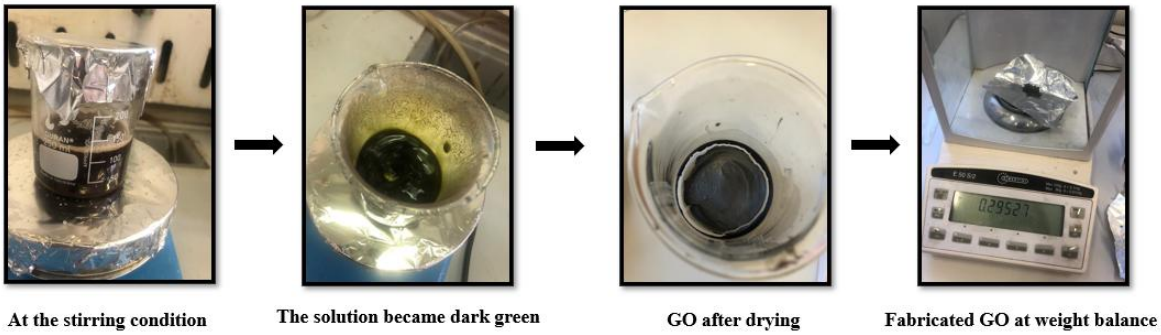

Figure 5. 2 Photographs Taken during the experiment

5.1.2 Characterisation of Graphene Oxide (GO)

- **XRD Analysis of GO**

Figure 5.3 shows the XRD spectrum of GO. XRD of GO was done by using a powder assembly of the Panalytical X'Pert Pro diffract meter, using Cu K radiation (1.5406 Å). The diffraction peak of GO was observed at 10.3°, corresponding to the d-spacing of 8.48 Å (0.84 nm), showing 001 indices. This peak indicates that the graphite powder is fully oxidised into GO. One other peak was observed at 42.6 degrees with indices 111 corresponding to the interlayer spacing of about 2.12 Å (0.21nm). No extra peak has been found, which confirms the crystallinity of the sample.

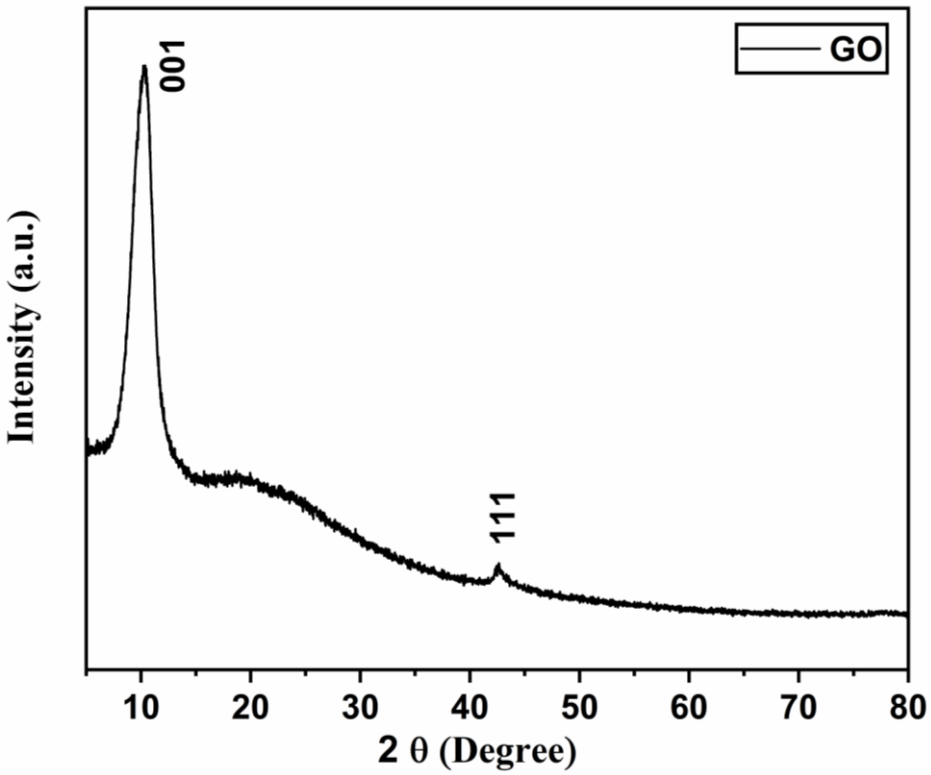

Figure 5. 3 XRD of Graphene Oxide by Modified Hummer's Method

The average crystallite size and lattice strain are calculated by using the built-in Scherrer calculator in Xpert High Score,

$$\boldsymbol{D} = \frac{\mathbf{K\lambda}}{\boldsymbol{\beta}\mathbf{cos\theta}}$$

where D is crystalline size, K is Scherrer's constant, and it is usually taken as 0.9. is the wavelength of X-rays, i.e., = 1.54 Å . And β is FWHM (full width at half maximum).

The formula for lattice strain, which is set up in Xpert high score, is

$$\varepsilon = \frac{\boldsymbol{\beta}}{\mathbf{4tan\theta}}$$

Where **β** is full width half maximum.

And, the dislocation density is calculated by using this formula.

$$\textbf{Dislocation density} = \frac{\mathbf{1}}{(\mathbf{D^2})}$$

Where D is the crystallite size.

Table 5. 1 Crystallite size, lattice strain, and dislocation density calculation for GO

S.No	hkl	d-spacing (nm)	2θ(degrees)	FWHM	Crystallite size (nm)	Lattice Strain	Dislocation density
1	001	0.84	10.3	0.16	50.2	0.808	0.0003
2	111	0.21	42.6	0.1	92.7	0.111	0.0001

From Table 1, we can calculate the average crystallite size, average lattice size and average dislocation density of GO. The average crystallite size is 71.45 nm, the average lattice strain is 0.45, and the average dislocation density is 0.0002.

- **Raman Analysis of GO**

A Raman spectrometer was also used to record information on structural and vibrational modes. The vibrational modes were observed at 1350 and 1598 cm^{-1}. The mode at 1350 cm^{-1} is directly associated with the D band, which comes due to the defects, vacancies, and distortions

in the sp^2 states of the lattice. The mode observed at 1598 cm^{-1} is known as the G band, and it is due to the stretching of the C-C bond in the sp^2 region. [107]. The peak intensity ratios of D and G bands (I_D/I_G) are calculated to be 0.98, which agrees with the literature.

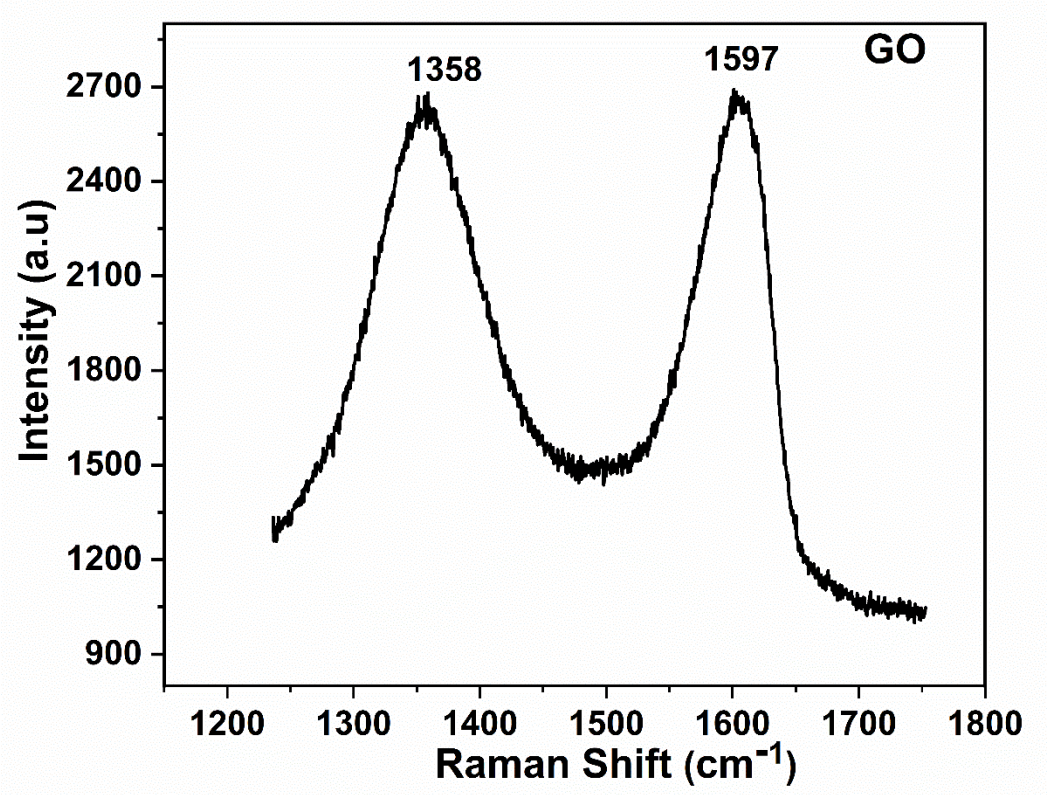

Figure 5. 4 Raman Analysis of GO

- **FTIR Analysis of GO**

FTIR spectroscopy was performed on the GO powder to characterise the presence of functional groups in GO, which contains oxygen functional groups. This analysis was performed using a Nicolet iN10 Thermo Fisher FTIR spectrophotometer in transmission mode. The spectra were obtained in the range 4000cm^{-1} - 980cm^{-1}, 512 scans for 51 seconds, using a cool detector. The powder of graphene oxide is very absorbent, so the transmission measurements are too noisy. Therefore, this measurement was acquired, focusing the spot on an area only marginally occupied by the sample, and we increased the scans to 512. This peculiar mode of measurement causes the presence of carbon dioxide in the spectrum.

Figure 5.5 shows the transmission spectrum of the GO sample. The functional groups, such as O-H, C-O, COOH, and C-OH, can be observed. A broad band around 3300 cm^{-1} due to the stretching mode of hydroxyl group bonds to the carbon backbone (C-OH, COOH, H_2O)[108, 109]. The peaks at 2957 cm^{-1} and 2867 cm^{-1} are due to symmetric and asymmetric CH_2-CH_3

stretching of GO. The absorption peak of the atmospheric CO_2 can be observed at 2350 $cm^{-1,}$ while the peak at 1733cm^{-1} is ascribed to C=O stretching of the carboxyl group. And at 1608cm^{-1} the stretching of the sp^2 carbon backbone (C=C)[110]. Finally, from 1280cm^{-1} to 980 cm^{-1} the graph reports the area of overlapped bands of C–O–C and C–O stretching, due to the presence of different oxygen functionalities bonded on the carbon backbone[111].

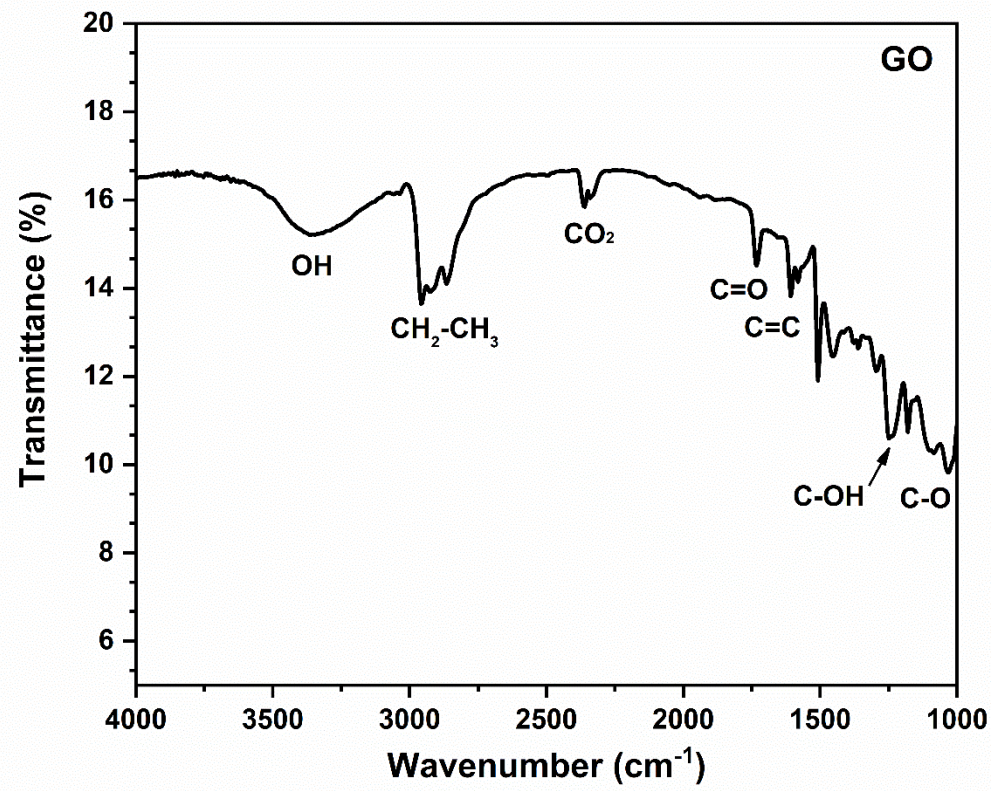

Figure 5. 5 Fourier transform infrared (FTIR) spectrum of graphene oxide (GO)

- **SEM Analysis of Graphite Powder**

Figure 5.6 shows the SEM images of Graphite powder, which shows the layered and flaky morphology. The graphite powder showed tigtly stacked and irregular structure. At low magnification, the graphite powder shows agglomerated clusters showing strong interlayer attractions, while high magnification images display smooth planes and some wrinkle-like morphology.

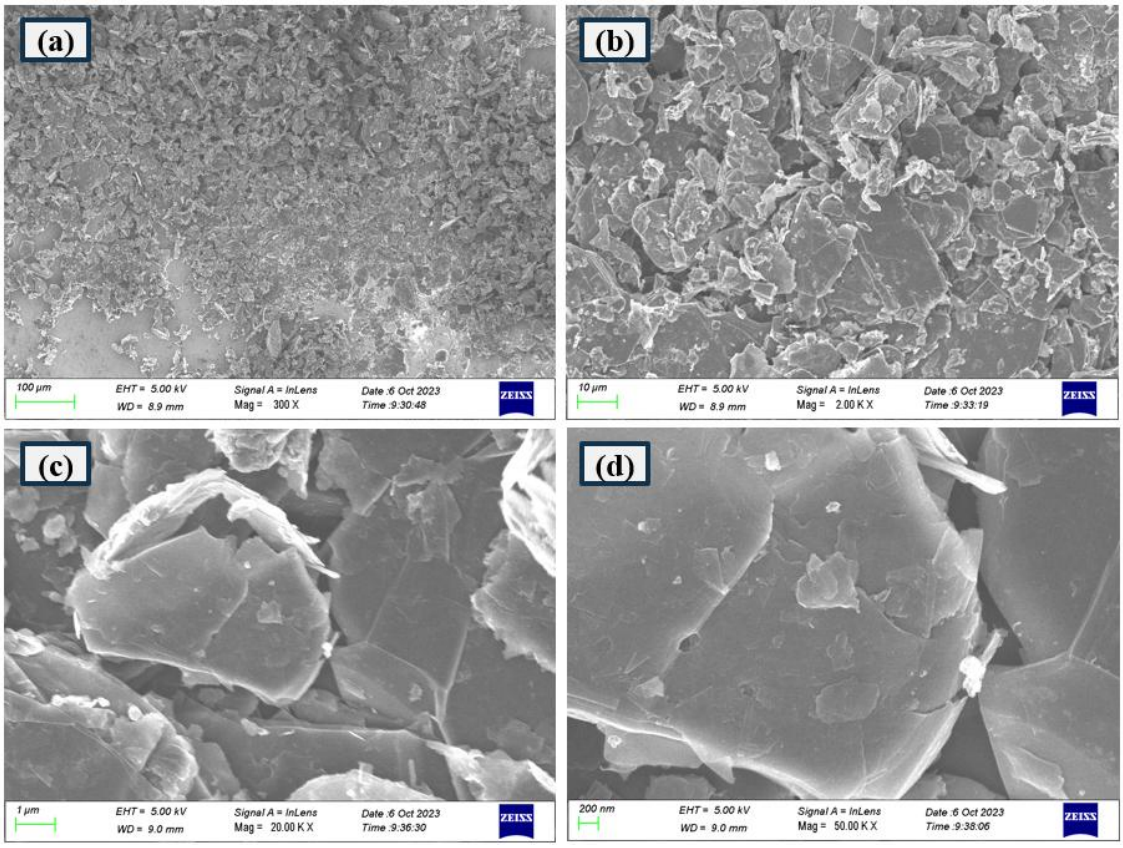

Figure 5. 6 SEM analysis of graphite powder showing surface morphology at different length scales: (a) 100 µm, (b) 10 µm, (c) 1 µm, and (d) 200 nm.

- **SEM Analysis of Graphene Oxide (GO)**

SEM images of Graphene Oxide (GO) show an altered morphology as compared to graphite powder, confirming the successful formation of GO by using Modified Hummers' method. The GO sheet exhibits wrinkled, thin and folding sheet-like morphology, which is consistent with the literature[112]. These morphology changes are due to the introduction of oxygen species (hydroxyl, carboxyl and epoxy groups) that disturb the π-π stacking of layers and enhance the interlayer spacing. We can see that the GO is more loosely stacked as compared to graphite powder, which has a densely packed morphology.

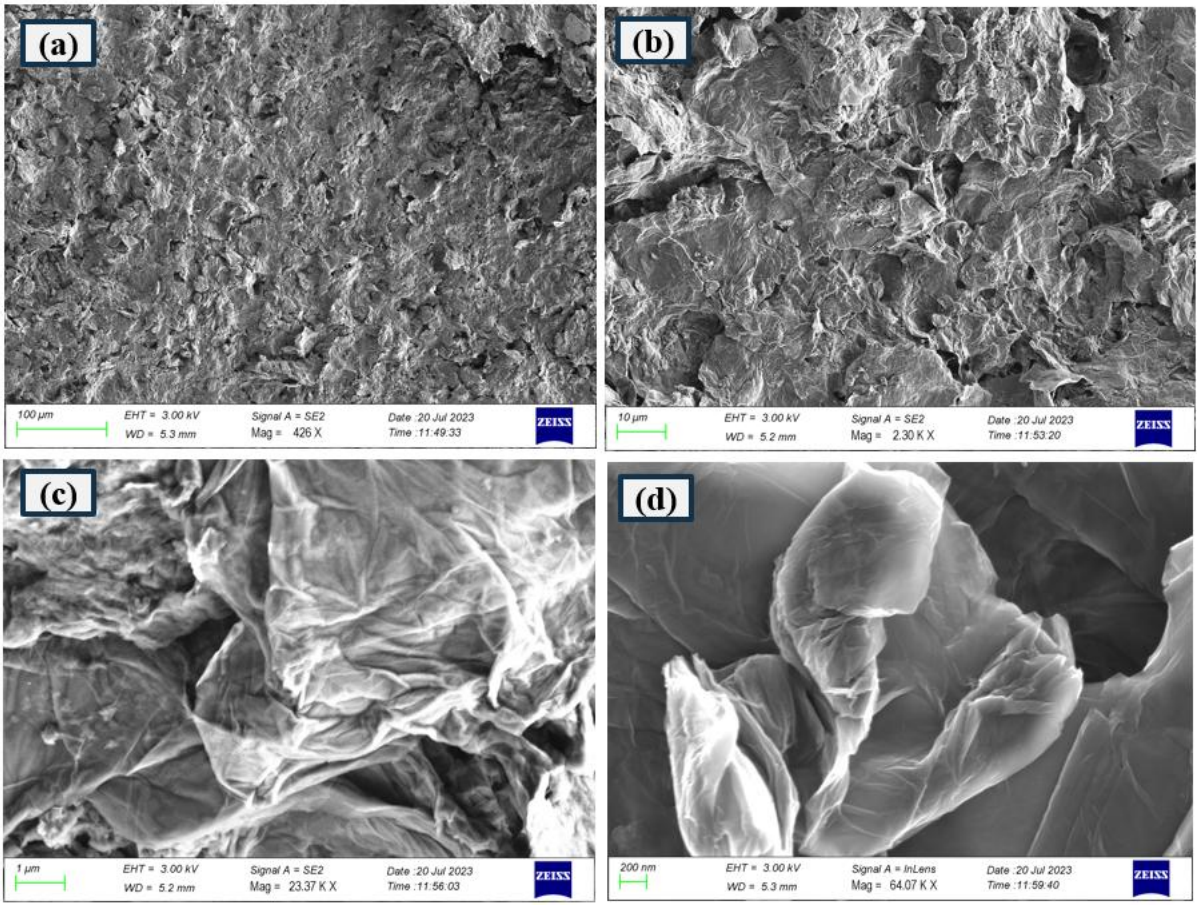

Figure 5. 7 SEM analysis of Graphene Oxide (GO) showing surface morphology at different length scales: (a) 100 µm, (b) 10 µm, (c) 1 µm, and (d) 200 nm.

- **Bath Sonication of Graphite Powder and Graphene Oxide**

After the formation of GO, I started experimentation of reducing the size of the graphene oxide (GO) by using different methods. Initially, I used the straightforward bath sonication for 12h to reduce both GO and Graphite powder (GP). The images from the scanning electron microscope revealed that this approach exfoliated the GO into individual thin sheets.

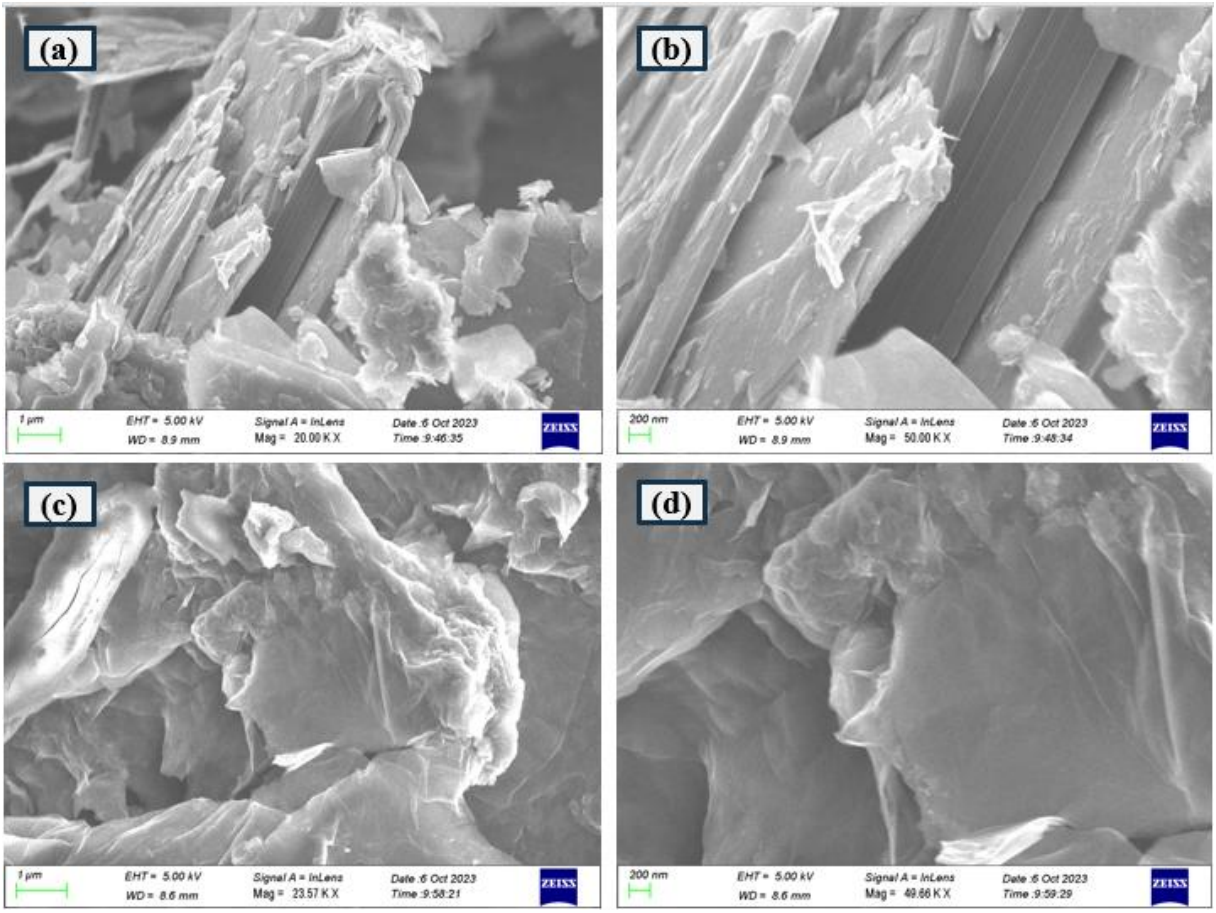

Figure 5. 8 SEM images of (a, b) graphite powder after 12 h bath sonication and (c, d) graphene oxide (GO) powder after 12 h bath sonication.

- **TEM Analysis of GO**

Figures (a–d) show TEM images of graphene oxide (GO) sheets at a length scale of 2 µm. The GO sheets have thin, clear and wrinkled morphological features, which means exfoliation was successful. The fact that there are folded edges and areas of overlapping indicates the presence of few-layer GO structures.

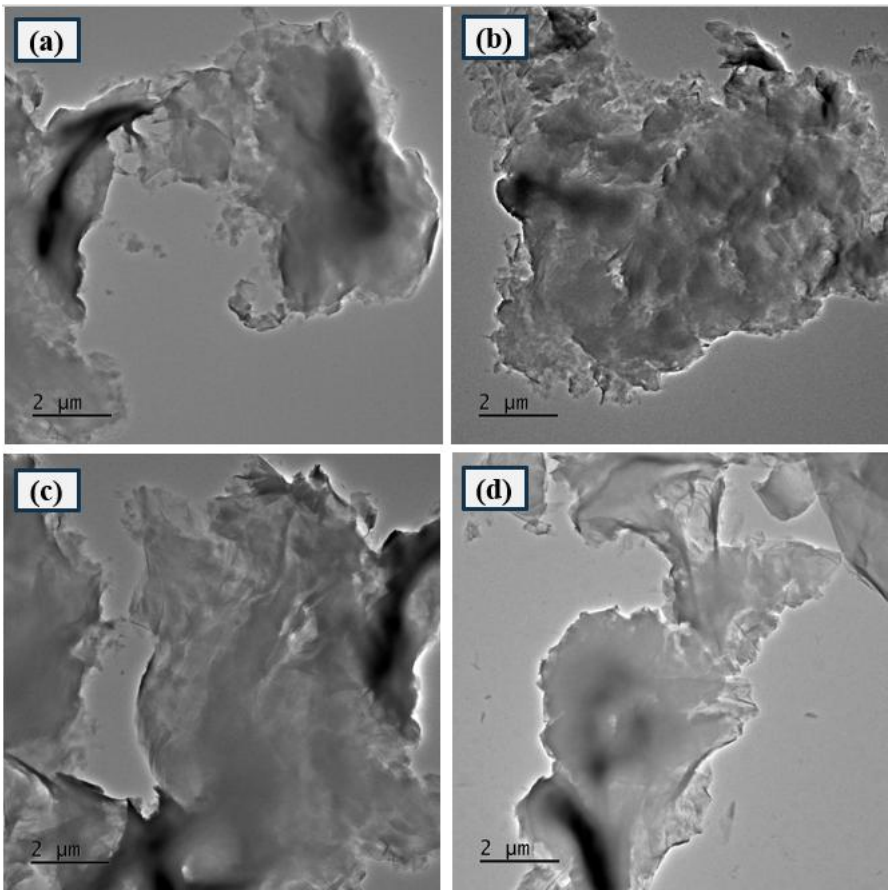

Figure 5. 9 TEM image of graphene oxide (GO) with a length scale of 2 µm

- **EDX Mapping of GO**

The composition of the elements of graphene oxide (GO) was investigated using energy-dispersive X-ray spectroscopy (EDS). The spectrum of EDS confirms carbon and oxygen as the major components, which is in line with the oxygen-functionalized sheet of graphene. Elemental mapping reveals that there is a homogeneous distribution of oxygen and carbon within the GO flakes, which means that the oxidation is homogeneous. A weak sulfur signal is also seen, which can be explained by the remaining sulfur-containing groups from the synthesis of GO

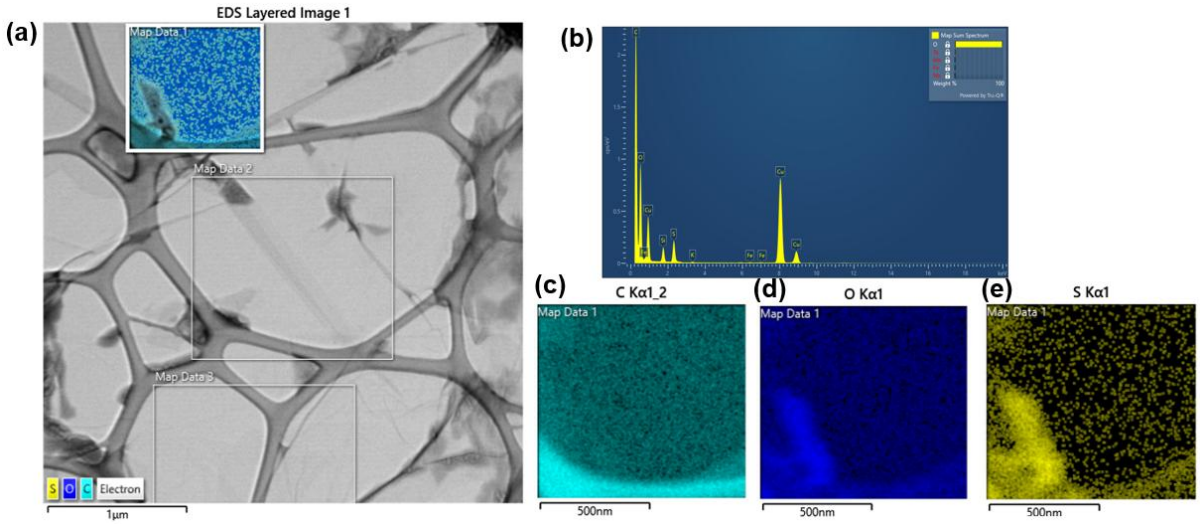

Figure 5. 10 EDS analysis of graphene oxide (GO): (a) TEM image showing the mapped regions, (b) EDS spectrum, and elemental mapping of c) Carbon (C) d) Oxygen (O) e) Sulfur (S)

Table 5. 2 Overview of graphene oxide (GO) synthesis, processing steps, and downstream applications.

Batch No.	**Method**	**Average GO Yield per Reaction (g)**	**Purpose**
GO-1 to GO-5	Modified Humer's method	~0.229	Preliminary synthesis and optimisation of GO, used for structural and chemical characterisation (XRD, FTIR, Raman, SEM, etc.) to confirm successful GO formation
GO-6 to GO-8	Modified Humer's method	~0.229	Size reduction of GO sheets via sonication for improved dispersion and suitability for textile deposition
GO-8 to GO-27	Modified Humer's method	~0.229 (used 0.4 g per reaction)	Precursor material for graphene quantum dots (GQDs) synthesis; each GQD reaction utilized ~0.4 g of GO

GO-27 to GO-31	Modified Humer's method	~0.229	GO precursor for reduced graphene oxide (rGO)/metal oxide composite synthesis

5.2 Introduction to Quantum Dots

In the past few years, nanostructured materials have attracted great interest because they can bridge the gap between the molecular level and the bulk level and lead to new applications, specifically in electronics, biology, sensing and optoelectronics. When a solid shows distinct variations of electronic and optoelectronic properties with the change of particle size, like < 100 nm, it can be known as a nanostructured material, and it is then classified into two-dimensional 2D, such as quantum wells and thin-films, one-dimensional 1D, such as quantum wires, and zero-dimensional 0D or dots. Within the last few decades, a great interest has been directed towards the applications of Quantum dots. A QD is a nanoscale particle with exceptional quantum mechanical properties. The range of the QDs is typically 1 to 10 nm in diameter show unique optical and electronic behaviour because of their size-dependent quantum confinement effects.

QDs were first discovered in early 1981 by Alexey Ekimov. He observed the quantum confinement effect in semiconductor materials, now called QDs. They used a chemical synthesis method to fabricate cadmium selenide (CdSe) nanocrystals incorporated in a glass matrix. They observed optical properties that differed from bulk CdSe and could not be explained by classical physics.

One of the main differences in bulk materials and quantum dots (QDs) is the size-dependent bandgaps, as shown in Figure 5.11. In bulk materials, the bandgap does not alter with the size because the bandgap is an intrinsic property of bulk materials, while in QDs, the bandgap varies inversely to the particle size. The size of the particle can define the strength of the quantum confinement effect. Controlling the size of the QDs during synthesis is challenging, and it is an important factor in the new development and fabrication of new devices and applications.[113] Nowadays, Graphene quantum dots have gained significant interest as compared to conventional quantum dots due to their structure, tunable optical properties and biocompatibility.

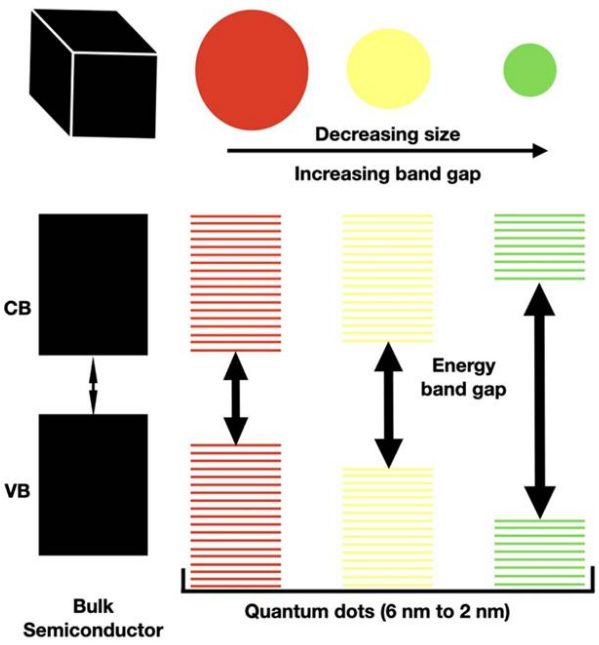

Figure 5. 11 Schematics of energy band structures in bulk materials and quantum dots (adapted from **[113]**

5.2.1 Graphene Quantum Dots

In recent years, carbon quantum dots (CQDs), particularly graphene quantum dots (GQDs), have attracted significant research interest due to their unique physicochemical properties. Unlike conventional metal-based quantum dots, GQDs exhibit excellent chemical stability, high water solubility, good biocompatibility, stable photoluminescence, and low toxicity. In addition, they possess several tunable characteristics, such as size-dependent and pH-dependent optical behavior[114].

Owing to these advantageous features, GQDs have demonstrated great potential in a wide range of applications, including solar cells[115], bioimaging, and biosensing[116] and photocatalysis[117]. Furthermore, their ultra-small particle size results in a high density of oxygen-containing functional groups, structural defects, and vacancies on the surface. These characteristics make GQDs highly suitable for gas sensing applications. When integrated with other sensing materials to form p–n or p–p heterojunctions, GQDs can significantly enhance the sensitivity and detection limits for toxic gas molecules[118]. Whereas, reduced graphene quantum dots (rGOQDs) are synthesised by partially reducing the oxygen-containing groups through a hydrothermal process. By this method, it restores the sp^2 hybridised carbon network with a greater ratio, which is good for the electron transport path for electronic and sensing applications[119].

Among the various synthesis strategies, both top-down and bottom-up approaches have been widely reported for the preparation of graphene quantum dots (GQDs). Yang et al.[120] reported a top-down method for GQD synthesis based on the thermal treatment of crude graphite sheets at 300 °C under alkaline and dry conditions. Using this approach, GQDs with particle sizes ranging from approximately 5 to 14 nm were obtained. The synthesised quantum dots contained abundant oxygen-containing functional groups, which contributed to their good water solubility. Under ultraviolet irradiation, the GQDs exhibited bright yellow-green fluorescence. Furthermore, these GQDs were employed as selective chemosensors for uranyl ions, achieving trace-level detection down to 10^{-7} M through a fluorescence quenching mechanism. Tian et al.[121] A one-step solvothermal approach was demonstrated for the synthesis of graphene quantum dots using hydrogen peroxide (H_2O_2) as an oxidising agent to cleave graphite sheets in a DMF solution. This method minimises the need for extensive purification steps such as dialysis; however, unreacted graphite remains as a separate byproduct. The resulting graphene quantum dots exhibited an average lateral size of approximately 35 nm and a quantum yield of about 15%. Based on these characteristics, the authors suggested that the synthesised quantum dots are suitable for biomedical and optical applications. Pan et al.[122] reported a hydrothermal synthesis route combined with ultrasonic treatment for the preparation of graphene quantum dots from graphene oxide sheets. In their study, the pH of the graphene oxide dispersion was adjusted to approximately 8 before being transferred into an autoclave and treated at 200 °C for 10 hours. Using this approach, graphene quantum dots with an average particle size of about 9.6 nm were obtained. The synthesized quantum dots exhibited blue photoluminescence under ultraviolet excitation.

Based on previous studies, both chemical cutting and sonication play important roles in controlling the size of graphene quantum dots during top-down synthesis. Therefore, this chapter investigates the effect of different sonication techniques on graphene quantum dot size, while also examining chemical cutting methods under varying reaction times and temperatures. Several experiments were conducted to study the influence of the sonication method, chemical environment and reaction conditions on particle size, morphology and end yield.

- **Effect of Sonication Method On Graphene Quantum Dots**

To investigate the influence of different sonication methods on graphene quantum dot size, three initial experiments were conducted using different sonication strategies and are

designated as GQDs-1, GQDs-2, and GQDs-3. The experimental setup diagram is shown in the figure.

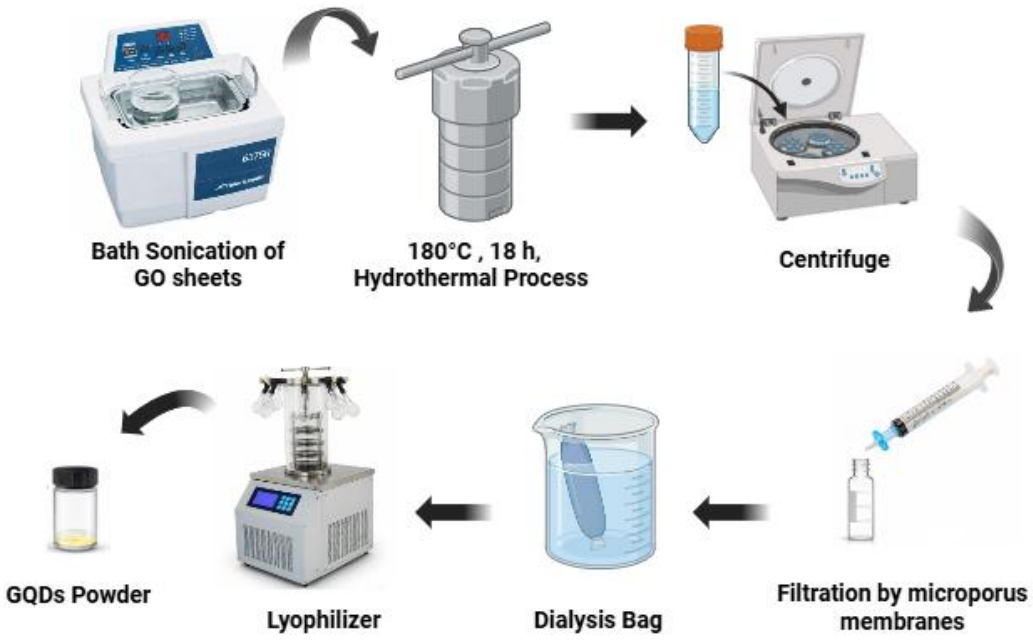

Figure 5. 12 Experimental Setup for Graphene Oxide Quantum Dots

- **Bath Sonication GQDs 1**

Graphene oxide (GO) sheets were first oxidised using a mixed acid solution of sulfuric acid (H_2SO_4) and nitric acid (HNO_3) in a 1:3 ratio, followed by bath sonication for 12 hours. The resulting sonicated mixture was then diluted, thoroughly washed with deionised water, and dried in an oven. Subsequently, 0.4 g of the dried GO was transferred into a Teflon-lined autoclave and subjected to hydrothermal treatment at 180 °C for 18 hours in an oven. After naturally cooling to room temperature, the obtained solution was filtered using 0.22 µm microporous membranes. The clear filtrate was collected and placed into dialysis bags, where it was dialysed for 48 hours under continuous stirring to remove residual impurities. Finally, the purified solution was freeze-dried in a lyophilizer for two days to obtain the final product.

- **TEM Analysis**

TEM images showed the quasi-spherical quantum dots with an average size of approximately 49.5 nm. Comparatively larger size observed in the TEM images is due to the partial aggregation of small particles of quantum dots. According to previous reports, graphene-based particles with lateral dimensions below 100 nm are often classified as graphene quantum dots [123, 124].

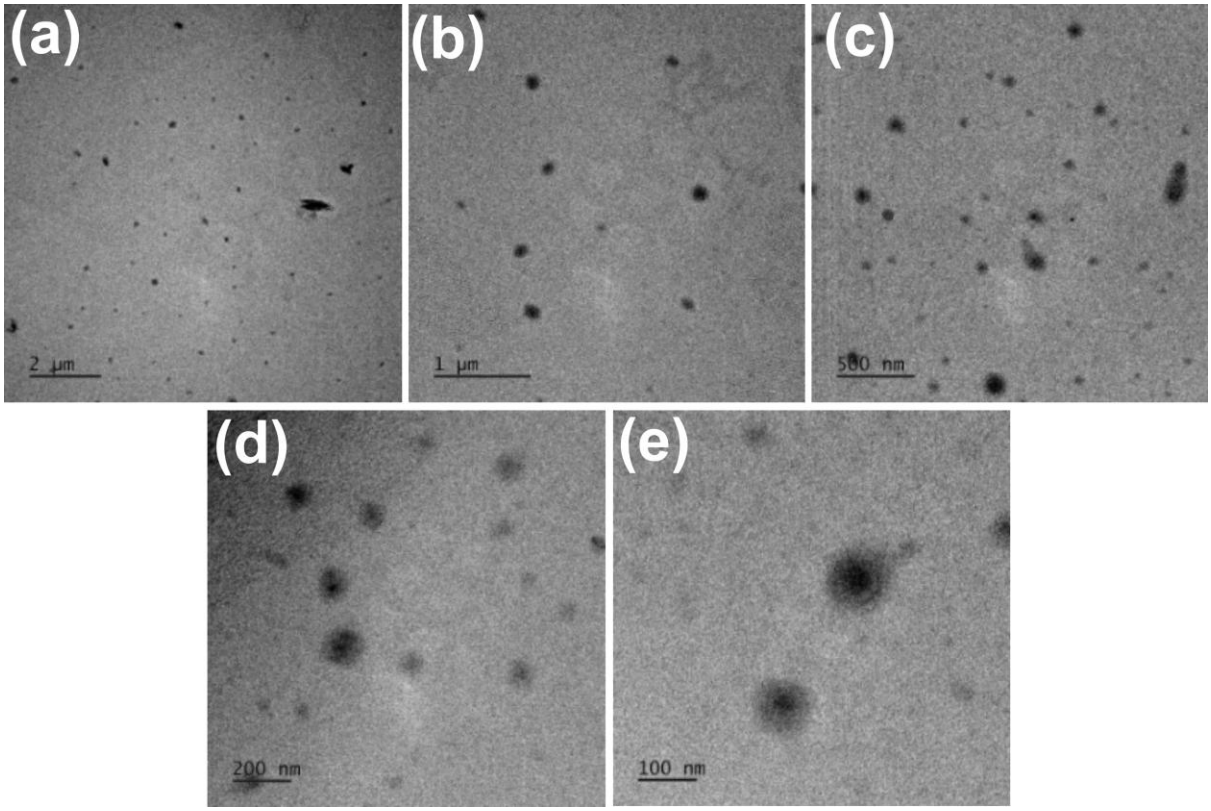

Figure 5. 13 TEM images of GQDs 1 (Synthesised by bath sonication)

- **ImageJ Analysis**

The particle size distribution of GQDs was analysed from TEM images using ImageJ software. TEM image with a scale bar of 500 nm was opened in the ImageJ software to determine the diameter of each particle. Approximately 30 particles were randomly measured, and then the measured values were exported to Origin to plot this histogram, from which an average particle size of around 49.5 nm was obtained, fabricated from the first (Bath sonication) method.

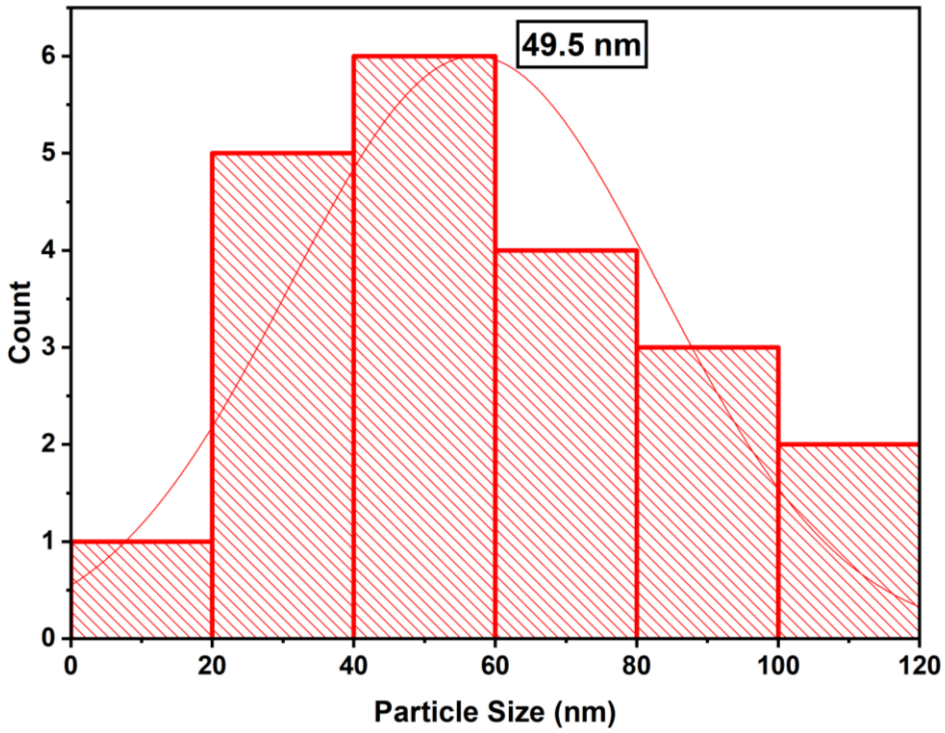

Figure 5. 14 TEM image Analysis of GQDs 1 (synthesised by bath sonication) using ImageJ software

- **Bath + Probe Sonication GQDs 2**

In the second experiment, I used the entire synthesis procedure, which I used in the first experiment and an additional sonication step before dialysis. After filtration, the obtained solution was sonicated with a probe sonicator for 20 minutes to further breakdown of graphene based structures. After the probe sonication, the solution was transferred into dialysis bags and dialysed for 48 hours under stirring. The further steps were carried out in the same way as described in the first experiment.

- **TEM Analysis**

The TEM images reveal the formation of small-sized particles with nanoscale dimensions and an irregular spherical morphology, indicating that probe sonication plays a significant role in reducing particle size. Furthermore, distinct lattice fringes observed in Figure 5.15(f) suggest the coexistence of amorphous and crystalline domains within the synthesised quantum dots.

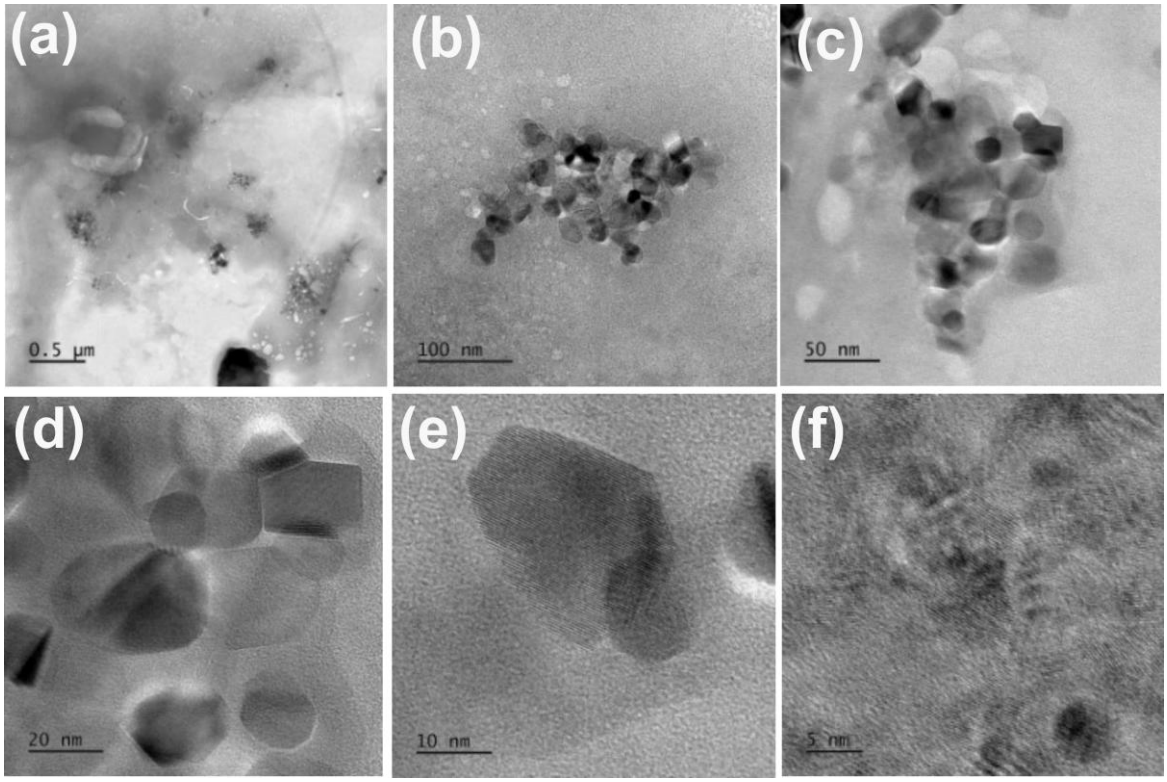

Figure 5. 15 TEM images of GQDs 2

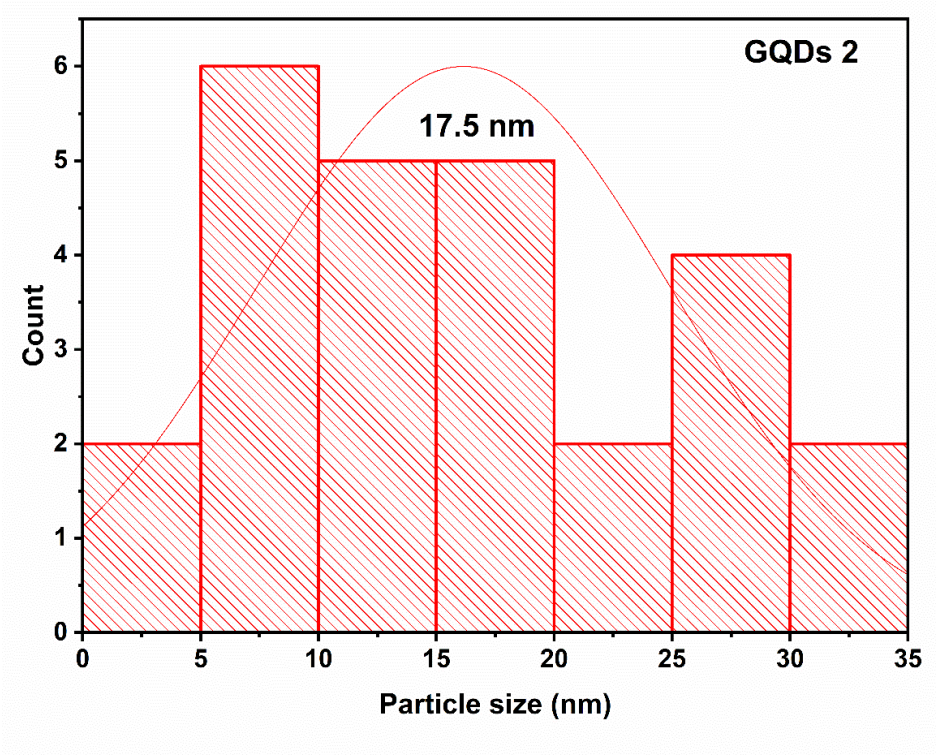

Figure 5. 16 ImageJ analysis of GQDs 2

- **Two-Step Probe Sonication GQDs 3**

After the second experiment, it became evident that probe sonication played a significant role in reducing particle size. Based on this observation, probe sonication was first applied to exfoliate the graphene oxide, followed by heat treatment, centrifugation, and filtration through a microporous membrane. Subsequently, an additional probe sonication step was introduced prior to purification using a dialysis bag. This modified sequence resulted in further size reduction of the quantum dots. As a result, the majority of the particles obtained were below 10 nm, with an average particle size of 6.4 nm.

- **TEM Analysis**

The TEM images confirm the formation of graphene quantum dots, which appear as dark contrast spots distributed across the TEM grid. The particles do not exhibit a perfectly spherical morphology; however, high-resolution TEM images reveal the presence of lattice fringes within the quantum dots. These lattice fringes indicate partial crystallinity, which is consistent with previously reported observations for graphene quantum dots.

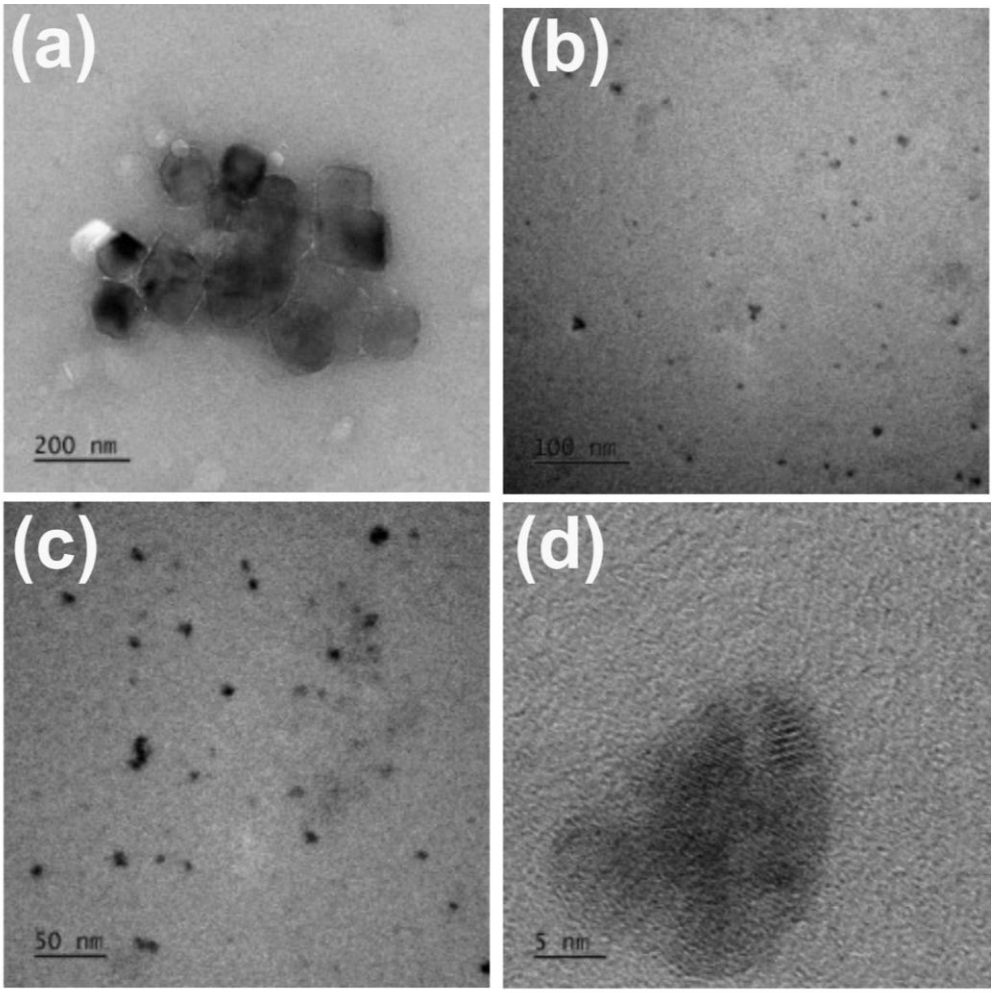

Figure 5. 17 TEM images of GQDs 3

- **ImageJ Analysis**

The two-step probe sonication method was found to be highly effective in reducing the particle size of graphene quantum dots. Quantitative size analysis was performed using ImageJ software on the TEM images of GQDs-3. Particle diameters were measured from a 50 nm scale TEM image by analyzing multiple individual quantum dots. The measured size distribution was then plotted using Origin software, yielding an average particle size of 6.4 nm.

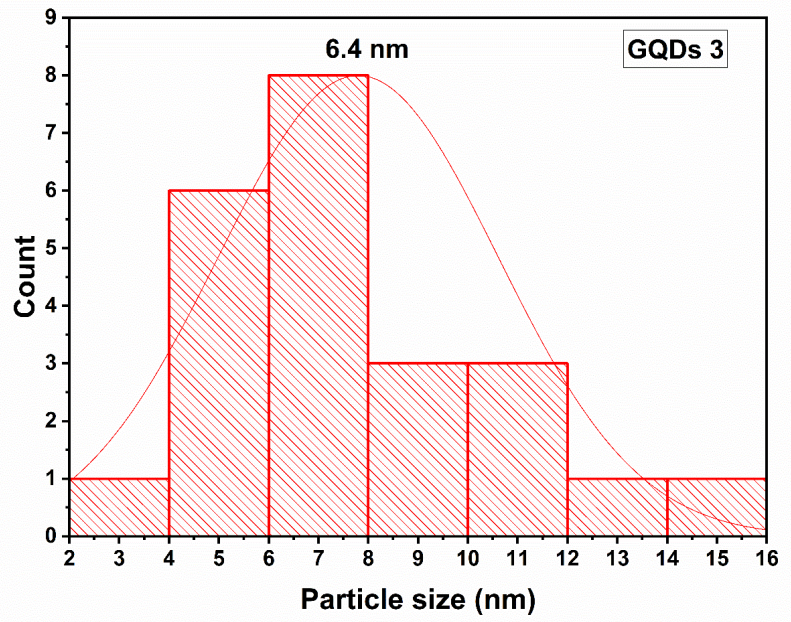

Figure 5. 18 ImageJ analysis of GQDs 3

- **Comparative Discussion of Sonication Method**

TEM analysis of the three experiments indicates a progressive reduction in the size of reduced graphene quantum dots with the introduction of probe sonication. Compared to bath sonication, probe sonication provides higher energy input, enabling more effective exfoliation of graphene oxide sheets and enhanced fragmentation into smaller quantum dots. Based on these observations, the two-step probe sonication approach was selected as the standard method for subsequent experiments to achieve improved size control and product yield.

- **Effect of Purification Method: Role of Dialysis Bag**

During the synthesis of graphene quantum dots (GQDs), the reaction mixture contains a heterogeneous distribution of carbon-based species, including graphene sheets, graphene quantum dots, unreacted fragments, and residual acids or salts. As observed in the TEM micrographs (Figure 5.19(a-b)), samples examined before dialysis show the presence of large, irregular sheet-like structures, indicating partial aggregation of graphene-derived materials. In contrast, after dialysis (Figure 5.19(c–d)), these large sheet-like features are no longer observed, and predominantly round-shaped particles with reduced dimensions are clearly visible.

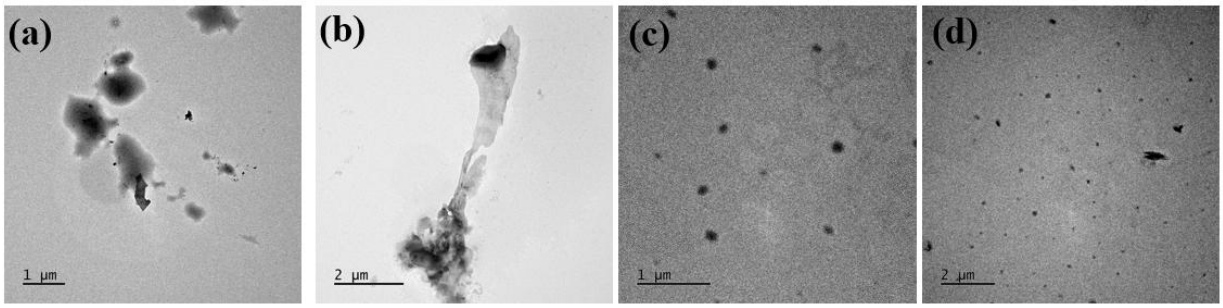

Figure 5. 19 TEM images of Graphene quantum dot (a-b) before dialysis (c-d), after dialysis to check the effect of dialysis purification on size

Dialysis bag purification exploits diffusion through a semipermeable membrane to remove the small particles from the main solution to maintain the quantum dots inside. The following figure demonstrates this process in two steps: a) at the start of the dialysis, b) at equilibrium. A dialysis bag contains a concentrated solution holding small and large fragments is inside the dialysis bag. Driven by concentration, small species diffuse through the pores of a semipermeable membrane into the outside solution, and large species remain inside the bag due to the size which exceeds the membrane cut-off limit. As this process continues and it attains equilibrium, solvent exchange repeatedly occurs and leads to the removal of low molecular weight species, which results a purified solution containing nanoscale species.

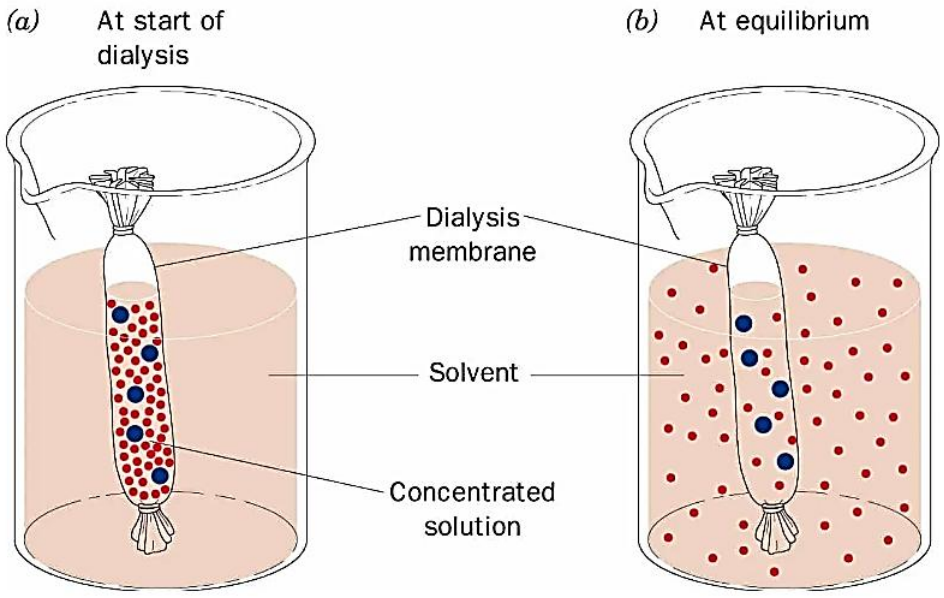

Figure 5. 20 Dialysis Purification Steps a) at the start of dialysis b) At equilibrium

- **Structural Characterisation of Graphene Quantum Dots**
- **XRD**

The structural characteristics of the synthesised GQDs 1 were examined using X-ray diffraction (XRD). As shown in Figure C, the XRD pattern of GQDs exhibits a broad diffraction peak centred at 23.8°, which corresponds to the (002) plane of graphitic carbon. A similar diffraction feature has been widely reported in the literature for graphene quantum dots**[124]**. The absence of additional diffraction peaks indicates that no crystalline impurities are present in the sample.

Since XRD provides information on the crystal structure of the material, the analysis was performed only for the first experiment (GQDs), which confirms the successful formation of graphene quantum dots. In this study, the subsequent modifications involved changes in sonication conditions, which were primarily employed to control the particle size of the quantum dots through enhanced exfoliation and fragmentation of graphene oxide, rather than to alter the crystal structure.

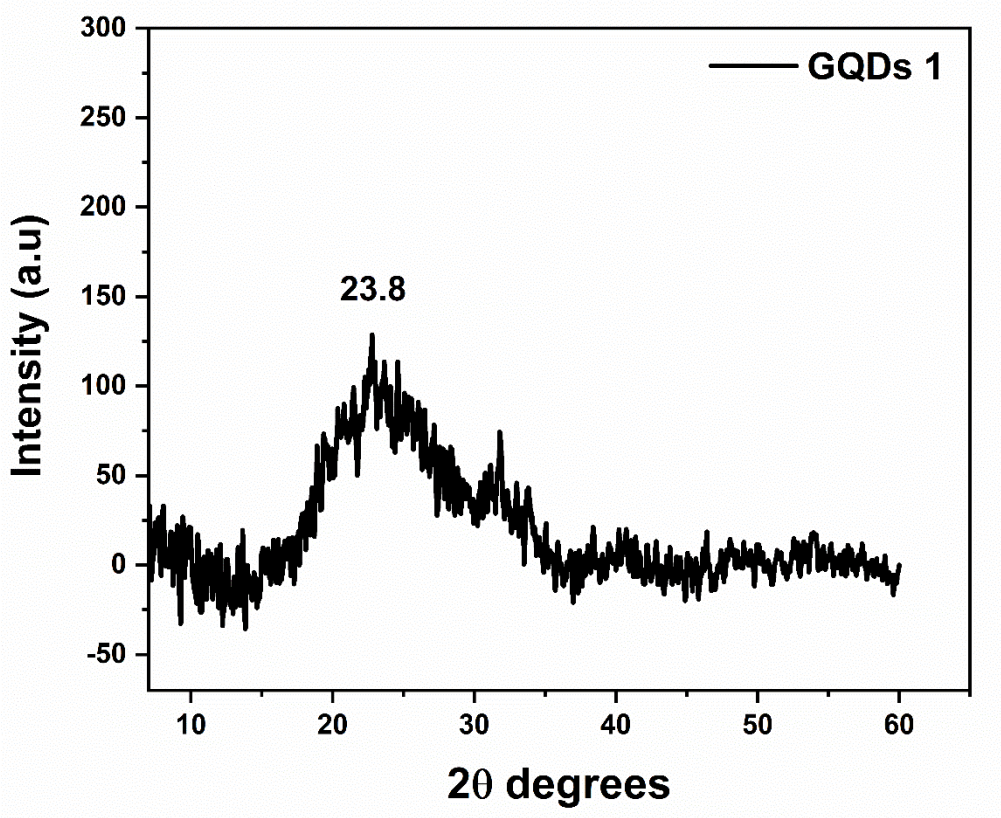

Figure 5. 21 XRD of rGOQDs

- **Optimisation of Reaction Parameters and Yield Enhancement**

Using the two-probe sonication as the standard exfoliation method, a series of hydrothermal reactions was employed to optimise the synthesis parameters and improve the end yield of quantum dots.

- **Rationale for Using Chemical-Assisted Cutting (NaOH)**

Although probe sonication effectively exfoliated the graphene quantum dots, the yield gained under sonication experiments remained low. To enhance the efficiency of cutting graphene oxide and increase the yield of the end product, the addition of NaOH was explored.

Previous studies have reported the use of sodium hydroxide (NaOH) in pH-controlled reactions to facilitate the reduction of graphene oxide sheets into graphene quantum dots [125]. NaOH has also been shown to decrease the lateral dimensions and thickness of graphene oxide under alkaline hydrothermal conditions, promoting the formation of nanoscale structures[126]. Based on these reports, NaOH was introduced in the present study to examine its effect on the yield and morphology of the synthesised graphene quantum dots.

- **Effect of reaction time and Temperature**

Using the two-step probe sonication method, two experiments were conducted with identical amounts of graphene oxide and NaOH, while all other parameters were kept constant. The effect of reaction temperature and duration was examined by carrying out the hydrothermal process at 180 °C for 18 hours (GQDs-4) and at 200 °C for 6 hours (GQDs-7). ImageJ analysis of the TEM images yielded average particle sizes of 2.97 nm and 2.88 nm for GQDs-4 and GQDs-7, respectively. These results indicate that variations in reaction temperature and time within the studied range do not significantly influence the quantum dot size, but they affect the morphology and dispersion. In contrast, the introduction of NaOH resulted in smaller particle sizes and improved morphology compared to the sonication-only experiments.

- **Morphology Comparison**

TEM images were captured from different regions of the TEM grids for GQDs 4 and GQDs 7 to analyse the morphology of the temperature and time effect on quantum dots. The TEM images of GQDs-4 show quantum dots embedded within a partially continuous, sheet-like background, indicating incomplete fragmentation and partial aggregation.

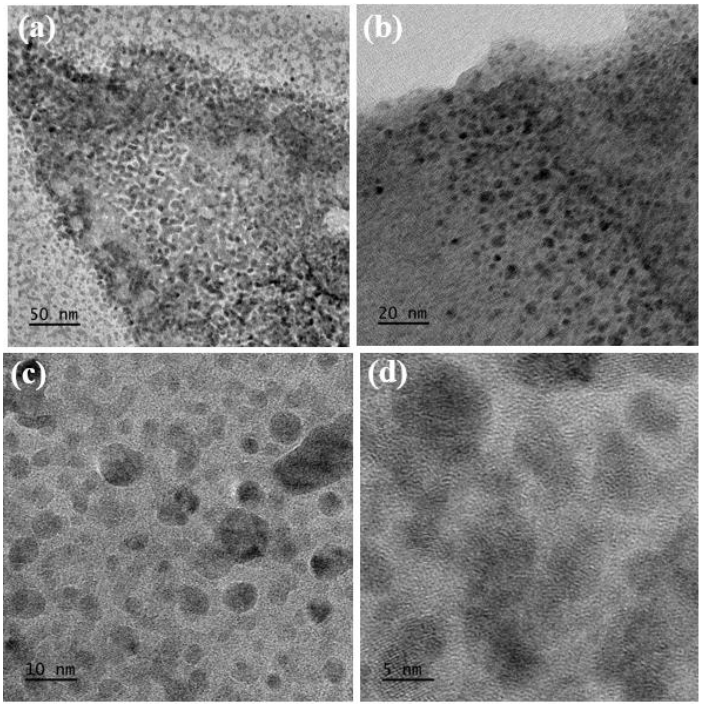

Figure 5. 22 TEM images of GQDs 4 a) at 50 nm b) at 20 nm c) at 10 nm and d) at 5 nm

In contrast, GQDs-7 exhibits more uniformly dispersed quantum dots with reduced sheet-like features, suggesting improved fragmentation and dispersion under modified thermal conditions.

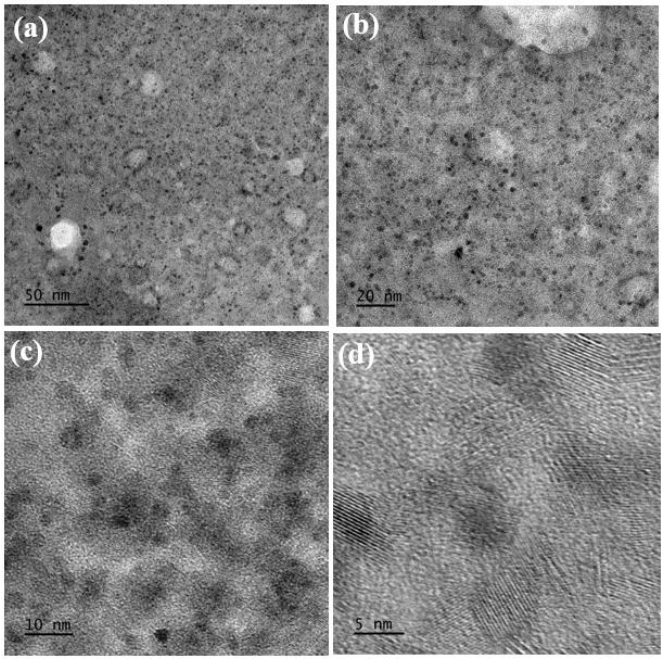

Figure 5. 23 TEM images of rGO-QDs 4 a) at 50 nm b) at 20 nm c) at 10 nm and d)at 5 nm

- **Image J analysis**

ImageJ software was used to perform particle size analysis on TEM images acquired at a 20 nm scale bar. For each sample, 50 individual quantum dots were measured to ensure an equal number of data points for reliable size comparison. The quantitative analysis revealed average particle sizes of 2.97 nm and 2.98 nm for rGOQDs-4 and rGOQDs-7, respectively. These results indicate that, under identical graphene oxide and NaOH concentrations and using a two-step probe sonication approach, variations in reaction temperature and reaction time do not significantly influence the particle size of the synthesized graphene quantum dots.

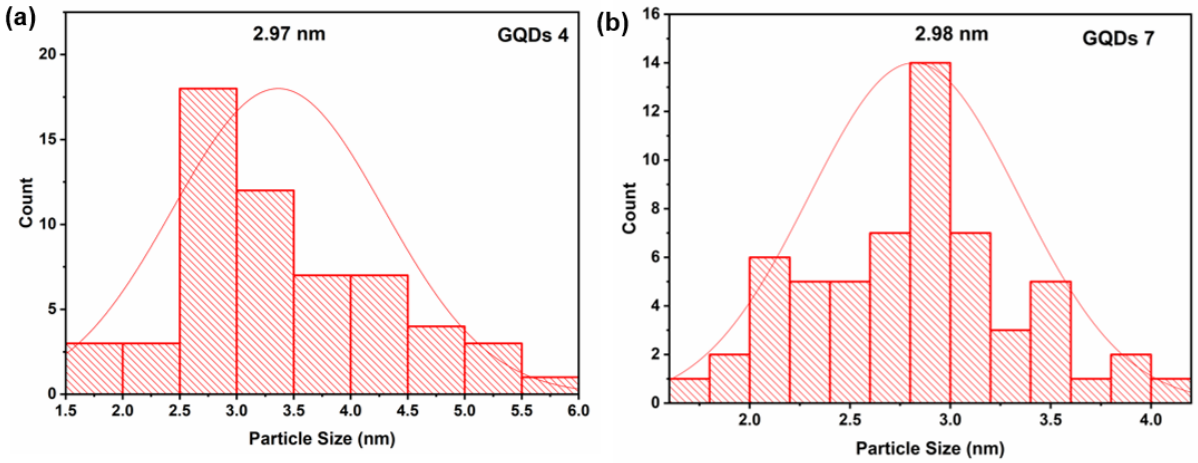

Figure 5. 24 ImageJ analysis of a) GQDs 4 b) GQDs 7

- **Effect of Reaction Temperature and Time on the Final Yield**

The final product yield was evaluated for both GQDs-4 and GQDs-7 after freeze-drying. Under reaction conditions of 180 °C for 18 hours (GQDs-4), a dry product yield of 0.00054 g was obtained. In contrast, the reaction carried out at 200 °C for 6 hours (GQDs-7) resulted in a lower dry yield of 0.00013 g after lyophilisation. These results indicate that reaction temperature and duration significantly influence the final product yield, even though they do not markedly affect the particle size. The overall yield obtained under both conditions remained very low, limiting the practical applicability of the synthesised graphene quantum dots for device fabrication and related applications.

- **Optical Characterisation of GQDs**
- **UV- VIS, and PL spectroscopy Analysis**

The UV–visible absorption spectrum of graphene quantum dots (GQDs) shows strong absorption in the deep-UV region, along with a gradual absorption tail extending into the near-UV range, which is characteristic of π–π* transitions of sp^2-hybridised carbon domains and surface-related states in graphene quantum dots in Figure BB a). The Tauc plot, obtained from UV–visible absorption spectroscopy, indicates an optical bandgap of about 3.37 eV for the GQDs produced by the hydrothermal method. This bandgap showed quantum confinement effects in nanoscale GQDs, where reducing particle size results in discrete energy levels and an increased bandgap compared to bulk graphene. The relatively broad bandgap implies that the GQDs are small (generally under 10 nm) and exhibit strong quantum confinement, which leads to spatial confinement of charge carriers and discrete electronic energy levels within the sp^2 carbon core. This value aligns with the typical GQD bandgap range reported in the literature (2.5–4.5 eV), confirming the successful synthesis of quantum-confined nanostructures with semiconducting properties[127, 128].

The PL spectrum shows three emission peaks at 349 nm, 367 nm, and 414 nm, reflecting multiple radiative recombination pathways in figure BB b). The dominant peak at 367 nm (3.38 eV) is attributed to intrinsic electronic transitions within the quantum-confined sp^2 carbon core and closely matches the optical bandgap obtained from UV-visible analysis, indicating core-state-dominated emission. The blue-shifted peak at 349 nm represents higher-energy core transitions, possibly from smaller GQD populations or higher quantum states. The red-shifted emission at 414 nm (2.99 eV) originates from surface defects and oxygen-containing functional groups that create trap states within the bandgap, enabling lower-energy radiative recombination. This multi-peak emission pattern demonstrates the dual contribution of intrinsic quantum confinement and extrinsic surface chemistry, characteristic of hydrothermally synthesized GQDs and consistent with established literature on their complex photophysical behavior.

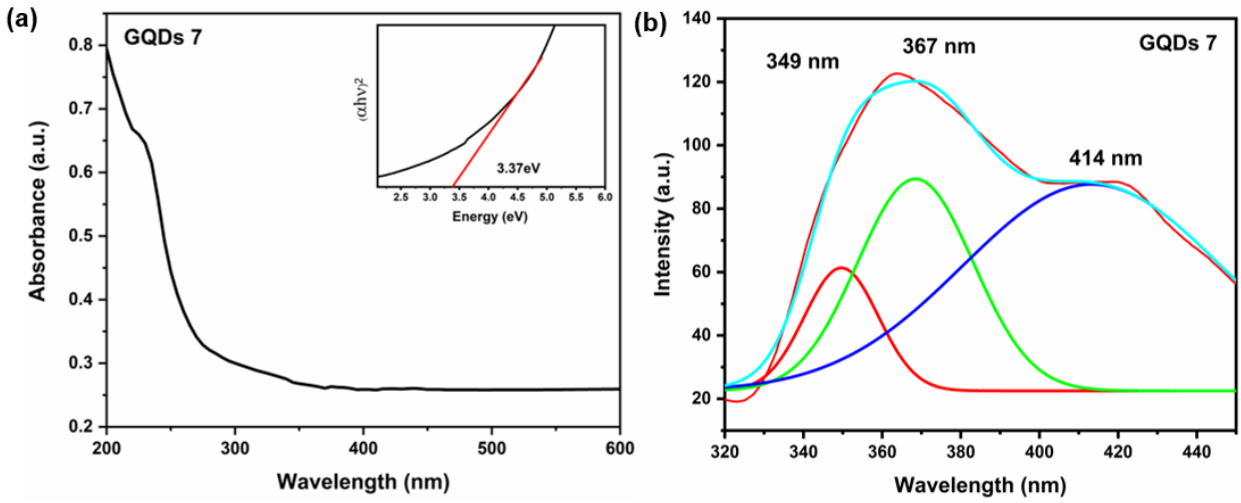

Figure 5. 25 UV–visible absorption spectrum of GQDs 7 with the corresponding Tauc plot (inset) used to estimate the optical band gap b) Photoluminescence spectrum of GQDs 7 showing Gaussian deconvolution into three emission components.

5.3 Reduced Graphene Oxide/Metal Oxides

Following the successful synthesis of graphene quantum dots, the work was extended towards the development of reduced graphene oxide/metal oxide quantum dot composites. In particular, a ternary rGO/CuO/SnO_2 nanocomposite was synthesised to explore controlled integration of metal oxide quantum dots with rGO. This study focuses on material synthesis and detailed structural and morphological characterisation, forming a foundation for future functional applications.

5.3.1 Background and Literature Review of rGO/CuO/SnO_2

Reduced graphene oxide (rGO)-metal oxide hybrid nanomaterials have been of continuous interest due to the strong conductive and high surface area characteristics of rGO that inhibit nanoparticles from clumping together and ensure the transport of charges across interstitial spaces[129]. In the article [130] rGO/SnO_2 composites have been reported for gas sensing applications where the incorporation of rGO significantly enhanced sensor response, selectivity, and reduced operating temperature due to improved charge transfer at the rGO–SnO_2 interface. Cu-doped SnO_2/rGO [131]ternary nanocomposites have been reported as highly effective low-temperature H_2S gas sensing materials, where introducing both Cu dopants and rGO significantly outperforms pristine SnO_2 CQDs and Cu–SnO_2. The study shows ultrahigh sensitivity (156.6 ppm^{-1}), a 50 ppb detection limit, fast response (~31 s at 2 ppm), and stable operation even at high humidity (90%), demonstrating strong practical

potential. A rGO/PANI/CuO/SnO_2 nanocomposite[132] has been reported as an efficient faradaic supercapacitive electrode, delivering high specific capacity and energy density comparable to vanadium redox flow batteries. The composite also demonstrated successful real-time operation in a DC–DC switched capacitor converter, confirming its practical energy storage capability. Recently rGO/CuO/SnO_2 nanocomposite [133] was synthesised via a simple sol–gel method and demonstrated high photocatalytic efficiency toward the degradation of various organic dyes, attributed to its strong oxidation–reduction capability and synergistic interfacial interactions among rGO, CuO, and SnO_2. In addition, the nanocomposite exhibited excellent antibacterial activity against both Gram-positive and Gram-negative bacteria, including *Escherichia coli*, *Staphylococcus aureus*, *Bacillus subtilis*, and *Pseudomonas aeruginosa*, highlighting its multifunctional potential for environmental and biomedical applications.

Despite the numerous studies on binary and ternary rGO and metal oxide nanocomposites, there are limited literature reports specifically on the design of rGO/CuO/SnO2 nanocomposites using SnO2 quantum dots. In particular, systematic synthesis and full structural and morphological characterization of such quantum-dot-based ternary heterostructures are not widely studied. This deficiency in the literature is the motivation for the current work, which is a controlled synthesis and detailed characterization of a novel rGO/CuO/SnO_2 quantum dot nanocomposite that offers a platform of materials for future functional studies

5.3.2 Experimental Method for rGO/CuO/SnO_2

The rGO/CuO/SnO_2 quantum-dot nanocomposite was synthesised using pre-prepared SnO_2 quantum dots, which were adopted from the PhD work of Zhou Chen (University of Cambridge) and published work related to SnO_2[134]. Before composite formation, the SnO_2 quantum dots were cleaned to remove residual impurities. Specifically, 1 mL of the SnO_2 quantum dot solution was mixed with 4 mL of isopropyl alcohol (IPA) and centrifuged at 5300 rpm for 30 minutes. After discarding the supernatant, the pellet was redispersed in deionised (DI) water, and 2 mL of the cleaned SnO_2 quantum dot dispersion was used for further synthesis. In parallel, 0.070 g of graphene oxide (GO) was dispersed in 48 mL of deionised (DI) water, followed by the addition of 2 mL of ammonium hydroxide (NH_4OH), and the mixture was bath-sonicated for 20 minutes to obtain a homogeneous GO suspension.

Separately, 0.094 g of $CuSO_4 \cdot 5H_2O$ was dissolved in 2 mL of deionised water under stirring, and the cleaned SnO_2 quantum dot solution was added to this copper precursor and stirred for 15 minutes to ensure uniform mixing. This Cu–SnO_2 solution was then added to the GO suspension and stirred for an additional 30 minutes. The resulting mixture was transferred into a Teflon-lined stainless-steel autoclave and subjected to hydrothermal treatment at 140 °C for 20 hours. After natural cooling to room temperature, the product was centrifuged, washed several times with deionised water, and finally dried at 80 °C overnight to obtain the rGO/CuO/SnO_2 quantum-dot nanocomposite.

- **Characterisation of rGO/CuO/SnO_2 Quantum dots**
- **XRD of rGO/CuO/SnO_2 Quantum Dots**

X-ray diffraction (XRD) analysis was used to investigate the crystalline structure of the rGO/CuO/SnO_2 quantum-dot nanocomposite. The diffraction peaks observed at ~26.3°, 33.9°, 51.8°, 77.5° and 83.3° correspond to the (110), (101), (211), (321) and (222) planes of tetragonal rutile SnO_2, confirming the formation of crystalline SnO_2 quantum dots which are in good agreement with the standard JCPDS card No. 77-0452. In addition, the peaks appearing at 32.5°, 35.6°, 38.7°, 48.7°, 53.5°, 58.2°, 61.6°, 65.8°, 67.8°, 72.1°, and 75.1°can be indexed to the (110), ($\bar{1}$**10**), (111), ($\bar{2}$02), (020), (202), ($\bar{1}$**13**), ($\bar{3}$**11**), (220), (311), and ($\bar{2}$22) planes of monoclinic CuO, indicating the successful incorporation of CuO into the composite, matching well with JCPDS card No. 01-080-1916. Some diffraction peaks partially overlap due to the coexistence of CuO and SnO_2 phases, particularly in the 37–39° and 61–62° regions. A peak around ~24–26° may be attributed to the (002) reflection of reduced graphene oxide (rGO), which is masked by the intense SnO_2 (110) peak. A similar behaviour has been reported in the literature for rGO/SnO_2 nanocomposites, where the SnO_2 diffraction peak dominates the XRD pattern and leads to the suppression or masking of the characteristic rGO (002) reflection[135].

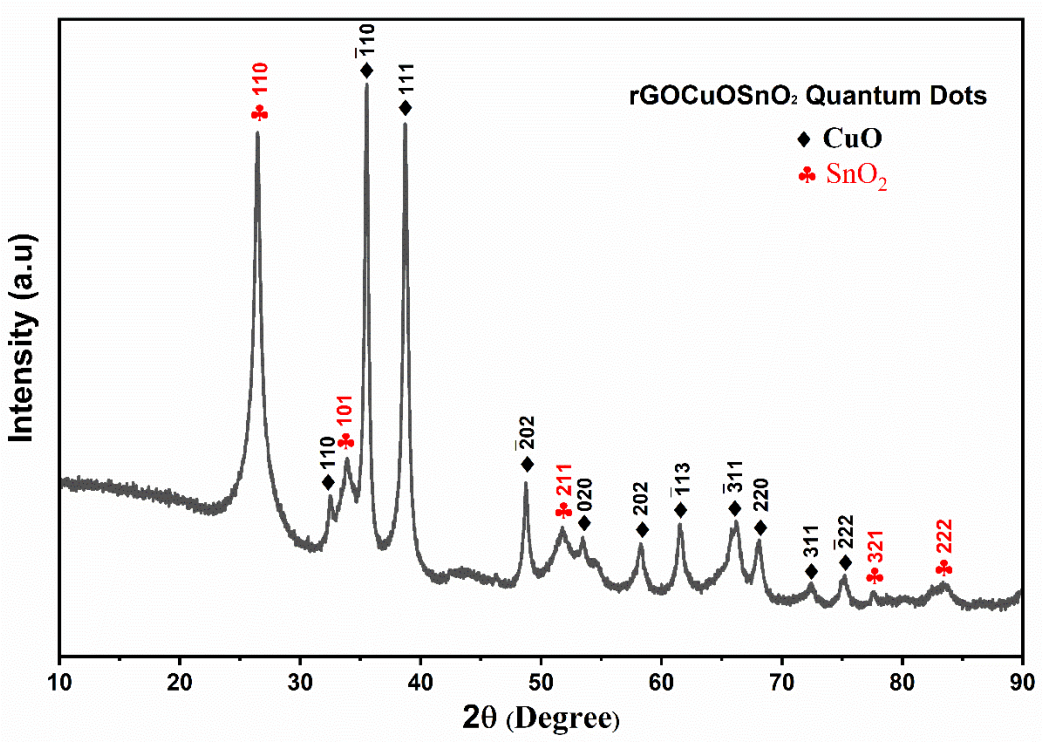

Figure 5. 26 XRD pattern of the rGO/CuO/SnO_2 quantum-dot nanocomposite

- **FTIR Analsysis of rGO/CuO/SnO_2**

The FTIR spectrum of the rGO/CuO/SnO_2 Quantum dot nanocomposite exhibits a broad band at 3200–3400 cm^{-1} corresponding to O–H stretching vibrations from surface hydroxyl groups and adsorbed water[130]. The band around 2920 cm^{-1} is attributed to C–H stretching vibrations. The absorption bands at ~1720 cm^{-1} and ~1598 cm^{-1} correspond to C=O stretching and C=C stretching of sp^2-hybridized carbon in rGO, respectively. Bands observed in the region 1400–1450 cm^{-1} and around 1050–1100 cm^{-1} are assigned to C–OH and C–O–C stretching vibrations of residual oxygen-containing functional groups on rGO[136, 137]. The absorption below 700 cm^{-1} is attributed to Cu–O and Sn–O–Sn lattice vibrations, confirming the successful formation of the rGO/CuO/SnO_2 nanocomposite.

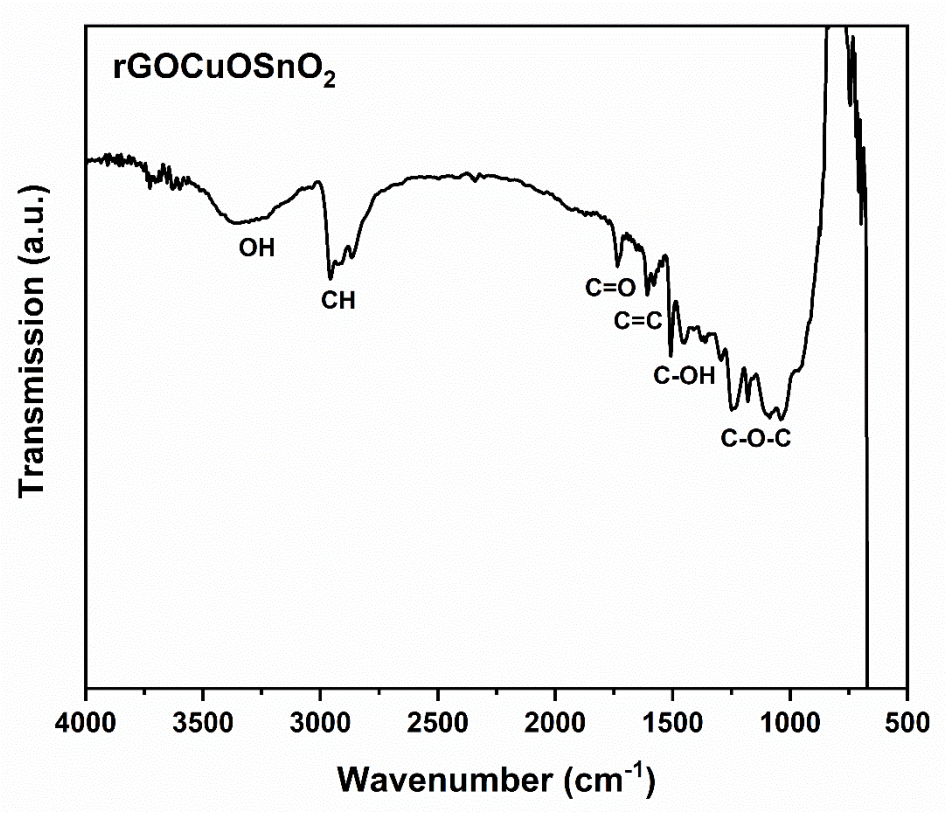

Figure 5. 27 FTIR spectrum of the rGO/CuO/SnO_2 nanocomposite showing characteristic functional groups of rGO and metal oxygen

- **TEM Analysis of SnO_2**

The TEM images of the synthesised SnO_2 quantum dots show the formation of uniformly distributed in Figure 5.28 ultrasmall nanoparticles with sizes in the quantum-dot regime. The low-magnification image shows closely packed SnO_2 quantum dots without significant agglomeration, indicating controlled nucleation and growth. The HRTEM image exhibits well-defined lattice fringes with an interplanar spacing of ~0.31 nm, which corresponds to the characteristic lattice planes of rutile SnO_2, confirming the crystalline nature of the quantum dots. These results demonstrate the successful synthesis of crystalline SnO_2 quantum dots, which were further used in the fabrication of the rGO/CuO/SnO_2 nanocomposite.

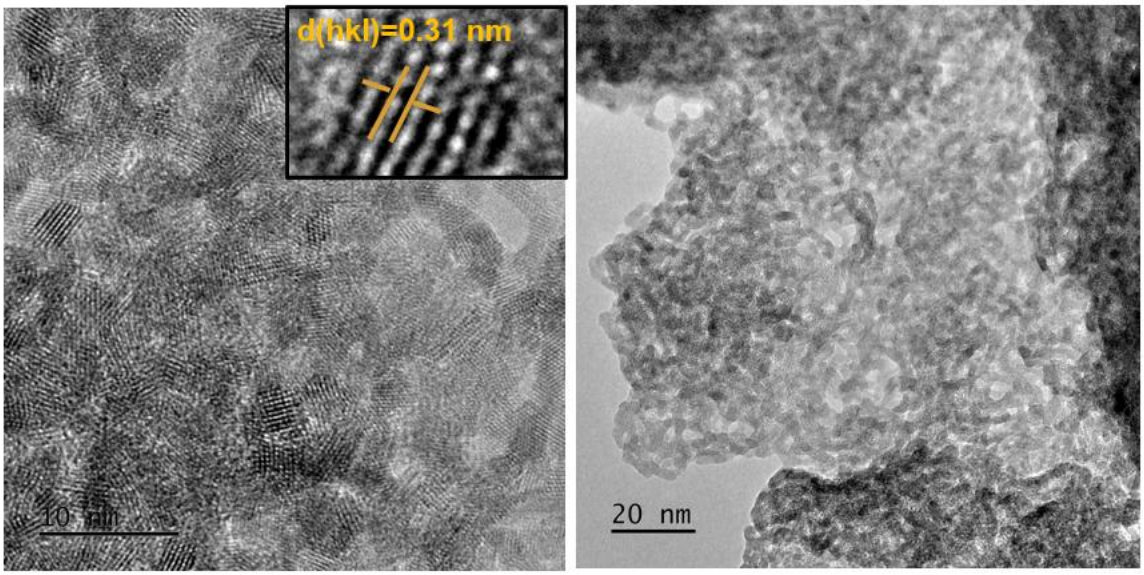

Figure 5. 28 TEM images of SnO_2 quantum dots, a) at 10 nm, b) 20 nm

- **TEM of rGO/CuO/SnO_2**

The TEM images of the rGO/CuO/SnO_2 nanocomposite reveal a hierarchical heterostructure consisting of wrinkled rGO sheets, CuO nanoparticles, and ultrasmall SnO_2 quantum dots. The low-magnification images show wrinkled rGO sheets acting as a supporting matrix, while the darker and relatively larger aggregated regions correspond to CuO particles on the rGO surface. In contrast, the high-magnification TEM images clearly show uniformly distributed SnO_2 quantum dots with an average particle size of ~2.55 nm, which is confirmed by the particle size distribution histogram. The TEM image at 20 nm exhibits distinct lattice fringes, demonstrating the crystalline nature of the SnO_2 quantum dots and their intimate contact with both CuO and rGO. This multicomponent architecture, consisting of CuO clusters and SnO_2 quantum dots well dispersed on conductive rGO sheets, provides a large interfacial area and is favorable for efficient charge transfer and enhanced functional performance.

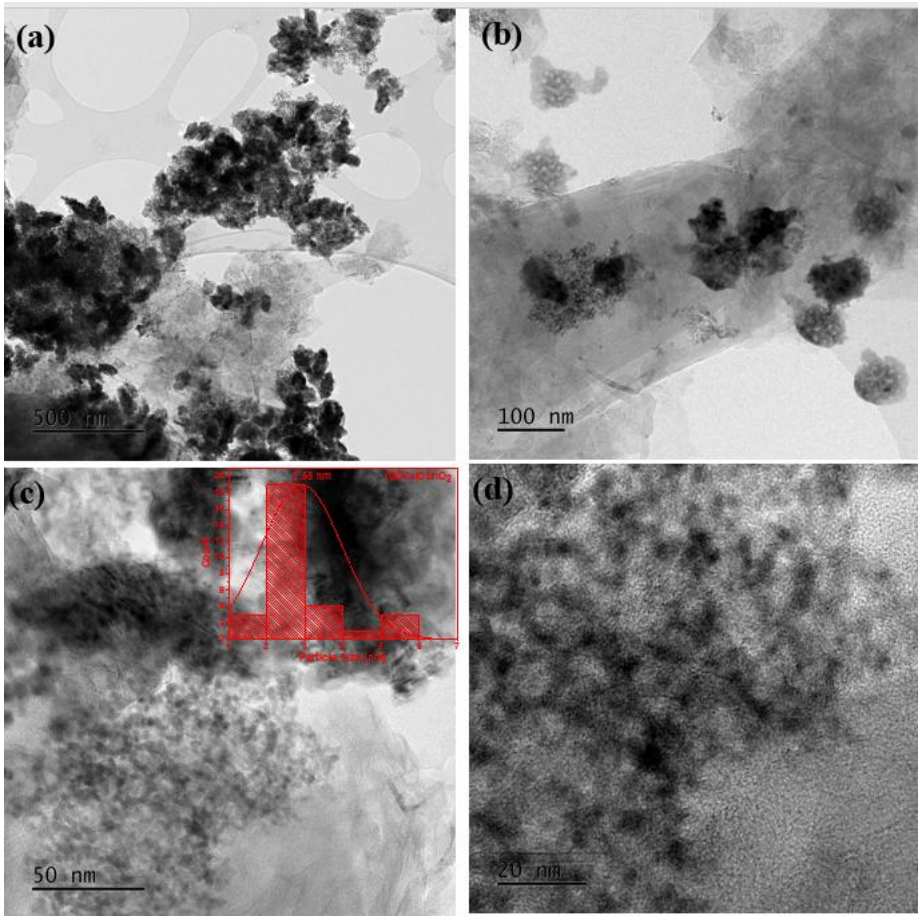

Figure 5. 29 TEM images of rGO/CuO/SnO_2, a) at 500 nm, b) 100 nm, c) 50 nm, with an inset graph imageJ analysis showing 2.55 nm size and d) at 20 nm

- **EDX Mapping Of rGO/CuO/SnO_2**

The TEM–EDX analysis was used to investigate the elemental composition of the rGO/CuO/SnO_2 nanocomposite. The TEM image confirms the presence of metal oxide particles on the rGO matrix. The corresponding EDX spectrum reveals the characteristic peaks of C, O, Cu, and Sn, confirming the successful incorporation of rGO, CuO, and SnO_2 in the composite. Elemental mapping further demonstrates a uniform distribution of carbon throughout the analysed region, indicating a continuous rGO framework, while copper appears in localised areas corresponding to larger CuO particles, and Sn is homogeneously dispersed, confirming the presence of SnO_2 quantum dots. Minor peaks observed in the EDX spectrum, such as Au, Si, Fe, and trace elements, are attributed to the TEM grid and instrumental background, and do not indicate impurity phases in the nanocomposite. Overall, the TEM–EDX results confirm the synthesis of rGO/CuO/SnO_2 nanocomposite.

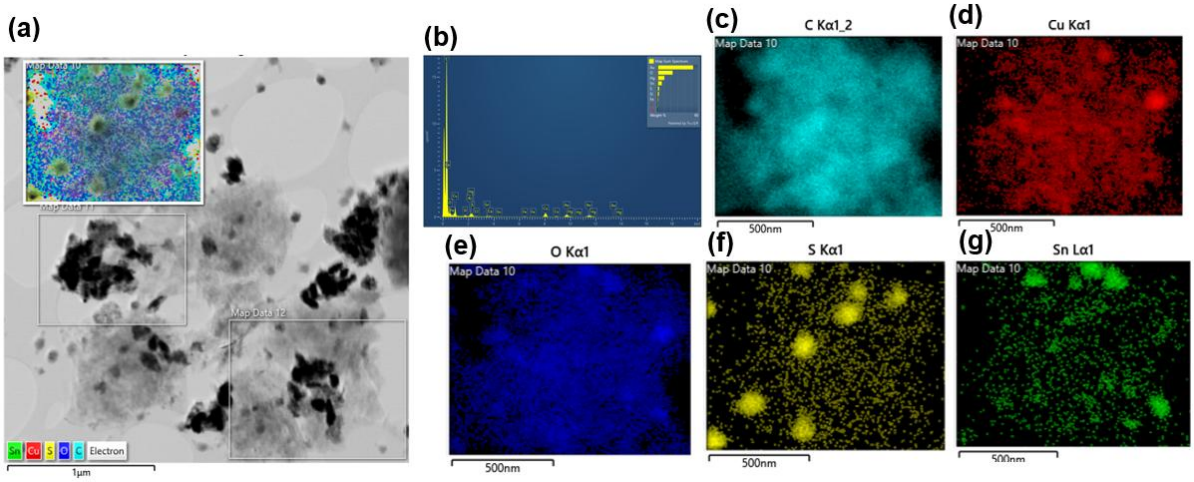

Figure 5. 30 TEM–EDX analysis of the rGO/CuO/SnO_2 nanocomposite: (a) TEM image of the analysed region, (b) EDX spectrum, and (c–g) elemental maps of C, Cu, O, and Sn showing uniform distribution of the constituent elements

- **SEM analysis of rGO/CuO/SnO_2 Quantum dots**

Figure 5.31 shows the SEM images of the rGO/CuO/SnO_2 nanocomposite deposited on a nylon substrate at different magnifications. Figure X(a) shows the low-magnification SEM image, where the nylon fabric is clearly visible and uniformly coated with the rGO/CuO/SnO_2 nanocomposite. The presence of the coating over the entire fiber network indicates successful and homogeneous deposition of the nanocomposite on the nylon. Figure X(b) shows the higher-magnification SEM image, showing that the nylon fibres are covered with rGO/CuO/SnO2 quantum dots.

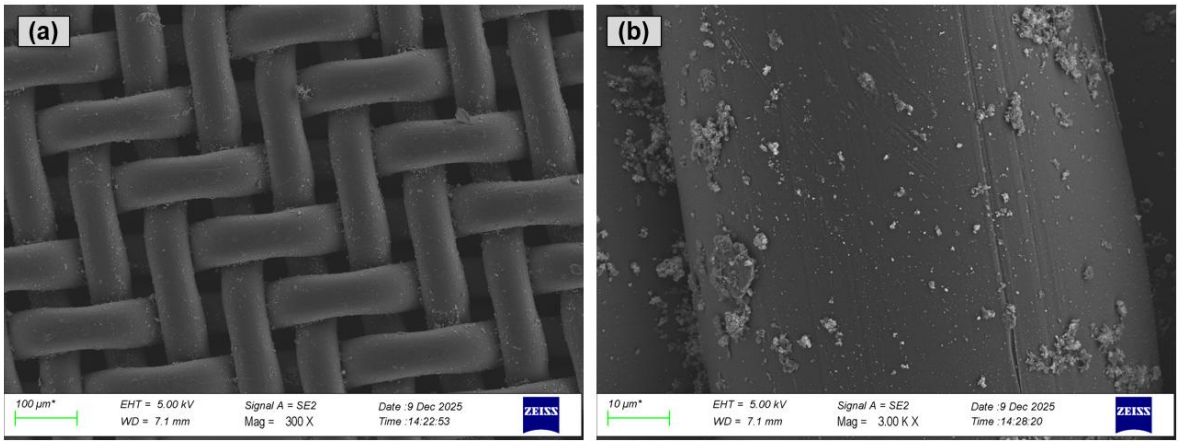

Figure 5. 31 SEM image of rGO/CuO/SnO_2 dropcasted on nylon

5.4 Summary

In this chapter, Graphene oxide (GO) was successfully synthesised via modified Hummers' method, with comprehensive characterisation (XRD, FTIR, RAMAN, SEM, TEM and EDX mapping) confirming its layered structure and functional groups. Graphene quantum dots (GQDs) were successfully fabricated by using the hydrothermal method with probe sonication. Different investigations of sonication methods employed have shown that probe sonication plays a critical role in controlling particle size. Morphological, structural and optical analysis confirmed the synthesis of nanoscale reduced graphene quantum dots with partially crystalline and characteristic quantum dot behaviour.

Additional optimisation through NaOH-assisted chemical cutting and adjustments to thermal conditions showed that reaction temperature and duration primarily affect the morphology and final product composition, rather than quantum dot size. NaOH addition promoted greater fragmentation while also altering morphology. Although synthesis yielded nanoscale quantum dots successfully, the overall yield after purification and lyophilisation stayed very low, hindering practical deposition on textiles for wearable gas sensing devices. Thus, this thesis focuses on rGO/CuO nanocomposites to develop flexible gas sensors.

Additionally, rGO/CuO/SnO_2 nanocomposites were synthesised, with XRD peaks clearly confirming the successful formation of CuO and SnO_2 phases on rGO sheets, corroborated by TEM, EDX mapping, and FTIR analyses demonstrating uniform hybrid morphology and chemical interactions. These materials show promise for gas sensing applications, though device integration remains unexplored in this work. Future studies will focus on depositing rGO/CuO/SnO_2 onto embroidered textile electrodes to evaluate chemiresistive NO_2 and NH_3 sensing performance, selectivity, and stability.

CHAPTER 6 Fabrication of Smart Textile Gas Sensors Using Hand-Embroidered and Inkjet Printing Electrodes with rGO–Metal Oxide Inks

This chapter focuses on the development of a textile-based gas sensing device. The research presented was carried out at the Cambridge Graphene Centre (CGC), University of Cambridge, United Kingdom, during an overseas research period under the supervision of Professor Tawfique Hasan, with co-supervision from Dr Osarenkhoe Ogbeide (Ozzy). The chapter presents a significant step towards the realisation of a low-cost and flexible gas sensor incorporating hand-embroidered electrodes and reduced graphene oxide (rGO)/metal oxide–based sensing inks. The device was evaluated towards multiple target gases, including nitrogen dioxide (NO_2), ammonia (NH_3), carbon dioxide (CO_2), and formaldehyde, with measurable sensing responses observed for NO_2 and NH_3. A comparative study examining the effect of single and double metal oxide compositions on device performance is presented for NO_2 sensing. In addition, preliminary work on an inkjet-printed electrode-based gas sensing device is introduced, and the fabricated prototype is presented as part of ongoing research.

6.1 State of the Art in Gas Sensing

Textile substrates have attracted increasing attention for gas sensing applications owing to their flexibility, lightweight nature, and potential for seamless integration into functional systems. However, the inherent porosity and mechanical deformability of textiles introduce significant challenges for device fabrication, material deposition, and long-term electrical stability.

6.1.1 Materials for Gas Sensing

A wide range of materials has been extensively investigated for gas-sensing applications, ranging from conducting polymers to two-dimensional (2D) materials. This section focuses on the key material classes employed in this research, highlighting their fundamental properties, inherent limitations, and synthesis routes.

- **Metal Oxides for Gas Sensing**

Metal oxide (MOx) materials are widely used in gas sensors because they effectively detect combustible, reducing, and oxidising gases[138]. These MOx materials fall into two categories based on their electronic properties: (1) transition metal oxides (such as Fe_2O_3 and NiO); and (2) non-transition metal oxides (like SnO_2). For gas sensing, MOx can take various nanostructure forms, including one-dimensional (1D) nanotubes, two-dimensional (2D) nanosheets, and three-dimensional (3D) shapes like nanorods, nanocubes, microspheres, and microporous crystals. In 3D MOx nanostructures, synthesis techniques such as vapour

deposition, oxidation, and hydrothermal methods can create structures with specific active crystal faces that influence sensing performance[139]. MOx nanostructures can also be modified with additional materials to enhance their gas detection capabilities. Each nanostructure type offers unique advantages and limitations, but studies generally show that porous nanostructures match the sensitivity of functionalized thin films, and both outperform plain thin films[140].

The basic mechanism of gas sensing in metal oxide sensors is attributed to the trapping of electrons at the adsorbed molecules and the subsequent band bending that takes place at the surface of the material. When oxygen molecules in the surrounding atmosphere are adsorbed onto the metal oxide surface, as shown in Figure 6.1, oxygen molecules remove electrons from the conduction band and immobilise them as surface ions. This process causes an electron-depleted region, commonly called the space-charge layer, causing band bending and a large decrease in the conductivity relative to the flat band case. This is a reversible interaction between the gas and the semiconductor surface, a fundamental feature of conductometric sensors, especially of n-type oxides such as ZnO and SnO_2[138].

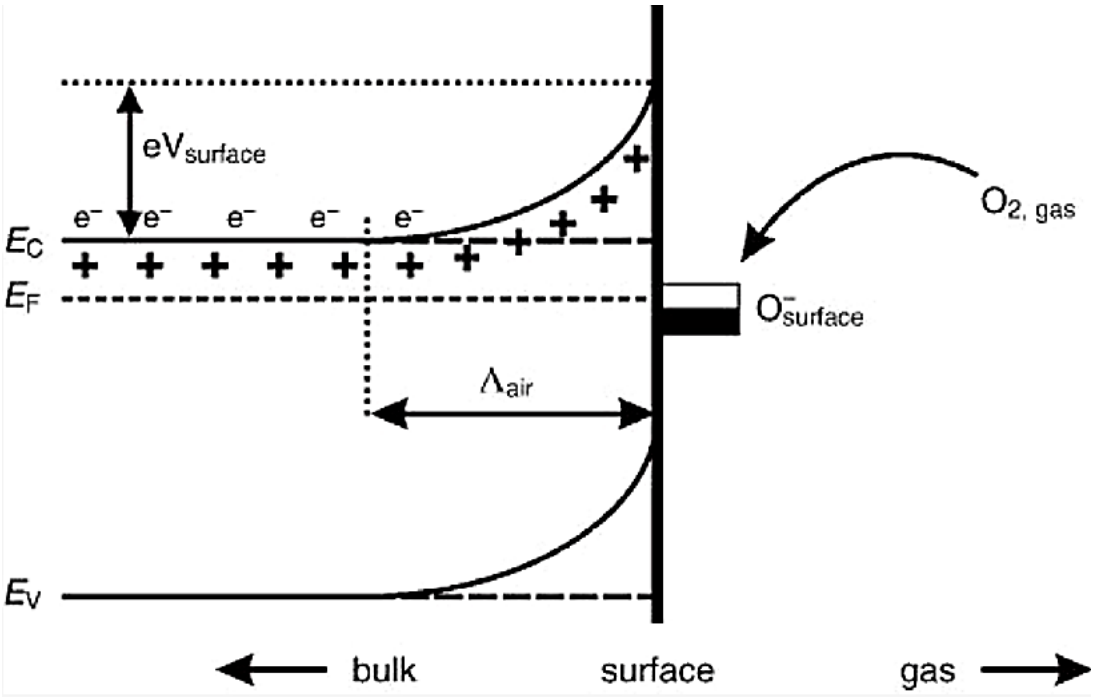

Figure 6. 1 Schematic diagram of band bending after chemisorption of charged species (specifically oxygen ionosorption) Adapted from **[138]**

Figure 6.2 illustrates the structural model and band model, which further clarifies why this conductivity is modulated when a target gas is present. When the reducing gas (e.g. carbon monoxide, CO) comes into contact with the sensor, the gas interacts and is oxidised by the pre-adsorbed oxygen ions, which subsequently release the trapped electrons to the bulk material. This reaction reduces the surface oxygen species and reduces the space-charge layer thickness. As a result, the Schottky barrier between adjacent grains is reduced, and electrons have an easy time passing through the sensing layers. The resultant rise in conductivity (or fall in resistance) gives a visible signal that is then utilised in measuring the concentration of the targeted gas.

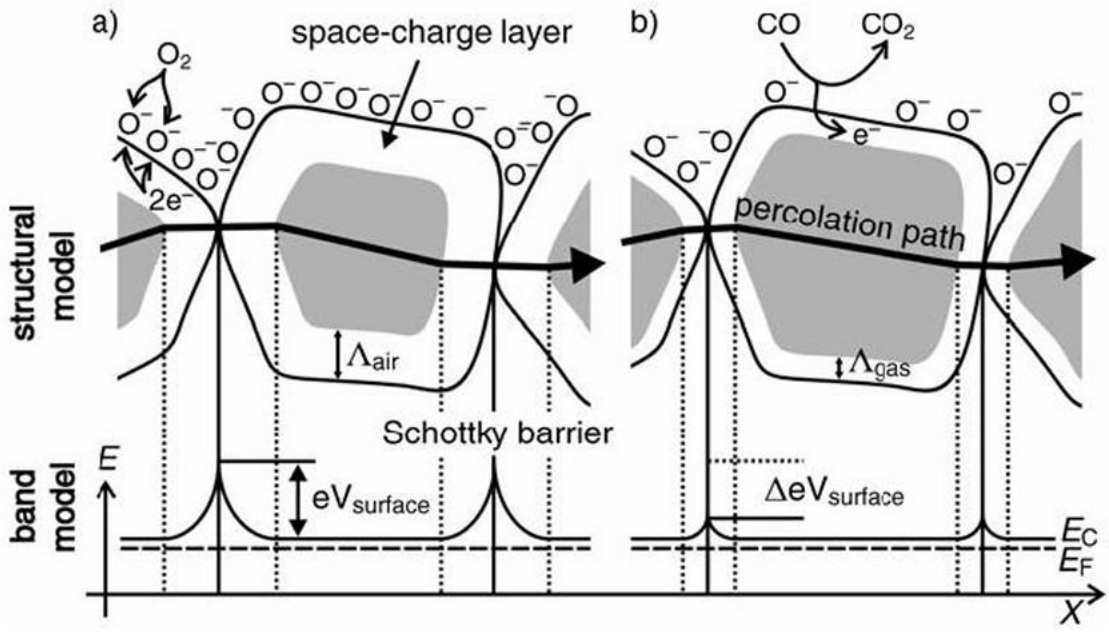

Figure 6. 2 Structural and band models of conductive mechanism upon exposure to reference gas. (a) with or (b) without CO Adapted from **[138]**

High catalytic activity of metal nanoparticle dopants, including gold nanoparticles (Au NPs), to gas reactions on the surface and their ability to enhance sensor sensitivity via the spillover effect to multiply the amount of adsorbed oxygen species on the surface of sensing material are well studied [140]. Moreover, adding other metal oxide semiconductors can also enhance the performance of doped metal oxides in gas sensing by creating heterojunctions that add more active sites and enhance charge transfer mechanisms[141]. Table 6.1 summarises the semiconducting behaviour of the commonly used metal oxide materials.

Table 6. 1 Semiconducting behaviour of Metal Oxides

Materials	**Type of Conductivity**		
	n	**p**	**n,p**
Metal Oxides	SnO_2, ZnO, TiO_2 In_2O_3, MoO_3, MgO, WO_3 CaO, Ga_2O_3 MgO, V_2O_5 Al_2O_3,	NiO, CeO2 Mn_2O_3, CuO Cr_2O_3, PdO Ag_2O, Bi_2O_3 TeO_2, La_2O_3 Y_2O_3	Fe_2O_3, HgO_2

- **Graphene-related Materials for Gas Sensing**

Of the 2D materials, graphene has received the most attention in gas sensing, due to its sp^2 hybridised carbon atoms in a hexagonal honeycomb structure, which create delocalized 5 orbitals. This zero-bandgap semimetal architecture provides a conductive and adsorbent-sensitive structure based on charge transfer, van der Waals, and zero interactions[142]. Solution processing of graphite is cost-effective, though, creating graphene containing defects such as oxidation and functional groups (e.g. epoxy, hydroxyl) to produce graphene oxide (GO). They can suppress certain applications but increase gas sensing by increasing the strength of interaction of analytes with graphene than with pristine graphene, as indicated by higher binding energies of NO_2 (0.078 eV with pristine vs. stronger chemisorption with hydroxyl groups; shorter distances mean physisorption-chemisorption shift)[143]. Epoxy functional groups in GO repel NO_2, and the single-molecule sensitivity of graphene is known to highlight its potential. The GO can be reduced to create reduced graphene oxide (rGO) by removing such groups through the high-temperature/pressure process. Although graphene displays outstanding characteristics, pure substances are too selectivity-poor and any gas changes conductivity; functional groups are therefore specific to advantage.

- **Graphene Hybrid Materials**

As it has been mentioned above, the surfaces of 2D materials complement metal oxide (MOx) materials, which can be used as scaffolds containing functional units. It is shown in the literature that the solvothermal/hydrothermal synthesis, thermal hydrolysis, sol-gel, electrodeposition etc methods to hybridize MOx with non-graphene 2D materials significantly

leads to improvement in gas sensing performance compared to the individual precursors[100, 144]. These syntheses are dominated by the hydrothermal method, which is simple and economical: precursors and solvents are placed in a Teflon-lined autoclave, and high temperatures and pressures are produced by the solvent vapour. This method is also applicable in separate MOx production. In the case of GO in aqueous solutions, the oxygen-based groups will be reduced by the supercritical water to recover the aromatic structure of the graphene lattice. At the same time, GO sheets promote the nucleation of MOx nanoparticles (NP) to promote the growth of uniform nanocrystals and prevent aggregation of NPs[145]. The hydroxyl (-OH) and carboxyl (-COOH) groups of GO present anchoring sites, which facilitate covalent metal-O-C bonding[146].

The nucleation and growth of MOx nanoparticle (NP) on GO during hydrothermal synthesis depends on several factors. As an example, precursors in the Teflon-lined vessel may not be uniformly distributed, resulting in non-uniform NP coverage; improper mixing will result in agglomeration and the GO sheets stacking up and losing their isolated structure, both of which reduce their functionality as sensing platforms. Moreover, these aggregated composites are of greater masses, making it difficult to use them in a precise deposition technique to make devices[147]. Precursor concentration (e.g. the concentration of metal salt) has a very strong influence on the morphology of MOx nanocrystals: high concentrations result in large nanocrystals, whereas low concentrations result in small nanocrystals[148]. One of the biggest industrial benefits of these hybrids is the reduction of operating temperatures of MOx sensing, which are made possible by the introduction of conductive 2D material such as graphene. In addition to personal material advantages, hybrids have high sensitivity and selectivity due to the presence of metal-semiconductors heterojunction created between graphene and MOx.

These heterojunctions produce additional active sites of gas adsorption and transduction. This article[149] will analyse MOx/graphene interactions through a machine-intelligent inkjet-printed α-Fe_2O_3/rGO sensor to detect NO_2 in ambient humidity. The sensor ink is synthesised by a one-pot hydrothermal process, and the sensor mechanism (Figure 6.3) is the following: p-type rGO donating electrons to NO_2, which becomes NO_2^-; n-type α-Fe_2O_3 donating electrons to ambient O_2, becoming O^{2-}. NO_2 is then oxidised by the surface O_2^- on the α-Fe_2O_3 to generate NO_3^- intermediate. Since the work function rGO (~5.2 eV) is lower than that of α-Fe_2O_3 (~5.9 eV), electrons move on rGO to the α-Fe_2O_3, equilibrating the Fermi levels, increasing hole density in rGO and decreasing resistance when NO_2 is present.

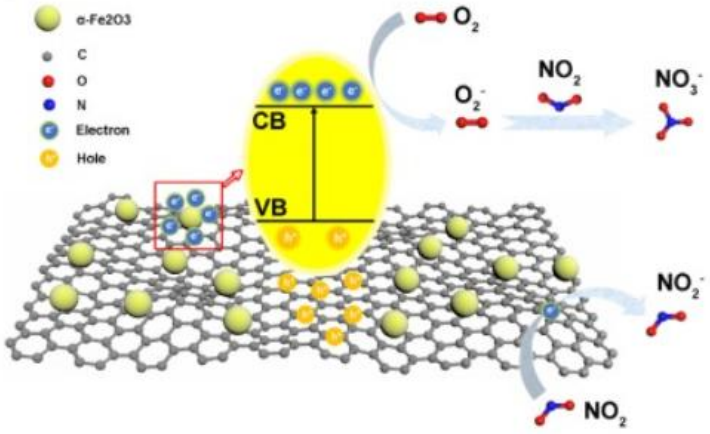

Figure 6. 3 Sensing mechanism for NO_2 detection in air using α-Fe_2O_3/rGO heterostructure. (Inset) Band diagram at the α-Fe_2O_3/rGO interface[149]

6.1.2 Architecture of Gas Sensing Devices

Electrically-transduced gas sensor designs (except in rare cases) typically fall into five categories: chemiresistors, chemical capacitors, chemical diodes, electrochemical sensors and field-effect transistors (FETs) (Figure 6.4)[8]. Even though industry may frequently use large, expensive electrochemical sensors, this work focuses on chemiresistors, which are ideal for preliminary screening of new sensing materials.

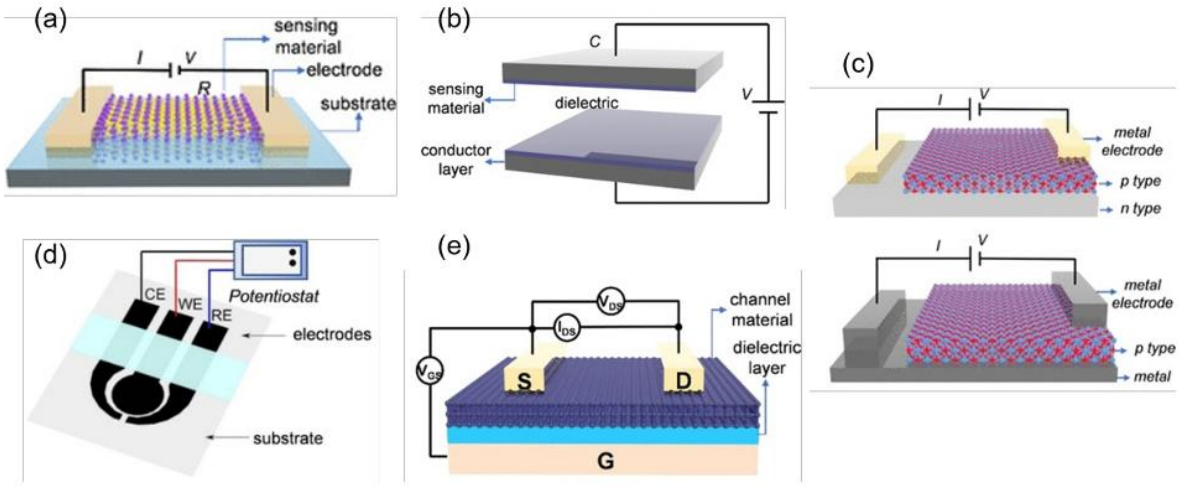

Figure 6. 4 Architectures of electrically-transduced gas sensors (a) chemiresistor sensor; (b) chemical capacitor; (c) chemical diode; (d) electrochemical sensor; (e) field-effect transistor (FET).[8]

Chemiresistive sensor is popular in gas sensing because of ease of use, low cost, compatibility with DC circuits and ease of precise measurements[8]. They allow fast prototyping of new materials such as rGO/MOx hybrids, which are low-power, high-sensitivity, and

reproducible[150]. The structure is characterised by the presence of source/drain electrodes and sensing material deposited on an insulating substrate(Figure 6.4 (a).The sensing material can be (metallic, such as graphene, or semiconducting, such as MOx/TMDCs) on an insulating substrate Figure 6.4 a). Gas exposure can tune resistance through dolping/ Schottky barrier-effect or junction distance [151]. The device total resistance R is the sensing material resistance $R_{material}$ plus contact resistance $R_{contact}$ from the metal electrode or the sensing material. Equation 6.1[8]

$$\boldsymbol{R = R_{material} - R_{contact}} \tag{6.1}$$

The response (S) of the sensor is given by

$$\boldsymbol{S = \frac{\Delta R}{R_o} = \frac{R_{analyte} - R_o}{R_o} \times 100\%} \tag{6.2}$$

Or

$$\boldsymbol{S = \frac{\Delta I}{I_o} = \frac{I_{analyte} - I_o}{I_o} \times 100\%} \tag{6.3}$$

Where R_o and I_o are the resistance and current of the circuit, with applied voltage and $R_{analyte}$ and $I_{analyte}$ are the resistance and current exposure to analyte, respectively[86].

Electrode arrangement is a vital factor: interdigitated electrodes (IDEs) on chemiresistors have demonstrated twofold response with IDEs on SnO_2 (Figure 6.5 a) compared to IDEs positioned beneath the surface (Figure 6.5 b), since diffusion and contact of the electrodes were better. Bottom SnO_2 designs restrict analyte access and transduction and have lower sensitivity. This underscores optimum configuration benefits of optimisation[152].

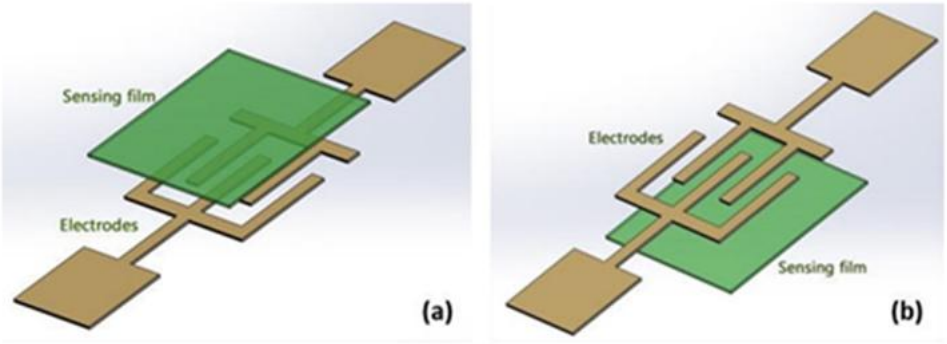

Figure 6. 5 Interdigitated electrode (IDE) configurations in chemiresistive gas sensors. Schematics showing: (a) IDE beneath sensing film; (b) IDE atop sensing film**[152]**.

6.1.3 Textile-based gas sensor

The growing demand for gas sensing technologies that can operate at room temperature, consume low power, and be deployed outside laboratory environments has driven increasing interest in alternative sensing materials and platforms. Conventional gas sensors often rely on rigid substrates, elevated operating temperatures, and complex fabrication processes, which limit their accessibility and widespread adoption. In contrast, textile-based gas sensors offer a unique opportunity to combine lightweight, flexible substrates with simple fabrication techniques, enabling distributed and wearable monitoring solutions. Such approaches are particularly relevant for localized safety monitoring in resource-limited or low-income settings, where access to sophisticated sensing infrastructure may be constrained. In this regard, the progress of new material systems and fabrication strategies that can be used with textile is one of the significant directions in which practical gas sensing applications can be implemented.

Although metal oxide gas sensors are effective in the detection of dangerous gases, these sensors have high operating temperatures, thus restricting integration into textile[23]. Flexible sensors are becoming crucial in providing a means of incorporating detectors into wearable materials, which are flexible, durable, and cheap[153]. When coated with sensing materials, textiles can detect different gases, reflecting the innovative technologies in fabrics and clothing to perform electronic functions.

Textile gas sensors that detect nitrogen dioxide (NO_2) with high sensitivity were produced by coating commercial cotton with reduced graphene oxide. The coating was applied by immersing cotton fabric in a graphene oxide solution and then subjecting the GO-covered textiles to thermal reduction at 190 to 400 °C to vary the reduction extent. The sample reduced at 190 °C showed the largest response, 45.90% toward 10 ppm NO_2 at room temperature. This has been mainly contributed by the maintenance of hydroxyl functional groups as well as the tubular lumen structure of the fibers that gives the fibers many active sites[154].

In this article, Yun et al.[153] developed a resistance-based gas sensor through electrostatic self-assembly of graphene oxide (GO) onto bovine serum albumin (BSA)-treated cotton and polyester yarns. Low-temperature reduction of the GO yielded reduced graphene oxide (rGO) sensor yarns capable of detecting nitrogen dioxide (NO_2). The concentration of holes was escalated by exposure to NO_2, which reduced the resistance of the yarn; the effect of which was verified visually by incorporating the yarn in a circuit to a light-emitting

diode (LED), which would light up when exposed to the gas indicating a switching of its insulating to conductive behavior. The sensor exhibited selectivity for NO_2 up to 250 ppm.

Park et al.[155] developed a reduced graphene oxide nanofibrous mesh fabric (RGONMF) by integrating RGO nanosheets with electrospun nylon-6 nanofibers, that provided a high-surface-area porous platform, and with bovine serum albumin (BSA) used as a "molecular glue" to positively charge the nylon fibers, uniform electrostatic assembly of monolayer GO flakes could be achieved with a resulting p-type sensor showing a high response to 1 ppm of NO_2 at room temperature (13.6%). It is interesting to note that the sensor was highly selective, with an 11-times increase in response to NO_2 compared with other gases such as ammonia, benzene, and acetone. Zhu et al.[156] utilised inkjet-printed rGO on a 3D porous textile decorated with palladium nanoparticles to achieve six times the sensitivity of conventional flat membranes. To maintain accuracy during extreme mechanical deformation, machine learning (PCA) was employed to decouple bending-induced signals from gas concentration data. Although the sensor demonstrates high durability over 10,000 cycles, it is limited by significant thermal sensitivity, where high temperatures can reduce the hydrogen response by up to 60%. Pattanarat et al.[157] developed a high-performance ammonia sensor through decorating the cotton yarn with a polyaniline (PANi)-decorated polystyrene polydioxide polydimethyl sulfoxide polydithiopropanol (PEDOT/PSS) heterostructure using a simple dip-and-dry method. This sensor reported a high electrical conductivity of 1343 S cm^{-1} and a limit of detection of 5 ppm without using the conventional acid doping. An important benefit of this architecture is that it has a humidity-independent sensing response, which overcomes a common limitation in polymer-based textile sensors. The sensing system is based on the reversible deprotonation and protonation of the PANi film, which changes the resistance when exposed to ammonia. Moreover, the device also showed high levels of durability, with a stable performance of 1100 stretching and 10 washing cycles. According to Maity et al.[158], a lead-free halide perovskite ($CH_3NH_3SnI_3$ or MASI) as a sensor on fabric has been created by a basic one-step solution process that detects ammonia at room temperature. The sensor provides two-mode detection by changing its visual colour, going from black to brown, and the electrical response of the sensor with approximately 85 per cent sensitivity at 100 ppm. Shiu et al.[159] designed a conductive woven fabric of PEDOT-functionalized and ethanol gas sensor by throwing electrospun PVP/PEDOT:PSS/TiO_2 micro/nanofibers over it. Working at room temperature, the sensor had a sensitivity of up to 12.06% at 6250 ppm of ethanol, which is much better than

single individual components because of the synergistic P-N heterostructure that exists between the conductive polymer and the metal oxide. Kim et al.[160] fabricated an e-textile made of $Ti_3C_2T_x$ MXene functionalized with CMC-DA ligands, which served as an oxidation protective layer and adhesive bond between cotton and hemp fabrics. This was done to make the sensor oxidation resistant to last more than 30 days and also exhibit a stable electrical response following intense machine washing. The resulting room-temperature NO_2 sensor had a detection limit of 200 ppb with high selectivity to ammonia and ethanol. It is also worth noting that the CMC-DA ligands overcame a significant shortcoming of pristine MXene by reducing the adsorption energy of NO_2, which prevents irreversible "super-strong" binding that makes sensor recovery challenging This feature was utilized to real-time human breath analysis and healthcare monitoring.

Recent research by Skrzetuska et al.[161] highlights the advancement of textronic chemical sensors as a sustainable and portable alternative to traditional, plastic-housed gas detectors for health and safety monitoring. By evaluating screen-printed carbon-based pastes against machine embroidery using silver-coated polyamide threads, the study demonstrated that while printing offers high chemical sensitivity on porous cotton substrates, it is highly susceptible to mechanical degradation. Specifically, printed conductive layers tend to wash away after approximately 20 cycles and experience a significant loss of conductivity when subjected to tensile stretching. Conversely, embroidered sensors exhibit superior mechanical robustness, maintaining stable electrical properties after 30 washes and even showing improved resistance values under tensile stress, making them ideal for garments that are frequently stretched or cleaned. Furthermore, while embroidery increases material thickness more than printing, it uniquely improves fabric breathability by creating additional spaces between the weaves within the embroidered pattern. These findings establish a clear technical precedent for the mechanical superiority of stitched conductive paths over printed films in wearable safety applications. Consequently, while industrial machine methods demonstrate durability, further exploration into hand embroidery offers a promising opportunity to investigate whether manual tensioning and precision placement can further optimise the integration and sensory performance of these robust textronic systems. The recent trend of e-textile gas sensor study underlines the trend to room temperature working and application of high-surface-area material such as rGO and metal-based hybrids to meet the environmental monitoring objectives. Advanced processes like inkjet printing have been embraced with more and more applications due to their non-contact patterning and cost-effectiveness, but have practical constraints when using other materials like

fibers. Specifically, the wetting and spreading characteristics of functional inks on substrates like nylon can impede the precision required for complex interdigitated electrode geometries, often restricting printed designs to simple conductive lines.

To overcome these challenges, this research investigates a dual fabrication strategy that balances high-tech patterning with traditional textile integration techniques. While inkjet printing was utilised for simplified electrode configurations, hand embroidery provided a reliable alternative for achieving the interdigitated patterns necessary to optimise signal collection in conductometric sensing. These hand-embroidered electrodes are combined with a simple, inexpensive drop-casting technique to rGO/metal-based inks in order to use the 3D porous microstructure of the fabric to maximise the contact area of gas molecules. Moreover, comparative analysis of rGO/CuO and rGO/CuCoOx composite inks were performed on hand-embroidered electrodes at 10 ppm NO_2 to study the effects of the metal oxide composition in sensing. This strategy has managed to produce a device that is functional and one that can detect 6 ppm NO_2 at room temperature, proving that robust and sensitive flexible platforms can be achieved using available and scalable fabrication platforms that do not require the expensive industrial equipment.

6.2 Formulation of inks, Characterisation and Device Fabrication

6.2.1 Formulation of rGO/CuO ink

The rGO/CuO ink was prepared by using the one-pot hydrothermal route. First, 0.07 g of Graphene Oxide (GO), fabricated by using the modified Hummers' method, was dispersed in 48 mL of deionised (DI) water. The GO dispersion was stirred for 20 minutes (15-second ON, 15-second OFF mode) using probe sonication. Next, 2 mL of ammonium hydroxide (NH_4OH) was mixed to the GO solution. Separately, a copper precursor mixture was prepared by dispersing 0.094 g of copper sulfate pentahydrate ($CuSO_4.5H_2O$) in 2 mL of DI water and stirring for 10 minutes. This solution was then added to the GO solution, after which the solution was stirred for 1 hour. The combined suspension was transferred to a Teflon-lined autoclave and heated at 150℃ for 20 h. After that, this was allowed to cool to room temperature. Upon completion, the solution was centrifuged at 5300 rpm for 30 minutes to remove the unreacted species and impurities. Next, the pellet was sonicated for 10 minutes and washed thrice with DI water, 20 minutes per wash. The purified product was then dried in an oven at 60 ℃ and dried powder was stored in a lab desiccator. A stable functional ink was then prepared by dispersing the material in a mixed solvent of isopropanol (IPA) and deionised (DI)

water. This dispersion was sonicated for 30 minutes to achieve uniform mixing prior to drop-casting. This ink was prepared at the University of Milano-Bicocca and used for the fabrication of Devices 1, 4, and 5 at the University of Cambridge during the abroad period, as summarised in Table 6.2.

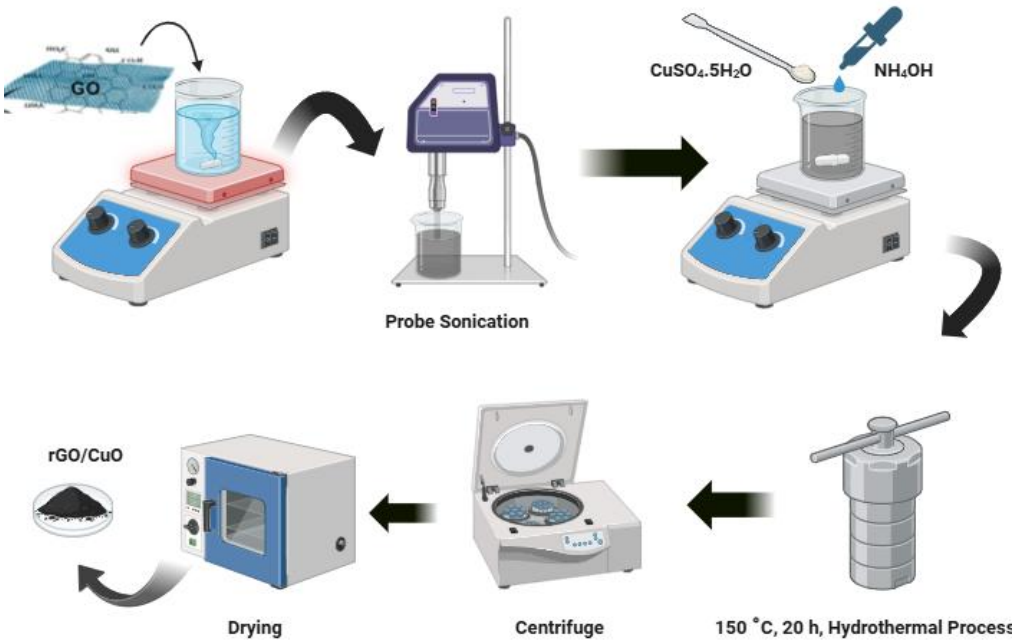

Figure 6. 6 Experimental setup of the fabricated rGO/CuO sensing material

6.2.2 Formulation of rGO/CuCoOx ink

The rGO/CuOx/CoOx hybrid ink used in this work was prepared by Dr Ozzy et al. [162]. I used this ink during my period abroad at the University of Cambridge, and it was used as it is for device fabrication. Detailed synthesis procedures are as follows:

Briefly, graphene oxide (GO, 23 mg) was dispersed in 22 mL of deionised water by magnetic stirring and sonication. Ammonium hydroxide was then added, followed by sodium nitrate, cobalt nitrate, and copper nitrate under continuous stirring. The resulting mixture was transferred to a Teflon-lined autoclave and heated at 180 °C for 12 h. After cooling, the product was vacuum-filtered using a 0.22 µm PTFE membrane, rinsed repeatedly with deionised water, and dried at 60 °C. The dried CuOx/CoOx-decorated rGO flakes were subsequently dispersed in a 9:1 isopropanol/2-butanol solvent mixture, sonicated, and centrifuged[162]. This ink was used for the fabrication of Devices 2, 3, 6 and 7 as summarised in Table 6.2.

6.2.3 Characterisation of functional Ink rGO/CuO

- **XRD of rGO/CuO**

Figure 6.7 shows the XRD spectra of the synthesized reduced graphene Copper Oxide (rGO/CuO) annealed at 250℃. The XRD pattern of rGO/CuO shows the diffraction peak at 2θ, 25°, indicating the reduction of graphene oxide to rGO. The other diffraction peaks correspond to the CuO monoclinic structure at 2θ, such as 32.4°, 35.4°, 38.6°, 46.1°, 48.6°, 53.4°, 58.2°, 61.5 °, 65.8°, 67.8°, 72.1°, and 75.1°, assigned to the index planes (110), ($\bar{1}10$), (111), ($11\bar{2}$), ($\bar{2}02$), (020), (202), ($\bar{1}13$), ($\bar{3}11$), (220), (311), and ($\bar{2}22$) respectively. These planes are in good agreement with JCPDS card # 01-080-1916, which provides clear evidence of the successful formation of rGO/CuO.

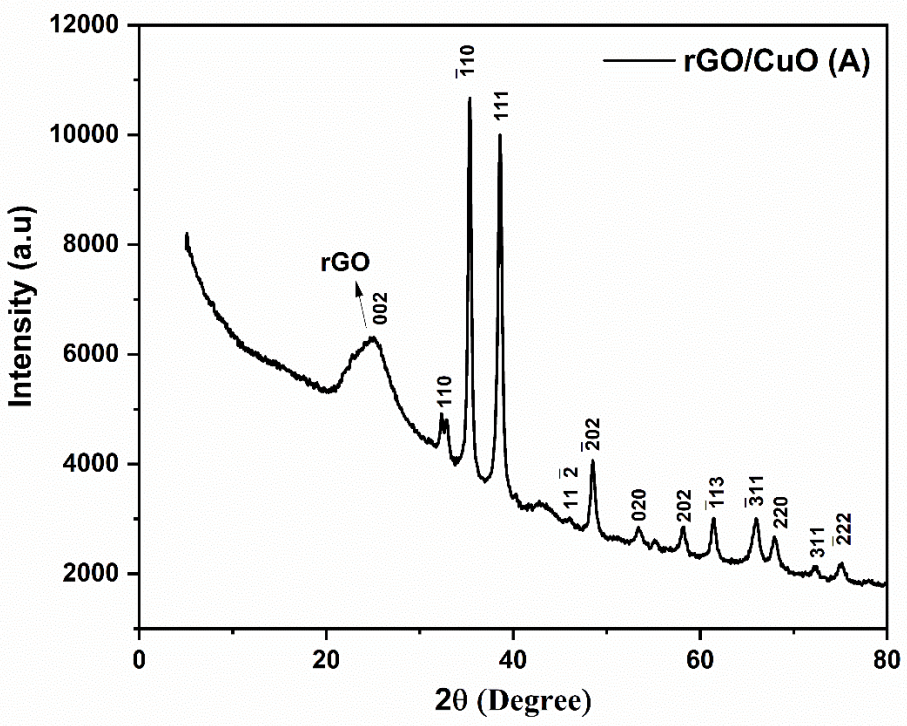

Figure 6. 7 XRD of rGO/CuO (A) annealed at 250℃

- **Scanning Electron Microscope (SEM)**

To investigate the structural properties of the rGO/CuO sensing material, a scanning electron microscope (SEM) is used. The SEM image shows the characteristic sheet-like morphology of rGO, decorated by CuO particles that display a mixture of well-defined microspheres and irregular forms. Figure 6.8 clearly shows microspheres on the rGO sheets, appearing as aggregates instead of a uniform coating.

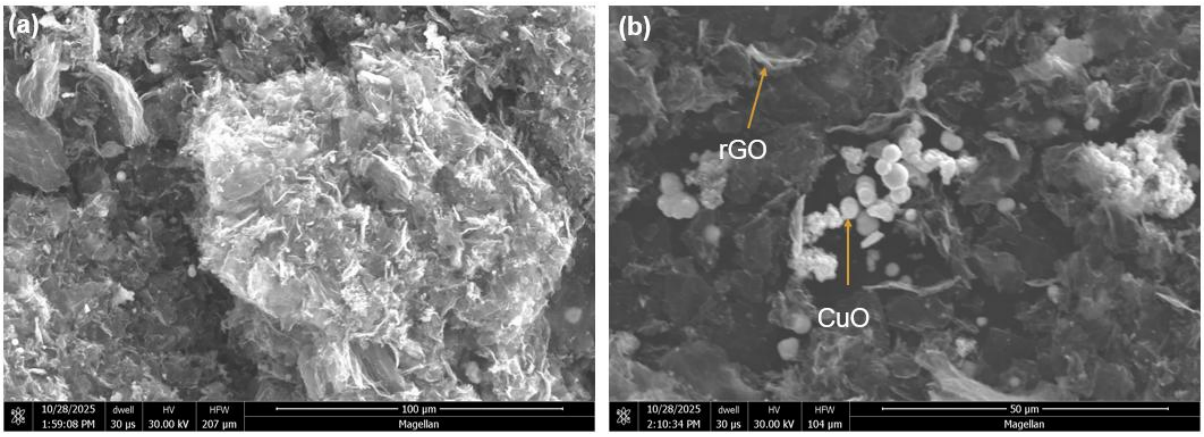

Figure 6. 8 SEM image of a) as-synthesised rGO/CuO, b) uniform microspheres of CuO and their sizes, c) Histogram analysis of particle size distribution

- **SEM Images of Nylon and rGO/CuO on Nylon**

Figure 6.9 shows the SEM images of the nylon textile 6.9a) before drop-casting rGO/CuO ink and 6.9b) after the drop-casting rGO/CuO ink. The twill-weave-like pattern is clearly visible in the pristine sample (Figure 6.9a). The nylon exhibits a uniform and smooth characteristic of synthetic polyamide fibres, confirming the pristine and ink-free surface of the nylon. After drop casting of rGO/CuO ink (Figure 6.9b), significant changes in surface morphology are noticed compared to the ink-free surface. The drop-casted ink partially covered the surface, but a clearly visible deposition on the nylon surface. The smooth nylon becomes roughened and deposited with clusters and aggregates, showing successful adhesion of the rGO/CuO ink to the nylon substrate.

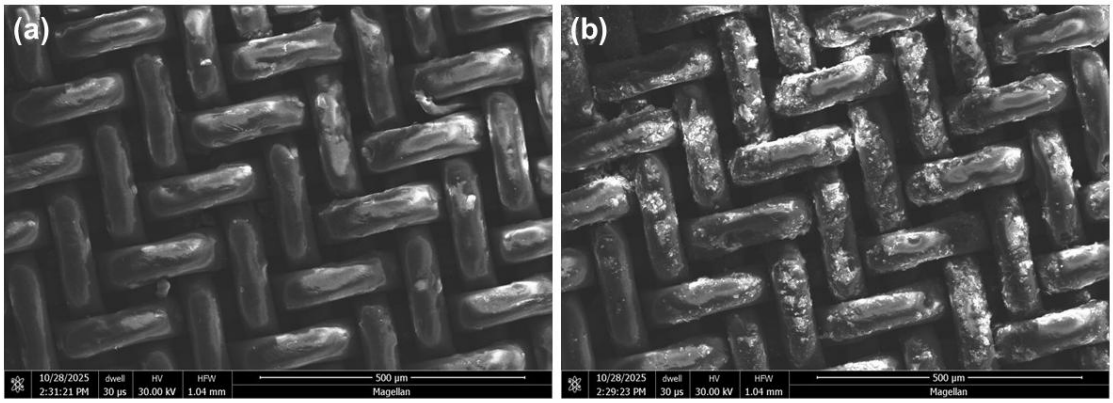

Figure 6. 9 SEM images a) Pristine nylon, b) rGO/CuO ink deposited on nylon

- **Transmission Electron Microscope (TEM)**

To better understand the structural features of rGO/CuO ink, TEM images of the ink are studied. Figure 6.10a) indicates that rGO has a thin, clear, and wrinkled sheet-like structure. Figures 6.10b) and 6.10c) indicate that the nanoparticles of CuO are effectively deposited and uniformly spread at the surface of rGO with slight agglomeration. As can be seen in Figure 6.10d), the TEM image at a high-magnification view provides a nanosized distribution of the CuO nanoparticles, indicating that the CuO was successfully anchored on the rGO matrix.

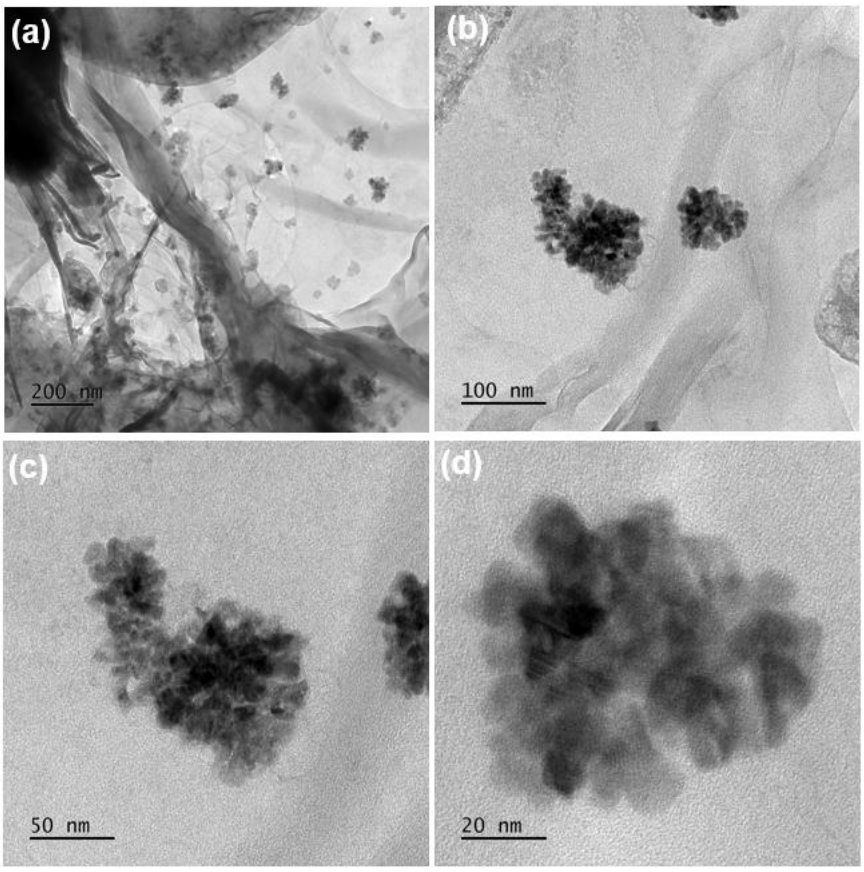

Figure 6. 10 TEM images of rGO/CuO ink at different magnifications showing wrinkled rGO sheets decorated with CuO

- **EDS MAPPING**

The spatial distribution of the constituent elements was further examined using energy-dispersive X-ray spectroscopy (EDS) elemental mapping in conjunction with scanning transmission electron microscopy (STEM). Figure 6.11a) demonstrates wrinkled rGO sheets covered with darker CuO domains. The EDS spectra (Figure 6.11b-f) of the corresponding sample are used to verify the presence of C, O, Cu, and S elements. Elemental mapping reveals a uniform distribution of carbon across the region, while oxygen and copper are well dispersed on the rGO sheets, indicating homogeneous incorporation of CuO. A weak sulfur signal is also

observed and might be due to some remaining functional groups. The spatial overlap of Cu and O with the carbon framework confirms strong interfacial interaction between CuO and rGO

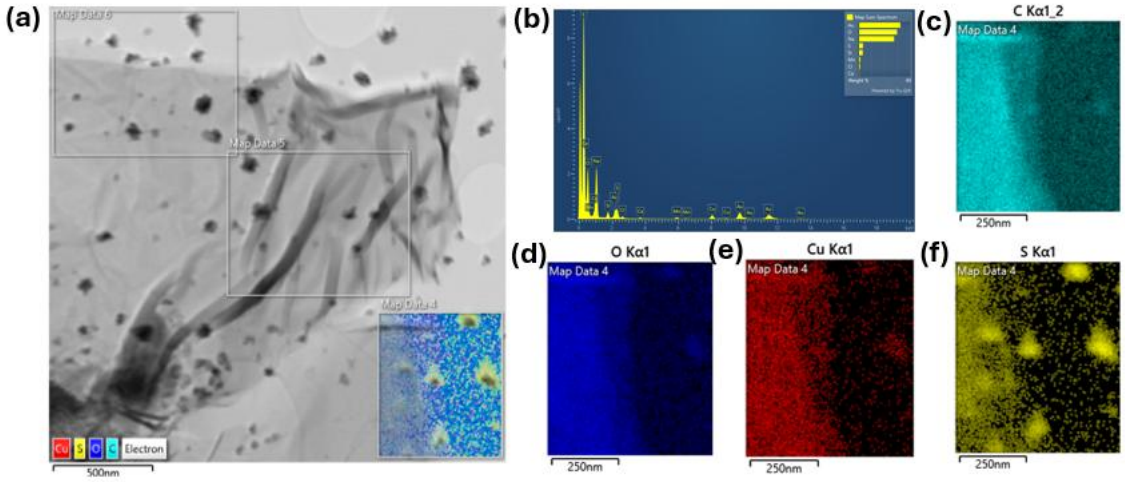

Figure 6. 11a) TEM image, b) EDX, and (c-f) elemental mapping of C, O, Cu, and S for rGO/CuO ink, confirming uniform distribution of CuO on the rGO framework.

- **Raman Spectroscopy**

Raman analysis is also used to further investigate the structural composition of GO and rGO/CuO in Figure 6.12. In the GO Raman, two strong characteristic D and G bands are observed at approximately 1360 cm^{-1} and 1608cm^{-1}, respectively[163]. The intensity ratio of the bands D and G I_D/I_G for GO is 1.009. In the Raman spectra of rGO/CuO, the same bands D and G are found, with a slightly lower shift of the G band, and a slight increase in I_D/I_G ratio (1.10). This rise confirms the successful reduction of GO to rGO, introducing defects via rGO-CuO and disruption in the sp^2 network. Additionally, the other peaks are observed in the inset Raman spectra at 289 cm^{-1} and 634 cm^{-1} [164], which are not present in the GO scattering spectrum. These peaks confirm the fabrication of rGO/CuO by using the hydrothermal method.

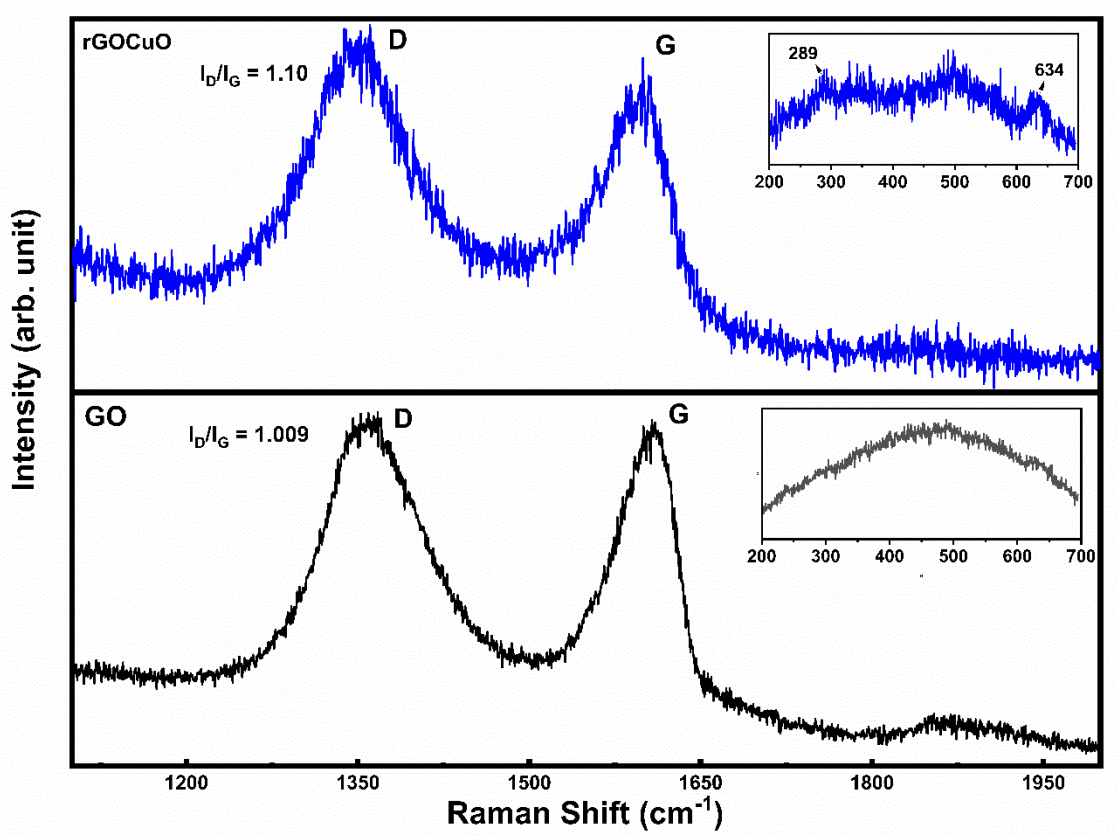

Figure 6. 12 Raman spectra of GO and rGO

6.2.4 Fabrication of gas-sensing devices

- **Hand-embroidered Device**

Interdigitated electrodes (IDEs) were fabricated on a nylon substrate through a low-cost hand-embroidery technique using commercially available silver-coated conductive threads and a sewing needle. This approach enables scalable, equipment-free fabrication of textile-based sensing devices. The sensing ink was subsequently deposited onto the embroidered IDE sensing region by drop-casting on a hot plate maintained at 80 °C. Figure 6.13a) shows the schematic design and the fabricated textile-based device. The schematic illustrates the layout of the silver thread electrodes and the sensing window on the fabric substrate, while the photograph shows the corresponding fabricated device. Figure 6.13b) shows the fabricated device with an overall length of approximately 2 cm, as indicated by the scale.

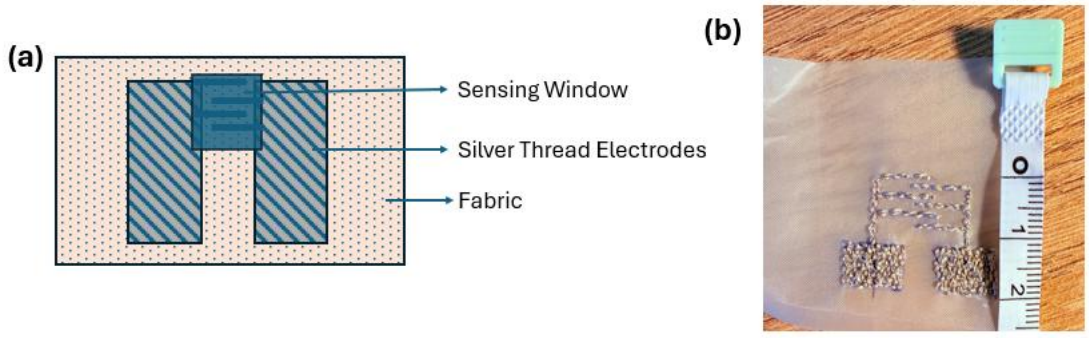

Figure 6. 13 (a) Schematic of the fabricated textile-based gas sensor (b) Photograph of the fabricated hand-embroidered device with scale.

The gas-sensing ink was prepared by sonicating 5 mg of rGO/CuO in 2 mL of solvent (1.5 mL IPA and 0.5 mL DI water), resulting in a concentration of 2.5 mg/mL. For device fabrication, approximately 3–4 drops of this ink (each drop containing 50–100 µL) were applied, giving a total drop-cast volume of roughly 150–400 µL on the embroidered IDE sensing window. The deposited ink was then dried on the hot plate. Figure 6.14 shows the fabricated embroidered device 1 with rGO/CuO sensing ink.

Figure 6. 14 Photograph of the Embroidered IDE-rGO/CuO Gas Sensor

- **Silver Conductive Thread**

Figure 6.15 (a-b) represent the SEM images of the silver conductive thread. Figure 6.15 c) shows the EDX of silver conductive thread, and Figure 6.15 d) represents the resistance change of silver conductive thread after each washing cycle. In these SEM images, it can be observed that the thread is coated with silver, showing a fibre-like structure. The thread is completely covered with silver, but it is not smooth. Tiny particles and small voids can be seen in the SEM images 6.15 a) and b). In the EDX analysis Figure 6.15 c), Ag is identified as the main element,

confirming the presence of a silver coating on the thread. Oxygen (O) and Carbon (C) are also shown, which justifies the oxygen-containing functional group of the underlying fibre[165].

I also performed a washing durability test on the silver conductive thread. I cut 15 cm long silver thread from the bobbin and washed it with Dixan detergent using a magnetic stirrer for 10 minutes per washing cycle. After each cycle, the silver thread was dried at approximately 100℃ for 15 minutes. The electrical resistance of the thread was measured before washing and after each washing cycle showing in Figure 6.15 d). The resistance of the thread before washing was 4.33 $\boldsymbol{\Omega}$, and till the first four cycles, the resistance was gradually decreased to 4.21$\boldsymbol{\Omega}$, which might be due to the removal of some loosely attached or extra silver particles, and it improves the contact of the silver thread. After the fifth cycle, a significant increase in resistance to 4.42 $\boldsymbol{\Omega}$, then 5.29 $\boldsymbol{\Omega}$, and after the seventh wash, resistance increased to 6.87 $\boldsymbol{\Omega}$. After this cycle, the thread was damaged and split, showing mechanical degradation of the structure of the silver conductive thread.

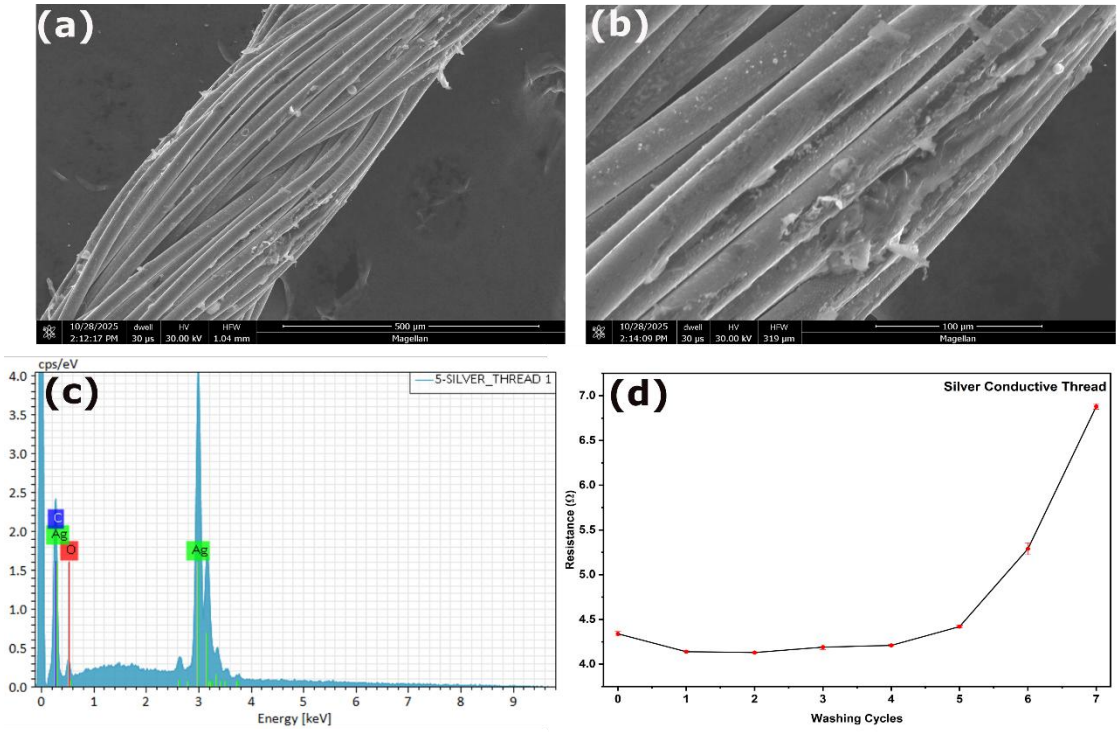

Figure 6. 15 a-b) SEM Images of silver conductive thread c) EDX elemental analysis of silver conductive thread d) Electrical resistance changes of silver conductive thread during washing cycles

- **Inkjet Printing Devices**

Inkjet printing deposits patterns onto substrates via ejected drops from an ink reservoir. The main approaches are continuous inkjet (CIJ) and drop-on-demand (DOD[166]. In CIJ, a continuous jet of drops passes through an electrostatic field that charges select drops, which deflect toward the substrate while uncharged ones recycle via a gutter; this enables high speeds and suits volatile, low-clogging inks[1]. DOD generates drops only as needed, such as via piezoelectric (P-DOD) voltage pulses that deform the actuator to eject ~1–100 pL drops, yielding 30–100 μm features[17]. Electrohydrodynamic (EHD) printing, a DOD variant, uses external fields to pull drops from the nozzle for ~1 μm resolution, but requires small nozzles prone to clogging, mitigated by dilute inks (impacting quality) or dual-channel designs. As the slowest technique due to print-head scanning, speeds can reach ~10 m min^{-1} with more nozzles[167]. The inkjet printer and the printhead cartridge are shown in Figure 6.16.

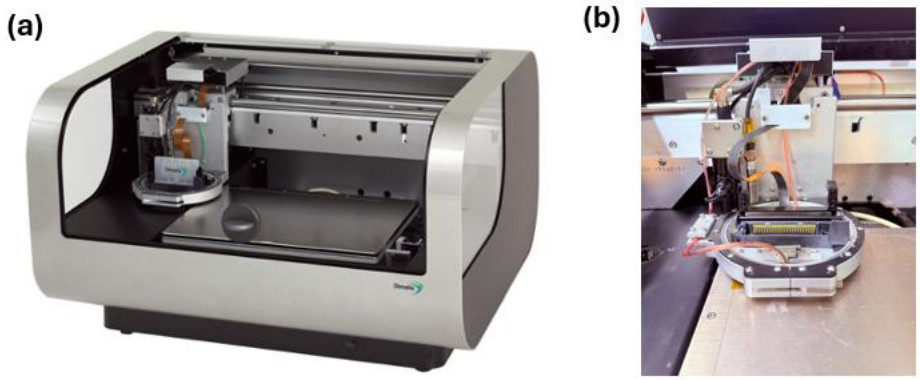

Figure 6. 16 a) Faujifilm Dimatix Inkjet Printer b) Printhead cartridge of Fujifilm Dimatix

The inkjet printing behaviour of the droplet formation during high-speed imaging was used to examine the behaviour of droplet formation of the ink, as indicated in Figure 6.17. After the actuation, the liquid meniscus extends to the form of a ligament, which then fractures into primary and smaller satellite droplets as a result of capillary instabilities. The availability of satellite droplets indicates that the jetting behaviour is affected by the rheological characteristics of the ink, and the conditions of actuation applied. Printability on inkjet is typically measured by the dimensionless Z-number, which is given by

$$\boldsymbol{Z = \frac{1}{Oh} = \frac{\sqrt{\rho \gamma a}}{\mu}} \qquad 6.4$$

Where $\boldsymbol{\rho}$ is the ink density, $\boldsymbol{\gamma}$ is surface tension, a is the nozzle's diameter, and $\boldsymbol{\mu}$ is the dynamic viscosity. The range of Z-value between 1 and 14 normally provides stable droplet formation in the inkjet printing. Any variations outside this range can result in long ligaments or satellite droplets, as can be observed in the time-resolved images. These findings underline the significance of maximising the properties of inks and printing conditions to be able to achieve controlled and stable jetting.

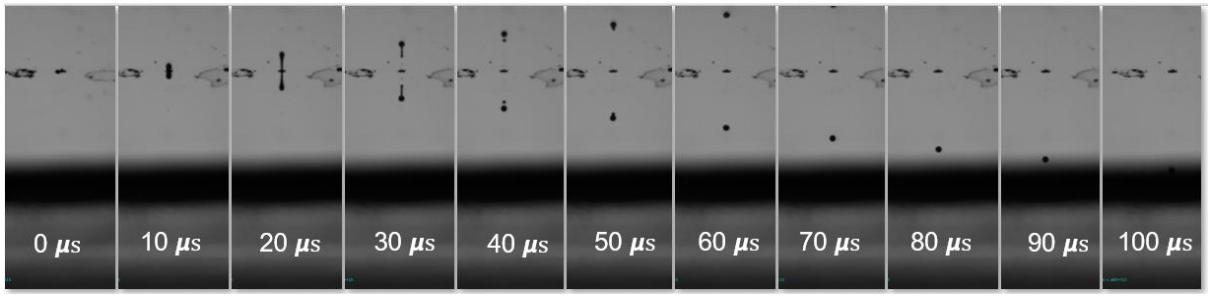

Figure 6. 17 Visualisation of inkjet droplet ejection during printing

The electrode patterns were designed using printer control software, where printing parameters such as layer count, drop spacing, and interlayer delay were defined before deposition. Figure 6.18 shows the pattern design interface and the corresponding printed silver electrode array on a nylon substrate. These parameters were also adjusted to print the electrodes at some distance. The printed electrodes exhibit good pattern fidelity and continuity, confirming the suitability of the selected printing parameters for flexible substrate fabrication. These electrodes with the same parameters used in the fabrication of device 7 on the PEDOTPSS/nylon substrate.

(a) (b)

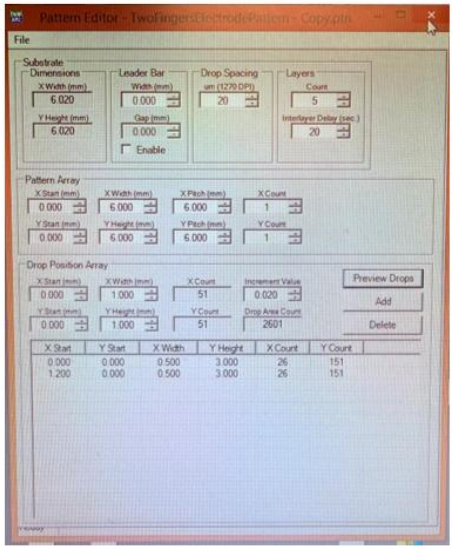

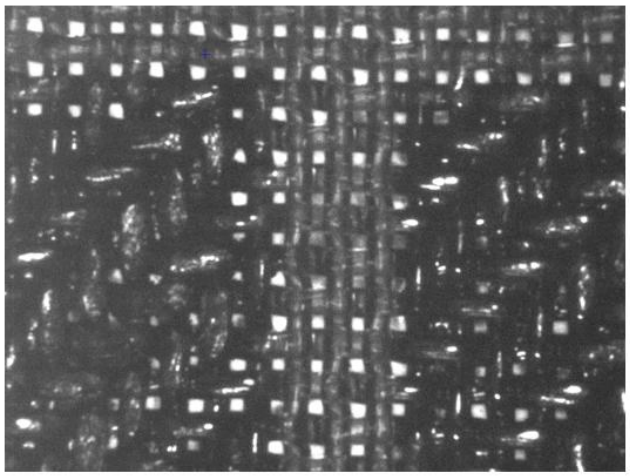

Figure 6. 18 Inkjet-printed silver electrode pattern on nylon: (a) pattern design interface and printing parameters, and b) Optical image of printed silver electrodes on nylon using an inkjet printer camera

Figure 6.19 a) presents an alternative electrode pattern designed and fabricated using the different inkjet printing parameters on a nylon substrate. Prior to printing, the nylon was treated with UV–ozone to improve surface wettability and ink adhesion. Silver ink was deposited in five successive layers, with a drying interval of 1 minute between each layer to prevent ink spreading, while the substrate temperature was maintained at 60°C to promote solvent evaporation and pattern definition. The printed silver electrodes exhibit good continuity and well-defined edges, confirming the suitability of the selected printing conditions for nylon substrates. This electrode pattern is intended for use in future work, where a sensing ink will be subsequently deposited within the patterned region to complete the device fabrication.

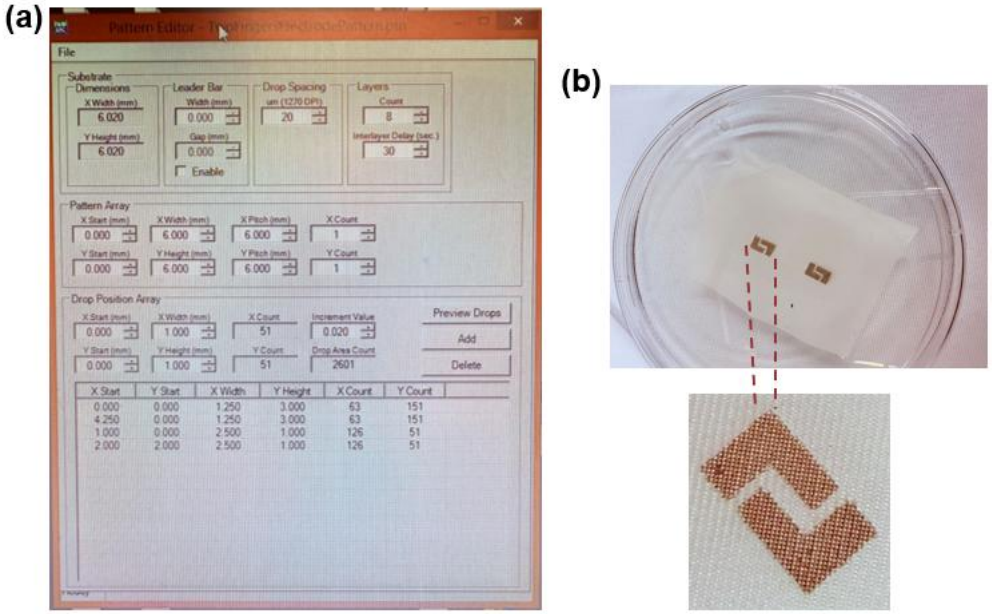

Figure 6. 19 Inkjet-printed silver electrode pattern on nylon: (a) pattern design interface and printing parameters, and (b) Printed electrode pattern on the nylon substrate.

- **Inkjet Printing of PEDOTPSS**

Following the printing of silver electrodes, PEDOT:PSS was also deposited on UV–ozone-treated nylon to evaluate its suitability as a conductive electrode material. Due to the wetting behavior of PEDOT:PSS on nylon, achieving uniform and well-defined patterns was challenging. After depositing five successive layers, the PEDOT:PSS film became electrically conductive. To further improve film smoothness and coverage, a PVA layer was deposited before PEDOT:PSS printing in figure b. The five-layer PEDOT:PSS electrode was

subsequently used in Device 3, where PEDOT:PSS acted as the electrode material and rGO/$CuCoO_x$ ink was drop-cast onto the PEDOT:PSS surface as the sensing layer. This device was tested in a gas sensing setup for NO_2, NH_3, CO_2, and CHOH; however, no clear or repeatable sensing response was observed. To improve electrode definition and device performance, a simplified electrode geometry consisting of four straight silver lines was printed on UV–ozone-treated nylon, and this configuration was designated as Device 7, as shown in Figure X.

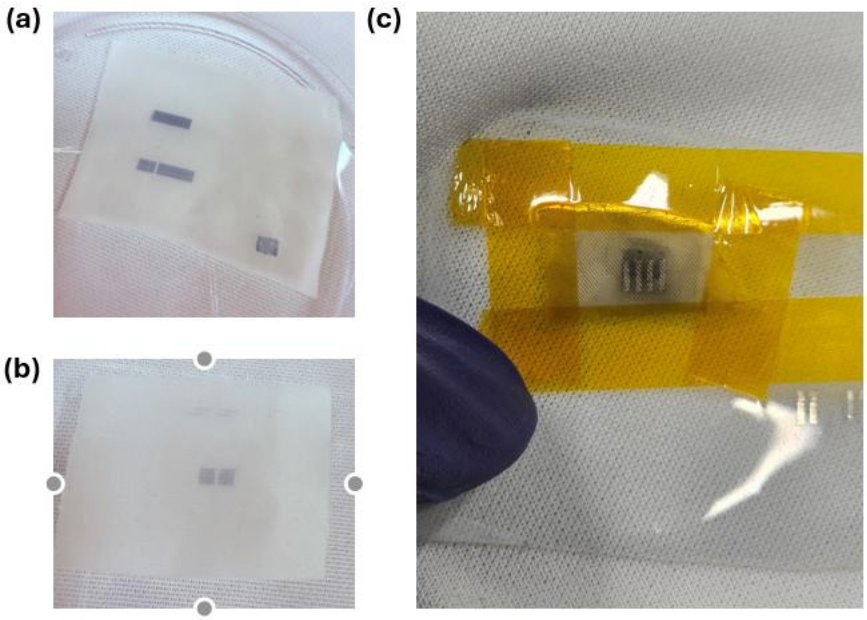

Figure 6. 20 Photograph of a) 5 layers of PEDOT:PSS printed on nylon b) 5 layers printed on PVA coated Nylon c) Device 7 (Printed Silver electrodes on Printed PEDOT: PSS on Nylon and drop cast rGO/CuCoOx ink)

Figure 6.21 shows the images of SEM of PEDOT:PSS deposited on the nylon substrate prior to and after the deposition of sensing layer. Figure 6.21a) shows a uniform PEDOT:PSS coating conformally covering the nylon fibers, indicating good deposition on the textile substrate. Figure 6.21 b) shows the PEDOT:PSS-coated nylon after deposition of rGO/$CuCoO_x$ ink, where the sensing layer is observed to be distributed over the underlying PEDOT:PSS deposition. The SEM images confirm the deposition of the layers successfully, the fibrous structure of the nylon substrate being maintained.

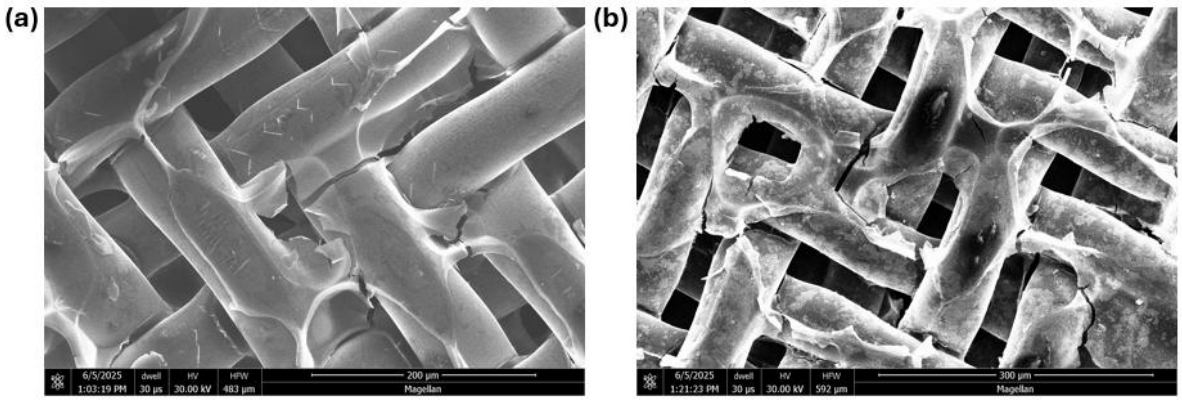

Figure 6. 21 SEM image of a) PEDOTPSS deposited on nylon b) rGO/CuCoOx dropcasted on PEDOTPSS coated nylon

Table 6. 2 Fabricated devices for Gas sensing measurements

Devices	Devices Name	Electrodes	Sensing ink
1	Embroidered nylon with rGO/CuO ink	Hand-embroidered with silver thread	rGO/CuO
2	Embroidered nylon with rGO-CuCoOx ink	Hand-embroidered with silver thread	rGO/CuCoOx
3	Nylon printed with PEDOT:PSS and drop-cast rGO/CuCoOx ink	Inkjet printed PEDOT:PSS	rGO/CuCoOx
4	Embroidered polyester with rGO/CuO ink	Hand-embroidered with silver thread	rGO/CuO
5	Embroidered Nylon with rGO/Fe_2O_3	Hand-embroidery with silver thread	rGO/Fe_2O_3
6	Printed electrodes on drop-cast PEDOT: PSS and drop-cast rGO-CuCoOx ink	Inkjet-Printed Silver electrodes And Drop casted PEDOT:PSS	rGO/CuCoOx
7	Printed Silver electrodes on Printed PEDOT: PSS	Inkjet Printed Silver Electrodes and PEDOTPSS	rGO/CuCoOx

	on Nylon and drop cast rGO/CuCoOx ink		

6.3 Equipment Setup and Sensing Measurements

A Kenosistec gas characterisation system was used to carry out all gaseous measurements at ambient pressure (1 atm) and room temperature, and at a fixed bias voltage of 1 V to maintain consistency in measurements. Figure 6.22 represents an illustration of the experimental setup. Individual analyte gas cylinders are linked to the system by means of calibrated mass flow controllers (MFCs), which adjust the rate of delivery of the gas through each cylinder depending on the density of each available gas. In the test, the flow of gas was started by opening the valve of the respective cylinders, and the analyte entered the system. The required concentration of the gases was attained by keeping the ratio of the target gas and the carrier gas (synthetic dry air) constant while maintaining a constant overall flow rate of 500 sccm.

Figure 6. 22 Image of the Kenosistec Gas Characterisation System

Figure 6.23 showing image of devices 1 and 6 sensors on the measurement platform. It can be clearly seen that the source and drain electrodes are probed by the system, delivering a 1 V applied voltage during measurements.

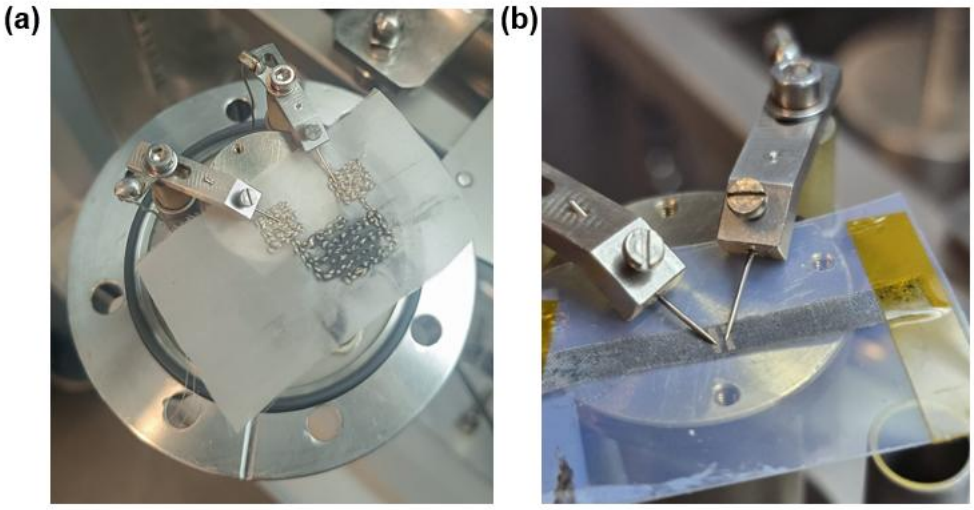

Figure 6. 23 Image of my **a)** Device 1 and b) Device 6 on the Kenosistec Gas Characterisation platform.

6.3.1 Sensing Mechanism and Performance of the Devices

1. **Device 1 (Embroidered IDE-rGO/CuO Gas Sensor) response to NO_2 at 10 ppm**

Figure 6.24 shows the response for the rGO/CuO gas sensor with 10 ppm NO_2 gas concentrations. The gas response (S) can be $\boldsymbol{S = (R_{air} - R_{gas})/R_{gas}}$ where $\boldsymbol{R_{air}}$ is the resistance at the initial stage, when no gas is exposed, and $\boldsymbol{R_{gas}}$ is the resistance when the targeted gas is exposed. These measurements are taken at room temperature. The gas response of the hand-embroidered sensor with four cycles at 10 ppm NO_2 is shown in the Figure. During the initial cycle, the resistance sharply decreased from 1181 kΩ to 967 kΩ. In the following cycle, it reduced from 1047 kΩ to 904 kΩ. The third cycle showed a further drop from 994 kΩ to 869 kΩ, and in the fourth cycle, the resistance declined from 947 kΩ to 836 kΩ.

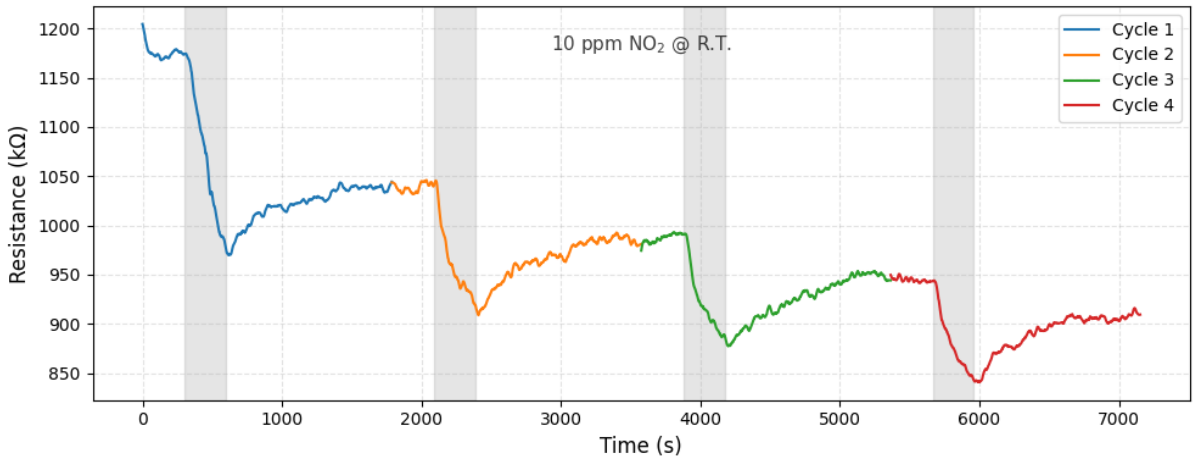

Figure 6. 24 Resistance (kΩ) vs Time (s) graph of Embroidered IDE-rGO/CuO Gas Sensor at 10 ppm NO_2

The 10 ppm NO_2 exposure intervals in each cycle are highlighted in grey. The total sensing time inside the gas chamber was approximately 119 minutes (about 1 hour and 59 minutes) for the four cycles. Between exposures, the sensor was allowed to recover in air for about 1489 seconds, which corresponds to roughly 24.8 minutes. Each sensing interval lasted about 297 seconds, or around 5 minutes at 10 ppm NO_2.

As shown in Figure 6.25, the response values for the first, second, third, and fourth cycles are 21.3%, 14%, 12.2%, and 12.5%, respectively, calculated by using the above equation, multiplying by 100. The noticeably higher response in the first cycle is attributed to a surface-conditioning effect, during which the sensing film undergoes structural and electrical adjustment upon its initial interaction with NO_2. After this initial exposure, the responses decrease to 14%, 12.2%, and 12.5%, which are much closer in value. This indicates that the sensor reaches a stable operating state following the first cycle. A similar behaviour has been reported in previous gas-sensing studies [24], where the first exposure produces the strongest response, and subsequent cycles reflect the steady-state performance of the device.

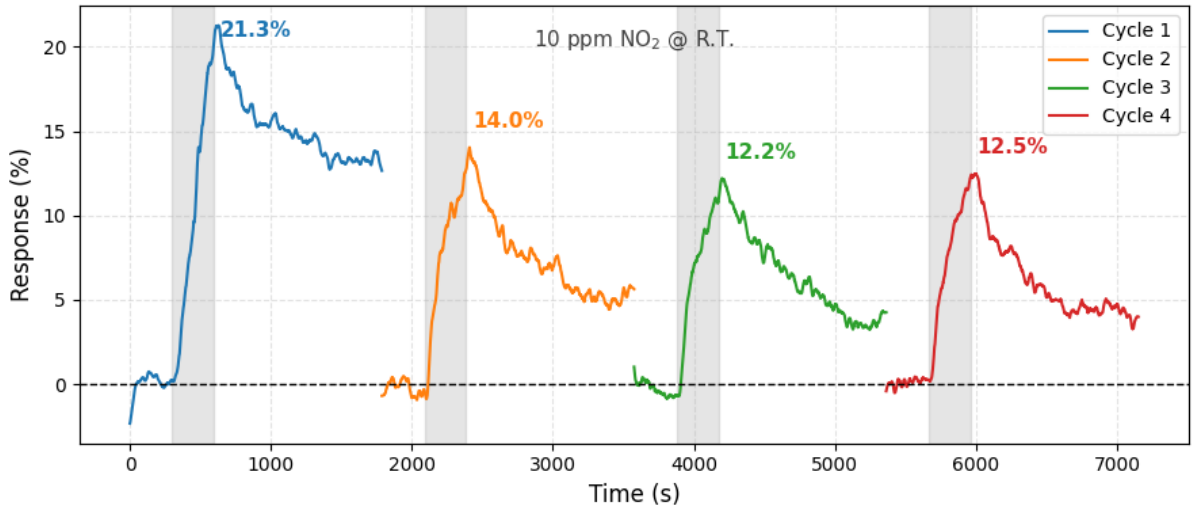

Figure 6. 25 Response (%) vs Time (s) graph of Embroidered IDE-rGO/CuO Gas Sensor at 10 ppm NO_2

2. Device 1 response to NO_2 at different concentrations

To investigate the concentration-dependent sensing behavior and evaluate the sensitivity of the embroidered IDE–rGO/CuO gas sensor, NO_2 was introduced at different concentrations

ranging from 4 to 10 ppm at room temperature. As shown in Figure 6.26, the sensor exhibited a systematic decrease in resistance with increasing NO_2 concentration, indicating a typical p-type semiconductor response. No measurable resistance change was observed at 4 ppm NO_2, suggesting that this concentration lies below the detectable limit of the sensor. However, at higher concentrations, a pronounced and reproducible response was observed. Exposure to 6 ppm NO_2 resulted in a resistance decrease from 1329 kΩ to 1209 kΩ, while increasing the concentration to 8 ppm caused a larger drop from 1290 kΩ to 1139 kΩ. At the highest tested concentration of 10 ppm, the resistance further decreased from 1149 kΩ to 1009 kΩ.

This monotonic increase in resistance change with NO_2 concentration demonstrates a clear concentration-dependent response, which is essential for estimating sensor sensitivity and the theoretical limit of detection. The observed behavior can be attributed to enhanced charge carrier modulation resulting from increased adsorption of oxidizing NO_2 molecules on the rGO/CuO surface.

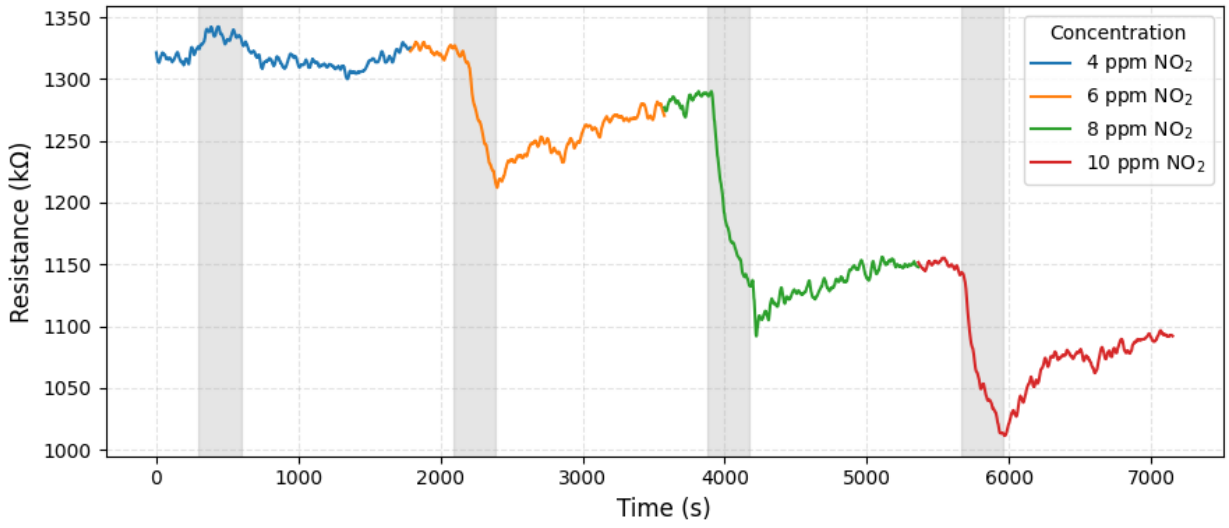

Figure 6. 26 Gas-response of rGO/CuO ink sensor for different NO_2 concentrations. Time vs Resistance (4ppm to 10 ppm) at room temperature

The corresponding resistance response percentage as a function of NO_2 concentration is shown in Figure 6.27. The calculated response percentages were 8.9%, 12.8%, and 13.5% for 6, 8, and 10 ppm NO_2, respectively, indicating a clear concentration-dependent sensing behaviour. Based on these results, the practical detection limit of the embroidered IDE–rGO/CuO sensor is estimated to be approximately 6 ppm. The response and recovery times were determined to be approximately 297 s and 1489 s, respectively, for all tested concentrations. Notably, the

sensor did not fully return to its initial baseline resistance during the recovery phase, indicating incomplete desorption of NO_2 molecules from the sensing surface. This behavior can be attributed to the strong interaction between oxidizing NO_2 molecules and the rGO/CuO sensing layer, which leads to slow desorption kinetics commonly observed in metal-oxide-based gas sensors. In addition, the fibrous and porous nature of the embroidered textile substrate may contribute to prolonged recovery by physically trapping gas molecules within the inter-fibre spaces, thereby delaying their complete removal during the recovery phase. Such phenomena have been observed for metal-oxide-based gas sensors and are commonly linked to slow desorption rate and partial surface desorption[168, 169].

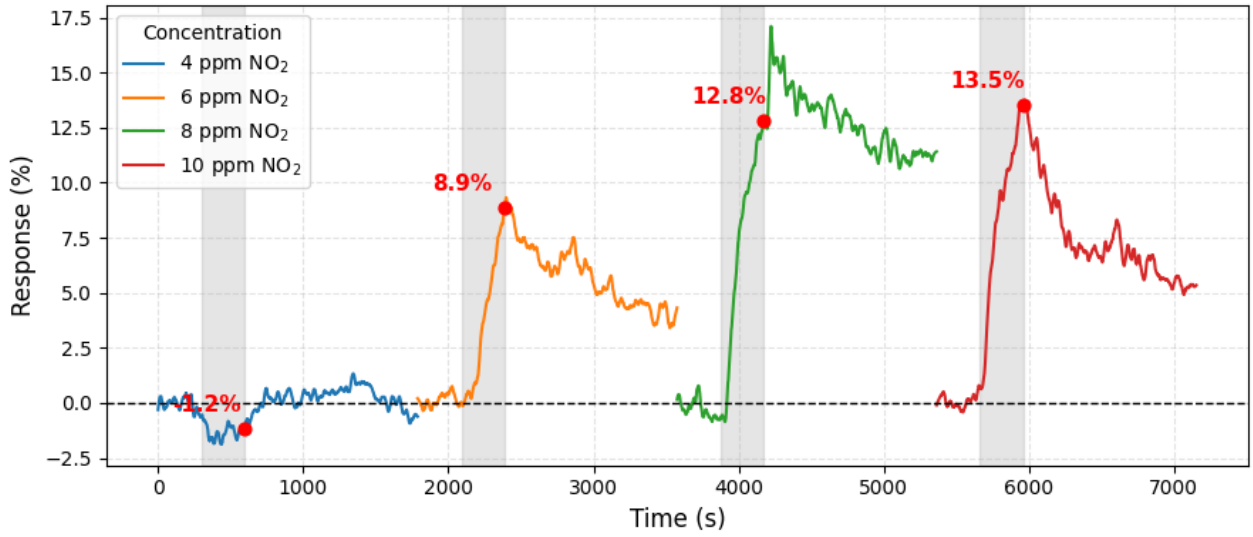

Figure 6. 27 Gas-response of rGO/CuO ink sensor for different NO2 concentrations Time vs Resistance response % (4 ppm to 10 ppm) at room temperature

- **Device 1 (Embroidered IDE-rGO/CuO Gas Sensor) response to NH_3 at 10 ppm**

Figure 6.28 shows the dynamic resistance response of the embroidered IDE–rGO/CuO sensor fabricated on nylon fabric when exposed to 10 ppm NH_3 over four successive cycles at room temperature. The sensor exhibited a consistent increase in resistance upon NH_3 exposure, confirming its p-type semiconducting behaviour and reversible gas–surface interaction. In the first cycle, the baseline resistance increased from 70.4 kΩ to 73 kΩ, while subsequent cycles showed stabilised baseline and peak resistance values, indicating improved sensing stability after initial exposure. All cycles demonstrated reliable recovery following gas removal, with a response time of approximately 297s.

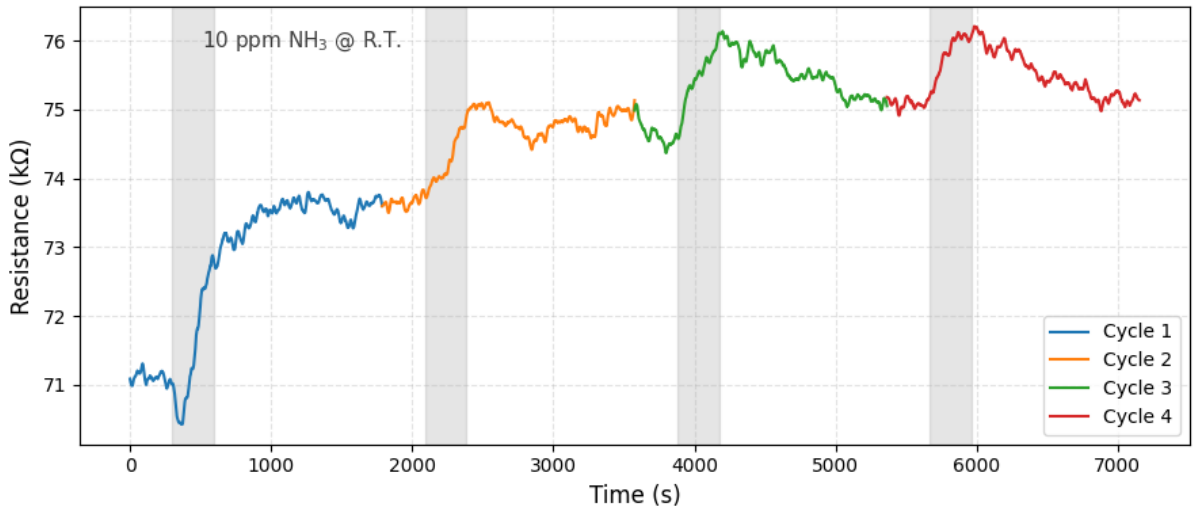

Figure 6. 28 Resistance (kΩ) vs Time (s) graph of Embroidered IDE-rGO/CuO Gas Sensor at 10 ppm NH_3 Room Temperature

The resistance response percent was also calculated by using S% = $\boldsymbol{R_{gas} - R_{air}/R_{air}} \times 100$ where $\boldsymbol{R_{gas}}$ is the peak resistance when gas is on and $\boldsymbol{R_{air}}$ is the initial resistance. As shown in Figure 6.29, the first exposure cycle yielded the highest response of 3.8%, attributed to effective NH_3 adsorption on the CuO/rGO sensing layer. Subsequent cycles exhibited responses of 1.9%, 2.1%, and 1.5%, resulting in an average response of 2.3% across four cycles.

Several studies report that room temperature flexible sensors typically show low single-digit responses at 10 ppm NH_3. For example, ZnO ceramic nanofibers with poly(styrene sulfone) gave 4.61% response at 10 ppm NH_3[170]. Similarly, the Fe_2O_3/PANI flexible paper-based sensor exhibits a 1.99-9% response to NH_3 concentrations of 0.5-50 ppm[171], and SnO_2 film with Ti_3C_2Tx MXene nanocomposites achieved 3.1% at 10 ppm [172]. In contrast to these systems, which rely on complex material synthesis routes and multi-step fabrication processes, the embroidered sensor presented in this study is produced using a simple hand-stitching and drop-casting approach on a commercially available textile substrate. Despite its simplicity, the sensor achieves a comparable average response of 2.3% at 10 ppm NH_3. This highlights the potential of hand-embroidered sensing platforms to enable gas sensor fabrication by non-specialists, without the need for advanced infrastructure or specialised facilities. Such an approach opens opportunities for decentralized manufacturing, rapid prototyping, and deployment of textile-based sensors or field-deployable gas sensors in low-resource environments and diverse real-world settings.

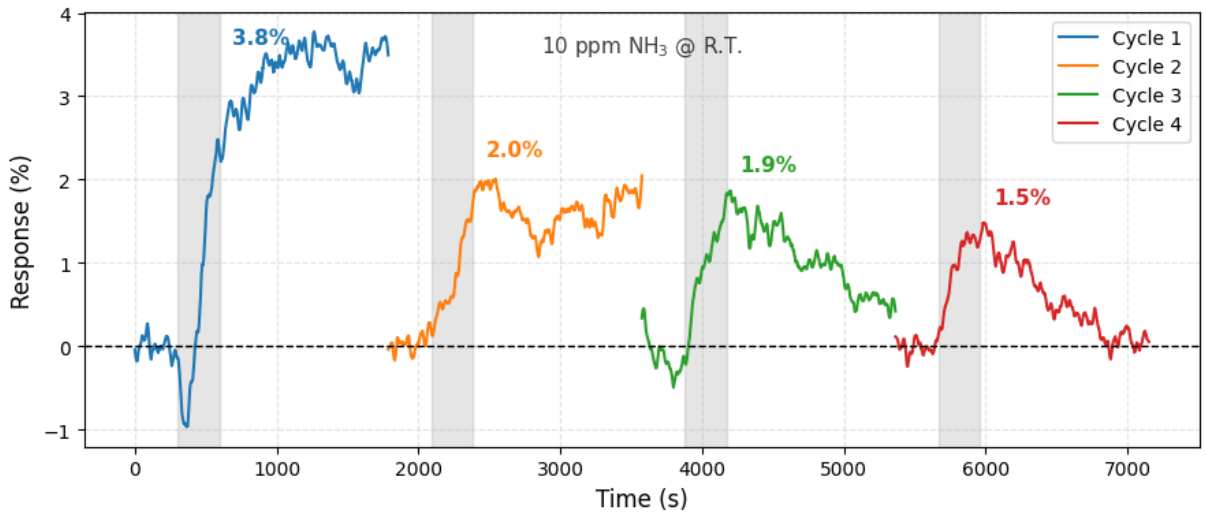

Figure 6. 29 Resistance Response Per cent (%) vs Time (s) graph of Embroidered IDE-rGO/CuO Gas Sensor at 10 ppm NH_3 Room Temperature

- **Device 1 (Embroidered IDE-rGO/CuO Gas Sensor) response to CH_2O**

Figure 6.30 shows the resistance vs time graph of the embroidered rGO/CuO device to 1 ppm CH_2O at room temperature. The response was taken in four consecutive cycles, and in every cycle, when gas is on, the resistance shows a similar trend. We can see that there is a small change in every cycle, but this decrease is relative to the baseline when the gas is off, giving a small response of 0.66 % in the first cycle. From this trend, we can say that the sensor can detect CH_2O at 1 ppm, but with a very small signal amplitude. The overall trend in the graph shows visible noise and very slow baseline drift, and the response when gas is on is similar to these fluctuations. Therefore, the 1 ppm response is weak, not a quantitative response. So, this plot is used to indicate that the device showed an identical response at 1 ppm.

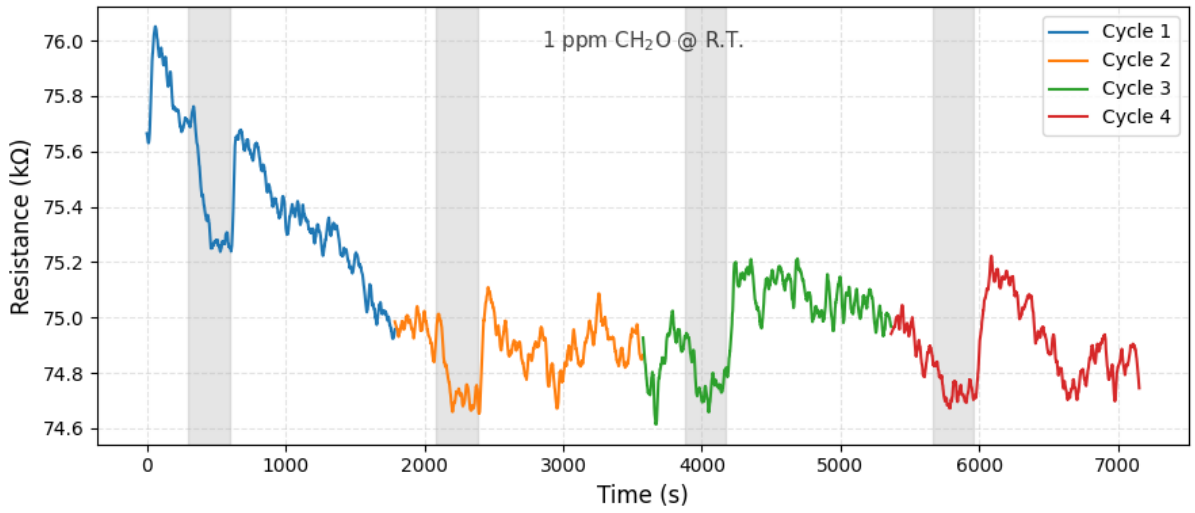

Figure 6. 30 Resistance (kΩ) vs Time (s) graph of Embroidered IDE-rGO/CuO Gas Sensor at 1 ppm CH_2O Room Temperature

Figure 6.31 compares the gas sensing response of Device 1 toward different target gases, including NO_2 (4, 6, 8, and 10 ppm), NH_3 (10 ppm), CH_2O (1 ppm), and CO_2 (100,000 ppm), all measured at room temperature. The sensor exhibits a clear concentration-dependent response to NO_2, with increasing response magnitude as the gas concentration increases. Based on the observed response behavior, the limit of detection (LOD) for NO_2 is estimated to be approximately 6 ppm for this device. In addition to NO_2, the sensor demonstrates measurable responses to NH_3 at 10 ppm and CH_2O at 1 ppm, highlighting its capability to detect multiple chemically distinct gases despite being fabricated using a low-cost, simplified process without the need for advanced instrumentation or cleanroom facilities. In contrast, no visible response is observed upon exposure to CO_2, even at a high concentration of 100,000 ppm, indicating a degree of selectivity toward more chemically active gases.

These results collectively demonstrate that the embroidered IDE–rGO/CuO sensor combines multi-gas sensitivity with inherent selectivity, achieved through an accessible and scalable fabrication approach.

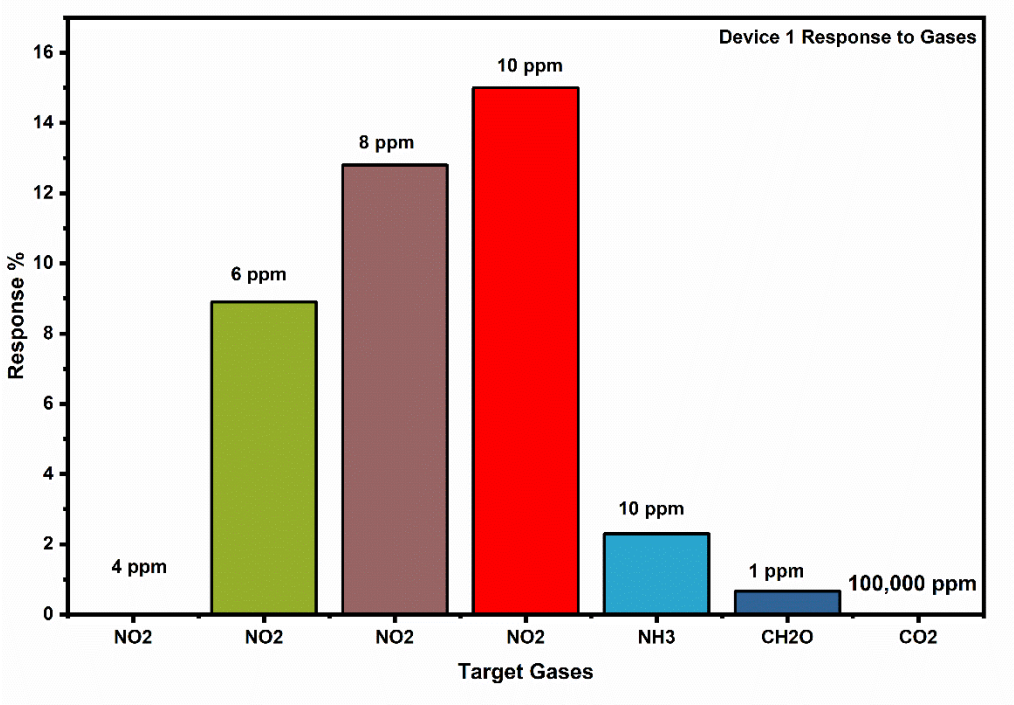

Figure 6. 31 Response of Device 1 to different gases and concentrations

The choice of the target gases in the case of the first device, i.e., NO_2, NH_3, and CH_2O, was used by the fact that they are relevant to practical environments where textile-integrated sensors can provide unique benefits. NO_2 is a widespread pollutant in urban and industrial areas: it originates from combustion processes, vehicle emissions, and electricity production and is among the most important indicators of the indoor and outdoor quality. NH_3 is also very widespread in the natural settings of agriculture, such as livestock farming and greenhouses, where the textile-based sensors may be incorporated in a curtain, protective clothes, or structural fabrics to continuously monitor it. One of the largest indoor air pollutants emitted by building materials, furniture, and textiles is formaldehyde (CH_2O), which is especially applicable when integrating sensing wearables or home-based sensing is needed.

Device 2 (Embroidered IDE-rGO/CuCoOx gas sensor)

Initially, rGO/CuO ink prepared via the hydrothermal method, as described above, was used for gas sensing on handmade embroidery. During an abroad research period in Professor Tawfique Hassan's group, Dr. Osarenkhoe Ogbeide developed rGO/$CuCoO_x$ bimetallic sensing ink for his PhD work. This ink was tested on PET porous substrates, demonstrating high sensitivity, stability, and room-temperature NO_2 detection with a 50 ppb limit of detection. [173]. Impressed by the bimetallic oxide concept, this ink was adopted for the present work by drop-casting rGO/$CuCoO_x$ onto handmade embroidered IDE nylon to fabricate a gas sensor.

SEM Images of Nylon and rGO/CuCoOx on Nylon

Figure 6.32 shows the SEM images of a) Pristine Nylon and b) rGO/CuCoOx ink drop casted on nylon. These images confirm the successful integration of rGO/CuCoOx sensing ink on the nylon surface, and the surface becomes roughened. As compared to the rGO/CuO ink deposition, rGO/CuCoOx ink deposition provides a uniform coating with nanoparticles and a higher active surface area.

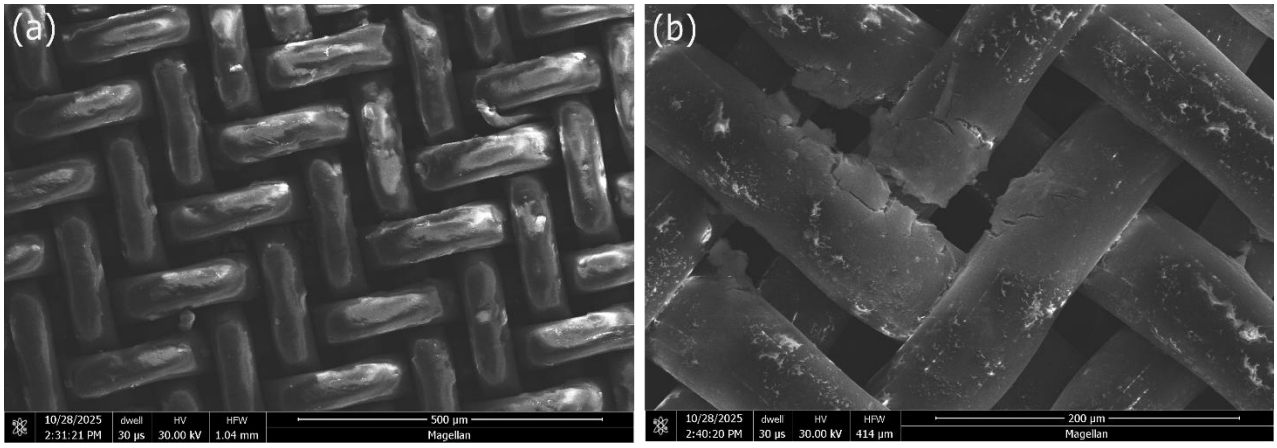

Figure 6. 32 SEM images a) Pristine nylon, b) rGO/CuCoOx ink deposited on nylon

Device 2 (Embroidered IDE-rGO/CuCoOx gas sensor) response to NO_2

Figure 6.33 shows the resistance response of rGO/$CuCoO_x$ drop-cast on a handmade embroidered sensor to repeated 10 ppm NO_2 at room temperature, where a pronounced surface-conditioning effect during the first sensing cycle (shown as an inset due to its significantly higher response) is followed by stabilized and reproducible responses in subsequent cycles. With the first exposure to NO_2, rGO/CuCoOx sensor showed an intense decrease in resistance (39229.34 kΩ to 11928.40 kΩ), due to deep adsorption sites. NO_2 acts as a strong oxidising gas that withdraws electrons from the rGO/CuCoOx and oxygen vacancies, creating a hole accumulation layer that reduces resistance[174].

The enhanced sensing performance may also be explained by the presence of a p–p heterojunction between CuO and CoO nanoclusters distributed on the rGO sheets. These heterojunctions facilitate efficient charge transfer and carrier modulation under exposure to NO_2, leading to increased resistance changes and better signal stability. The presence of multiple p-type oxide interfaces also contributes to reduced electrical noise by suppressing random carrier fluctuations, thereby enhancing the signal-to-noise ratio during sensing.

Following the first sensing cycle, partial occupation of deep adsorption sites leads to a moderated resistance change in the second cycle, where the resistance decreases from 14,838 kΩ to 8,476 kΩ. By the third and fourth cycles, the sensor reaches a stabilised operating regime and exhibits consistent and repeatable responses to NO_2 exposure. Specifically, resistance decreases from 11,471 kΩ to 7,755 kΩ in the third cycle and from 10,473 kΩ to 7,538 kΩ in the fourth cycle, confirming reliable sensing performance after surface stabilisation.

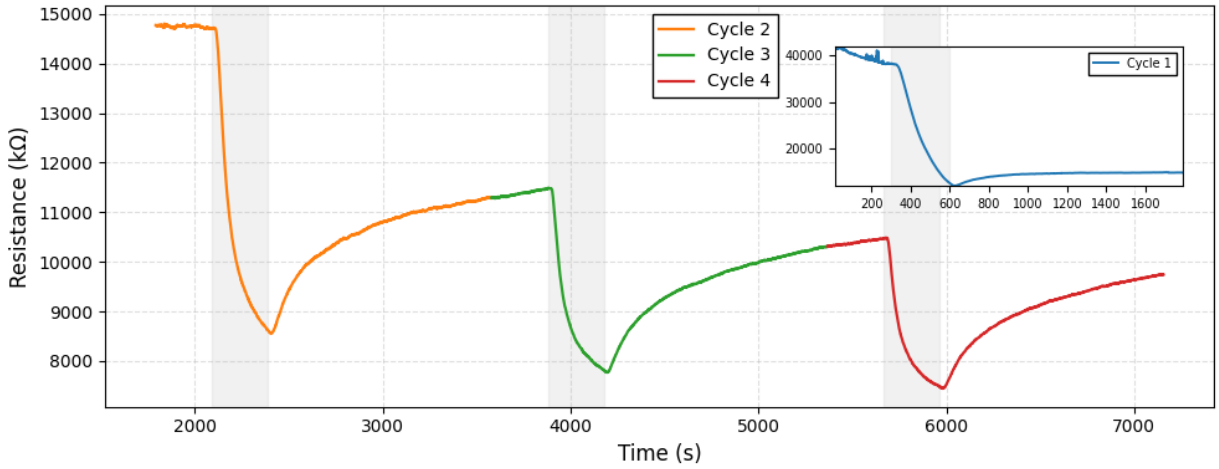

Figure 6. 33 Resistance (***Ω***) vs Time (s) graph of Embroidered IDE-rGO/CuCoOx Gas Sensor at 10 ppm NO_2 Room Temperature

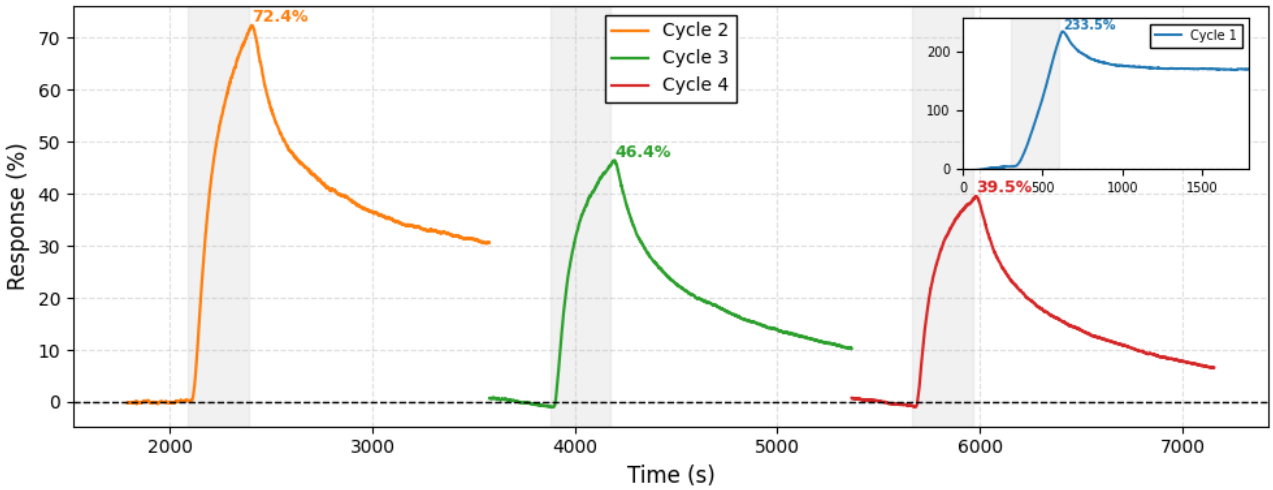

Figure 6. 34 Resistance Response Percent (%) vs Time (s) graph of Embroidered IDE-rGO/CuCoOx Gas Sensor at 10 ppm NO_2 Room Temperature

Figure 6.34 shows the resistance response curve of rGO/CuCoOx sensor with 10 ppm NO_2. By using this equation $(\boldsymbol{R_{air} - R_{gas}})/\boldsymbol{R_{gas}x\,100}$, the resistance response per cent was calculated. The sensor exhibits gas response values of 233.5%, 72.4%, 46.4%, and 39.5% during the first, second, third, and fourth exposure cycles to 10 ppm NO_2, respectively. I calculate the signal-to-noise ratio (SNR) for three stable cycles. The measured values are 278.54, 57.33 and 56.65 for the second, third and fourth cycles, respectively.

Device 2 (Embroidered IDE-rGO/CuCoOx gas sensor) response to NH_3

Figure 6.35 shows the resistance–time response of the embroidered rGO/$CuCoO_x$ sensor to repeated exposure of 1 ppm NH_3 at room temperature for Cycles 2–4. The first sensing cycle is not shown, as it is mainly affected by initial surface conditioning and an unstable baseline. During each NH_3 exposure, the sensor exhibits a clear and reversible change in resistance, confirming stable p-type sensing behaviour. Cycles 3 and 4 display better surface conditioning, with a more stable baseline and consistent resistance changes, demonstrating reliable and repeatable sensor performance at low NH_3 concentration.

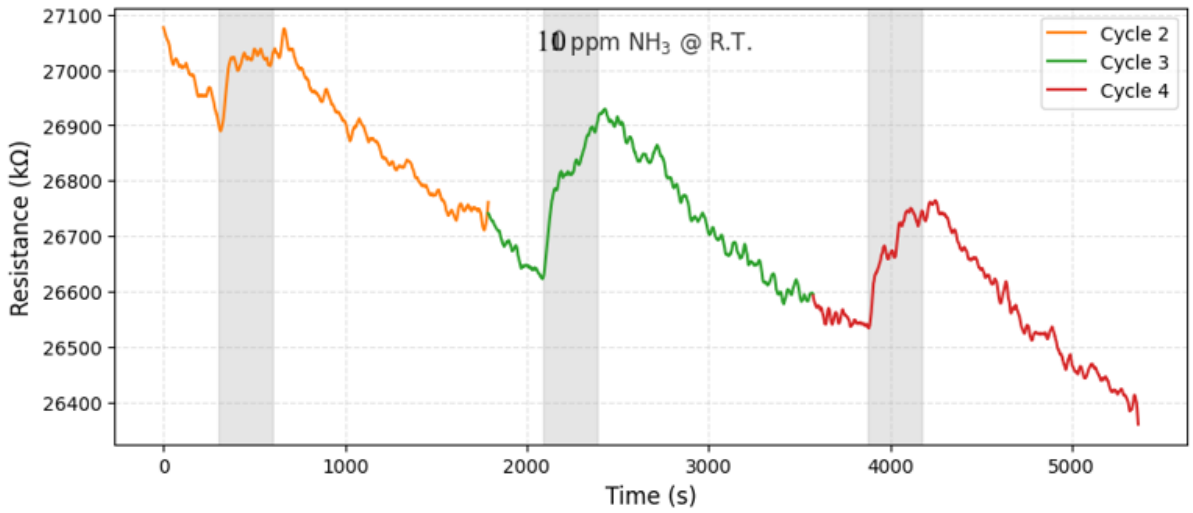

Figure 6. 35 Resistance (***Ω***) vs Time (s) graph of Embroidered IDE-rGO/CuCoOx Gas Sensor at 10 ppm NH_3 Room Temperature

Figure 6.36 shows the resistance response percentage of the embroidered rGO/$CuCoO_x$ sensor during repeated exposure to 10 ppm NH_3 at room temperature for Cycles 2–4. Cycle 2 shows an unstable baseline, which is likely due to the sensor surface still settling after the initial conditioning cycle and the slow release of trapped gas from the porous textile structure. In comparison, Cycles 3 and 4 show more stable baselines and clearer response peaks, indicating improved surface conditioning. The response values of about 0.2%, 0.9%, and 0.8% for Cycles 2, 3, and 4 represent the relative change in resistance during NH_3 exposure and confirm repeatable sensing behavior at room temperature.

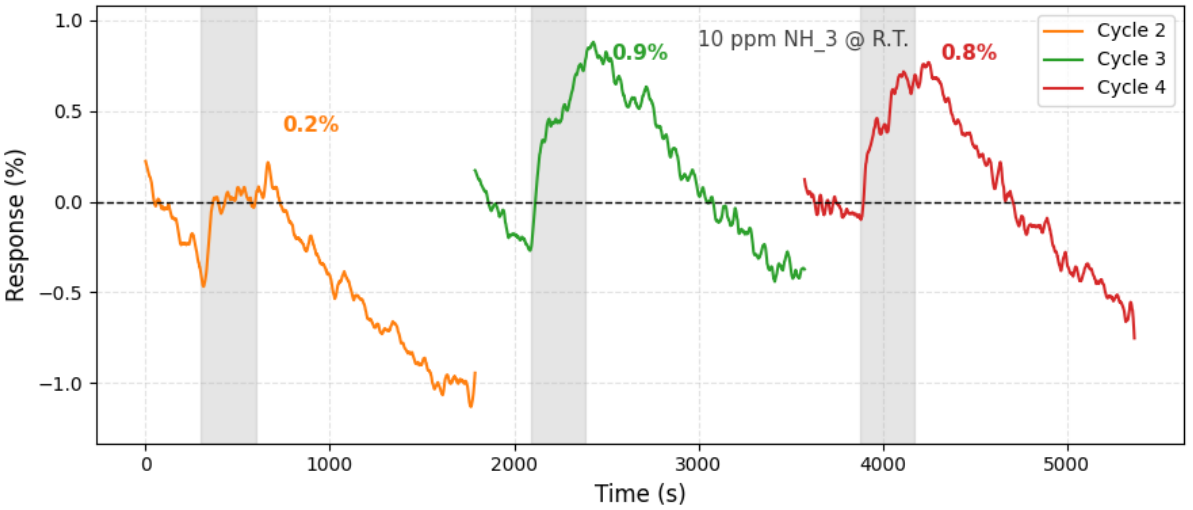

Figure 6. 36 Response(%) vs Time (s) graph of Embroidered IDE-rGO/CuCoOx Gas Sensor at 10 ppm NH_3 Room Temperature

In addition to NH_3 and NO_2 sensing, Device 2 was also tested for CH_2O and CO_2; however, no measurable response was observed under the present experimental conditions. This absence of response is likely related to instrumental or testing limitations rather than the sensing material itself, as rGO/$CuCoO_x$ inks have previously demonstrated strong sensitivity toward formaldehyde. These measurements will therefore be repeated and further optimized in future work.

A comparison between Device 1 (rGO/CuO) and Device 2 (rGO/$CuCoO_x$) highlights the influence of the sensing ink composition on gas response. For NO_2 at 10 ppm, Device 2 exhibits a significantly higher response (~52%) compared to Device 1 (~14%), indicating the beneficial role of the bimetallic Cu–Co oxide system in enhancing charge transfer and gas–surface interactions. In contrast, for NH_3 sensing, Device 1 shows a higher response (~2.3%) than Device 2 (~0.6%), suggesting that the rGO/CuO ink is more favourable for NH_3 interaction under room-temperature conditions. Overall, these results demonstrate that while the rGO/$CuCoO_x$ ink offers superior performance for oxidising gases such as NO_2, the rGO/CuO system exhibits comparatively better sensitivity toward NH_3, emphasising the importance of ink composition in tailoring gas selectivity and sensor performance. Overall, these results demonstrate that hand-embroidered textile sensors with the dropcast method can effectively differentiate gas response behaviour through simple ink modification, while maintaining low-cost fabrication and practical applicability.

- **Other Fabricated Devices**

Device 3 was initially fabricated by directly printing five layers of PEDOT:PSS onto a nylon substrate using a Dimatix printer, without incorporating a defined electrode design. The rGO/$CuCoO_x$ sensing ink was drop-cast onto the PEDOT:PSS printed layer. However, this configuration did not exhibit any measurable gas response, which is due to the absence of a proper electrode design and inefficient charge collection across the sensing layer.

To address this limitation, the device design was optimised, resulting in the fabrication of Device 7 shown in Figure 6.38. In this optimised design, five layers of IDE were first printed onto the nylon substrate using the Dimatix printer and annealed at 100 °C for 1 hour to improve conductivity and adhesion. Following this, five layers of PEDOT:PSS were printed to serve as a conductive interfacial layer. Finally, the rGO/$CuCoO_x$ sensing ink was drop-cast onto the device. The final Device 7 structure, from top to bottom, consists of the silver electrodes,

rGO/$CuCoO_x$ sensing layer, PEDOTPSS 5 printed laters and the nylon textile substrate. This optimized multilayer configuration enables improved electrical contact and charge transport, thereby providing a suitable platform for subsequent gas-sensing evaluation.

Another printed configuration (Device 6) was fabricated by printing silver electrodes directly onto a PEDOT: PSS-coated nylon strip, as shown in Figure 6.37 a). Sensing data for these printed devices were not collected due to the limited time available during the research stay at the University of Cambridge.

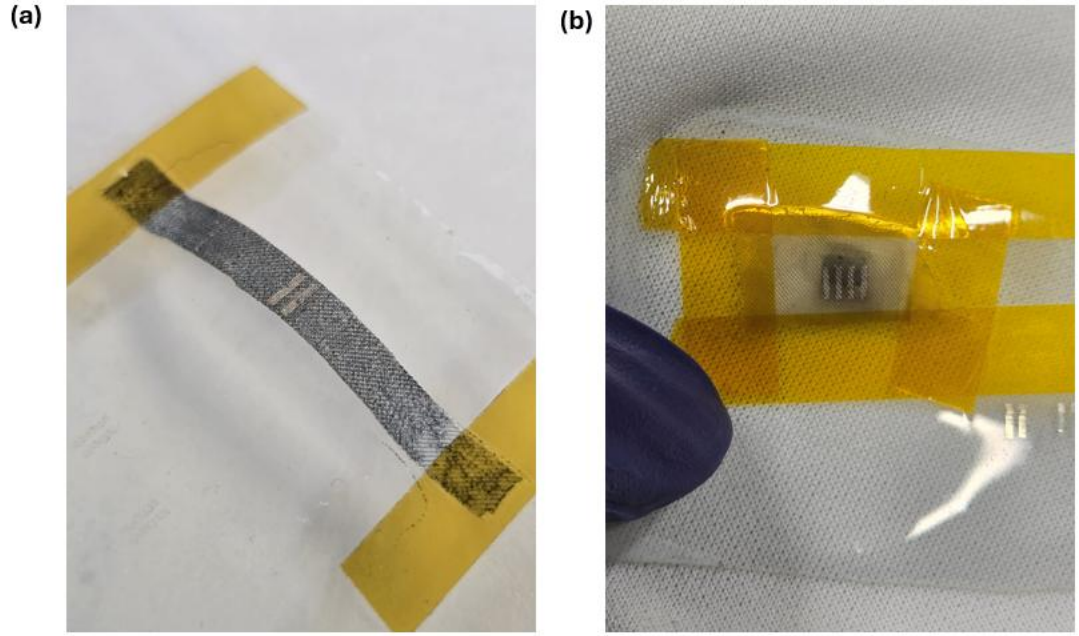

Figure 6. 37 Photograph Images of a) Device 6 and b) Device 7

To address this, we made a dedicated gas-sensing measurement setup at the University of Milano-Bicocca, as shown in Figure 6.38. Future work will also utilize this setup to carry out comprehensive sensing studies on the remaining devices, including Device 4, Device 5, Device 6, and Device 7.

Figure 6. 38 Gas sensing setup at University of Milano Bicocca

6.4 Summary

This chapter introduces a novel textile-based gas sensor addressing the growing need for low-cost, flexible environmental monitoring, featuring hand-embroidered silver interdigitated electrodes (IDEs) paired with drop-cast rGO/CuO sensing ink, alongside inkjet-printed silver/PEDOT:PSS configurations. The rGO/CuO sensing ink was synthesised via a hydrothermal method and comprehensively characterised using spectroscopic and microscopic techniques to evaluate its structural and morphological properties. Hand-embroidered sensor devices fabricated on nylon substrates were investigated using both single metal oxide (rGO/CuO) and double metal oxide (rGO/CuCoOx) hybrid inks to assess performance enhancement. Seven devices fabricated on nylon substrates demonstrated selective chemiresistive detection: Device 1(Embroidered nylon with rGO/CuO) achieved 14.5% response to 10 ppm NO_2 (LOD 6 ppm, 8.9%), 2.3% to 10 ppm NH_3, and 0.66% to 1 ppm CH_2O with no detectable response to CO_2. Device 2 (Embroidered nylon with rGO/$CuCoO_x$) boosted NO_2 sensitivity to 53.5% while retaining NH_3 response at ~1%; indicating the beneficial role of double metal oxide functionalization with NO_2. In contrast, Device 3, fabricated using printed PEDOT:PSS and drop-casted rGO/CuCoOx ink, showed negligible response, highlighting the importance of electrode design, which was also optimised by printing silver electrodes on Device 3 and fabricated Device 7 (Printed Silver electrodes on Printed PEDOT: PSS). My Findings offer a scalable, low-cost, and textile-compatible gas sensing platform that does not require advanced fabrication facilities and is suitable for indicative and distributed gas monitoring in industrial and resource-limited environments, as its flexible textile-based design allows direct installation on working shirts (e.g., collars or sleeves) or in industrial curtains,with future potential for indoor air-quality monitoring following further sensitivity optimization. Future work will focus on systematic evaluation of inkjet-printed sensor devices and on optimizing the hand-embroidered sensors through the incorporation of rGO/CuO/SnO_2 quantum dots to further enhance sensing performance.

CHAPTER 7

7.1 Conclusion

This thesis has systematically investigated the surface modification of polymer substrates, the synthesis of graphene-based functional nanomaterials, and their integration into flexible, textile-based gas sensing devices, with the overarching goal of enabling scalable, feasible sensing platforms suitable for real-world deployment. By combining surface engineering, material development, and device fabrication, the work establishes a coherent framework for translating fundamental surface and material insights into practical sensing applications, particularly in environments where conventional microfabrication approaches are impractical.

The first part of this thesis focused on understanding the effects of oxygen plasma treatment and subsequent ageing on polymer surfaces. In Chapter 3, the ageing behaviour of plasma-treated PTFE was examined, revealing that plasma pressure plays a critical role in governing surface morphology, chemical functionalization, and long-term wettability evolution. The results demonstrated that plasma treatment induces significant morphological and chemical changes, while ageing leads to a dynamic competition between surface roughness and chemical functionality before reaching a stabilised state. These findings provide fundamental insight into hydrophobic recovery and long-term surface stability, which are essential considerations for functional polymer surfaces used in advanced applications.

Building on this foundation, Chapter 4 extended the ageing study to nylon textiles, a material of direct relevance to wearable and textile-based devices. Oxygen plasma treatment was shown to dramatically enhance surface wettability and induce persistent morphological changes, while ageing resulted in partial hydrophobic recovery governed by both surface chemistry and topography. Importantly, this chapter demonstrated the practical significance of surface activation by showing that plasma-treated nylon enables improved deposition and adhesion of rGO/CuO coatings. These results establish a clear link between plasma-induced surface modification and enhanced functional material integration, providing a critical bridge between surface science and device fabrication.

Chapter 5 addressed the synthesis and characterization of graphene-based nanomaterials for sensing applications. Graphene oxide and graphene quantum dots were successfully synthesized and comprehensively characterized, with detailed analysis revealing the influence of synthesis parameters on morphology, structure, and yield. While graphene quantum dots

exhibited promising nanoscale and optical properties, their low yield limited their immediate applicability in textile-based devices. Consequently, the focus shifted toward rGO/metal oxide hybrid nanocomposites, including rGO/metal oxides systems, which demonstrated well-defined hybrid structures and strong potential for gas sensing. This chapter established the material basis for developing functional sensing inks compatible with flexible and textile substrates.

The final part of the thesis, presented in Chapter 6, integrated the surface-engineered textiles and graphene-based hybrid materials into functional gas sensing devices. A novel textile-based chemiresistive gas sensor was developed using hand-embroidered silver interdigitated electrodes and solution-processable rGO/metal oxide inks, alongside inkjet-printed electrode configurations. The fabricated devices demonstrated selective detection of environmentally relevant gases, with single metal oxide rGO/CuO sensors showing measurable responses to NO_2, NH_3, and CH_2O, and double metal oxide rGO/$CuCoO_x$ sensors exhibiting a substantial enhancement in NO_2 sensitivity. These results highlight the critical role of material hybridization and electrode design in improving sensing performance. Moreover, the textile-based and flexible nature of the devices enables direct installation on working garments or industrial textiles, supporting their use in distributed and indicative gas monitoring.

Overall, this thesis demonstrates that the combination of plasma-assisted surface modification, graphene-based hybrid nanomaterials, and textile-compatible fabrication techniques enables the development of scalable, and flexible gas sensing platforms. Building upon fundamental studies of surface and material behaviour with practical device realisation, this work offers viable solutions for gas monitoring in industrial, rural, and resource-limited environments. Ultimately, while the objectives of this research have been successfully achieved, several areas remain where further improvement is possible, particularly bending and durability tests. These limitations highlight important directions for future work towards wearable sensors, including more ambitious strategies for sensor integration and real-world deployment. With continued optimisation of sensing materials, electrode architectures, and inkjet-printed device configurations, the proposed platform also holds strong potential for future indoor air-quality monitoring applications. Collectively, the outcomes of this thesis contribute to advancing the field of smart textiles and flexible sensors, paving the way

toward accessible and deployable sensing technologies for real-world environmental monitoring

7.2 Future Work

Wearable gas sensors are increasingly needed for indoor environments due to prolonged human exposure to indoor air pollutants and volatile organic compounds released from household materials, cleaning agents, and furnishings. Integrating sensing devices into wearable textiles enables continuous, real-time monitoring of air quality close to the human body, providing early warnings of harmful gas exposure. Such systems can support improved indoor safety, personal health assessment, and smart living applications without disrupting daily activities.

In future, this research will be extended in two main directions. First, efforts will focus on identifying and optimizing suitable printing techniques for depositing rGO/metal-oxide–based inks onto textile substrates, with the aim of achieving uniform, durable, and scalable fully printed wearable sensor. Alongside this, the sensing performance of the fabricated devices will be evaluated toward a wider range of target gases to broaden their applicability. Second, graphene quantum dots and rGO/CuO/SnO_2 quantum-dot–based sensing layers will be explored to further enhance sensitivity, selectivity, and stability. These developments are intended to optimize the overall device performance and enable the fabrication of flexible, lightweight, and reliable wearable sensors. Ultimately, the goal is to develop textile-integrated sensing platforms that are compatible with indoor environments and capable of continuously monitoring volatile organic compounds (VOCs) relevant to human health and indoor air quality.

7.3 Acknowledgements

This project has been carried out within the MUSA – Multilayered Urban Sustainability Action – project, funded by the European Union – NextGenerationEU, under the National Recovery and Resilience Plan (NRRP) Mission 4 Component 2 Investment Line 1.5: Strengthening of research structures and creation of R&D “innovation ecosystems”, set up of “territorial leaders in R&D”

References

1. Dai, J., et al., *Printed gas sensors.* Chemical Society Reviews, 2020. 49(6): p. 1756-1789.
2. Middleton, W.D., *Frank Julian Sprague: electrical inventor & engineer*. 2009: Indiana University Press.
3. Barry, M.J.E.R.J., *Canaries in the coal mine*. 2013, European Respiratory Society. p. 1469-1471.
4. Bai, J. and B.X. Zhou, *Titanium Dioxide Nanomaterials for Sensor Applications.* Chemical Reviews, 2014. 114(19): p. 10131-10176.
5. Donarelli, M. and L. Ottaviano, *2D Materials for Gas Sensing Applications: A Review on Graphene Oxide, MoS2, WS2 and Phosphorene.* Sensors, 2018. 18(11).
6. Mao, S., G.H. Lu, and J.H. Chen, *Nanocarbon-based gas sensors: progress and challenges.* Journal of Materials Chemistry A, 2014. 2(16): p. 5573-5579.
7. Shimizu, Y. and M. Egashira, *Basic aspects and challenges of semiconductor gas sensors.* Mrs Bulletin, 1999. 24(6): p. 18-24.
8. Meng, Z., et al., *Electrically-Transduced Chemical Sensors Based on Two Dimensional Nanomaterials.* Chemical Reviews, 2019. 119(1): p. 478-598.
9. Liu, H., et al., *Microhotplates for metal oxide semiconductor gas sensor applications—Towards the CMOS-MEMS monolithic approach.* Micromachines, 2018. 9(11): p. 557.
10. Tomchenko, A.A., et al., *Semiconducting metal oxide sensor array for the selective detection of combustion gases.* Sensors and Actuators B-Chemical, 2003. 93(1-3): p. 126-134.
11. Sun, Y.F., et al., *Metal Oxide Nanostructures and Their Gas Sensing Properties: A Review.* Sensors, 2012. 12(3): p. 2610-2631.
12. Comini, E. and G. Sberveglieri, *Metal oxide nanowires as chemical sensors.* Materials Today, 2010. 13(7-8): p. 28-36.
13. Li, Z.J., et al., *Advances in designs and mechanisms of semiconducting metal oxide nanostructures for high-precision gas sensors operated at room temperature.* Materials Horizons, 2019. 6(3): p. 470-506.
14. Georgakilas, V., et al., *Functionalization of Graphene: Covalent and Non-Covalent Approaches, Derivatives and Applications.* Chemical Reviews, 2012. 112(11): p. 6156-6214.
15. Li, Z.B. and S.L. Wong, *Functionalization of 2D transition metal dichalcogenides for biomedical applications.* Materials Science and Engineering C-Materials for Biological Applications, 2017. 70: p. 1095-1106.
16. Khan, M., et al., *Graphene based metal and metal oxide nanocomposites: synthesis, properties and their applications.* Journal of Materials Chemistry A, 2015. 3(37): p. 18753-18808.
17. Hu, G.H., et al., *Functional inks and printing of two-dimensional materials.* Chemical Society Reviews, 2018. 47(9): p. 3265-3300.
18. Nawab, Y. and K. Shaker, *Textile engineering: an introduction*. 2023: Walter de Gruyter GmbH & Co KG.
19. Weng, W., et al., *Smart electronic textiles.* 2016. 55(21): p. 6140-6169.

20. Zhou, H.P., et al., *Wearable, Flexible, Disposable Plasma-Reduced Graphene Oxide Stress Sensors for Monitoring Activities in Austere Environments.* Acs Applied Materials & Interfaces, 2019. 11(16): p. 15122-15132.
21. Xu, L.L., et al., *Coolmax/graphene-oxide functionalized textile humidity sensor with ultrafast response for human activities monitoring.* Chemical Engineering Journal, 2021. 412.
22. Qureshi, S., et al., *Silver Conductive Threads-Based Embroidered Electrodes on Textiles as Moisture Sensors for Fluid Detection in Biomedical Applications.* Materials, 2021. 14(24).
23. Kang, M.A., et al., *Highly sensitive and wearable gas sensors consisting of chemically functionalized graphene oxide assembled on cotton yarn.* Rsc Advances, 2018. 8(22): p. 11991-11996.
24. Anwer, A.H., et al., *State-of-the-Art advances and challenges in wearable gas sensors for emerging applications: Innovations and future prospects.* Chemical Engineering Journal, 2024. 502.
25. Szulc, J., et al., *Low temperature plasma for textiles disinfection.* International Biodeterioration & Biodegradation, 2018. 131: p. 97-106.
26. Kale, K.H. and A.N. Desai, *Atmospheric pressure plasma treatment of textiles using non-polymerising gases.* Indian Journal of Fibre & Textile Research, 2011. 36(3): p. 289-299.
27. Strobel, M. and C.S. Lyons, *PLASMA SURFACE MODIFICATION OF POLYMERS - RELEVANCE TO ADHESION - GUEST EDITORIAL.* Journal of Adhesion Science and Technology, 1994. 8(4): p. 303-304.
28. Morent, R., et al., *Non-thermal plasma treatment of textiles.* Surface & Coatings Technology, 2008. 202(14): p. 3427-3449.
29. Primc, G. and M. Mozetic, *Surface Modification of Polymers by Plasma Treatment for Appropriate Adhesion of Coatings.* Materials, 2024. 17(7).
30. Dai, L.M., H.J. Griesser, and A.W.H. Mau, *Surface modification by plasma etching and plasma patterning.* Journal of Physical Chemistry B, 1997. 101(46): p. 9548-9554.
31. Friedrich, J., W. Unger, and A. Lippitz, *PLASMA MODIFICATION OF POLYMER SURFACES.* Macromolecular Symposia, 1995. 100: p. 111-115.
32. Puliyalil, H. and U. Cvelbar, *Selective Plasma Etching of Polymeric Substrates for Advanced Applications.* Nanomaterials, 2016. 6(6).
33. Nageswaran, G., L. Jothi, and S. Jagannathan, *Plasma assisted polymer modifications*, in *Non-thermal plasma technology for polymeric materials*. 2019, Elsevier. p. 95-127.
34. Hegemann, D., et al., *Deposition of Functional Plasma Polymers Influenced by Reactor Geometry in Capacitively Coupled Discharges.* Plasma Processes and Polymers, 2016. 13(2): p. 279-286.
35. Vesel, A., et al., *Applications of highly non-equilibrium low-pressure oxygen plasma for treatment of polymers and polymer composites on an industrial scale.* Plasma Physics and Controlled Fusion, 2020. 62(2).
36. Azároff, L., *Overview of X-Ray Diffraction Methods for Nondestructive Testing*, in *Nondestructive Evaluation of Materials*. 1979, Springer. p. 1-19.

37. Bunaciu, A.A., E.G. UdriŞTioiu, and H.Y.J.C.r.i.a.c. Aboul-Enein, *X-ray diffraction: instrumentation and applications.* 2015. 45(4): p. 289-299.
38. Prevéy, P.S.J.S.P., The, *Problems with non-destructive surface x-ray diffraction residual stress measurement.* 1992. 5(4): p. 5-11.
39. Connolly, J.R.J.E.P.S.o.J., *Introduction to X-ray powder diffraction.* 2007. 4: p. p400.
40. Reimer, L., *Transmission electron microscopy: physics of image formation and microanalysis*. Vol. 36. 2013: Springer.
41. Beane, R.J., *Using the scanning electron microscope for discovery based learning in undergraduate courses.* Journal of Geoscience Education, 2004. 52(3): p. 250-253.
42. Chang, H.-H., et al., *Application of scanning electron microscopy and X-ray microanalysis: FE-SEM, ESEM-EDS, and EDS mapping for studying the characteristics of topographical microstructure and elemental mapping of human cardiac calcified deposition.* 2014. 406(1): p. 359-366.
43. Walock, M., *Nanocomposite coatings based on quaternary metalnitrogen*. 2012, Paris, ENSAM.
44. Moecher, D.P., *Characterization and identification of mineral unknowns: A mineralogy term project.* Journal of Geoscience Education, 2004. 52(1): p. 5-9.
45. Ferraro, J.R., *Introductory raman spectroscopy*. 2003: Elsevier.
46. Smith, E. and G. Dent, *Modern Raman spectroscopy: a practical approach*. 2019: John Wiley & Sons.
47. Ferrari, A.C. and D.M.J.N.n. Basko, *Raman spectroscopy as a versatile tool for studying the properties of graphene.* 2013. 8(4): p. 235-246.
48. Graves, P. and D.J.S. Gardiner, *Practical raman spectroscopy.* 1989.
49. John, N. and S. George, *Raman spectroscopy*, in *Spectroscopic methods for nanomaterials characterization*. 2017, Elsevier. p. 95-127.
50. Nikolic, A.J.K.v., *Fourier transform infrared spectroscopy (FTIR).* 2007.
51. Genkawa, T., et al., *Development of a near-infrared/mid-infrared dual-region spectrometer for online process analysis.* 2012. 66(7): p. 773-781.
52. Bacsik, Z., J. Mink, and G.J.A.s.r. Keresztury, *FTIR spectroscopy of the atmosphere. I. Principles and methods.* 2004. 39(3): p. 295-363.
53. Mbonyiryivuze, A., et al., *Fourier transform infrared spectroscopy for sepia melanin.* 2015.
54. Smith, B.C., *Fundamentals of Fourier transform infrared spectroscopy*. 2011: CRC press.
55. Perkampus, H.-H., *UV-VIS Spectroscopy and its Applications*. 2013: Springer Science & Business Media.
56. Termtanun, M., *Photocatalytic degradation of pesticides using TiO2 nanoparticles*. 2013, University of Nottingham.
57. Penner, M.H., *Basic principles of spectroscopy*, in *Food analysis*. 2017, Springer. p. 79-88.
58. Clark, B., T. Frost, and M. Russell, *UV Spectroscopy: Techniques, instrumentation and data handling*. Vol. 4. 1993: Springer Science & Business Media.

59. Xiang, Y.J., et al., *Temperature Dependence of Water Contact Angle on Teflon AF1600.* Langmuir, 2022. 38(4): p. 1631-1637.
60. Reznickova, A., et al., *Plasma treatment of PTFE at elevated temperature: The effect of surface properties on its biological performance.* Materials Today Communications, 2022. 31: p. 103254.
61. Bauer, J. and F. Frost. *Orientation-dependent nanostructuring of titanium surfaces by low-energy ion beam erosion*. in *Surface and Interface Analysis*. 2020. John Wiley and Sons Ltd.
62. Pachchigar, V., et al., *Hydrophobic to superhydrophobic and hydrophilic transitions of Ar plasma-nanostructured PTFE surfaces.* Plasma Processes and Polymers, 2022. 19(9).
63. Pachchigar, V., et al., *Self-cleaning and bouncing behaviour of ion irradiation produced nanostructured superhydrophobic PTFE surfaces.* Surface and Coatings Technology, 2021. 420.
64. Sprick, R.S., et al., *Polymer photocatalysts with plasma-enhanced activity.* Journal of Materials Chemistry A, 2020. 8(15): p. 7125-7129.
65. Akkan, C.K., et al., *Plasma and short pulse laser treatment of medical grade PEEK surfaces for controlled wetting.* Materials Letters, 2013. 109: p. 261-264.
66. López, C.D., et al., *Surface modification of polytetrafluoroethylene thin films by non-coherent UV light and water treatment for electrowetting applications.* Progress in Organic Coatings, 2020. 149.
67. Zanini, S., et al., *Modification of the PTFE wettability by oxygen plasma treatments: influence of the operating parameters and investigation of the ageing behaviour.* Journal of Physics D-Applied Physics, 2014. 47(32).
68. Al-Maliki, H., et al., *Surface characterization of polytetrafluoroethylene treated by atmospheric plasma.* International Review of Applied Sciences and Engineering, 2018. 9(1): p. 1-7.
69. Hubert, J., et al., *Synthesis and texturization processes of (super)-hydrophobic fluorinated surfaces by atmospheric plasma.* Journal of Materials Research, 2015. 30(21): p. 3177-3191.
70. Kang, H., S.H. Lee, and K. Kim, *Wettability of polytetrafluoroethylene surfaces by plasma etching modifications.* Plos One, 2023. 18(3).
71. Ryu, J., et al., *Nearly Perfect Durable Superhydrophobic Surfaces Fabricated by a Simple One-Step Plasma Treatment.* Scientific Reports, 2017. 7.
72. Kumari, S., et al., *Development of Superhydrophobic PTFE Surface Using Oxygen Plasma Processing.* Ieee Transactions on Plasma Science, 2024. 52(7): p. 2524-2532.
73. Salapare, H.S., et al., *Stability of the hydrophilic and superhydrophobic properties of oxygen plasma-treated poly(tetrafluoroethylene) surfaces.* Journal of Colloid and Interface Science, 2013. 396: p. 287-292.
74. Pachchigar, V., et al., *Hydrophobic to superhydrophobic and hydrophilic transitions of Ar plasma-nanostructured PTFE surfaces.* Plasma Processes and Polymers, 2022. 19(9).
75. Wilson, D.J., R.L. Williams, and R.C. Pond, *Plasma modification of PTFE surfaces Part I: Surfaces immediately following plasma treatment.* Surface and Interface Analysis, 2001. 31(5): p. 385-396.

76. Carbone, E.A.D., et al. *PTFE treatment by remote atmospheric Ar/O2 plasmas: a simple reaction scheme model proposal*. in *5th International Workshop and Summer School on Plasma Physics (IWSSPP)*. 2012. Kiten, BULGARIA.
77. Nakamatsu, J., et al., *Ageing of plasma-treated poly(tetrafluoroethylene) surfaces.* Journal of Adhesion Science and Technology, 1999. 13(7): p. 753-761.
78. König, U., et al., *Stability and ageing of plasma treated poly(tetrafluoroethylene) surfaces.* Colloids and Surfaces B-Biointerfaces, 2002. 25(4): p. 313-324.
79. Barni, R., et al., *Mass spectroscopy of oxygen plasmas with energetic ions.* AIP Advances, 2023. 13(6).
80. Kumari, S., et al., *Development of Superhydrophobic PTFE Surface Using Oxygen Plasma Processing.* IEEE Transactions on Plasma Science, 2023: p. 1-9.
81. Cho, Y. and C.H. Park, *Objective quantification of surface roughness parameters affecting superhydrophobicity.* Rsc Advances, 2020. 10(52): p. 31251-31260.
82. Roman, H.E., et al., *The fractal geometry of polymeric materials surfaces: surface area and fractal length scales.* Soft Matter, 2024. 20(14): p. 3082-3096.
83. Kumari, S., et al., *Development of Superhydrophobic PTFE Surface Using Oxygen Plasma Processing.* Ieee Transactions on Plasma Science, 2023.
84. Chien, H.H., et al., *Effects of plasma power and reaction gases on the surface properties of ePTFE materials during a plasma modification process.* Surface and Coatings Technology, 2013. 228(SUPPL.1): p. S477-S481.
85. Cheng, C.-Y., et al., *Surface modification of polytetrafluoroethylene by atmospheric pressure plasma-grafted polymerization.* Plasma Chemistry and Plasma Processing, 2020. 40: p. 1507-1523.
86. Okubo, M., et al., *Preparation of PTFE film with adhesive surface treated by atmospheric-pressure nonthermal plasma graft polymerization.* IEEE transactions on industry applications, 2010. 46(5): p. 1715-1721.
87. Almond, J., et al., *Determination of the carbonyl index of polyethylene and polypropylene using specified area under band methodology with ATR-FTIR spectroscopy.* E-Polymers, 2020. 20(1): p. 369-381.
88. Bradford, J.P., et al., *Low-Temperature Plasmas Improving Chemical and Cellular Properties of Poly (Ether Ether Ketone) Biomaterial for Biomineralization.* Materials, 2024. 17(1): p. 17.
89. Ding, Y.F., et al., *High performance n-type Ag2Se film on nylon membrane for flexible thermoelectric power generator.* Nature Communications, 2019. 10.
90. Palmer, R.J. and U.b.S.J.K.O.E.o.C. Technology, *Polyamides, plastics.* Kirk-Othmer Encyclopedia of Chemical Technology., 2000.
91. Shakiba, M., et al., *Nylon-A material introduction and overview for biomedical applications.* Polymers for Advanced Technologies, 2021. 32(9): p. 3368-3383.
92. Mukhopadhyay, S.K., *Manufacturing, properties and tensile failure of nylon fibres*. Handbook of Tensile Properties of Textile and Technical Fibres, ed. A.R. Bunsell. Vol. 91. 2009. 197-222.
93. Primc, G., *Surface Modification of Polyamides by Gaseous Plasma-Review and Scientific Challenges.* Polymers, 2020. 12(12).

94. Yip, J., et al., *Low temperature plasma-treated nylon fabrics.* Journal of Materials Processing Technology, 2002. 123(1): p. 5-12.
95. Thompson, R., et al., *Low-frequency plasma activation of nylon 6.* Applied Surface Science, 2021. 544.
96. Karande, S., et al., *Open-Air Plasma Treatment to Enhance Nanoparticle Adhesion on Nylon- and Cotton-Based Fabrics for Chemical Protection.* Acs Applied Materials & Interfaces, 2026.
97. Oshiro, M., K. Takashima, and Y. Furukawa, *Infrared Stark spectra for a Nylon 6 film.* Chemical Physics Letters, 2019. 728: p. 32-36.
98. Salapare, H.S., T. Darmanin, and F. Guittard, *Reactive-ion etching of nylon fabric meshes using oxygen plasma for creating surface nanostructures.* Applied Surface Science, 2015. 356: p. 408-415.
99. Balakrishnan, T., et al., *Recent Progress on Functionalized Graphene Quantum Dots and Their Nanocomposites for Enhanced Gas Sensing Applications.* Nanomaterials, 2024. 14(1): p. 25.
100. Sun, D.J., et al., *Graphene-enhanced metal oxide gas sensors at room temperature: a review.* Beilstein Journal of Nanotechnology, 2018. 9: p. 2832-2844.
101. Wang, C.Y., et al., *Review of recent progress on graphene-based composite gas sensors.* Ceramics International, 2021. 47(12): p. 18.
102. Novoselov, K.S., et al., *A roadmap for graphene.* Nature, 2012. 490(7419): p. 192-200.
103. Tan, C.L., et al., *Recent Advances in Ultrathin Two-Dimensional Nanomaterials.* Chemical Reviews, 2017. 117(9): p. 6225-6331.
104. Izquierdo-García, P., J.M. Fernández-García, and N. Martín, *Twenty Years of Graphene: From Pristine to Chemically Engineered Nano-Sized Flakes.* Journal of the American Chemical Society, 2024. 146(47): p. 32222-32234.
105. Tariq, M., et al., *Recent advances in graphene oxide and metal oxides composites synthesis and their applications in wastewater treatment: Removal of dyes, heavy metals, and pharmaceutical contaminants.* Separation and Purification Technology, 2025. 376: p. 20.
106. Elhenawy, S., et al., *Recent Developments and Advancements in Graphene-Based Technologies for Oil Spill Cleanup and Oil-Water Separation Processes.* Nanomaterials, 2022. 12(1).
107. Lee, B.-J., S.-C. Cho, and G.-H.J.C.A.P. Jeong, *Atmospheric pressure plasma treatment on graphene grown by chemical vapor deposition.* 2015. 15(5): p. 563-568.
108. Acik, M., et al., *Unusual infrared-absorption mechanism in thermally reduced graphene oxide.* Nature Materials, 2010. 9(10): p. 840-845.
109. Guo, H.L., et al., *A Green Approach to the Synthesis of Graphene Nanosheets.* Acs Nano, 2009. 3(9): p. 2653-2659.
110. Emiru, T.F., D.W.J.E.J.o.B. Ayele, and A. Sciences, *Controlled synthesis, characterization and reduction of graphene oxide: A convenient method for large scale production.* Egyptian Journal of Basic and Applied Sciences, 2017. 4(1): p. 74-79.

111. Zhang, T.Y. and D. Zhang, *Aqueous colloids of graphene oxide nanosheets by exfoliation of graphite oxide without ultrasonication.* Bulletin of Materials Science, 2011. 34(1): p. 25-28.
112. Méndez-Lozano, N., F. Pérez-Reynoso, and C. González-Gutiérrez, *Eco-Friendly Approach for Graphene Oxide Synthesis by Modified Hummers Method.* Materials, 2022. 15(20): p. 9.
113. Agarwal, K., H. Rai, and S. Mondal, *Quantum dots: an overview of synthesis, properties, and applications.* Materials Research Express, 2023. 10(6): p. 26.
114. Kim, S., et al., *Anomalous Behaviors of Visible Luminescence from Graphene Quantum Dots: Interplay between Size and Shape.* Acs Nano, 2012. 6(9): p. 8203-8208.
115. Panachikkool, M. and T. Pandiyarajan, *Graphene quantum dots as game-changers in solar cell technology: a review of synthetic processes and performance enhancement.* Carbon Letters, 2024. 34(1): p. 445-475.
116. Rasheed, P.A., et al., *Graphene quantum dots for biosensing and bioimaging.* Rsc Advances, 2024. 14(23): p. 16001-16023.
117. Balkanloo, P.G., K.M. Sharifi, and A.P. Marjani, *Graphene quantum dots: synthesis, characterization, and application in wastewater treatment: a review.* Materials Advances, 2023. 4(19): p. 4272-4293.
118. Balakrishnan, T., et al., *Recent Progress on Functionalized Graphene Quantum Dots and Their Nanocomposites for Enhanced Gas Sensing Applications.* Nanomaterials, 2024. 14(1).
119. He, S.J., et al., *Carbon monoxide gas sensor based on an α-Fe2O3/reduced graphene oxide quantum dots composite film integrated Michelson interferometer.* Measurement Science and Technology, 2022. 33(3).
120. Yang, S.L., et al., *A novel synthesis of graphene quantum dots via thermal treatment of crude graphite oxide in a dry and alkaline condition, and their application in uranyl detection.* Heliyon, 2020. 6(9).
121. Tian, R.B., et al., *Solvothermal method to prepare graphene quantum dots by hydrogen peroxide.* Optical Materials, 2016. 60: p. 204-208.
122. Pan, D.Y., et al., *Hydrothermal Route for Cutting Graphene Sheets into Blue-Luminescent Graphene Quantum Dots.* Advanced Materials, 2010. 22(6): p. 734-+.
123. Fang, X.L., et al., *Graphene quantum dots optimization of dye-sensitized solar cells.* Electrochimica Acta, 2014. 137: p. 634-638.
124. Joshi, P., R. Mishra, and R.J. Narayan, *Biosensing applications of carbon-based materials.* Current Opinion in Biomedical Engineering, 2021. 18: p. 9.
125. Kotsyubynsky, V., et al., *NaOH-assisted hydrothermal reduction of graphene oxide.* Journal of Physics-Condensed Matter, 2024. 36(49).
126. Fan, T.J., et al., *Controllable size-selective method to prepare graphene quantum dots from graphene oxide.* Nanoscale Research Letters, 2015. 10: p. 1-8.
127. Chhabra, V.A., et al., *Synthesis and spectroscopic studies of functionalized graphene quantum dots with diverse fluorescence characteristics.* Rsc Advances, 2018. 8(21): p. 11446-11454.

128. Zhu, S.J., et al., *Graphene quantum dots with controllable surface oxidation, tunable fluorescence and up-conversion emission.* Rsc Advances, 2012. 2(7): p. 2717-2720.
129. Norizan, M.N., et al., *Heterojunctions of rGO/Metal Oxide Nanocomposites as Promising Gas-Sensing Materials-A Review.* Nanomaterials, 2022. 12(13).
130. Li, G.D., et al., *Design and application of highly responsive and selective rGO-SnO2 nanocomposites for NO2 monitoring.* Materials Characterization, 2020. 163.
131. Chen, T.T., et al., *Cu-doped SnO2/rGO nanocomposites for ultrasensitive H2S detection at low temperature.* Microsystems & Nanoengineering, 2023. 9(1).
132. Viswanathan, A., A.N. Shetty, and V.J.F.B. Subburaj, *Faradaic supercapattery of rGO/PANI/CuO/SnO2 nanocomposite and its application in DC-DC switched capacitor convertors.* Future Batteries, 2025. 5: p. 100022.
133. AlSalhi, M.S., et al., *Construction of SnO2/CuO/rGO nanocomposites for photocatalytic degradation of organic pollutants and antibacterial applications.* Environmental Research, 2023. 222.
134. Chen, Z., et al., *Real-time, noise and drift resilient formaldehyde sensing at room temperature with aerogel filaments.* Science Advances, 2024. 10(6).
135. Naresh, N., et al., *Microwave-assisted hydrothermal synthesis of SnO2/reduced graphene-oxide nanocomposite as anode material for high performance lithium-ion batteries.* Journal of Materials Science-Materials in Electronics, 2018. 29(17): p. 14723-14732.
136. Dutta, S., et al., *Highly efficient photocatalytic activity of CuO quantum dot decorated rGO nanocomposites.* Journal of Physics D-Applied Physics, 2016. 49(31).
137. Hibino, T., et al., *Design of a Rechargeable Fuel-Cell Battery with Enhanced Performance and Cyclability.* Journal of the Electrochemical Society, 2016. 163(7): p. A1420-A1428.
138. Wang, C.X., et al., *Metal Oxide Gas Sensors: Sensitivity and Influencing Factors.* Sensors, 2010. 10(3): p. 2088-2106.
139. Gurlo, A., *Nanosensors: towards morphological control of gas sensing activity. SnO2, In2O3, ZnO and WO3 case studies.* Nanoscale, 2011. 3(1): p. 154-165.
140. Moon, H.G., et al., *Chemiresistive Electronic Nose toward Detection of Biomarkers in Exhaled Breath.* Acs Applied Materials & Interfaces, 2016. 8(32): p. 20969-20976.
141. Joshi, N., et al., *A review on chemiresistive room temperature gas sensors based on metal oxide nanostructures, graphene and 2D transition metal dichalcogenides.* Microchimica Acta, 2018. 185(4).
142. Shi, Z., et al., *MXene-Based Materials for Solar Cell Applications.* Nanomaterials, 2021. 11(12).
143. Guo, L., et al., *Improved NO2 Gas Sensing Properties of Graphene Oxide Reduced by Two-beam-laser Interference.* Scientific Reports, 2018. 8.
144. Zheng, H.C., et al., *Cube-like CuCoO nanostructures on reduced graphene oxide for H2 generation from ammonia borane.* Inorganic Chemistry Frontiers, 2018. 5(5): p. 1180-1187.

145. Lin, Q.Q., Y. Li, and M.J. Yang, *Tin oxide/graphene composite fabricated via a hydrothermal method for gas sensors working at room temperature.* Sensors and Actuators B-Chemical, 2012. 173: p. 139-147.
146. Li, Q., et al., *Graphene and its composites with nanoparticles for electrochemical energy applications.* Nano Today, 2014. 9(5): p. 668-683.
147. Jin, X.Y., et al., *Effects of hydrothermal temperature and time on hydrothermal synthesis of colloidal hydroxyapatite nanorods in the presence of sodium citrate.* Journal of Colloid and Interface Science, 2015. 450: p. 151-158.
148. Das, S. and V. Jayaraman, *SnO2: A comprehensive review on structures and gas sensors.* Progress in Materials Science, 2014. 66: p. 112-255.
149. Wu, T.C., et al., *Machine-intelligent inkjet-printed α-Fe2O3/rGO towards NO2 quantification in ambient humidity.* Sensors and Actuators B-Chemical, 2020. 321.
150. Shafiei, M., et al., *Platinum/Graphene Nanosheet/SiC Contacts and Their Application for Hydrogen Gas Sensing.* Journal of Physical Chemistry C, 2010. 114(32): p. 13796-13801.
151. Salehi-Khojin, A., et al., *On the Sensing Mechanism in Carbon Nanotube Chemiresistors.* Acs Nano, 2011. 5(1): p. 153-158.
152. Prajesh, R., et al., *Effect of IDE placement on response in metal oxide gas sensors.* Materials Research Express, 2018. 5(9).
153. Yun, Y.J., et al., *Ultrasensitive and Highly Selective Graphene-Based Single Yarn for Use in Wearable Gas Sensor.* Scientific Reports, 2015. 5.
154. Jung, W.T., et al., *High-response room-temperature NO2 gas sensor fabricated with thermally reduced graphene oxide-coated commercial cotton fabric.* Heliyon, 2024. 10(2).
155. Park, H.J., et al., *Highly flexible, mechanically stable, and sensitive NO2 gas sensors based on reduced graphene oxide nanofibrous mesh fabric for flexible electronics.* Sensors and Actuators B-Chemical, 2018. 257: p. 846-852.
156. Zhu, J.X., et al., *Machine learning-enabled textile-based graphene gas sensing with energy harvesting-assisted IoT application.* Nano Energy, 2021. 86.
157. Pattanarat, K., et al., *High Conductivity and Durability Textile Gas Sensor-Based Polyaniline-Decorated-Poly(3,4-ethylenedioxythiophene)/Poly(4-styrenesulfonate) for Ammonia Detection.* Acs Applied Polymer Materials, 2022. 4(12): p. 9006-9014.
158. Maity, A., S. Mitra, and B. Ghosh, *Textile Based Lead-Free Halide Perovskite CH3NH3SnI3 Ammonia Gas Sensor Working at Room Temperature.* Acs Applied Electronic Materials, 2024. 6(4): p. 2677-2682.
159. Shiu, B.C., et al., *Preparation and Characterization of PEDOT:PSS/TiO2 Micro/Nanofiber-Based Gas Sensors.* Polymers, 2022. 14(9).
160. Kim, S., et al., *Surface functionalized MXene ink-enabled washable smart e-textiles with exceptional gas sensing properties.* Materials Today, 2025. 88: p. 251-262.
161. Skrzetuska, E., P. Szablewska, and A. Patalas, *Manufacture and Analysis of a Textile Sensor Response to Chemical Stimulus Using Printing Techniques and Embroidery for Health Protection.* Sustainability, 2024. 16(22).

162. Ogbeide, O., et al., *Inkjet-Printed rGO/binary Metal Oxide Sensor for Predictive Gas Sensing in a Mixed Environment.* Advanced Functional Materials, 2022. 32(25).
163. Banotra, A., et al., *Impact of rGO concentration on the physical characteristics of CuO/rGO nanocomposite for sensing and optoelectronic applications.* ECS Journal of Solid State Science and Technology, 2023. 12(6): p. 067001.
164. Haldar, T., et al., *Exploring MOF-derived CuO/rGO heterostructures for highly efficient room temperature CO2 sensors.* Acs Sensors, 2024. 9(11): p. 5856-5865.
165. Sinha, A., et al., *Wearable humidity sensor embroidered on a commercial face mask and its electrical properties.* Journal of Materials Science, 2023. 58(4): p. 1680-1693.
166. Derby, B., *Inkjet Printing of Functional and Structural Materials: Fluid Property Requirements, Feature Stability, and Resolution*, in *Annual Review of Materials Research, Vol 40*, D.R. Clarke, M. Ruhle, and F. Zok, Editors. 2010. p. 395-414.
167. Ng, L.W., et al., *Printing of graphene and related 2D materials.* SPRINGER, 2019. 10: p. 978-3.
168. Khan, J., et al., *Flexible and Highly Selective No2 Gas Sensor Based on Direct-Ink-Writing of Eco-Friendly Aqueous Graphene Oxide for Smart Wearable Application.* Chemosphere.
169. Zhang, F., et al., *A flexible and wearable NO(2) gas detection and early warning device based on a spraying process and an interdigital electrode at room temperature.* Microsyst Nanoeng, 2022. 8: p. 40.
170. Andre, R.S., et al., *Sensitive and Selective NH3 Monitoring at Room Temperature Using ZnO Ceramic Nanofibers Decorated with Poly(styrene sulfonate).* Sensors, 2018. 18(4): p. 13.
171. Beniwal, A., et al., *Room-Temperature-Operated Fe2O3/PANI-Based Flexible and Eco-Friendly Ammonia Sensor With Sub-ppm Detectability.* Ieee Sensors Letters, 2025. 9(2): p. 4.
172. Zhu, X., et al., *Room temperature gas sensors for NH3 detection based on SnO2 films and lamellar-structured Ti3C2Tx MXene heterojunction nanocomposites.* Applied Surface Science, 2024. 660: p. 159976.
173. Ogbeide, O., et al., *Inkjet-Printed rGO/binary Metal Oxide Sensor for Predictive Gas Sensing in a Mixed Environment.* Advanced Functional Materials, 2022. 32(25): p. 9.
174. Hu, J., et al., *One-pot low-energy synthesis of rGO-CuO hybrid for detection of NO2 at room temperature.* Materials Science in Semiconductor Processing, 2022. 138: p. 106289.

Tesi di dottorato realizzata nell'ambito del progetto_MUSA-ECS_00000037-CUP:H43C22000550001_Cup